The Hofstadter spectrum of monolayer and bilayer graphene van der Waals heterostructures with boron nitride

Xi Chen

PhD Thesis

Submitted for the degree of Doctor of Philosophy

October 7, 2015

Declaration

Except where otherwise stated, this thesis is a result of the author's original work and has not been submitted completely or partly for the award of a higher degree elsewhere. The following parts of the thesis have been published, or submitted for publication, in peer reviewed journals:

Parts of chapter 3 published in:

X. Chen, J. R. Wallbank, M. Mucha-Kruczyński, E. McCann and V. I. Fal'ko. *Dirac edges of fractal magnetic minibands in graphene with hexagonal moire superlattices.* Phys. Rev. B **89**, 075401 (2014).

D. S. L. Abergel, J. R. Wallbank, X. Chen, M. Mucha-Kruczyński, V. I. Fal'ko. *Infrared absorption by graphene-hBN heterostructures.* New. J. Phys. **15**, 123009 (2013).

G. L. Yu, R. V. Gorbachev, J. S. Tu, A. V. Kretinin, Y. Cao, R. Jalil, F. Withers, L. A. Ponomarenko, B. A. Piot, M. Potemski, D. C. Elias, X. Chen, K. Watanabe, T. Taniguchi, I. V. Grigorieva, K. S. Novoselov, V. I. Fal'ko, A. K. Geim and A. Mishchenko. *Hierarchy of Hofstadter states and replica quantum Hall ferromagnetism in graphene superlattices.* Nat. Phys **10**, 525 (2014).

J. R. Wallbank, M. Mucha-Kruczyński, X. Chen and V. I. Fal'ko. *Moire superlattice effects in graphene/boron-nitride van der Waals heterostructures.* Ann. Phys. (Berlin), 1 (2015)

X. Chen and V. I. Fal'ko. *Hierarchy of gaps and magnetic minibands in graphene in the presence of the Abrikosov vortex lattice.* Submitted to Phys. Rev. Lett.

Parts of chapter 4 Unpublished original results obtained in collaboration with J. R. Wallbank, M. Mucha-Kruczyński, E. McCann and V. I. Fal'ko.

Parts of chapter 5 Unpublished original results obtained in collaboration with E. McCann.

Parts of chapter 6 Unpublished original results obtained in collaboration with E. McCann.

X. Chen

October 7, 2015

Abstract

In this thesis, we consider the electronic properties of materials created by stacking two-dimensional graphene layers. The first material is a heterostructure created by placing a graphene layer on top of a layer of hexagonal boron nitride. The energy bands are determined as well as the energy spectrum in the presence of a magnetic field applied in the direction perpendicular to the layers. There is a miniband structure that includes gaps and secondary Dirac points as well as a fractal structure of magnetic minibands known as Hofstadter's butterfly[1].

The second material is multilayer graphene, which consists of a small number of graphene layers stacked on top of one another. We determine the effect on the low-energy electronic band structure by applying a magnetic field in the direction parallel to the layers, and find that the parallel field can induce a dramatic change in the band structure, which is known as a Lifshitz transition. Furthermore, depending on the magnitude and the direction of the field within the plane of the graphene layers, it is possible to access different phase regions of the band structure.

We also model the electronic transport properties of multilayer graphene. We use both analytical mode-matching and the numerical recursive Green function methods to study the transport properties of electrons in multilayer graphene in the vicinity of zero energy, zero temperature and zero magnetic field.

[1]Technical terms used in the abstract will be introduced in the following chapters.

Acknowledgements

I thank Dr. McCann and Professor Fal'ko for their kind help, infinite patience and good ideas, which helped me to achieve progress in my research. It has been an immense pleasure and honour to learn from and work with these genius physicists.

Moreover, I would like to thank all the people I have worked at Lancaster University, including a special thanks to J. Wallbank, who is the main collaborator of my study in the theoretical evaluation of the butterfly spectrum, and answered numerous questions with patience. I also thank M. Mucha-Kruczyński, for his brief but insightful explanations of many topics. I offer greetings to him, his wife Amy and their daughter. I also thank D. Cosma for providing me a variety of information, related to everything from academic to British life.

I would like to thank my families, including both Chens and Rens for their support. In particular, I thank my mother and my wife Tina; for Tina, I am ever thankful for our predestined relationship and life together.

Finally, I would like to thank my master; although favour is so great, it makes saying thanks a pointless formality.

Contents

List of Figures

List of Tables

Chapter 1

Introduction

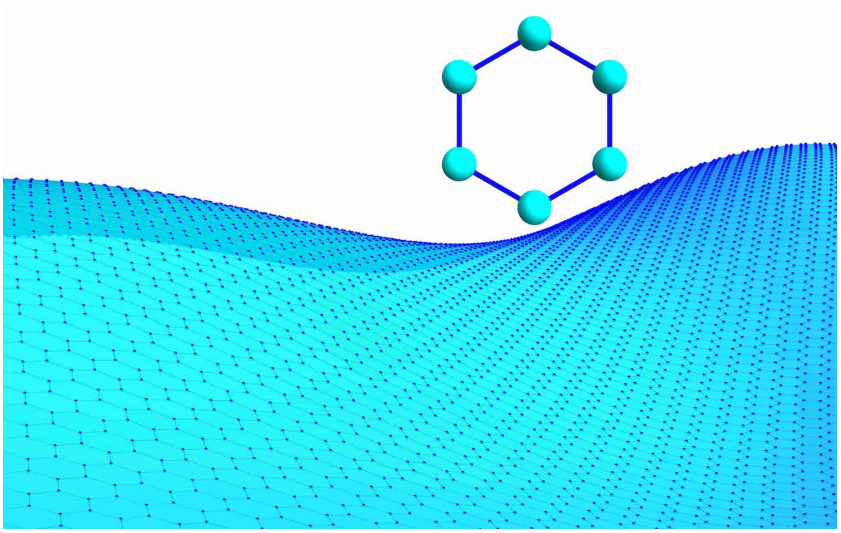

Figure 1.1: Graphene is a two-dimensional material consisting of a single layer of carbon atoms arranged with a honeycomb crystal structure.

Graphene is a two-dimensional material consisting of a single layer of carbon atoms. It can be thought of as being one layer of bulk three-dimensional graphite [1]. Due to its unique properties, graphene is considered to be a promising candidate material for the development of electronic devices [2]. In 2010, the Nobel Prize for Physics was awarded to A. Geim and K. Novoselov [3] for "groundbreaking experiments regarding the two-dimensional material graphene" [4] [1].

In addition to being a two-dimensional material, graphene is chemically stable [5] and is an excellent electronic conductor [6–8], an excellent thermal conductor

[1] All terminologies mentioned in the Chap.1 will be explained systematically in the following chapters.

[9, 10] and is flexible but strong [11, 12] while being transparent to visible light [13]. Graphene generally has great potential for applications in biology [14], chemistry [15] and electronic devices [16].

Electrons in graphene [2] exhibit a Dirac-like spectrum [7] with a linear dispersion relation and an additional spin-like degree of freedom known as pseudospin (the origin of which will be explained in Chap. 2). Electrons in graphene are chiral [17, 18], meaning that the direction of an electron's pseudospin is linked to the direction of its momentum. These electrons are analogous to massless relativistic particles. The unique electronic properties of graphene are manifest in the integer quantum Hall effect [19–26] and in transport as well as scattering properties [27–34].

Soon after the first experiments on graphene, studies involving other two-dimensional materials commenced, including materials such as silicene [35], hexagonal boron nitride (*h*-BN) [36, 37], and graphene oxide [38]. In other words, the work by Profs. Geim and Novoselov [3] opened a new field of physics, that of two-dimensional materials [2, 39].

Recently, research in graphene and other two-dimensional materials has been extended to two-dimensional heterostructures consisting of combinations of different two-dimensional materials. By stacking layers of different two-dimensional materials on top of one another, it is possible to create new two-dimensional heterostructures with novel properties [40–43]. Furthermore, the possibility of producing ideally clean two-dimensional heterostructures has been proven experimentally [44]. The first and, by now, the most developed of these heterostructures is formed by placing graphene on hexagonal boron nitride. Both materials are made from a single layer of atoms arranged with a honeycomb structure. However, in contrast to graphene which is a gapless semiconductor [6, 16], *h*-BN is an insulator with a band gap of approximately 6 electron volts [45]. For this reason, *h*-BN was

[2] Actually, all features described here are for the collective behavior of electrons in graphene, i.e. quasi particle in graphene. For simplicity, we call them "electrons in graphene" from now on.

initially used as a substrate to preserve graphene's electronic properties [36]. The small difference ($\simeq 1.8\%$) between the lattice constants of the two crystals and their crystallographic misalignment generates a large-scale quasi-periodic hexagonal pattern, which is known as the moiré[3] superlattice (mSL) [37, 46, 47]. The smaller the misalignment angle between the two lattices, the larger the moiré superlattice. The huge superlattice (i.e. the size of the super unit cell, maximum $\simeq 14\,\text{nm}$) allows for a much larger magnetic flux per super unit cell as compared to the magnetic flux per unit cell of conventional material. In the moiré-perturbed magnetic fractal spectrum of graphene, there is a peculiar quantum Hall effect [48], which includes a systematic repetition of Dirac-like features at the edges of consecutive minibands. These Dirac-like features form a hierarchy of gaps in the surrounding magnetic spectrum, and are manifest as incompressible states observed via variations of carrier density and of magnetic field [49, 50].

In this thesis, we also study the magnetic minibands of a heterostructure consisting of bilayer graphene and hexagonal boron nitride. A new feature here is that, because the inversion-symmetry is broken by the substrate, the valley symmetry of the electronic spectra is also broken. Despite the existence of perturbations due to the moiré potential, a zero-energy Landau level exists, although its degeneracy is reduced. We also discuss the behaviour of electrons near zero energy in the presence of simple-fraction magnetic flux.

Furthermore, we also consider the electronic properties of multilayer graphene, which consists of a small number of graphene layers stacked on top of one another. There have been many studies regarding the influence of a perpendicular magnetic field [19] on graphene, multilayer graphene and a tilted magnetic field [21–26]. Conversely, there have been few studies [20] that consider the role of a magnetic field parallel to the substrate because the magnetic flux magnitude is severely limited by the small distance between graphene layers. However, at very-low energy, there is an unusual feature of the electronic spectrum of multilayer graphene,

[3]The term "moiré" originates from a French type of textile, traditionally of silk, with a "watered" appearance.

known as a Lifshitz transition. We therefore determine whether the weak effect of the parallel magnetic field is sufficient to influence the Lifshitz transition, and discuss some new features of the electronic spectrum.

Furthermore, we model the electronic transport properties of multilayer graphene [31, 34]. The minimum conductivity of graphene (i.e. the lowest conductivity value measured as a function of gate voltage) does not scale neatly with the number of layers and depends on the temperature and aspect ratio of the sample [29, 30]. From a theoretical perspective, different methodologies have led to different predictions [184]. In this thesis, we compare and contrast two different methods to study the conductivity of graphene.

In addition to this introductory chapter, my thesis is organized as follows. Chapter 2 introduces the electronic properties of graphene and the theoretical models used. In Chapter 3, we present the fractal spectrum of moiré-perturbed single-layer graphene in a magnetic field and we discuss the incompressible states. In Chapter 4, we focus on the peculiar zeroth Landau level of bilayer graphene with a moiré-perturbation in a magnetic field. In Chapter 5, we investigate the electronic energy band structure of multilayer graphene in a parallel magnetic field and compare this with the band structure in the presence of strain. In Chapter 6, we analytically and numerically study the electronic transport properties of graphene, single layer and multilayer graphene.

Chapter 2

Theoretical background

2.1 Crystal structure of graphene

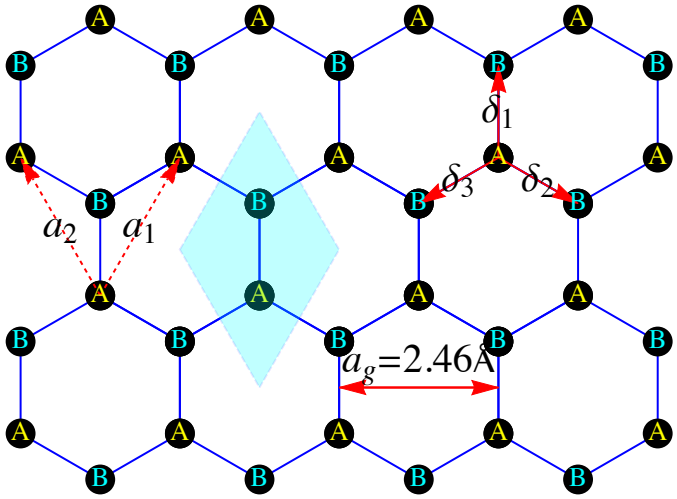

Figure 2.1: Schematic of the crystal structure of SLG. The black dots represent carbon atoms with "A" and "B" as sublattices, and the solid lines between atoms represent covalent bonds. The cyan rhombus is a unit cell.

As shown in Fig. 2.1, graphene is a one-atom-thick sheet composed of carbon atoms [51, 52], arranged in a honeycomb pattern. This crystal structure of single layer graphene (SLG) consists of a hexagonal Bravais lattice with a basis of two non-equivalent atomic sites at each lattice site [53]. In the figure, these two non-equivalent atomic sites are referred to as A and B, (because one can not connect them by primitive lattice vector), and the graphene structure can be taken as consisting of an A sublattice and a B sublattice. Vectors $\boldsymbol{a}_1 = a_g(\frac{1}{2}, \frac{\sqrt{3}}{2})$ and

$\boldsymbol{a}_2 = a_g(-\frac{1}{2}, \frac{\sqrt{3}}{2})$ are two primitive lattice vectors of the graphene Bravais lattice where $a_g = 2.46\,\text{Å}$ is the lattice constant [53]. An arbitrary lattice vector may be written as $\boldsymbol{R} = n_1\boldsymbol{a}_1 + n_2\boldsymbol{a}_2$, $n_1, n_2 \in \mathbb{Z}$. For any atomic site A, the relative positions of the nearest three neighbouring B atomic sites are $\boldsymbol{\delta}_1 = \frac{a_g}{\sqrt{3}}(0, 1)$, $\boldsymbol{\delta}_2 = \frac{a_g}{\sqrt{3}}(\frac{\sqrt{3}}{2}, -\frac{1}{2})$ and $\boldsymbol{\delta}_3 = \frac{a_g}{\sqrt{3}}(-\frac{\sqrt{3}}{2}, -\frac{1}{2})$, where $|\delta_i| = 1.42\,\text{Å}$.

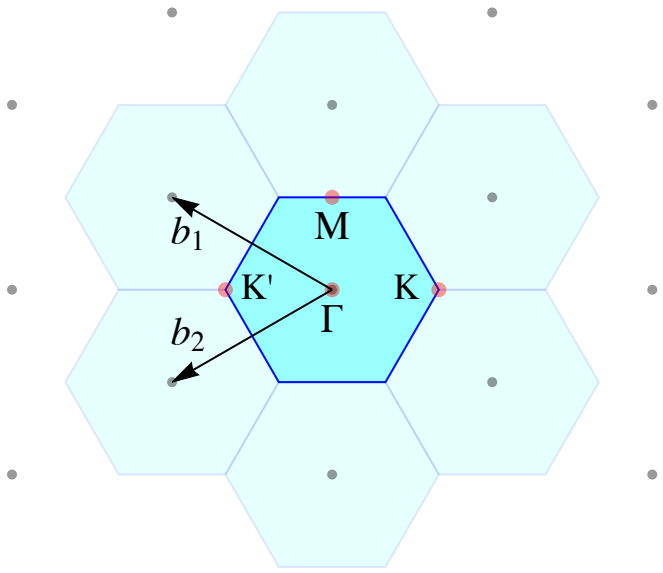

Figure 2.2: Schematic of the reciprocal lattice of SLG, in which dots indicate reciprocal lattice points, the blue hexagon is the first Brillouin zone, and the cyan hexagons are the six nearest Brillouin zones. Some symmetric points are notified too.

Primitive reciprocal lattice vectors $\boldsymbol{b}_1$ and $\boldsymbol{b}_2$ may be determined by using the relation between lattice and reciprocal lattice vectors [1].

$$\boldsymbol{a}_i \cdot \boldsymbol{b}_j = \delta_{ij} 2\pi, \quad |\boldsymbol{a}_i||\boldsymbol{b}_j| = \frac{4\pi}{\sqrt{3}}. \tag{2.1}$$

Given this,

$$\boldsymbol{b}_1 = \frac{4\pi}{a_g}(-\frac{\sqrt{3}}{2}, \frac{1}{2}), \quad \boldsymbol{b}_2 = \frac{4\pi}{a_g}(-\frac{\sqrt{3}}{2}, -\frac{1}{2}). \tag{2.2}$$

As shown in Fig. 2.2, the reciprocal lattice of graphene is a hexagonal lattice and the first Brillouin zone is a hexagon.

[1] This is simplified from the three-dimensional relation $\boldsymbol{b}_i = \boldsymbol{a}_j \times \hat{\boldsymbol{l}}_z / [\boldsymbol{a}_i \cdot (\boldsymbol{a}_j \times \hat{\boldsymbol{l}}_z)]$. Here, $\hat{\boldsymbol{l}}_z$ is the unit vector along $\boldsymbol{z}$ direction, i.e. perpendicular to the substrate.

2.2 Atomic orbitals of graphene

One isolated carbon atom has six electrons [53]. Among these six electrons, two are core electrons, whereas the other four populate $2s$ and $2p$ orbitals. The carbon atoms in graphene are sp^2 hybridized, meaning that the three electrons in orbitals $2s$, $2p_x$ and $2p_y$ form strong covalent bonds connecting three adjacent atoms lying in the plane of the graphene sheet. These bonds are shown as solid lines in Fig. 2.1. The strong carbon-carbon bond is one of the reasons behind graphene's strength and flexibility. The other atomic orbital, $2p_z$, which is perpendicular to the graphene plane, forms a π orbital when combined with the neighbouring $2p_z$ atomic orbitals of the adjacent atoms. Note that we use a model which considers only the $2p_z$ orbital of each atom. This model is able to adequately describe the behaviour of the electrons in graphene in the vicinity of the Fermi level [53].

2.3 Tight-binding model of SLG

2.3.1 Hamiltonian of SLG

Following [53], in this subsection, we provide a description of the behaviour of electrons in graphene, using the tight-binding model and Bloch's theorem. The former assumes that the wave functions of the electrons may be constructed from the atomic orbitals of isolated atoms. The latter provides a recipe for how to treat electrons in space-periodic systems, and is therefore the basis for the theory of solids.

We consider graphene to be translationally invariant. Each unit cell has two $2p_z$ atomic orbitals denoted by ϕ_l, where $l \in [1, 2]$ represents the two sublattices in one unit cell. We can build a tight-binding Bloch wave function Φ_l of one sublattice, which depends on position vector $\boldsymbol{r}$ and wave vector $\boldsymbol{k}$, as

$$\Phi_l(\boldsymbol{r}, \boldsymbol{k}) = \frac{1}{\sqrt{N}} \sum_{i=1}^{N} e^{i\boldsymbol{k}\cdot\boldsymbol{R}_{i,l}} \phi_l(\boldsymbol{r} - \boldsymbol{R}_{i,l}), \tag{2.3}$$

where $\boldsymbol{R}_{i,l}$ represents the position of the lth atomic orbitals in the ith unit cell and N is the number of unit cells [2] . For simplicity, we set $\hbar = 1$ from this point onward. The electron wave function of jth band $\Psi_j(\boldsymbol{r}, \boldsymbol{k})$of each unit cell can then be expressed as a linear superposition of Bloch wave functions, i.e.

$$\Psi_j(\boldsymbol{r}, \boldsymbol{k}) = \sum_{l=1}^{2} c_{j,l} \Phi_l(\boldsymbol{r}, \boldsymbol{k}), \tag{2.4}$$

where $c_{j,l}$ are the coefficients of expansion.

Based on the electron wave function $\Psi_j(\boldsymbol{r}, \boldsymbol{k})$, we can formally express the jth energy eigenvalue $E_j(\boldsymbol{k})$ of the Hamiltonian of the system $\hat{\mathcal{H}}$ as

$$E_j(\boldsymbol{k}) = \frac{\left\langle \Psi_j | \hat{\mathcal{H}} | \Psi_j \right\rangle}{\langle \Psi_j | \Psi_j \rangle} = \frac{\sum_{i,l}^{2} c_{ji}^* c_{jl} \left\langle \Phi_i | \hat{\mathcal{H}} | \Phi_l \right\rangle}{\sum_{i,l}^{2} c_{ji}^* c_{jl} \langle \Phi_i | \Phi_l \rangle}. \tag{2.5}$$

To minimize the energy E_j in locality, we calculate the derivative of E_j with respect to coefficient c_{ji}^*, and set $\partial E_j / \partial c_{ji}^* = 0$. Thus, we obtain equations

$$\begin{aligned} &\sum_{l=1}^{2} \hat{H}_{il} c_{jl} = E_j \sum_{l=1}^{2} S_{il} c_{jl}, \\ &\hat{H}_{il} = \left\langle \Phi_i | \hat{\mathcal{H}} | \Phi_l \right\rangle, \quad S_{il} = \langle \Phi_i | \Phi_l \rangle . \end{aligned}$$

As each unit cell contains two sublattices, A and B, and on each sublattice only one $2p_z$ atomic orbital, so we can use label A to replace index $l = 1$ and label B to replace index $l = 2$. The 2×2 matrix equation is then

$$\begin{aligned} &\hat{H}\psi_j = E_j S \psi_j, \quad \psi_j = \begin{pmatrix} c_{j1} & c_{j2} \end{pmatrix}^T, \\ &\hat{H} = \begin{pmatrix} \hat{H}_{AA} & \hat{H}_{AB} \\ \hat{H}_{BA} & \hat{H}_{BB} \end{pmatrix}, \quad S = \begin{pmatrix} S_{AA} & S_{AB} \\ S_{BA} & S_{BB} \end{pmatrix}, \end{aligned} \tag{2.6}$$

where $\hat{H}$ is called the transfer integral matrix, and S is the overlap integral matrix.

[2] Although this form seems a localized function, a simple translation operation $\hat{T}_{\boldsymbol{a}}$ can show that this function holds the translational invariance, i.e. $\hat{T}_{\boldsymbol{a}} \Phi_l(\boldsymbol{r}, \boldsymbol{k}) = e^{i\boldsymbol{k}\cdot\boldsymbol{a}} \Phi_l(\boldsymbol{r}, \boldsymbol{k})$, where $\boldsymbol{a} \in \boldsymbol{R}_{i,l}$.

The energy E_j can be obtained by solving the determinant of the secular equation

$$\det(\hat{H} - ES) = 0. \tag{2.7}$$

We will use two assumptions to simplify the equation above:

(1) In the diagonal entries $\hat{H}_{AA}$ ($\hat{H}_{BB}$), the dominant contribution arises from the same site, i.e. $\boldsymbol{R}_i = \boldsymbol{R}_j$. The contribution of other sites is omitted, which stems from the central idea of "tight-binding". Therefore,

$$\begin{aligned}\hat{H}_{AA} &= \frac{1}{N}\sum_{i=1}^{N}\sum_{j=1}^{N} e^{i\boldsymbol{k}\cdot(\boldsymbol{R}_{\boldsymbol{A},j}-\boldsymbol{R}_{\boldsymbol{A},i})}\left\langle \phi_A(\boldsymbol{r}-\boldsymbol{R}_{\boldsymbol{A},i})|\hat{\mathcal{H}}|\phi_A(\boldsymbol{r}-\boldsymbol{R}_{\boldsymbol{A},j})\right\rangle \\ &\simeq \frac{1}{N}\sum_{i=1}^{N}\epsilon_{2p} = \epsilon_{2p},\end{aligned} \tag{2.8}$$

where parameter ϵ_{2p} of the $2p$ orbital is

$$\epsilon_{2p} = \left\langle \phi_A(\boldsymbol{r}-\boldsymbol{R}_{\boldsymbol{A},i})|\hat{\mathcal{H}}|\phi_A(\boldsymbol{r}-\boldsymbol{R}_{\boldsymbol{A},i})\right\rangle. \tag{2.9}$$

In addition, $\hat{H}_{BB} = \hat{H}_{AA}$.

With this first assumption, the diagonal element S_{AA} of the overlap matrix is given by

$$\begin{aligned}S_{AA} &= \frac{1}{N}\sum_{i=1}^{N}\sum_{j=1}^{N} e^{i\boldsymbol{k}\cdot(\boldsymbol{R}_{\boldsymbol{A},j}-\boldsymbol{R}_{\boldsymbol{A},i})}\left\langle \phi_A(\boldsymbol{r}-\boldsymbol{R}_{\boldsymbol{A},i})|\phi_A(\boldsymbol{r}-\boldsymbol{R}_{\boldsymbol{A},j})\right\rangle \\ &\simeq \frac{1}{N}\sum_{i=1}^{N} 1 = 1.\end{aligned} \tag{2.10}$$

We assume that the atomic wave function is normalized, where

$$\left\langle \phi_A(\boldsymbol{r}-\boldsymbol{R}_{\boldsymbol{A},i})|\phi_A(\boldsymbol{r}-\boldsymbol{R}_{\boldsymbol{A},j})\right\rangle = 1. \tag{2.11}$$

In addition, $S_{BB} = S_{AA} = 1$.

(2) In the off-diagonal entries $\hat{H}_{AB}$ ($\hat{H}_{BA}$), the dominant contribution arises

from the three nearest neighbouring atomic sites, so

$$\begin{aligned}
\hat{H}_{AB} &= \frac{1}{N}\sum_{i=1}^{N}\sum_{j=1}^{N} e^{i\boldsymbol{k}\cdot(\boldsymbol{R_{B},}_{j}-\boldsymbol{R_{A},}_{i})} \left\langle \phi_A(\boldsymbol{r}-\boldsymbol{R_{A},}_{i})|\hat{\mathcal{H}}|\phi_B(\boldsymbol{r}-\boldsymbol{R_{B},}_{j})\right\rangle \\
&\simeq -\frac{1}{N}\sum_{i=1}^{N}\sum_{j=1}^{3} e^{i\boldsymbol{k}\cdot(\boldsymbol{R_{B},}_{j}-\boldsymbol{R_{A},}_{i})}\gamma_0 \\
&= -\gamma_0 f(\boldsymbol{k}), \\
S_{AB} &= \frac{1}{N}\sum_{i=1}^{N}\sum_{j=1}^{N} e^{i\boldsymbol{k}\cdot(\boldsymbol{R_{B},}_{j}-\boldsymbol{R_{A},}_{i})} \langle \phi_A(\boldsymbol{r}-\boldsymbol{R_{A},}_{i})|\phi_B(\boldsymbol{r}-\boldsymbol{R_{B},}_{j})\rangle \\
&\simeq \frac{1}{N}\sum_{i=1}^{N}\sum_{j=1}^{3} e^{i\boldsymbol{k}\cdot(\boldsymbol{R_{B},}_{j}-\boldsymbol{R_{A},}_{i})} s_0 \\
&= s_0 f(\boldsymbol{k}),
\end{aligned} \tag{2.12}$$

where the tight-binding parameters γ_0 and s_0 are defined as

$$\begin{aligned}
\gamma_0 &= -\left\langle \phi_A(\boldsymbol{r}-\boldsymbol{R_{A},}_{i})|\hat{\mathcal{H}}|\phi_B(\boldsymbol{r}-\boldsymbol{R_{B},}_{j})\right\rangle, \\
s_0 &= \langle \phi_A(\boldsymbol{r}-\boldsymbol{R_{A},}_{i})|\phi_B(\boldsymbol{r}-\boldsymbol{R_{B},}_{j})\rangle .
\end{aligned} \tag{2.13}$$

Note that the minus sign before the expression for parameter γ_0 ensures that $\gamma_0 > 0$ in practice. In addition,

$$f(\boldsymbol{k}) = \sum_{j=1}^{3} e^{i\boldsymbol{k}\cdot\boldsymbol{\delta}_j}, \tag{2.14}$$

which accounts for the phase factor acquired by hopping between nearest neighbours. For clarity, Fig. 2.1 shows vectors $\boldsymbol{\delta}_1$, $\boldsymbol{\delta}_2$ and $\boldsymbol{\delta}_3$.

Consequently, the tight-binding Hamiltonian of graphene is

$$\hat{H} = \begin{pmatrix} \epsilon_{2p} & -\gamma_0 f(\boldsymbol{k}) \\ -\gamma_0 f^*(\boldsymbol{k}) & \epsilon_{2p} \end{pmatrix}, \quad S = \begin{pmatrix} 1 & s_0 f(\boldsymbol{k}) \\ s_0 f^*(\boldsymbol{k}) & 1 \end{pmatrix}. \tag{2.15}$$

By solving the secular equation [3], Eq. (2.7), the dispersion relation is obtained as

$$E_{\pm} = \frac{\epsilon_{2p} \pm \gamma_0 |f(\boldsymbol{k})|}{1 \mp s_0 |f(\boldsymbol{k})|}. \tag{2.16}$$

Once the value of parameters γ_0 and s_0 are known, the band structure of SLG is known.

2.3.2 Band structure of SLG

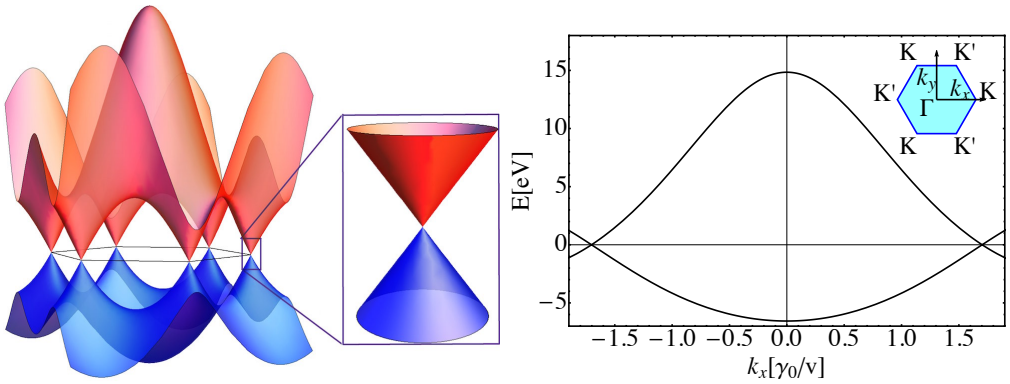

Figure 2.3: (Left)The band structure of SLG is shown, the Dirac cone in the vicinity of the $\boldsymbol{K}$ in reciprocal space is shown in the middle. Note that the solid lined hexagon in the left band structure is the first Brillouin zone. (Right) The two-dimensional dispersion of the tight-binding model of graphene based on $k_y = 0$, is shown with the upper-right inset indicating the location of the $\boldsymbol{K}$ ($\boldsymbol{K}'$) valley in the first Brillouin zone. Parameters $\gamma_0 = 3.16\,\text{eV}$ and $s_0 = 0.129$ are taken from the Slonczewski - Weiss - McClure parameters [55–58].

The tight-binding model cannot determine the values of γ_0 and s_0. To determine them theoretically, we could use a numerical method, such as density-functional theory (DFT). Alternatively, we could take an approach that fits experimental data. In the commonly-used Slonczewski - Weiss - McClure parameters [55–58] for graphite, $\gamma_0 = 3.16\,\text{eV}$ and $s_0 = 0.129$ [4]. Furthermore, we would not

[3] Actually, this secular equation is not solved by treating it as two simultaneous equations. In the solving process, one will notice that they are the same equations, and one can not find any new information (about the relation between different components) from them. Besides, the normalization gives same coefficients to the two components. So to set the determinant of secular equation to be zero is a shortcut to solve it, and this makes sure that the solved wave function is non-trivial (not a zero wave function).

[4] Most of the unique features of graphene, such as the Dirac cone, pseudospin or chirality described later are determined by its symmetric properties, but not the exact value of parameters. Even if the parameters for graphite are not the most accurate ones for graphene, these phenomena still hold.

expect a small change in the value of γ_0 to have a qualitative impact on the electronic band structure. Therefore, we will use parameter values for bulk graphite and apply them to graphene-related calculations [55].

The energy band structure of SLG, i.e. Eq. (2.16), is shown in the left panel of Fig. 2.3, in which ϵ_{2p} is set to zero for simplicity. The asymmetry between the top and bottom bands is generated by non-zero s_0. The valence and conduction bands touch at the six Brillouin zone corners, which are called Dirac points (DP). Of these six points, only two are non-equivalent; we call them the $\boldsymbol{K}$ and $\boldsymbol{K'}$ valleys. As shown in Fig. 2.3, the three $\boldsymbol{K}$ valleys are located at $\frac{4\pi}{3a_g}(1,0)$, $\frac{4\pi}{3a_g}(-\frac{1}{2},\frac{\sqrt{3}}{2})$, $\frac{4\pi}{3a_g}(-\frac{1}{2},-\frac{\sqrt{3}}{2})$, while the three $\boldsymbol{K'}$ valleys are at $\frac{4\pi}{3a_g}(-1,0)$, $\frac{4\pi}{3a_g}(\frac{1}{2},-\frac{\sqrt{3}}{2})$, $\frac{4\pi}{3a_g}(\frac{1}{2},-\frac{\sqrt{3}}{2})$ in the reciprocal space. At each of these $\boldsymbol{K}(\boldsymbol{K'})$ points, the coupling between the two bands, i.e. the off-diagonal element of Eq. (2.15), vanishes because

$$f(\boldsymbol{K}) = e^0 + e^{i2\pi/3} + e^{-i2\pi/3} = 0. \tag{2.17}$$

This indicates that there is no hopping between adjacent A and B atoms. In other words, the A and B sublattices are not connected. However, each sublattice supports identical electronic states, leading to a degeneracy (i.e. crossing) in the band structure. The absence of gaps and therefore the existence of DPs makes graphene a gapless semi-conductor.

2.3.3 Massless chiral quasiparticles in SLG

To study the electronic and transport properties of graphene in the low-energy range, as the band structure shown in the middle panel of Fig. 2.3, we can simplify Eq. (2.15) by expanding the off-diagonal matrix element, i.e. Eq. (2.14), in the vicinity of valley $\boldsymbol{K} = \frac{4\pi}{3a_g}(1,0)$. We define $\boldsymbol{p}$ as the momentum measured from the point $\boldsymbol{K}$ point, i.e. $\boldsymbol{p} = \boldsymbol{k} - \boldsymbol{K}$, and expand in powers $\boldsymbol{p}$, where $pa/\hbar \ll 1$.

Then, to first order in $\boldsymbol{p}$

$$f(\boldsymbol{k}) \simeq -\frac{\sqrt{3}a_g}{2}(p_x - ip_y). \tag{2.18}$$

Following this expansion, the contribution of s_0 in Eq. (2.16) appears only in quadratic-in-momentum terms, so it is possible to neglect s_0 at low energy without comprising accuracy [5]. Then, for the first order in $\boldsymbol{p}$, the modified eigenvalue equation $\hat{H}\psi_j = E_j S\psi_j$ is simplified to $\hat{H}\psi_j = E_j\psi_j$, where the effective Hamiltonian is

$$\hat{H} = v\begin{pmatrix} 0 & \hat{\pi}^\dagger \\ \hat{\pi} & 0 \end{pmatrix} = v\hat{\boldsymbol{p}}\cdot\boldsymbol{\sigma}, \tag{2.19}$$

where $\hat{\pi} = \hat{p}_x + i\hat{p}_y$, $v = \sqrt{3}a_g\gamma_0/2 \simeq 10^6\,\mathrm{m\,s^{-1}}$ and $\boldsymbol{\sigma} = \sigma_x\hat{i} + \sigma_y\hat{j}$ is a vector consisting of Pauli matrices. This 2×2 Hamiltonian acts in the space of two-components wave functions describing electron's amplitudes on A and B sublattices of honeycomb lattice of carbons, with the basis choice (ϕ_A, ϕ_B) in valley $\boldsymbol{K}$ and $(\phi_B, -\phi_A)$ in valley $\boldsymbol{K}'$. This choice provides us with the same form of the Dirac Hamiltonian in both valleys.

To first order in $\boldsymbol{p}$, the rotational symmetry and electron-hole symmetry are recovered and the low energy band structure is a perfect cone, as shown in the middle panel of Fig. 2.3. The eigenvalues and eigenfunctions of Eq. (2.19) are

$$E_\pm = \pm v|\boldsymbol{p}|, \quad \psi_\pm = \frac{1}{\sqrt{2}}\begin{pmatrix} 1 \\ \pm e^{i\varphi} \end{pmatrix} e^{i\boldsymbol{p}\cdot\boldsymbol{r}}, \tag{2.20}$$

where φ is the polar angle of momentum $\boldsymbol{p}$, $\boldsymbol{p} = |\boldsymbol{p}|(\cos(\varphi), \sin(\varphi))$. As shown in Fig.2.3, this linear dispersion, $E_\pm = \pm v|\boldsymbol{p}|$ is valid in $E \leq 2\mathrm{eV}$ [6].

[5] The Taylor expansion of Eq. (2.16) is $E_\pm(\boldsymbol{k}) = \epsilon_{2p} \pm \frac{\sqrt{3}}{2}a|k|(\gamma_0 + \epsilon_{2p}s_0) \pm a^2k^2(\gamma_0 + \epsilon_{2p}s_0)(6s_0 + \cos(3\theta))$, where $\hbar = 1$, θ is the direction angle of momentum. In the case of $\epsilon_{2p} = 0$, the dependence of s_0 to momentum is quadratic.

[6] Here, actually we are in the mesoscopic region, which means the characteristic length of the electron in this system is much longer than the lattice constant. In the discussion below, the

The two-component structure of the effective Hamiltonian, i.e. Eq. (2.19), and wave function Eq. (2.20) is reminiscent of the two components of spin-1/2. In graphene, this spin-like property, i.e. the two components of the wave function has different amplitudes but same module, is called pseudospin; however, its origin has nothing to do with an electron's real spin and instead merely arises from the fact that the electronic wave vector has different amplitudes on the A and B sublattices. In addition, the direction of the pseudospin is related to the direction of momentum $\boldsymbol{p}$, (i.e., the direction of $\boldsymbol{p}$ determines the distribution of the wave function on the sublattice sites in a unit cell), which is a property known as chirality[7]. Pseudospin is an intrinsic property of quasiparticles in graphene that can be manifested in experimental measurements [7].

2.4 Tight-binding model for BLG

2.4.1 Tight-binding Hamiltonian of BLG

Bilayer graphene (BLG) consists of two SLGs stacked together. Depending on the stacking-order configurations, BLG can either be AA-stacked or AB-stacked (i.e. Bernal-stacked). In the former, carbon atoms of the upper layer are located on the top of the equivalent atoms in the bottom layer. AA-stacked BLG is relatively unstable [64–67] with respect to the mechanical displacement of the layers in relation to one another. AB-stacked BLG is more stable [68], and therefore, in this thesis, we focus on AB-stacked BLG, referring to it simply as BLG.

The schematic lattice structure of BLG is shown in Fig. 2.4. The honeycomb crystal lattice and hexagonal Brillouin zone of BLG are the same as those of SLG. In each unit cell of BLG, there are four atomic sites, i.e. $A1$, $B1$, $A2$ and $B2$; here,

wave length of electron (plain wave) $\lambda \simeq 350\,\text{Å}$ for $\epsilon = 0.35\,\text{eV}$ is much larger than the lattice constant of graphene $a_g = 2.46\,\text{Å}$. With the decreasing of energy, this approximation becomes more robust.

[7]To see this, one can calculate the expectation value of the pseudo-spin operator, $\langle\psi_\pm|\boldsymbol{\sigma}|\psi_\pm\rangle$ with respect to the eigen function $\psi_\pm$ in Eq. (2.20), where $\boldsymbol{\sigma} = (\sigma_x, \sigma_y, \sigma_z)$ is Pauli matrices. The result is $\langle\psi_\pm|\boldsymbol{\sigma}|\psi_\pm\rangle = \pm(\cos(\varphi), \sin(\varphi), 0)$, which explicitly shows the relation between pseudospin and direction pf momentum, i.e. chirality.

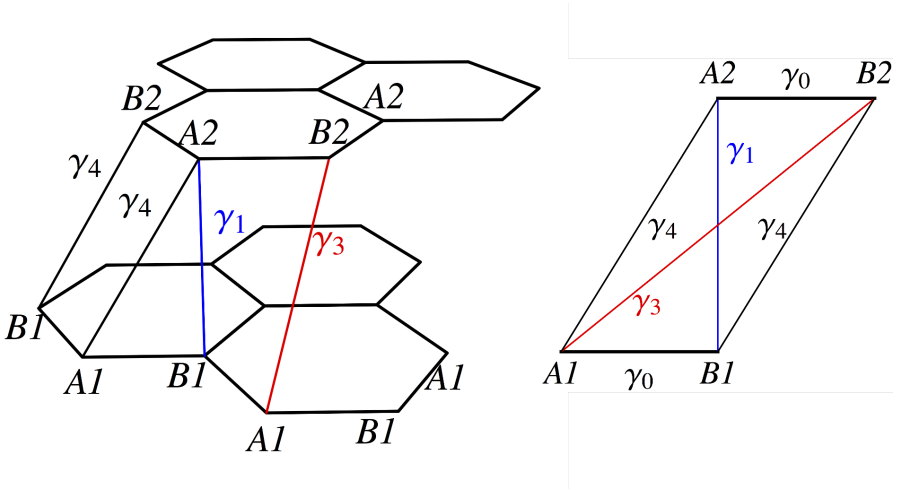

Figure 2.4: Schematic of the crystal lattice with Slonczewski-Weiss-McClure parameterization [55–57], in which dimer site $A2$ sits directly above site $B1$ in AB-stacked order. The solid lines between different atomic sites here represent different hopping parameters.

index "1" refers to the bottom layer, whereas index "2" refers to the top layer. In BLG, site $A2$ sits directly above site $B1$, and the distance between layers is $d = 3.3\,\text{Å}$ [53], which is longer than the lattice constant $a_g = 2.46\,\text{Å}$, as shown in Fig. 2.4.

In the tight-binding model, we use the basis of Bloch wave function (ϕ_{A1}, ϕ_{B1}, ϕ_{A2}, ϕ_{B2}) for valley $\boldsymbol{K}$ and (ϕ_{B1}, $-\phi_{A1}$, ϕ_{B2}, $-\phi_{A2}$) for valley $\boldsymbol{K}'$, this choice provides us the same form of the Dirac Hamiltonian in both valleys. If we keep the transfer integral of intralayer and interlayer nearest-neighbour sites, and only keep the overlap integral of intralayer nearest-neighbour sites, the Hamiltonian of BLG can be written as [54, 68–70]:

$$\hat{H} = \begin{pmatrix} \epsilon_{2p} & -\gamma_0 f(\boldsymbol{k}) & -\gamma_4 f(\boldsymbol{k}) & -\gamma_3 f^*(\boldsymbol{k}) \\ -\gamma_0 f^*(\boldsymbol{k}) & \epsilon_{2p} & \gamma_1 & -\gamma_4 f(\boldsymbol{k}) \\ -\gamma_4 f^*(\boldsymbol{k}) & \gamma_1 & \epsilon_{2p} & -\gamma_0 f(\boldsymbol{k}) \\ -\gamma_3 f(\boldsymbol{k}) & -\gamma_4 f^*(\boldsymbol{k}) & -\gamma_0 f^*(\boldsymbol{k}) & \epsilon_{2p} \end{pmatrix}. \tag{2.21}$$

In the above Hamiltonian, the upper-left/lower-right blocks describe the intralayer behaviour of bottom layer ($A1$ - $B1$)/top layer ($A2$ - $B2$). The off-diagonal blocks describe the interlayer hopping. Fig. 2.4 shows a schematic sketch of atomic sites

connected by each parameter. In Eq. (2.21), $f(\boldsymbol{k})$ describes the phase factor acquired by hopping to nearest-neighbour sites in the same layer, γ_0 describes intralayer hopping, γ_1 describes vertical interlayer hopping, γ_3 and γ_4 describe the skewed interlayer hopping. Once we know the value of parameters γ_0, γ_1, γ_3 and γ_4, the band structure of BLG is known [8].

2.4.2 Hierarchy of parameters

From the above tight-binding Hamiltonian, we observe that the addition of more atomic sites in the basis introduces more ways to hop between atoms, requiring additional tight-binding parameters. Therefore, in this subsection, we will present a systematic introduction to the tight-binding parameters of graphene.

As graphene is essentially one layer of graphite, commonly-used parameter sets for graphite are suitable for graphene. The most well-known example is the aforementioned Slonczewski - Weiss - McClure parameters [55–58]. The connection between the tight-binding parameters and those of the Slonczewski - Weiss - McClure model is discussed in [60]. Throughout this thesis, all values of hopping parameters of graphene are taken from Slonczewski - Weiss - McClure parameters [58] unless otherwise stated. Definitions and values of the hopping parameters in this model, as well as their influence on the band structure of graphene, are summarized in Table. 2.1.

The onsite energy ϵ_{2p} of an atomic $2p_z$ orbital is not necessarily zero, but its effect is only to shift the entire band structure with respect to the zero of energy. In a practical experiment, such a shift could be achieved using a gate voltage. Throughout this thesis, the onsite energy is set to zero, unless otherwise stated, because this does not lead to a loss of generality.

Parameter γ_0, defined in Eq. (2.13), accounts for intralayer hopping between

[8] One may wonder, why s_0 in the effective Hamiltonian of SLG is absent in BLG (and further TLG). The reason is that the main effect of s_0 is to cause asymmetry between conduction and valence band, and this effect can be absorbed into γ_4 effect (as we shall see in the later sections). It is not necessary to keep s_0 further in multi-layer graphene, but SLG does not have γ_4 parameter, so s_0 is necessary for SLG.

Parameter	Hopping	Lattice Sketch	Value [eV][58]	Value [eV][136]	Band structure
ϵ_{2p}	Onsite energy of atomic orbital $2p_z$	Fig. 2.1	-0.24	-0.206	-
γ_0	Overlap of intralayer atomic orbitals $2p_z$. Intralayer hopping. $A \leftrightarrow B$	Fig. 2.1	3.16	3.12	Fig. 2.3
γ_1	Overlap of interlayer atomic orbitals $2p_z$, nearest interlayer vertical hopping. $A_2 \leftrightarrow B_1$	Fig. 2.4	0.39	0.377	High energy bands, shown in Fig. 2.5 and Fig. 2.6
γ_2	Next nearest interlayer vertical hopping (without middle layer) $B_3 \leftrightarrow A_1$ of TLG-ABC and $A_3 \leftrightarrow A_1$ of TLG-ABA	TLG-ABC and TLG-ABA are shown in Fig. 2.7 and Fig. 2.10	-0.02	-0.020	Trigonal warping in TLG-ABC, shown in Fig. 2.8 and Fig. 2.9; gap in TLG-ABA shown in Fig. 2.11 and Fig. 2.12
γ_3	Nearest interlayer skewed hopping $B_2 \leftrightarrow A_1$	Fig. 2.4	0.315	0.29	Trigonal warping in BLG, shown in Fig. 2.5 and Fig. 2.6
γ_4	Nearest interlayer skewed hopping $A_2 \leftrightarrow A_1$ and $B_2 \leftrightarrow B_1$	Fig. 2.4	0.044	0.12	Electron-hole asymmetry in BLG and TLG-ABC, shown in Fig. 2.6 and Fig. 2.9, respectively
γ_5	Next nearest interlayer vertical hopping (with middle layer) $B_3 \leftrightarrow B_1$	Fig. 2.10	0.038	0.0125	Gap in TLG-ABA, shown in Fig. 2.11 and Fig. 2.12

Table 2.1: The Slonczewski - Weiss - McClure parameter sets [55–58] for graphite and their influence on the band structure of graphene.

nearest neighbours.

The simplest model describing multilayer graphene employs only one additional parameter γ_1, which describes vertical hopping between the closest interlayer atomic sites, those are directly above or below one another. Such sites, e.g. $B1$ and $A2$ in Fig. 2.4, are referred to as dimer sites. Their coupling by parameter γ_1 results in the energy bands associated with their orbitals being shifted away from zero energy by $\pm\gamma_1$.

In general, the parameters γ_0 and γ_1 are the dominant parameters that contribute to the tight-binding model of graphene multilayers. Depending on the level of approximation required, other parameters can be treated as a perturbation or simply neglected. As they are relatively small, when considering parameters other than γ_0 and γ_1, it is usually possible to consider them individually. One exception here is that other parameters can significantly change the band structure at very low energy (i.e. $E \ll \gamma_1$).

The skewed interlayer hopping parameter γ_3 connects non-dimer sites (e.g. $A1$ and $B2$ in BLG, Fig. 2.4), and its magnitude is the third highest among the given parameters. This parameter's physical effects include: (a) the trigonal warping effect in BLG, explained in Section 2.4; (b) its significant impact on the transport properties of graphene, which is described in Section 6.4 and (c) its interesting interactions with parallel magnetic fields, which is introduced in Section 5.2.

Amongst all the nearest interlayer hopping parameters, parameter γ_4 is relatively weak as it describes skew interlayer hopping between dimer and non-dimer sites. Furthermore, it provides electron-hole asymmetry, as discussed in Section 2.4.3 and Ref. [19]. In what follows, the effect of γ_4 is omitted unless otherwise stated.

For completeness and convenience, we next describe two additional parameters that only occur in multilayer graphene for layers $n \geq 3$. These parameters are next-nearest interlayer vertical hopping parameters γ_5 and γ_2.

The simplest graphene material which includes γ_2 or γ_5 is trilayer graphene

(TLG) whether ABC-stacked as described in Section 2.5.1 or ABA-stacked as described in Section 2.5.2. The presence of γ_2 in TLG-ABC leads to a Lifshitz transition (will be explained later) [63], though there is no γ_5 in TLG-ABC. The existence of γ_2 and γ_5 in TLG-ABA leads to a gap formation in the dispersion.

There is one point for parameter γ_2 and γ_5 to be mentioned. In graphite, there is (at least, approximately) translational invariance in the z direction. So each layer of graphite always has two next-nearest neighbor layers, γ_2 and γ_5 are used to describe this interlayer hopping. But in TLG, top (bottom) layer only has one next-nearest neighbor layer, so a intuitive way of counting this effect is to introduce a 1/2 coefficient to γ_2 and γ_5, as we will see in the later sections. A detailed discussion about this can be found in [58] and[136].

2.4.3 Effective Hamiltonian of BLG

With the tight-binding Hamiltonian of BLG, i.e. Eq. (2.21) [68] and parameter values from Ref. [136], we can plot the band structure of BLG in the Brillouin zone, as shown in the left panel of Fig. 2.5.

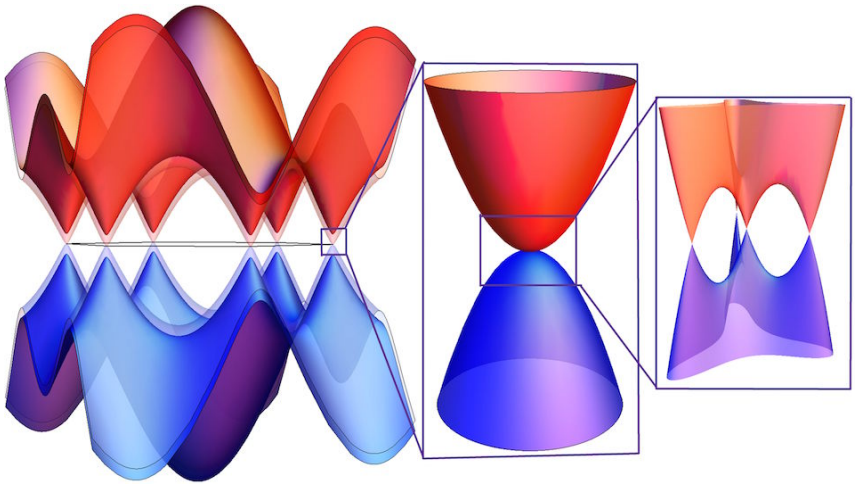

Figure 2.5: (Left) The band structure of BLG in momentum space, the hexagon in the centre of the bands is the first Brillouin zone. Among the four bands, the transparent two bands represent low-energy dispersion, which touch one another. The other two opaque bands represent the high-energy bands, which are separated from one another by energy scale γ_1. All four bands are quadratic dispersion except in low energy. (Middle) Quadratic Dirac cone of the non-dimer site of BLG around the $\boldsymbol{K}$ valley. (Right) The trigonal-warping of bands of BLG (Lifshitz transition [63]) in the vicinity of zero energy.

Within this model, the band structure of BLG features four bands. At the corners of the Brillouin zone, i.e. at $\boldsymbol{K}$ and $\boldsymbol{K}'$ valleys, two of the four bands are separated by γ_1, whereas the other two bands touch one another. To investigate the behaviour of electrons in the vicinity of points $\boldsymbol{K}/\boldsymbol{K}'$, it is convenient to expand the phase factor term $f(\boldsymbol{k})$ in Eq. (2.21) to yield the resulting Hamiltonian on the basis $A1$, $B1$, $A2$ and $B2$, i.e.

$$\hat{H} = \begin{pmatrix} 0 & v\hat{\pi}^\dagger & v_4\hat{\pi}^\dagger & v_3\hat{\pi} \\ v\hat{\pi} & 0 & \gamma_1 & v_4\hat{\pi}^\dagger \\ v_4\hat{\pi} & \gamma_1 & 0 & v\hat{\pi}^\dagger \\ v_3\hat{\pi}^\dagger & v_4\hat{\pi} & v\hat{\pi} & 0 \end{pmatrix}, \tag{2.22}$$

where $v_i = \sqrt{3}a_g\gamma_i/2$ are the velocities corresponding to each of the hopping parameters, $v_0 = v$. Note that Bloch wave function is on the basis of (ϕ_{A1}, ϕ_{B1}, ϕ_{A2}, ϕ_{B2}) for valley $\boldsymbol{K}$ and (ϕ_{B1}, $-\phi_{A1}$, ϕ_{B2}, $-\phi_{A2}$) for valley $\boldsymbol{K}'$. The diagonal elements (i.e. those describing the onsite energy) are set to zero. Here, $\gamma_1 \simeq 0.1\gamma_0$ [55–57] describes hopping between the nearest interlayer sites, which sits directly above one another (e.g. $A2$-$B1$). Furthermore, $\gamma_3 \simeq 0.1\gamma_0$ ($A1$-$B2$) represents skewed interlayer hopping as does $\gamma_4 \simeq 0.01\gamma_0$ ($A1$-$A2$ and $B1$-$B2$) [55–57].

The simplest model of BLG, which only includes the dominant parameters γ_0 and γ_1, has a dispersion relation describing the four bands as

$$E = s_1\gamma_1/2 + s_2\frac{1}{2}\sqrt{\gamma_1^2 + 4k^2v^2}, \quad s_1,\ s_2 = \pm 1. \tag{2.23}$$

This dispersion shows a linear dispersion in the large momentum region $\gamma_0 \gg vk \gg \gamma_1$ and quadratic dispersion in the low momentum region $vk \simeq \gamma_1$.

Among the four BLG bands, the energy of the two dimer sites (i.e. $B2$, $A1$) is lifted by vertical hopping γ_1, so their bands are also separated by γ_1 as shown in the left panel of Fig. 2.6. Therefore, to study behaviour near zero energy, i.e. $E \ll \gamma_1$, we can perform a Schrieffer-Wolff transformation [61, 62] on Eq. (2.22)

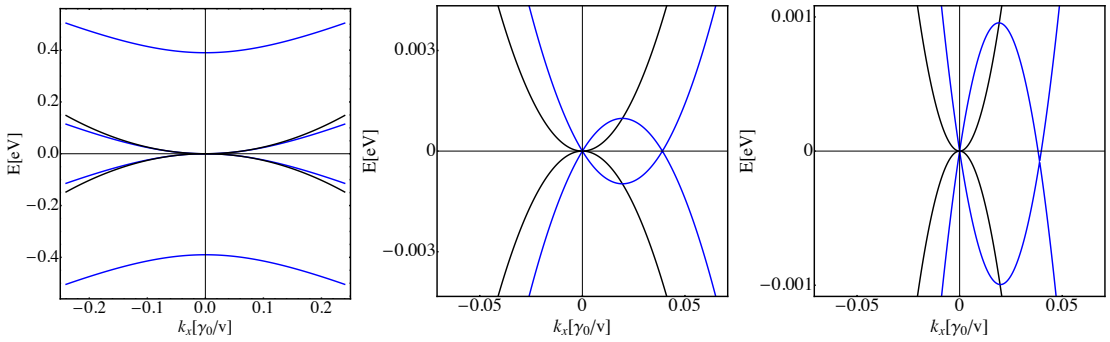

Figure 2.6: (Left) The low-energy band structure of the tight-binding Hamiltonian of BLG with Eq. (2.22) in blue and Eq. (2.24) in black for $k_y = 0$ and $v_3 = v_4 = 0$. (Middle) The low-energy band structure of BLG, i.e. Eq. (2.24), for $k_y = 0$ and $v_4 = 0$, $v_3 = 0.1v$ (blue) and $v_3 = 0$ (black). (Right) The low-energy band structure of BLG, i.e. Eq. (2.24), for $k_y = 0$ and $v_3 = 0$, $v_4 = 0.01v$ (blue) and $v_4 = 0$ (black).

to eliminate components describing the two dimer sites, and obtain a simplified two-component Hamiltonian [9], i.e.

$$H_2 = -\frac{1}{2m}\begin{pmatrix} 0 & \hat{\pi}_+^2 \\ \hat{\pi}_-^2 & 0 \end{pmatrix} + v_3\begin{pmatrix} 0 & \hat{\pi}_- \\ \hat{\pi}_+ & 0 \end{pmatrix} - \frac{2v_4 v\hat{k}^2}{\gamma_1}\begin{pmatrix} 1 & 0 \\ 0 & 1 \end{pmatrix}, \quad (2.24)$$

where $m = \gamma_1/2v^2 \simeq 0.032m_e$ is the effective mass of quasiparticles in BLG and m_e is the rest mass of the electron. Note that the basis is (ϕ_{A1}, ϕ_{B2}) for valley $\boldsymbol{K}$ and (ϕ_{B2},$-\phi_{A1}$) for valley $\boldsymbol{K}'$. This Hamiltonian describes a massive charge carrier, and its dominant dispersion relation is quadratic. In the absence of γ_3 and γ_4, the eigenvalue and eigenfunction of effective 2×2 Hamiltonian (Eq. (2.24)) are

$$E_\pm = \pm\frac{p^2}{2m}, \quad \psi_\pm = \frac{1}{\sqrt{2}}\begin{pmatrix} 1 \\ \mp e^{2i\varphi} \end{pmatrix} e^{i\boldsymbol{p}.\boldsymbol{r}}, \quad (2.25)$$

where φ is the polar angle of momentum $\boldsymbol{p}$, $\boldsymbol{p} = |\boldsymbol{p}|(\cos(\varphi), \sin(\varphi))$. The dispersion is shown in the middle panel of Fig. 2.5 and the left panel of Fig. 2.6.

[9] The idea of Schrieffer-Wolff transformation is to project the effect of unnecessary state on to the favored state. One can consider this process as solving several simultaneous equations, eliminate unnecessary variables and derive an expression of favored variables. This transformation itself is exact, but some approximation can significantly simplify the process and result. Here, for BLG, the favored state is the low-energy state $A1$ and $B2$, the effect of dimer state $B1$ and $A2$ are projected onto the low-energy state. In this process, an approximation $\gamma_1 \gg E, vp, v_3p, v_4p$ is used.

The dispersion relation containing γ_3 (γ_4 is set to zero to emphasize the effect of γ_3) [71] is

$$E_{\pm} = \pm\sqrt{v_3^2 p^2 - v_3 \frac{p^3}{m}\cos(3\varphi) + \left(\frac{p^2}{2m}\right)^2}, \tag{2.26}$$

where φ is the polar angle of the electron's momentum.

The above equation describes three-fold rotational symmetry. Fig. 2.5 shows the dispersion of the effective Hamiltonian.

In the very low energy region, the effect of γ_3 becomes increasingly important. When $E \simeq \frac{1}{4}\gamma_1\gamma_3^2/\gamma^2 \simeq 1$meV, the bands will split into four pockets, as shown in the middle and right subplots of Fig. 2.5. This phenomenon is called Lifshitz transition [63] and is discussed in detail in Chapter 5; its impact on transport properties is described in Chapter 6. Note that the asymmetries (along the x-axis) in the middle and right subplots of Fig. 2.6 are due to the trigonal warping of γ_3.

Trigonal warping in BLG originates from the interference of the matrix elements connecting $A1$ - $B2$ sites as follows: the path $A1$ - $B1$ - $A2$ - $B2$ yields a phase factor $e^{2i\pi}$, and the direct path $A1$ - $B2$ via γ_3 yields $e^{-i\pi}$. The difference between these phase factors causes the trigonal warping effect in the low-energy band structure of BLG, as shown in the right panel of Fig. 2.5.

As shown in the right panel Fig. 2.6, the existence of $\gamma_4 \simeq \gamma_3/100$ produces asymmetry between electrons and holes [19]. Because this phenomenon is very weak and negligible, we ignore terms containing γ_4 in the future discussion.

2.5 Tight-binding model of TLG

A system with three graphene layers is known as trilayer graphene (TLG). There are two distinct stable arrangements, i.e. ABC and ABA. In the subsection that follow, we will discuss TLG-ABC and TLG-ABA.

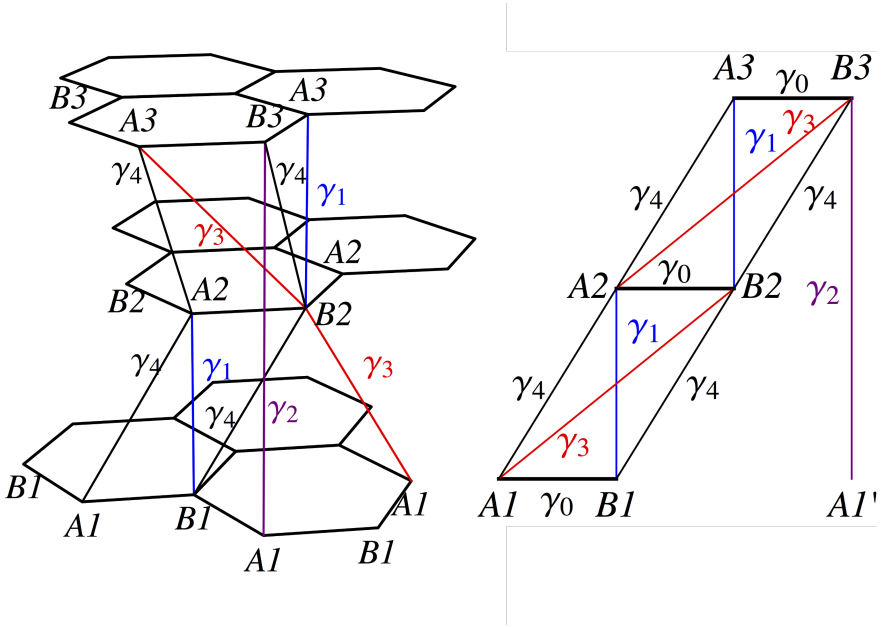

Figure 2.7: Schematic of the crystal structure of TLG-ABC. Dimer site $A2$ sits directly above site $B1$, site $A3$ sits directly above $B2$ and there is next-nearest layer hopping between sites $B3$ and $A1$.

2.5.1 Band structure of TLG-ABC

TLG-ABC has the same Bravais lattices and reciprocal lattices as those of SLG. As shown in Fig. 2.7, the unit cell of TLG-ABC consists of six atomic sites rather than two; these six sites are labelled $A1$, $B1$, $A2$, $B2$, $A3$ and $B3$, where index "1" represents for the bottom layer, "2" represents the middle layer and "3" represents the top layer. The interlayer distance between layers $d = 3.3\,\text{Å}$ is the same as that of BLG. Sites $A3$ and $B2$, as well as $A2$ and $B1$ sit directly above one another in the nearest-layer, whereas sites $B3$ and $A1$ sit directly above one another in the next-nearest-layer.

Generalizing the procedure for SLG and BLG, we can write the tight-binding Hamiltonian of TLG-ABC using a basis of $2p_z$ orbitals on atomic sites $A1$, $B1$, $A2$, $B2$, $A3$ and $B3$. The Hamiltonian of TLG-ABC can be written on the basis of Bloch wave function (ϕ_{A1}, ϕ_{B1}, ϕ_{A2}, ϕ_{B2}, ϕ_{A3}, ϕ_{B3}) for valley $\boldsymbol{K}$ and (ϕ_{B1}, $-\phi_{A1}$,

ϕ_{B2}, $-\phi_{A2}$, ϕ_{B3}, $-\phi_{A3}$) for valley $\boldsymbol{K}'$, as [19]:

$$\hat{H} = \begin{pmatrix} \epsilon_{2p} & -\gamma_0 f(\boldsymbol{k}) & -\gamma_4 f(\boldsymbol{k}) & -\gamma_3 f^*(\boldsymbol{k}) & 0 & \gamma_2/2 \\ -\gamma_0 f^*(\boldsymbol{k}) & \epsilon_{2p} & \gamma_1 & -\gamma_4 f(\boldsymbol{k}) & 0 & 0 \\ -\gamma_4 f^*(\boldsymbol{k}) & \gamma_1 & \epsilon_{2p} & -\gamma_0 f(\boldsymbol{k}) & -\gamma_4 f(\boldsymbol{k}) & -\gamma_3 f^*(\boldsymbol{k}) \\ -\gamma_3 f(\boldsymbol{k}) & -\gamma_4 f^*(\boldsymbol{k}) & -\gamma_0 f^*(\boldsymbol{k}) & \epsilon_{2p} & \gamma_1 & -\gamma_4 f(\boldsymbol{k}) \\ 0 & 0 & -\gamma_4 f^*(\boldsymbol{k}) & \gamma_1 & \epsilon_{2p} & -\gamma_0 f(\boldsymbol{k}) \\ \gamma_2/2 & 0 & -\gamma_3 f(\boldsymbol{k}) & -\gamma_4 f^*(\boldsymbol{k}) & -\gamma_0 f^*(\boldsymbol{k}) & \epsilon_{2p} \end{pmatrix}. \quad (2.27)$$

Here, we adopted the Slonczewski - Weiss - McClure parameters [55–57] typically used to describe bulk graphite. Furthermore, $\gamma_1 \simeq 0.1\gamma_0$ [55–57] describes the hopping between nearest interlayer sites, which sit directly above one another (i.e. $A2$-$B1$ and $A3$-$B2$); $\gamma_3 \simeq 0.1\gamma_0$ (i.e. $A1$-$B2$ and $A2$-$B3$) and $\gamma_4 \simeq 0.01\gamma_0$ (i.e. $A1$-$A2$, $B1$-$B2$, $A2$-$A3$ and $B2$-$B3$) describe the skewed interlayer hopping [55–57]. A new parameter of TLG-ABC is $\gamma_2 \simeq -0.005\gamma_0$, which describes the hopping of electrons between sites in the top and bottom layers. With this new parameter value, the band structure is plotted in Fig. 2.8.

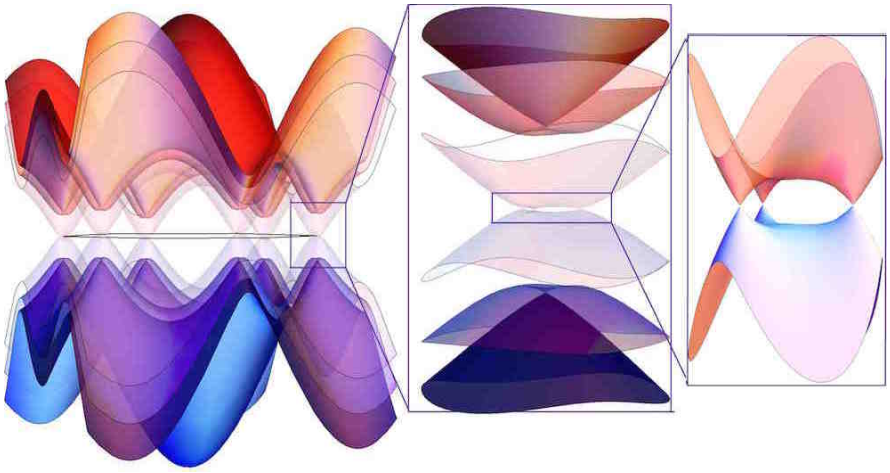

Figure 2.8: (Left) The band structure of TLG-ABC in momentum space; the hexagon in the centre of the bands is the first Brillouin zone. From the six bands, the two transparent bands exist due to the low-energy bands touching one another. The other four opaque bands are separated from one another by energy scale $2\gamma_1$. (Middle) Cubic Dirac cone due to around the $\boldsymbol{K}$ valley. (Right) The trigonal-warping effect in TLG-ABC (i.e. a Lifshitz transition) in the vicinity of zero energy.

Because the model represented by Eq. (2.27) includes six orbitals in the unit

cell, the band structure of TLG-ABC features six bands. In the corner of the Brillouin zone, i.e. at the $\boldsymbol{K}$ and $\boldsymbol{K}'$ valleys, four of the six bands are approximately separated by γ_1, whereas the other two touch one another. To investigate the behaviour of electrons in the vicinity of points $\boldsymbol{K}/\boldsymbol{K}'$, it is convenient to expand the phase factor term $f(\boldsymbol{k})$ in Eq. (2.28) with the resulting Hamiltonian determined as [19]

$$\hat{H} = \begin{pmatrix} 0 & v\hat{\pi}^\dagger & v_4\hat{\pi}^\dagger & v_3\hat{\pi} & 0 & \gamma_2/2 \\ v\hat{\pi} & 0 & \gamma_1 & v_4\hat{\pi}^\dagger & 0 & 0 \\ v_4\hat{\pi} & \gamma_1 & 0 & v\hat{\pi}^\dagger & v_4\hat{\pi}^\dagger & v_3\hat{\pi} \\ v_3\hat{\pi}^\dagger & v_4\hat{\pi} & v\hat{\pi} & 0 & \gamma_1 & v_4\hat{\pi}^\dagger \\ 0 & 0 & v_4\hat{\pi} & \gamma_1 & 0 & v\hat{\pi}^\dagger \\ \gamma_2/2 & 0 & v_3\hat{\pi}^\dagger & v_4\hat{\pi} & v\hat{\pi} & 0 \end{pmatrix}, \tag{2.28}$$

where $v_i = \sqrt{3}a_g\gamma_i/2$ are the velocities corresponding to each hopping parameter and $v_0 = v$. The diagonal elements (i.e. those describing onsite energy) are set to zero. Among the six bands of TLG-ABC, four bands are separated by $2\gamma_1$, as shown in the left panel of Fig. 2.9.

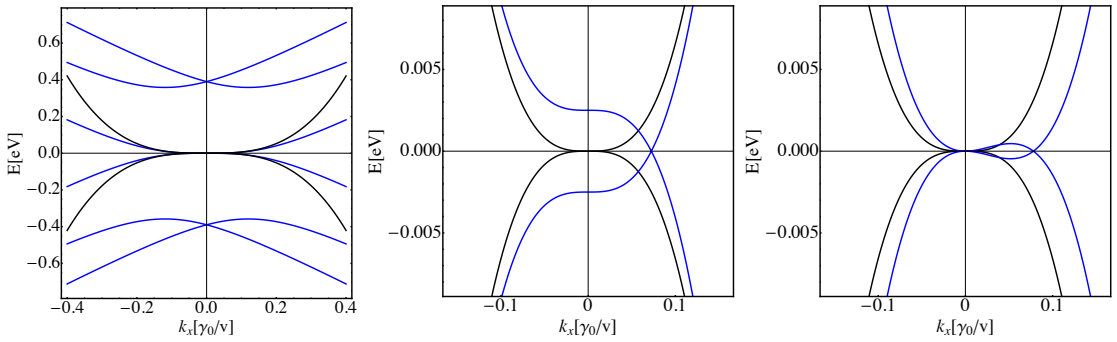

Figure 2.9: (Left) The low-energy band structure of the tight-binding Hamiltonian of TLG-ABC Eq. (2.28) in blue and Eq. (2.29) in black for $k_y = 0$, $\gamma_2 = 0$ $v_3 = 0$ and $v_4 = 0$. (Middle) The low-energy band structure of TLG-ABC, i.e. Eq. (2.29) for $k_y = 0$, $v_3 = 0$ and $v_4 = 0$, where $\gamma_2 = -0.005\gamma_0$ (blue) and $\gamma_2 = 0$ (black). (Right) The low-energy band structure of TLG-ABC, i.e. Eq. (2.29) for $k_y = 0$, $\gamma_2 = 0$ and $v_4 = 0$, where $v_3 = 0.1v$ (blue) and $v_3 = 0$ (black).

As shown in Fig. 2.9, the simplest model that includes only γ_0 and γ_1 is generally a good description for most of the energy region. To study the behaviour

around zero energy, i.e. $E \ll \gamma_1$, we can perform a Schrieffer-Wolff transformation [61, 62] on Eq. (2.28) to project the effect of the four dimer sites onto the two non-dimer sites, thus obtaining a simplified two-component Hamiltonian [19] as

$$\hat{H}_C = \frac{v^3}{\gamma_1^2}\begin{pmatrix} 0 & \hat{\pi}^{\dagger 3} \\ \hat{\pi}^3 & 0 \end{pmatrix} + \left(\frac{\gamma_2}{2} - \frac{vv_3}{\gamma_1}2k^2\right)\begin{pmatrix} 0 & 1 \\ 1 & 0 \end{pmatrix}. \tag{2.29}$$

Parameter γ_4 only provides a trivial asymmetry between electron and hole, therefore we omit it for simplicity. As shown in the left panel of Fig. 2.9, in the simplest model that includes γ_0 and γ_1 only, the dispersion of Eq. (2.29) is cubic, i.e. $E = v^3k^3/\gamma_1^2$.

In most cases, the other parameters can be considered as perturbations, especially with γ_3 and γ_2 introducing trigonal warping in the band structure. With a decrease in energy as well as momentum, parameter γ_2 dominates the behaviour of the very low energy dispersion as it is independent of momentum k. Similar to the effect of trigonal warping in BLG, the bands exhibit a Lifshitz transition at very low energy. For the Lifshitz transition of TLG-ABC, the isoenergetic line of TLG-ABC in the vicinity of point $\boldsymbol{K}$ breaks into three parts [19], whereas that of BLG breaks into four parts. The left-right asymmetry in the middle and right subplots of Fig. 2.9 is due to the effect of trigonal warping. Note that the effect that the Lifshitz transition has on the band structure of BLG and TLG is discussed in Chapter 5, and the effect that the Lifshitz transition has on the electronic transport properties of BLG and TLG is described in Chapter 6.

2.5.2 Band structure of TLG-ABA

TLG-ABA has the same Bravais lattices and reciprocal lattices as that of SLG. The unit cells of TLG-ABA consists of six atomic sites rather than two; these six sites are labelled $A1$, $B1$, $A2$, $B2$, $A3$ and $B3$, where index "1" represents the bottom layer, "2" represents the middle layer and "3" represents the top layer. The interlayer distance between layers $d = 3.3\,\text{Å}$ is the same as that of BLG. As

shown in Fig. 2.10, in TLG-ABA, sites $B1$, $A2$ and $B3$ sit directly above one another, i.e. there is a mirror reflection symmetry with the respect to the central layer of TLG-ABA.

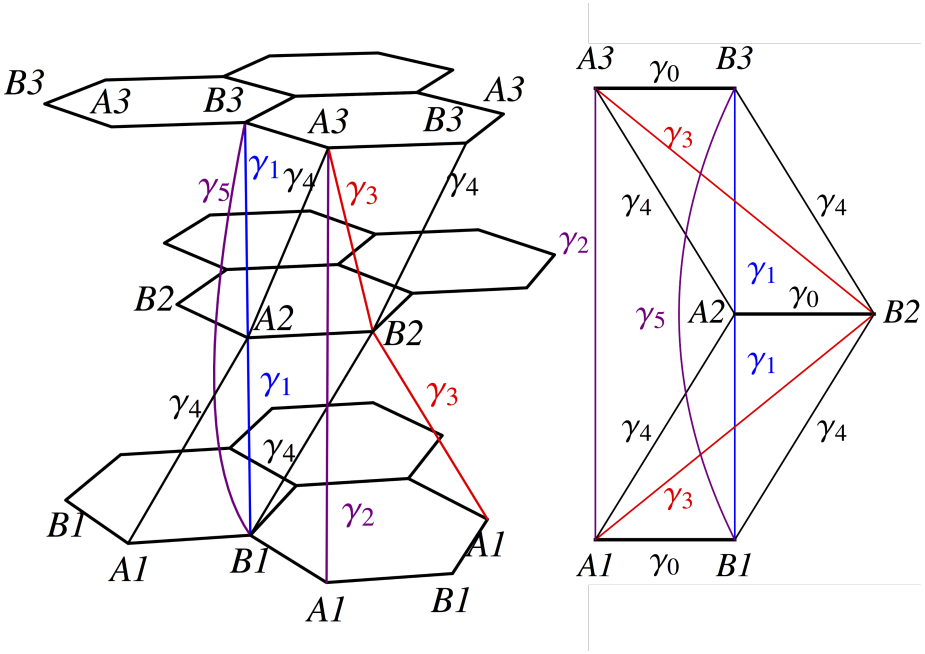

Figure 2.10: Schematic of the crystal lattice of TLG-ABA in which dimer sites $A2$ sit directly above site $B1$, $B3$ sit directly above sites $A2$ and there are two pairs of next nearest layer hoppings between sites $B3$-$B1$ and $A3$-$A1$.

The crystal structure of TLG-ABA is shown in Fig. 2.10. Following the same procedure as in previous sections, the Hamiltonian of TLG-ABA can be written on the basis of Bloch wave function (ϕ_{A1}, ϕ_{B1}, ϕ_{A2}, ϕ_{B2}, ϕ_{A3}, ϕ_{B3}) for valley $\boldsymbol{K}$ and (ϕ_{B1}, $-\phi_{A1}$, ϕ_{B2}, $-\phi_{A2}$, ϕ_{B3}, $-\phi_{A3}$) for valley $\boldsymbol{K}'$ [78–80],

$$\hat{H} = \begin{pmatrix} \epsilon_{2p} & -\gamma_0 f(\boldsymbol{k}) & -\gamma_4 f(\boldsymbol{k}) & -\gamma_3 f^*(\boldsymbol{k}) & \gamma_2/2 & 0 \\ -\gamma_0 f^*(\boldsymbol{k}) & \epsilon_{2p} & \gamma_1 & -\gamma_4 f(\boldsymbol{k}) & 0 & \gamma_5/2 \\ -\gamma_4 f^*(\boldsymbol{k}) & \gamma_1 & \epsilon_{2p} & -\gamma_0 f(\boldsymbol{k}) & -\gamma_4 f^*(\boldsymbol{k}) & \gamma_1 \\ -\gamma_3 f(\boldsymbol{k}) & -\gamma_4 f^*(\boldsymbol{k}) & -\gamma_0 f^*(\boldsymbol{k}) & \epsilon_{2p} & -\gamma_3 f(\boldsymbol{k}) & -\gamma_4 f^*(\boldsymbol{k}) \\ \gamma_2/2 & 0 & -\gamma_4 f(\boldsymbol{k}) & -\gamma_3 f^*(\boldsymbol{k}) & \epsilon_{2p} & -\gamma_0 f(\boldsymbol{k}) \\ 0 & \gamma_5/2 & \gamma_1 & -\gamma_4 f(\boldsymbol{k}) & -\gamma_0 f^*(\boldsymbol{k}) & \epsilon_{2p} \end{pmatrix}. \quad (2.30)$$

Here, we adopted the Slonczewski - Weiss - McClure parameters [55–57] typically used to describe the bulk graphite. Each 2×2 diagonal block describes the inter-

layer behaviour of the bottom layer ($A1$ - $B1$), the middle layer ($A2$ - $B2$) or the top layer ($A3$ - $B3$). The off-diagonal blocks describe the interlayer hopping.

The diagonal elements (i.e., those describing onsite energy), are set to zero. Here, $\gamma_1 \simeq 0.1\gamma_0$ [55–57] describes the hopping between nearest interlayer sites, which sit directly above one another (i.e. $A2$-$B1$ and $B3$-$A2$). Parameters $\gamma_3 \simeq 0.1\gamma_0$ (i.e. $A3$-$B2$ and $A1$-$B2$) and $\gamma_4 \simeq 0.01\gamma_0$ (i.e. $A1$-$A2$, $B1$-$B2$, $A2$-$A3$ and $B2$-$B3$) describe the skewed interlayer hopping [55–57]. The new parameters in TLG-ABA are $\gamma_2 \simeq -0.005\gamma_0$ and $\gamma_5 \simeq 0.002\gamma_0$, which describe the hopping of electron between sites in the top and bottom layers, respectively. The band structure of TLG-ABA Hamiltonian Eq. (2.30) is plotted in Fig. 2.11.

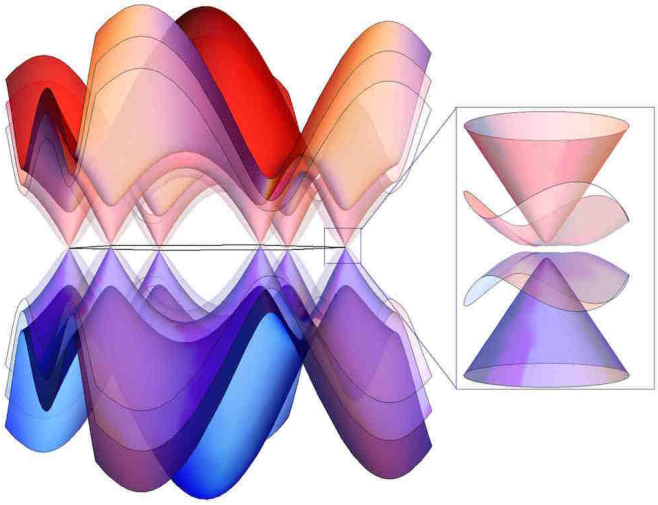

Figure 2.11: (Left) Band structure of TLG-ABA in the tight-binding model. (Right) Band structure of TLG-ABA in the vicinity of the K valley.

Because the model includes six orbitals per unit cell, the band structure of TLG-ABA features six bands. In the corner of the Brillouin zone, i.e. at the $\boldsymbol{K}$ and $\boldsymbol{K}'$ valleys, two of the six bands are approximately separated by roughly γ_1, whereas the other four approach zero energy.

To investigate the behaviour of electrons in the vicinity of points $\boldsymbol{K}$ and $\boldsymbol{K}'$ point, it is convenient to expand the phase factor term $f(\boldsymbol{k})$ in Eq. (2.30). Doing

so, the resulting Hamiltonian [78–80] is

$$\hat{H} = \begin{pmatrix} 0 & v\hat{\pi}^\dagger & v_4\hat{\pi}^\dagger & v_3\hat{\pi} & \gamma_2/2 & 0 \\ v\hat{\pi} & 0 & \gamma_1 & v_4\hat{\pi}^\dagger & 0 & \gamma_5/2 \\ v_4\hat{\pi} & \gamma_1 & 0 & v\hat{\pi}^\dagger & v_4\hat{\pi} & \gamma_1 \\ v_3\hat{\pi}^\dagger & v_4\hat{\pi} & v\hat{\pi} & 0 & v_3\hat{\pi}^\dagger & v_4\hat{\pi} \\ \gamma_2/2 & 0 & v_4\hat{\pi}^\dagger & v_3\hat{\pi} & 0 & v\hat{\pi}^\dagger \\ 0 & \gamma_5/2 & \gamma_1 & v_4\hat{\pi}^\dagger & v\hat{\pi} & 0 \end{pmatrix}, \tag{2.31}$$

where $v_i = \sqrt{3}a_g\gamma_i/2$ are the velocities corresponding to each hopping parameter, $v_0 = v$. The diagonal elements (i.e., those describing onsite energy) are set to zero.

Because TLG-ABA has mirror reflection symmetry, using a unitary transformation, we can separate odd wave functions $\psi_{A1} - \psi_{A3}$, $\psi_{B1} - \psi_{B3}$ from even wave functions $\psi_{A1} + \psi_{A3}$, $\psi_{B1} + \psi_{B3}$, ψ_{A2} and ψ_{B2}. The resulting Hamiltonian of TLG-ABA can then be expressed as

$$\hat{H} = \begin{pmatrix} \hat{H}_o & 0 \\ 0 & \hat{H}_e \end{pmatrix}, \quad \hat{H}_o = \begin{pmatrix} -\gamma_2/2 & v\hat{\pi}^\dagger \\ v\hat{\pi} & -\gamma_5/2 \end{pmatrix},$$
$$\hat{H}_e = \begin{pmatrix} \gamma_2/2 & \sqrt{2}v_3\hat{\pi} & -\sqrt{2}v_4\hat{\pi}^\dagger & v\hat{\pi}^\dagger \\ \sqrt{2}v_3\hat{\pi}^\dagger & 0 & v\hat{\pi} & -\sqrt{2}v_4\hat{\pi} \\ -\sqrt{2}v_4\hat{\pi} & v\hat{\pi}^\dagger & 0 & \sqrt{2}\gamma_1 \\ v\hat{\pi} & -\sqrt{2}v_4\hat{\pi}^\dagger & \sqrt{2}\gamma_1 & \gamma_5/2 \end{pmatrix}. \tag{2.32}$$

This transformed Hamiltonian of TLG-ABA is block-diagonal. The upper-left 2×2 block $\hat{H}_o$ is on the basis of odd wave functions $\psi_{A1} - \psi_{A3}$, $\psi_{B1} - \psi_{B3}$, and it is similar to a gapped Hamiltonian of SLG. The size of the gap is $(\gamma_2 - \gamma_5)/2$. The lower-right block $\hat{H}_e$ is on the basis of $\psi_{A1} + \psi_{A3}$, ψ_{B2}, ψ_{A2} and $\psi_{B1} + \psi_{B3}$, and it is similar to gapped BLG. Therefore, as shown in Fig. 2.12, we can expect the band structure of TLG-ABA features SLG-like and BLG-like parts [80].

As shown in the left plot of Fig. 2.12, a simple model containing only γ_0 and γ_1 produces SLG-like and BLG-like bands. The two next-nearest layer vertical

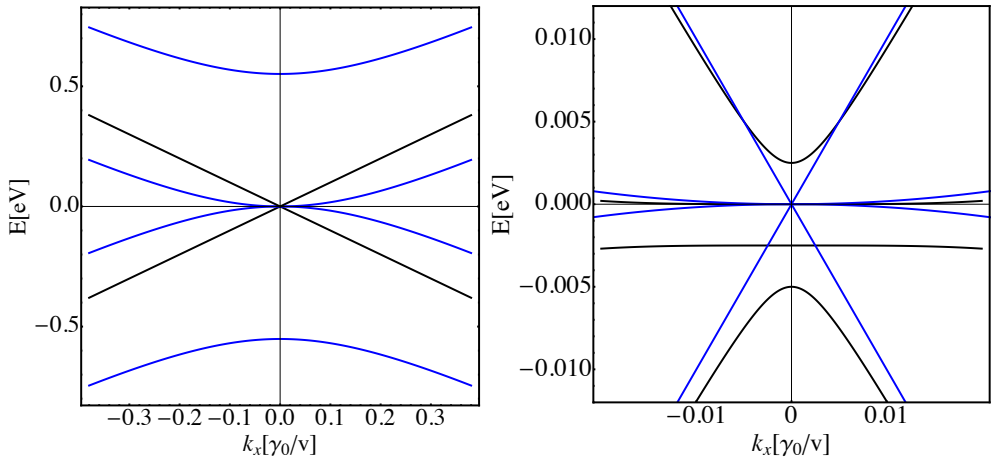

Figure 2.12: (Left) The low-energy band structure of the tight-binding Hamiltonian of TLG-ABA, i.e. Eq. (2.32) for $k_y = 0$, $\gamma_2 = \gamma_5 = 0$ and $v_3 = v_4 = 0$. SLG-like bands (black) and BLG-like bands (Blue) are explicitly shown. (Right) The band structure of TLG-ABA, i.e. Eq. (2.32) for $k_y = 0$, and $v_3 = v_4 = 0$, where the black line represents $\gamma_2 \simeq -0.005\gamma_0$ and the blue line represents $\gamma_2 = \gamma_5 = 0$.

hoppings γ_2 and γ_5 open a gap in both the SLG-like and the BLG-like bands, as shown in the right inset of Fig. 2.12.

2.6 The quantum Hall effect in graphene

2.6.1 Graphene in a magnetic field

When a perpendicular magnetic field is applied to graphene, a hierarchy of physics phenomena will emerge as the magnitude $B = |\boldsymbol{B}|$ of the magnetic field increases [51]. Such phenomena include:

(1) When the magnetic field is relatively weak, i.e. when B is less than several Tesla, the cyclotron radius is greater than the mean free path, meaning electrons are unable to complete a circle, and the Bohr-Sommerfeld quantization rule cannot be observed. Therefore, one will observe the classical Hall effect.

(2) Then, on increasing magnetic field $B \geq 10\,\mathrm{T}$, (temperature $T \leq 80\,\mathrm{K}$) the radius of a cyclotron orbit shrinks and become less than the free mean path. The cyclotron orbit completion makes the Bohr-Sommerfeld quantization rule applicable and Shubnikov-de Haas oscillations will appear [73–75].

(3) When the magnetic field is large enough, $B \geq 14\,\mathrm{T}$, (temperature $T \leq$

4K) to distinguish the cyclotron energy levels, the integer quantum Hall effect is observed. The cyclotron energy levels are the so-called Landau levels [72]. Here, the Hall conductivity displays an integer plateau with an increase in carrier density.

(4) If the magnetic field increases further ($B > 45\,\mathrm{T}$), the degeneracy of electronic spin is lifted, each Landau level is split, and the Zeeman effect appears. One observes more integer plateaux and more filling factors in the carrier density-magnetic field diagram (fan diagram) [188].

(5) When the magnetic field is huge (i.e. $B \simeq 10^5\,\mathrm{T}$), the amount of magnetic flux threading each unit cell becomes a significant factor. The periodic potential of the crystal imposes a translational symmetry on the wave function in addition to the magnetic vector potential, and their superstition determines the translational symmetry of the electronic wave function in a crystal in a magnetic field. In principle, the measurements of this system adhere to a fractional Hall effect, but the strength of the magnetic field required is generally too high to realize in practice. To observe this type of fractional Hall effect in a feasible magnetic field ($B \simeq 30\,\mathrm{T}$), we can utilize a superlattice, either by creating an artificial lattice or by employing a moiré pattern. The quantum Hall effect of a graphene superlattice is discussed in detail in Chapter 3 and 4.

2.6.2 Landau levels of graphene

Electrons in a perpendicular magnetic field follow cyclotron orbits, and their energy is quantized into separate levels known as Landau levels (LLs). The LLs are manifest in quantum oscillations such as the de Haas-van Alphen effect and the Shubnikov-de Haas effect in a low magnetic field as well as in the quantum Hall effect [73–75].

In a conventional two-dimensional electron gas (2DEG), the LL energy is $E_n = \omega_C(n + 1/2)$, where n is a non-negative integer and $\omega_C = eB/m_e$ is the cyclotron frequency of electrons. In such systems, the lowest LL energy $E_0 = \omega_C/2$, also known as the "zero-point energy", depends on the magnitude of the magnetic

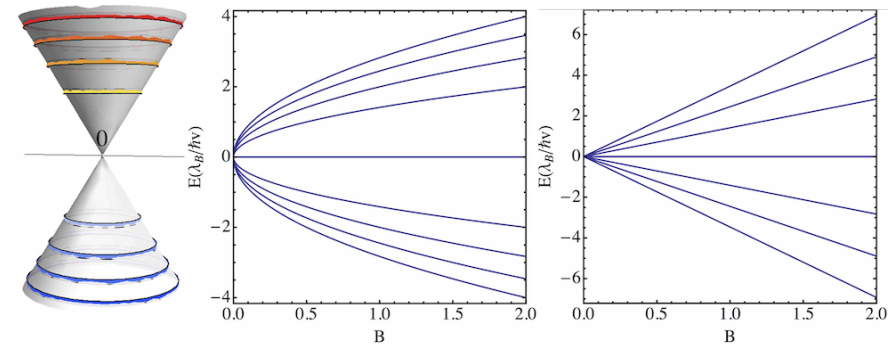

Figure 2.13: (Left) LL quantization of a Dirac cone, where the transparent cone is the dispersion of SLG in the absence of a magnetic field, and the embedded circles on the cone represent the discretized cyclotron energy levels. (Middle) The LL spectrum of SLG [71], in which each level follows $E \propto n\sqrt{B}$, where the magnetic field B is measured in natural units. (Right) The LL spectrum of BLG [71], in which each level follows $E \propto nB$, where magnetic field B is measured in natural units.

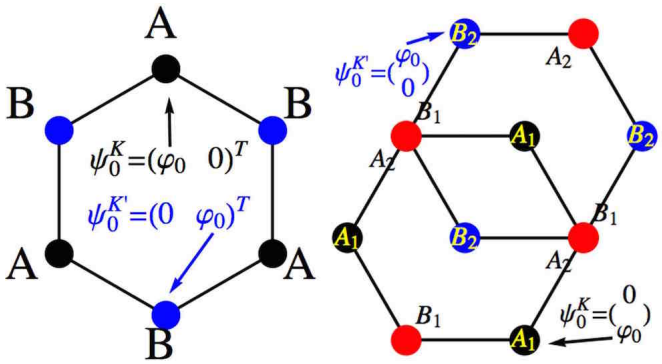

Figure 2.14: The distribution of the wave function corresponding to the zeroth LL SLG (left) and BLG (right) graphene in a perpendicular magnetic field in real space. The blue and black dots, respectively, represent non-dimer sites A and B in SLG and A_1 and B_2 in BLG, whereas the red dots represent dimer-sites B_1 and A_2. The solid line represents intralayer hopping. When $B > 0$, all wave functions concentrate on one atomic site in the zeroth LL of graphene.

field. In contrast, the LL spectrum in graphene has a zero energy level, which is independent of the magnetic field. Note that this is a characteristic feature of the Dirac cone and can be taken as originating from the unique Berry phase of graphene, as discussed in Section 2.7 and Appendix I.

In a magnetic field perpendicular to the graphene sheet, i.e. $\boldsymbol{B} = (0, 0, -B)$, we can use the vector potential in the Landau gauge [10] $\boldsymbol{A} = (0, -Bx, 0)$. The secular momentum of the electron in a magnetic field is expressed by Peierls substitution [83, 109, 112] [11] $\boldsymbol{p} \rightarrow \boldsymbol{p} + e\boldsymbol{A}$, where the charge of the electron is $-e$. Then, operator $\hat{\pi}$ in the Hamiltonian of Eq. (2.19) becomes a "lowering" operator for Landau functions (with a constant factor λ_B). By solving the equation $\hat{\pi}\phi_0 = 0$, we obtain an expression for the Landau wave function as [12]

$$\phi_l(x, y) = A_l \mathbb{H}_l \left(\frac{x}{\lambda_B} - p_y \lambda_B \right) \exp \left[-\frac{1}{2} \left(\frac{x}{\lambda_B} - p_y \lambda_B \right)^2 + i p_y y \right], \tag{2.33}$$

where $A_l = 1/\sqrt{2^l l! \sqrt{\pi}}$, $\mathbb{H}_l$ are Hermite polynomials of order l and $\lambda_B = \sqrt{1/|eB|}$. Accordingly, the action of lowering and raising operators is given by

$$\hat{\pi}\phi_l = -\frac{\sqrt{2}i}{\lambda_B}\sqrt{l}\phi_{l-1}, \qquad \hat{\pi}^\dagger \phi_l = \frac{\sqrt{2}i}{\lambda_B}\sqrt{l+1}\phi_{l+1}. \tag{2.34}$$

From the above equation, the LLs and their wave functions can be solved from

[10] We can choose the other gauge, because gauge invariance does not mean that the Hamiltonian or the wave function do not change. The gauge inveriance refers to the invariant physical observables, such as the energy, probability. Here, Landau gauge is a relatively easy gauge to keep translational invariance.

[11] The precondition of applying Peierls substitution is that the magnetic length λ is much larger than lattice constant. For example, $B = 10\,\mathrm{T}$, $\lambda = \sqrt{\hbar/(eB)} \simeq 800\,\text{Å} \gg a_g = 2.46\,\text{Å}$.

[12] Here, this state is also called "magnetic oscillation state". Because once we choose gauge that keeps the translational invariance on y direction, the form of the wave function is a product between a plain wave and a harmonic oscillator. Of course, by choosing another gauge (such as cylindrical gauge), the wave function is still in a magnetic oscillation form, but with an awkward mathematics, a 2D Harmonics.

Eq. (2.19) in the absence of γ_3 and γ_4 as following,

$$E_{l,\pm} = \pm\frac{\sqrt{2}v}{\lambda_B}, \quad \psi_{l,\pm} = \frac{1}{\sqrt{2}}\begin{pmatrix} \phi_l \\ \mp i\phi_{l-1} \end{pmatrix}, \quad \text{for } l \geq 1,$$
$$E_0 = 0, \quad \psi_0 = \begin{pmatrix} \phi_0 \\ 0 \end{pmatrix}, \quad \text{for } l = 0. \tag{2.35}$$

Similarly, based on Eq. (2.24), we can solve the LL and corresponding wave functions of BLG in a magnetic field as

$$E_{l,\pm} = \pm\frac{1}{m\lambda_B^2}\sqrt{l(l-1)}, \quad \psi_{l,\pm} = \frac{1}{\sqrt{2}}\begin{pmatrix} \phi_l \\ \pm\phi_{l-2} \end{pmatrix}, \quad \text{for } l \geq 2,$$
$$E_l = 0, \quad \psi_l = \begin{pmatrix} \phi_l \\ 0 \end{pmatrix}, \quad \text{for } l = 0, 1. \tag{2.36}$$

Fig. 2.13 shows both the LL spectra of SLG and BLG. By carefully considering the wave functions corresponding to the zeroth LL of SLG (ψ_0) in Eq. (2.36), and the zeroth and first LL of BLG ψ_0 and ψ_1 in Eq. (2.36), we can note that there is only one non-zero component. Remember that the basis is (ϕ_{A1}, ϕ_{B2}) for valley $\boldsymbol{K}$ and (ϕ_{B2},$-\phi_{A1}$) for valley $\boldsymbol{K}'$. It means that, when the direction of the magnetic field is downward ($\boldsymbol{B} = (0, 0, -B)$), the wave function is located on the $A1$ site at the $\boldsymbol{K}$ valley. Conversely, as shown in Fig. 2.14, the wave functions are concentrated on the $B2$ site at the zeroth and first LL at the $\boldsymbol{K}'$ valley. Once the direction of the magnetic field is flipped (i.e. $\boldsymbol{B} = (0, 0, B)$), the location of the electron wave function switches to the other sublattice. For the $\boldsymbol{K}$ valley, all of the wave function concentrates on $B2$ [13].

The interaction between the periodicity of two-dimensional materials and the vector potential is discussed in Chap. 3 and 4. The corresponding effect on the

[13]It seems peculiar that only one component is non-zero in zeroth LL wave function, as this implies that the electronic distribution in real space will be different. But consider that there are two valleys simultaneously, and each valley holds zeroth LL wave function on one sublattice, so this does not break symmetry.

localization of the wave function at zero energy is discussed in detail in Chap. 4.

2.7 Berry phase of graphene

In general, the Berry phase (i.e. geometrical phase) arises because an eigenstate of a Hamiltonian acquires an additional phase after it revolves around a loop in an external parameter space [91]. In the context of graphene, the Berry phase refers to the phase factor acquired by an eigenstate of the Hamiltonian after it completes a full cyclic adiabatic process[14] in momentum space at fixed energy in the vicinity of the DP, as schematically shown in Fig. 2.15.

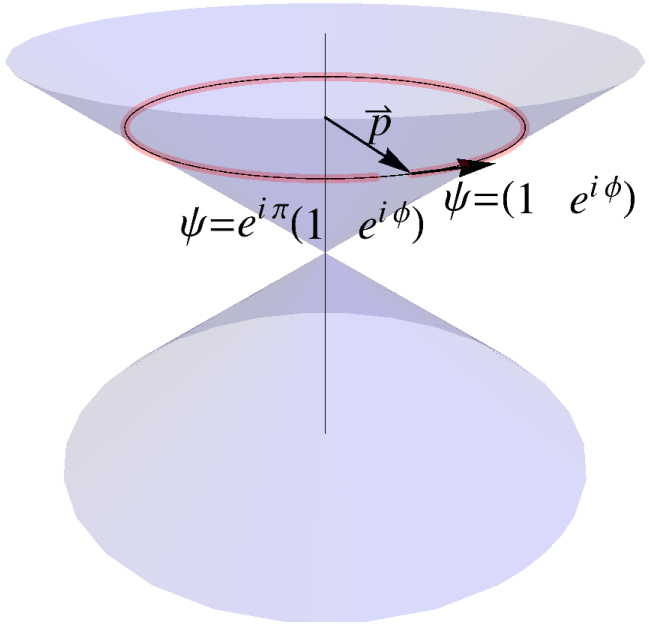

Figure 2.15: A schematic of graphene's Berry phase in which the blue cone is the band structure around the K valley of the DP in momentum space and the circle in the conduction band is the isoenergetic line. Note that an electron that completes a full circle along the isoenergetic line will acquire additional phase factor π.

The Berry phase Γ is given by [92]

$$\Gamma = -i \oint \psi^*(\boldsymbol{p}(t)) \frac{\partial}{\partial t} \psi(\boldsymbol{p}(t)) dt. \tag{2.37}$$

[14]The terminology adiabatic process is firstly used to describe the approximation in atomic physics, because of the significant mass difference between nucleon and electron, the relative movement of nucleon with respect to electron can be ignored. In thermodynamics, adiabatic means free of heat exchange. In quantum mechanics, it means free of change of energy state.

For example, we consider the eigenfunction of SLG in Eq. (2.20) as

$$E_{\pm} = \pm v|\boldsymbol{p}|, \quad \psi_{\pm} = \frac{1}{\sqrt{2}} \begin{pmatrix} 1 \\ \pm e^{i\varphi} \end{pmatrix} e^{i\boldsymbol{p}.\boldsymbol{r}},$$

where φ is the polar angle of momentum $\boldsymbol{p}$, $\boldsymbol{p} = |\boldsymbol{p}|(\cos(\varphi), \sin(\varphi))$. Substituting the above eigenfunction of SLG into Eq. (2.37) yields

$$\Gamma = -i \oint dt \frac{1}{2} \frac{\partial \varphi}{\partial t} + \oint dt \left(\frac{\partial \boldsymbol{p}}{\partial t} \cdot \boldsymbol{r} + \frac{\partial \boldsymbol{r}}{\partial t} \cdot \boldsymbol{p} \right) = \pi. \tag{2.38}$$

If we define $\Gamma \in [0, 2\pi)$, the above equation provides a non-trivial phase factor π, which further indicates that, after evolving along a closed contour path around the DP in momentum space, the eigenfunction in Eq. (2.20) of SLG acquires an extra phase factor π.

In the case of gapped SLG, the Hamiltonian is

$$\hat{H} = \begin{pmatrix} \Delta/2 & v\hat{\pi}^{\dagger} \\ v\hat{\pi} & -\Delta/2 \end{pmatrix}, \tag{2.39}$$

where Δ is the gap size. The Berry phase will be less than π, the difference as compared to perfect graphene depends on the size of the gap.

Similarly, we can calculate the Berry phase for the simplest model of BLG (i.e. Eq. (2.24)) or TLG (i.e. Eq. (2.29)) at low energy, and they give 2π and obtain 3π respectively. Further discussion regarding the Berry phase can be found in Appendix I.

Chapter 3

Magnetic minibands in SLG with a hexagonal moiré superlattice

3.1 Introduction

In this chapter, we consider a superlattice that is created when graphene is placed on top of hexagonal boron nitride (h-BN). We will discuss its band structure, quantum Hall effect and magnetic energy spectrum.

We begin by describing the origin of the "Hofstadter butterfly" with a simple model. Next, we describe the more complicated moiré superlattice of graphene, and then discuss its band structure in the absence of a magnetic field as well as its butterfly spectrum in a finite magnetic field.

3.1.1 Origin of the Hofstadter butterfly spectrum

As shown in Fig. 3.1, the "Hofstadter butterfly" spectrum is an interesting and beautiful phenomenon. It was first introduced by D. Hofstadter in 1976 [83]. Because it is one of the few fractal patterns[1] generated from physics rather than mathematics, it has since inspired many physicists [81, 107, 108].

[1] A fractal is a natural phenomenon or a mathematical set that exhibits a repeating pattern which is displayed at every scale or iteration. The statistical index of complexity or space-filling capacity of a fractal pattern can be measured by its fractal dimension D, which is not necessarily an integer. See Appendix A for more details.

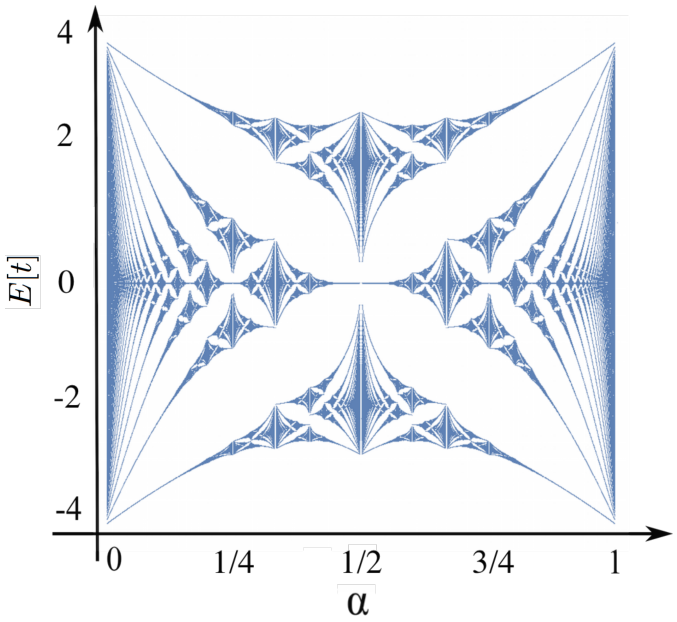

Figure 3.1: The fractal spectrum of an electron on a square crystalline lattice in a magnetic field, where the horizontal axis has units of $\alpha = \phi/\phi_0$, i.e. the magnetic flux threading a unit cell of the crystal, and the vertical axis represents energy E in terms of a natural unit E_0. Each point of this plot is an eigen energy calculated by diagonalizing the Hamiltonian matrix for given α, a location of Brillouin zone (here is Γ point). The fractal dimension of this plot is $D = 1.70017$. The Figure was generated numerically as described in the main text.

The fractal Hofstadter butterfly spectrum can be generated by considering a two-dimensional square lattice with lattice constant a, as shown in the top panel of Fig. 3.2. This system can be described by a simple Hamiltonian of the tight-binding model:

$$\hat{H} = \sum_{\langle i,j \rangle} t c_i^\dagger c_j + h.c., \tag{3.1}$$

where t is the transfer integral between neighboring sites located at $\boldsymbol{R}_j$ and $\boldsymbol{R}_i$, i.e. t is the (isotropic) hopping parameter, $c_i(c_i^\dagger)$ is the annihilation (creation) operator of site $\boldsymbol{r}_i = \hat{\boldsymbol{x}} m_i a + \hat{\boldsymbol{y}} n_i a$ and $m_i, n_i \in \mathbb{Z}$.

By applying a perpendicular magnetic field $\boldsymbol{B} = (0, 0, -B)$ and vector potential $\boldsymbol{A} = -B(0, x, 0)$, the Peierls substitution $\boldsymbol{k} \to \boldsymbol{k} - e\boldsymbol{A}$ shows that t depends on the relative position of the two sites $\delta_R = \boldsymbol{R}_j - \boldsymbol{R}_i$:

$$t \to t e^{-ie\boldsymbol{A}\cdot\delta_{\boldsymbol{R}}} = t e^{-ieBm_i a\cdot(n_j a - n_i a)} = t e^{\pm i 2\pi m_i \alpha}, \tag{3.2}$$

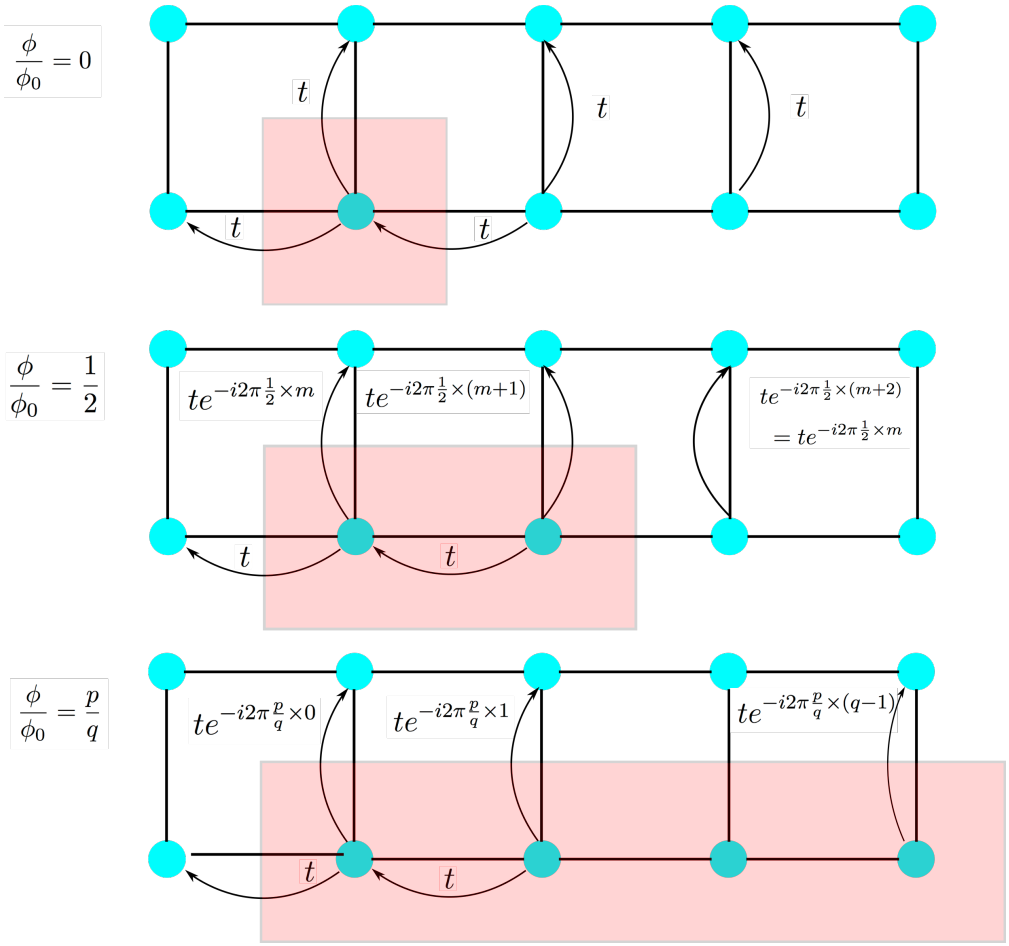

Figure 3.2: An electron in a square lattice in a magnetic field, $\boldsymbol{B} = \hat{z}B$, $\boldsymbol{A} = B(0, x, 0)$. The pink rectangles indicate the area of a unit cell. The arrows represent hopping between different sites, and the value of the transfer integral between different sites in zero magnetic field is t. (Top) Zero magnetic field, the unit cell area is a^2 and the transfer integral between different sites t is isotropic. (Middle) Magnetic field $B = \phi_0/(2a^2)$, so the Peierls substitution introduces an additional phase factor $e^{-i\pi m}$, where $x = ma$ is the coordinate of the site. Here $te^{-i\pi(m+2)} = te^{-i\pi m}$ and the unit cell contains two sites. (Bottom) Magnetic field $B = \phi_0 p/(qa^2)$, the unit cell contains q sites, and $te^{-i2\pi(m+q)} = te^{-i2\pi m}$.

where $n_j = n_i \pm 1$ represents neighboring sites of the square lattice, $\alpha = \phi/\phi_0$, $\phi = a^2 B$ is the magnetic flux threading a unit cell, and $\phi_0 = h/e$ is the flux quanta. This means that, in a magnetic field, the hopping parameter t depends on the coordinate $m_i a$. As shown in the middle and bottom panels of Fig. 3.2, once $q\alpha = p$, where $p, q \in \mathbb{Z}$, translational symmetry is recovered, i.e. $e^{\pm i2\pi(m_i+q)\alpha} = e^{\pm i2\pi m_i \alpha}$.

Therefore, we obtain the relation

$$\alpha = \frac{p}{q} = \frac{\phi}{\phi_0}, \tag{3.3}$$

which suggests that once the ratio between magnetic flux threading a unit cell and flux quanta is a rational number p/q, the translational symmetry of an electron in a square lattice in a magnetic field is recovered but reduced by q times. In this case, the unit cell is enlarged q times as shown in Fig. 3.2. Then, using the tight-binding model introduced in Chapter 2, we can build a $q \times q$ Hamiltonian matrix to describe a q-times enlarged unit cell. The eigenenergies of the bands can be obtained by diagonalizing the matrix for a given point in the magnetic Brillouin zone. By mapping the eigen energy for the rational value p/q, the butterfly spectrum can be built as shown in Fig. 3.1. Further details of this calculation are given in Appendix B.

Due to the nature of rational values, even a small deviation in the value of α drastically changes the values of p and q, leading to a significant change in the number of minibands[2]. This is the origin of the recursive structure of the butterfly spectrum, as shown in Fig. 3.1. Furthermore, because of the intrinsic discontinuity of rational numbers, the butterfly spectrum is also discontinuous. However, our vision intuitively suggests that this spectrum seems continuous. This is not an

[2]The reason we use "miniband" here are as following: (a) The unit cell is enlarged by q times for given magnetic field strength $\alpha = p/q$, so the Brillouin zone shrunk by q times, i.e. a smaller band. (b) Because the unit cell is enlarged by q times, thus the Hamiltonian matrix becomes $q \times q$ dimension. Therefore, the "original band" splits into q bands with smaller band width, i.e. narrower bands. In general, we call this smaller and narrower band of electron in crystal in magnetic field a "miniband".

illusion: all dots in α' spectrum are indeed approaching the α spectrum when α' approaches α [83]. Considering that every physical parameter in a practical experiment has uncertainty, such as magnetic field B applied to this square lattice, the final value of α observed is smeared. This smearing eliminates the discontinuity of the butterfly spectrum. To visualize this, we can imagine zooming out of Fig. 3.1 to obtain a low-resolution version. Also, all observable physical properties are not determined by the specific band structure, but rather eventually depend on the distribution of the number of states along a small but finite energy region, in which only a slight change occurs in the variation of α [82]. Therefore, the instability and discontinuity of the magnetic spectrum do not induce any disasters into actual physical observations.

In general, for an electron in a periodic lattice in a magnetic field, both the crystalline periodic lattice and the magnetic vector potential apply translational symmetry to the wave function of the electron. The two translational symmetries compete with one another and, once they satisfy the special relation expressed in Eq. (3.3), the translational symmetry of the wave function can be recovered, but it is reduced. Simultaneously, the degeneracy of eigenvalues of the Schrödinger equation are also lifted. For specific values of the magnetic field, each original band splits into numerous magnetic minibands. From a mathematical perspective, the instability of the denominator and numerator of the rational number $\alpha = p/q$ is the direct cause of the recursive structure of the spectrum. Translated into physical terminology, the competition between the two distinct translational symmetries determines the fractal butterfly spectrum.

3.1.2 Development of butterfly spectrum research

In general, by increasing the magnetic field strength, all electrons in a two-dimensional lattice are eventually fractured into multiple bands [82, 107, 108], as mentioned in Section 2.6.1. Since the sparsity of the spectrum increases for larger values of the denominator and numerator in p/q (hence, smaller gaps), the observation

of fractal magnetic bands in real crystals requires unsustainably strong magnetic fields, e.g. $B \simeq 10^5\,\mathrm{T}$ for a unit cell area of $S = 1\,\text{Å}^2$. Early efforts were focused on two-dimensional electrons in periodically patterned GaAs/AlGaAS heterostructures [84], where the superimposed superlattice period was large enough, so that the explicit fractal spectrum can be observed. More recent observations of moiré superlattices (this terminology will be explained later), both for twisted BLG [131, 132] and graphene residing on substrates with hexagonal facets [85], have illustrated an alternative way of creating a long-range periodic potential for electrons, i.e. by making lattice-aligned graphene heterostructures using a hexagonal crystal with an almost commensurate period.

Furthermore, superlattice perturbations for Dirac electrons have been discussed in various different contexts, some of which pre-date the realization of the graphene/*h*-BN heterostructure. Many studies have investigated the influence of one or two-dimensional electrostatic potentials on graphene electrons [143–165], which may be achievable using patterned gates [166, 167]. Magnetic and pseudo-magnetic field superlattices (the latter arising from periodically strained graphene) have also been extensively studied [152, 168–171] with steps towards experimental realizations [172, 173].

3.1.3 My work: quantum Hall effect of the graphene superlattice

In this subsection, we use the graphene/*h*-BN heterostructure as an example of moiré-perturbed graphene to study magnetic minibands. When the surface layer of the substrate is inversion symmetric [3] , the zero-magnetic-field spectrum displays an interesting Dirac-like band structure at the first miniband edge [86–88]. Because this "Dirac-like" structure is not located at zero energy, but rather in

[3]The reason we specifically mention "inversion symmetry" is that the substrate *h*-BN is not inversion symmetric. The two sublattices of *h*-BN, Boron and Nitride, are different. One can not get back to the initial kind of atomic site after a space inversion. However, this inversion symmetry breaking is not necessarily significant. So we firstly consider the situation that inversion symmetry holds.

the valence band, we denote this feature as the "secondary DP". Furthermore, when the magnetic flux threading a super unit cell is a rational number times the flux quantum, i.e. $B_{\frac{p}{q}} = p\phi_0/(q\sqrt{3}a^2/2)$, where ϕ_0 is the flux quantum, $p, q \in \mathbb{Z}$ and a is the superlattice constant, we find that a hierarchy of Dirac-like electrons systematically reappear at the edges of the magnetic minibands. The surrounding fractal spectrum found at $B_{\frac{p}{q}}$ consists of q-fold degenerate LLs of gapped Dirac-like electrons in an effective magnetic field $\delta B = B'_{\frac{p}{q}} - B_{\frac{p}{q}}$. As the Dirac model features a "zero-energy" LL, separated by the largest gap from the rest of the spectrum, the size of gap decreases between higher LLs. This feature determines a specific hierarchy of gaps in the Hofstadter butterfly, resulting in a peculiar sequence of dominant incompressible states of electrons in graphene-hBN heterostructures in a strong magnetic field.

This work was performed in collaboration with others. My contribution was the numerical calculation and a portion of the analytical evaluation, especially the fractal spectrum in a magnetic field.

3.2 Theoretical framework: zero magnetic field

3.2.1 The moiré superlattice

Two super-positioned lattices with the same Bravais lattice structure generate a supercell with the same lattice structure and a much larger lattice constant, the pattern formed by the supercell is called a moiré pattern. Considering that graphene and *h*-BN substrate are perfect crystals placed rigidly on top of one another, the corresponding moiré pattern is shown in Fig. 3.3. This geometrical effect can be observed, for example, using scanning tunneling microscopy or conductive atomic force microscopy [37, 40–42, 46, 47].

Note that the larger the misalignment angle θ, the smaller the superlattice constant a. The largest superlattice constant is $a = a_g/\delta$ [4] in the case of $\theta =$

[4] To understand this, a simple but not rigorous way is to consider the following situation: one lattice constant $a_g = 2$ and the other $a_{BN} = 3$, their difference is $\delta = 50\%$, so the commensurate

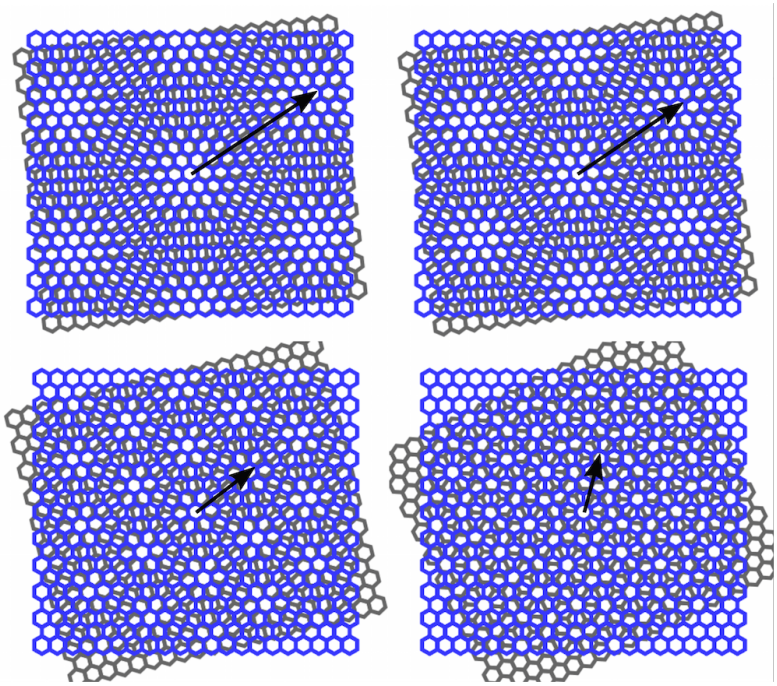

Figure 3.3: The moiré pattern results from the superposition of two two-dimensional substrates with similar Bravais lattices. Its period depends on the difference between the lattice constants and misalignment angle. The plots here show that the period of the moiré pattern decreases as the misalignment angle θ increases.

0, where a_g is the primitive lattice constant of the layered material, here being graphene. In this case, the superlattice vectors $\boldsymbol{a}_m$ and the lattice vectors of the layered material $\boldsymbol{a}'_m$ are

$$\boldsymbol{a}_m = \boldsymbol{a}'_m/\delta, \quad \boldsymbol{a}'_m = \hat{R}_{2\pi m/6}(a_g, 0), \tag{3.4}$$

where $\hat{R}_\theta$ is the rotation matrix of angle θ. The superlattice vectors $\boldsymbol{a}_1$ and $\boldsymbol{a}_2$ are shown in Fig. 3.4. The unit of length is set to $|\boldsymbol{a}_m|$ from now on. A detailed and insightful discussion of how to describe moiré pattern can be found in Appendix C as well as Ref. [195].

For the graphene/*h*-BN heterostructure, the lattice constant of *h*-BN is $a_{BN} = 2.50\,\text{Å}$, and the lattice constant of graphene is $a_g = 2.46\,\text{Å}$, so their difference is $\delta \simeq 1.8\%$. The period of the moiré pattern can be as long as 14 nm at misalignment angle $\theta = 0$, which provides a periodicity several thousands times larger than

length is $a = 6 = a_{BN}/\delta$. When the two lattice constants approximate each other, $a = a_g/\delta$ holds. A rigorous discussion is given in Appendix C.

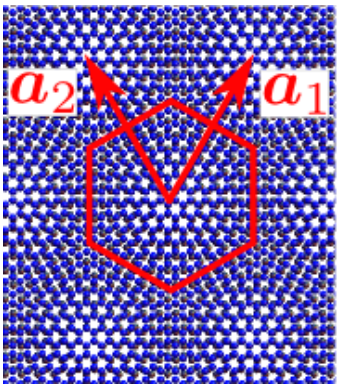

Figure 3.4: The primitive superlattice vectors of a moiré pattern in the case of misalignment angle $\theta = 0$, $\boldsymbol{a}_1 = a(\frac{1}{2}, \frac{\sqrt{3}}{2})$, $\boldsymbol{a}_2 = a(\frac{-1}{2}, \frac{\sqrt{3}}{2})$ and unit cell area $S = \frac{\sqrt{3}}{2}a^2$.

graphene's unit cell. Therefore, the fractal magnetic minibands can be observed in sustainable magnetic fields ($B \simeq 10\,\mathrm{T}$). In the subsection below, we use this superlattice constant (14nm at $\theta = 0$) unless otherwise stated [5].

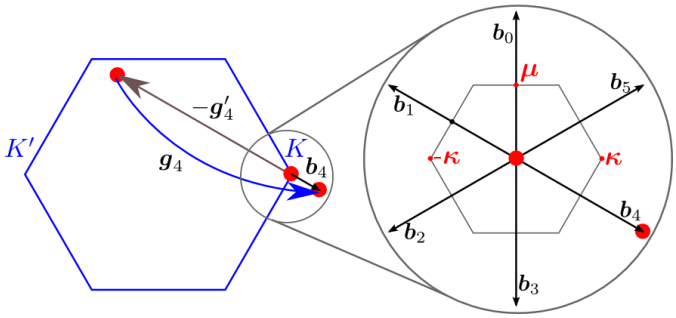

Figure 3.5: The Brillouin zones of graphene (left) and the moiré superlattices (right), with various highly symmetric points and reciprocal lattice vectors.

From Eq. (2.1) and (3.4), one can derive the expression of reciprocal superlattice vector $\boldsymbol{b}_m$ as,

$$\begin{aligned} \boldsymbol{b}_m &= \boldsymbol{g}_m - \boldsymbol{g}'_m \approx \delta \boldsymbol{g}_m, \quad m = 0, \cdots 5, \\ \boldsymbol{g}_m &= \hat{R}_{2\pi m/6}(0, 4\pi/\sqrt{3}a_g), \quad \boldsymbol{g}'_m = (1+\delta)^{-1}\boldsymbol{g}_m, \end{aligned} \tag{3.5}$$

[5] The reason that we use an exact misalignment angle $\theta = 0$ can be shown in two levels. The first reason is the magnitude of moiré perturbation $\mu \leq 10\,\mathrm{meV}$ is much smaller than the characteristic energy scale of this system $vb \simeq 350\,\mathrm{meV}$. We need to minimize vb to observe the effect of perturbation, therefore the smaller b, i.e. smaller θ, is preferred. Secondly, why do we need a exact zero θ but not finite value? This can be justified as following. The character of the system is determined by certain set of superlattice reciprocal lattice. If there is a finite value of θ, the moiré pattern will be definitely misaligned with the graphene lattice in real space. However, the Hamiltonian we use to describe graphene is Dirac Hamiltonian (Eq. (2.19)), which is isotropic, i.e. there is no characteristic direction to compare with the directions of moiré pattern. So even if θ is finite, its effect is to only rescale the band structure but no additional effect. For simplicity, we set $\theta = 0$.

where $\boldsymbol{g}_m$ is the graphene reciprocal lattice vector. The six (i.e. $m = 0, \cdots 5$) shortest reciprocal vectors of the moiré superlattice $\boldsymbol{b}_m$ are shown in Fig. 3.5. The area of the Brillouin zone is $S_{BZ} = b^2\sqrt{3}/2$, where $b = |\boldsymbol{b}_m|$. The corner of the hexagonal superlattice Brillouin zone is denoted as $\zeta\boldsymbol{\kappa} = \zeta(\boldsymbol{b}_4 + \boldsymbol{b}_5)/3$, where $\zeta = \pm 1$.

Then, the dominant effect of moiré perturbation on the graphene Dirac electrons can be modeled by scattering processes with non-zero reciprocal lattice vectors $\boldsymbol{b}_m$. One such process is shown in the left panel of Fig. 3.5 , an electron which is shown as a red point at graphene's Brillouin zone corner, $\boldsymbol{K}$, is scattered by $-\boldsymbol{g}_4'$. By adding a graphene reciprocal vector, the moiré superlattices perturbation provides intra-valley scattering by the simplest harmonics of moiré superlattices ($\boldsymbol{b}_4 = \boldsymbol{g}_4 - \boldsymbol{g}_4'$ in this case). One point to be emphasized is, although the process $\boldsymbol{b}_4 = \boldsymbol{g}_4 - \boldsymbol{g}_4'$ can be considered as a generalization of two successive scatterings, the starting point of our Hamiltonian (in next section) is the moiré superlattice vector. We are not relying on the direction of reciprocal lattice of graphene or h-BN.

3.2.2 Hamiltonian of moiré perturbed graphene

To describe the low-energy (i.e. $|\epsilon| \lesssim vb \simeq 0.35\,\mathrm{eV}$) behavior of electron in graphene/h-BN heterostructure, we use following the Hamiltonian [88],

$$\begin{aligned}\hat{H} =& v\hat{\boldsymbol{p}}\cdot\boldsymbol{\sigma} + vb\big(u_0^+ f_+ + u_0^- f_-\big) + \xi vb\sigma_3\big(u_3^+ f_- + u_3^- f_+\big) \\ &+ \xi v\boldsymbol{\sigma}\cdot\big[\boldsymbol{l}_z\times\nabla\big(u_1^+ f_- + u_1^- f_+\big)\big]. \end{aligned} \tag{3.6}$$

Here σ_i are the Pauli matrices, acting on Bloch states $(\phi_{AK}, \phi_{BK})^T$ in the $\boldsymbol{K}$ valley ($\xi = 1$) and $(\phi_{BK'}, -\phi_{AK'})^T$ in the $\boldsymbol{K}'$ valley ($\xi = -1$), $f_\pm = \sum_m (\pm 1)^{m+\frac{1}{2}} e^{i\boldsymbol{b}_m\cdot\boldsymbol{r}}$. In the Dirac term, $\hat{\boldsymbol{p}} = -i\nabla + e\boldsymbol{A}$ ($\hbar = 1$) describes momentum relative to the valley centre with $[\nabla \times \boldsymbol{A}]_z = B$. The detailed process of obtaining Hamiltonian of moiré perturbed graphene can be found in Appendix. D.

In addition to the dominance of the simplest moiré superlattice harmonics in the perturbation, the *h*-BN substrate can only affect the graphene electrons via the following three distinct mechanisms [88]: (1) an electrostatic potential, which does not distinguish between the two carbon sublattices; (2) a sublattice-asymmetric part of the potential; and (3) spatial modulation of the nearest neighbour carbon-carbon hopping amplitude. Each of these can be thought of as contributing either symmetrically or anti-symmetrically under in-plane spatial inversion. In the two limits where either (a) both boron and nitrogen sublattices perturb the Dirac electrons with almost the same strength or (b) the dominant perturbation arises from only one sublattice, it can be argued [88] that the inversion symmetry of the system would only be weakly broken. Then, the moiré superlattice potential can be modeled as a combination of a dominant inversion-symmetric part with the addition of a small inversion-asymmetric perturbation. Accordingly, the moiré superlattice perturbation can be parametrized by six phenomenological parameters that control the inversion symmetric (u_0^+, u_3^+, u_1^+) and inversion asymmetric (u_0^-, u_3^-, u_1^-) components of modulation mechanisms (1), (2) and (3) described above. Possible choices for values of the phenomenological parameters $u_i^\pm$ are discussed in the next section.

Using the anti-commutation properties of the Pauli matrices, it is possible to deduce the following relations [88] for band energy at different values of momentum $\boldsymbol{p}$ and parameters u_i^+s [6]:

$$\epsilon_{\boldsymbol{K}+\boldsymbol{p}}^{u_0^+,u_1^+,u_3^+} = -\epsilon_{\boldsymbol{K}-\boldsymbol{p}}^{-u_0^+,-u_1^+,u_3^+} = -\epsilon_{\boldsymbol{K}+\boldsymbol{p}}^{-u_0^+,u_1^+,-u_3^+} = \epsilon_{\boldsymbol{K}-\boldsymbol{p}}^{u_0^+,-u_1^+,-u_3^+}. \tag{3.7}$$

3.2.3 Band structure of moiré perturbed SLG

In Chapter 2, we discussed the first term of Eq. (3.6). In this subsection, we take the Dirac Hamiltonian the dominant term in the vicinity of zero energy and then

[6] The first equation can be derived by applying σ_3 onto the eigen equation, i.e. $\sigma_3\hat{H}\sigma_3\sigma_3\psi = \epsilon\sigma_3\psi$; the second can be derived by simply inverting the coordinate $\boldsymbol{r} \to -\boldsymbol{r}$; applying the two above operations simultaneously will lead to the third equation.

treat the rest of Eq.(3.6) as perturbations. By applying second-order perturbation theory (with details given in Appendix E), we can calculate the energy shift of the DP, E_{Shift}, the effective velocity v_{eff} and the size of the gap, Δ_0, of the "zero-energy" DP [43]:

$$\begin{aligned} E_{\text{Shift}} &= 12bv(u_1^+u_3^+ + u_1^-u_3^-), \\ \Delta_0 &= 24vb|u_1^+u_0^- + u_0^+u_1^-|, \\ v_{\text{eff}} &= v[1-6(u_1^+)^2 - 6(u_1^-)^2]. \end{aligned} \tag{3.8}$$

The second equation above shows that the breaking of inversion asymmetry, i.e. the existence of u_1^- and u_0^-, opens a gap. The third equation shows that the influence on velocity is small when $u_1^\pm \ll 1$.

Next we consider the secondary DP at the corner of the mini Brillouin zone $\zeta\boldsymbol{\kappa} = \zeta(\boldsymbol{b}_4 + \boldsymbol{b}_5)/3$ ($\zeta = \pm 1$) in the valence band of moiré perturbed graphene. Note that zone folding using Bragg vectors $\boldsymbol{b}_m$ brings together three degenerate plane-wave states $|\zeta\boldsymbol{\kappa}\rangle$, $|\zeta(\boldsymbol{\kappa}+\boldsymbol{b}_2)\rangle$, and $|\zeta(\boldsymbol{\kappa}+\boldsymbol{b}_1)\rangle$ at each of the two inequivalent corners of the moiré Brillouin zone. Using $\boldsymbol{k}\cdot\boldsymbol{p}$ theory[7], the vicinity of each moiré Brillouin zone corner can then be described by using an effective Hamiltonian acting on a three-component vector of smoothly varying envelope functions, which are written on the basis of the above three plane-wave states, Eq. (2.20). A matrix element of the effective Hamiltonian is $\langle\psi(\boldsymbol{\kappa}+\boldsymbol{b}_i+\boldsymbol{p})|\hat{H}|\psi(\boldsymbol{\kappa}+\boldsymbol{b}_j+\boldsymbol{p})\rangle$ (note that operator $\hat{p}$ measures momentum relative to the corner of the mini Brillouin zone)

[7]Note that $\boldsymbol{k}\cdot\boldsymbol{p}$ perturbation theory is an approximation scheme to calculate the band structure, which treats wave vector $\boldsymbol{k}$ in the Hamiltonian as a perturbation of momentum $\boldsymbol{p}$.

[88], i.e.

$$H = s\frac{bv}{\sqrt{3}}\begin{pmatrix} 1 & 0 & 0 \\ 0 & 1 & 0 \\ 0 & 0 & 1 \end{pmatrix} + \frac{1}{2}\zeta bv \begin{pmatrix} -\sqrt{3}u_0^- - 2su_1^+ + \sqrt{3}u_3^+ & 0 & 0 \\ 0 & \sqrt{3}u_0^- - 2su_1^+ + \sqrt{3}u_3^+ & 0 \\ 0 & 0 & 4su_1^+ - 2\sqrt{3}u_3^+ \end{pmatrix}$$
$$+ \frac{1}{2}bv \begin{pmatrix} u_0^+ - 2s\sqrt{3}u_1^- + 3u_3^- & 0 & 0 \\ 0 & u_0^+ + 2s\sqrt{3}u_1^- - 3u_3^- & 0 \\ 0 & 0 & -2u_0^+ \end{pmatrix}. \tag{3.9}$$

In other words, we use the eigen function of Eq. (2.20) to linearly expand the eigen function of Eq. (3.6). Each elements of the matrix is a coefficient of the eigen function of Eq. (3.6) on the basis of eigen function of Eq. (2.20). By diagonalizing this matrix, we can get the (approximated) eigen energies of Eq. (3.6). Therefore, the secondary DP location and gap size are

$$\begin{aligned} E_{mDP} &= sbv\left(\frac{u_0^+ - 2u_1^+ - \sqrt{3}u_3^+}{2} + \frac{1}{\sqrt{3}}\right), \\ \Delta_1 &= \sqrt{3}bv|u_0^- + 2s\zeta u_1^- - \sqrt{3}\zeta u_3^-|, \\ v_{mDP} &= v\left(\frac{1}{2} + \frac{3}{4}(\sqrt{3}u_0^+ + u_3^+)\right), \end{aligned} \tag{3.10}$$

where $\zeta = \pm 1$ accounts for $\boldsymbol{\kappa}$ and $\boldsymbol{\kappa}'$ and $s = \pm 1$ represents the conduction/valence band.

In general, an inversion-symmetric perturbation (i.e. $u_i^- = 0$), produces a gapless spectrum (i.e., $\Delta_0 = 0$), with a secondary DP either at the edge of the first miniband or embedded in a continuous spectrum at higher energies. The asymmetric part of the perturbation may open gaps both at the zero-energy DP, Δ_0, and at the secondary DP Δ_1 on the conduction/valence band side, as described in [90] and shown in Fig. 3.8.

Model	vbu_0^+[meV]	vbu_1^+[meV]	vbu_3^+[meV]
Potential modulation [47]	60	0	0
2D charge modulation [86]	$-\frac{V_0}{2}$	0	$\frac{\sqrt{3}V_0}{2}$
One-site G-hBN hopping [87]	1.6	$\frac{-3.2\delta}{\sqrt{\delta^2+\theta^2}}$	-2.8
Point charge lattice [88]	$\frac{\tilde{v}}{2}$	$\frac{-\tilde{v}\delta}{\sqrt{\delta^2+\theta^2}}$	$-\frac{\sqrt{3}\tilde{v}}{2}$

Table 3.1: Inversion-symmetric parameters vbu_i^+ for various models of the moiré superlattice. In the two-dimensional charge modulation model, V_0 is a phenomenological parameter. The G-hBN hopping model in [87] uses the hopping parameter from twisted BLG. Estimates in [88] show that the parameters using a model of point charges attributed to nitrogen sites is similar to that of the G-hBN hopping model. In the last line, $0.6 \leq \tilde{v} \leq 3.4$[meV]. [Table adopted from Ref. [88]]

3.2.4 Choice of superlattice parameters and their impact on the band structure

We emphasize that the parameters $u_i^{\pm}$ in Hamiltonian Eq. (3.6) are phenomenological. However, a microscopic model [178] based on hopping between graphene and *h*-BN predicts that

$$vb\{u^{\pm}_{i=0,1,3}\} = V^{\pm}\left\{\frac{\pm 1}{2}, \frac{-\delta}{\sqrt{\delta^2+\theta^2}}, \frac{-\sqrt{3}}{2}\right\}, \tag{3.11}$$

where V^+/V^- is the scale of symmetric and anti-symmetric perturbation, respectively. Details are provided in Appendix F. Furthermore, a microscopic model based on scattering by the graphene electrons of quadrupole electric moments in the *h*-BN substrates agrees with this. Table. 3.1 shows parameters predicted by several models.

Experimental signatures indicating that symmetric perturbation is dominant were observed in density of states measurements, performed in Ref. [47], and also in the transport measurements performed in Ref. [40]. In practice, by setting $V^+ = 0.063vb \simeq 22\,\text{meV}$ and with $V^- = 0$ in Eq. (3.11), the best agreement is archived [50]. Translating this V^+ value into u_i^+ parameters yields $u_0^+ = 0.032$, $u_1^+ = -0.063$ and $u_3^+ = -0.055$.

Based on this parameter set, the band structure of moiré perturbed SLG can be calculated, as shown in Fig. 3.6. Note that the DP structure is preserved around

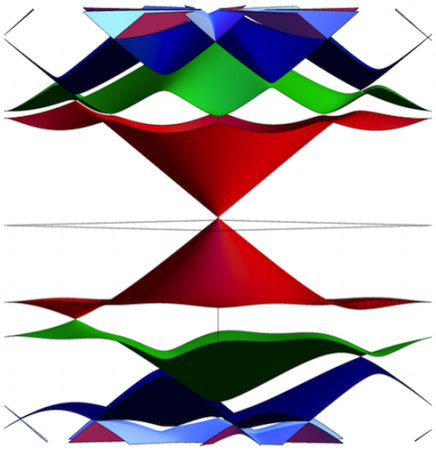

Figure 3.6: The band structure of moiré perturbed SLG, which is calculated using a zone folding method. The parameter set used here is $u_0^+ = 0.032$, $u_1^+ = -0.063$, $u_3^+ = -0.055$ and $u_i^- = 0$. The main DP is conserved. In the valence band, the moiré perturbation produces a secondary DP.

zero energy, but the moiré perturbation introduces a secondary DP in the valence band. Because of the conservation of inversion symmetry, both of the DPs are exactly gapless [49, 88].

3.3 Theoretical framework: finite magnetic field

3.3.1 Hamiltonian in non-orthogonal coordinates

To adapt the analysis of the electron spectrum in a magnetic field to the hexagonal symmetry of the moiré pattern, we use a non-orthogonal coordinate system, which is more capable of handling a perturbation in the form of the hexagonal harmonics $f_\pm = \sum_m (\pm 1)^{m+\frac{1}{2}} e^{i\boldsymbol{b}_m \cdot \boldsymbol{r}}$ in Eq. (3.6). A detailed introduction to non-orthogonal coordinates is provided in Appendix G. We introduce two new non-orthogonal basis vectors, i.e.

$$\hat{\boldsymbol{x}}_1 = \frac{\boldsymbol{a}_1}{a} = \frac{1}{2}\hat{\boldsymbol{x}} + \frac{\sqrt{3}}{2}\hat{\boldsymbol{y}}, \qquad \hat{\boldsymbol{x}}_2 = \frac{\boldsymbol{a}_2}{a} = -\frac{1}{2}\hat{\boldsymbol{x}} + \frac{\sqrt{3}}{2}\hat{\boldsymbol{y}}, \tag{3.12}$$

instead of the orthogonal basis $\hat{\boldsymbol{x}}$, $\hat{\boldsymbol{y}}$. From relations [8]

$$x\hat{\boldsymbol{x}} + y\hat{\boldsymbol{y}} = x_1\hat{\boldsymbol{x}}_1 + x_2\hat{\boldsymbol{x}}_2, \qquad x_1k_1 + x_2k_2 = xk_x + yk_y, \tag{3.13}$$

we can define non-orthogonal spatial coordinates x_1 and x_2 and momentum coordinates k_1 and k_2 as

$$\begin{cases} x_1 = x + \frac{1}{\sqrt{3}}y \\ x_2 = -x + \frac{1}{\sqrt{3}}y \end{cases}, \qquad \begin{cases} k_1 = \frac{1}{2}k_x + \frac{\sqrt{3}}{2}k_y \\ k_2 = -\frac{1}{2}k_x + \frac{\sqrt{3}}{2}k_y \end{cases}. \tag{3.14}$$

In the case, all $\boldsymbol{b}_m$ in non-orthogonal coordinate system are much simplified, as well as the further calculation. Note that

$$\hat{\boldsymbol{x}}_1 \cdot \hat{\boldsymbol{x}}_2 = 1/2, \qquad d^2r = dxdy = \frac{\sqrt{3}}{2}dx_1dx_2. \tag{3.15}$$

Here, the second equation comes from the Jacobian determinant. We define the Brillouin zone as the rhombus area defined by reciprocal vectors $\boldsymbol{b}_1$ and $\boldsymbol{b}_2$. Furthermore, we shift the centre of the Brillouin zone to point $(0, 0)$. Then the range of available values of k_1 and k_2 in non-orthogonal coordinates can be written in a "square" format, i.e. $k_1, k_2 \in \frac{\sqrt{3}b}{2}[-\frac{1}{2}, \frac{1}{2}]$, which is a rhombus Brillouin zone in the orthogonal coordinates system.

To study the magnetic field effect in non-orthogonal coordinates, we choose the Landau gauge as

$$\boldsymbol{A} = -Bx_1(-\boldsymbol{x}_1 + 2\boldsymbol{x}_2)/\sqrt{3}, \quad \boldsymbol{B} = \boldsymbol{\nabla} \times \boldsymbol{A} = (0, 0, -B). \tag{3.16}$$

Note that the curl operation $\boldsymbol{\nabla} \times \boldsymbol{A}$ is different when using non-orthogonal coordinates due to the Jacobian matrix. In this case, the Dirac Hamiltonian in Eq. (2.19)

[8] The first equation comes from the fact that a position vector in any arbitrary coordinate system is identical. The second equation comes from the fact the the dot product between corresponding coordinate of contra-variant and covariant vector is identical, and detailed discussion can be found in Appendix G.

is transformed into

$$\hat{H}_D = v \begin{pmatrix} 0 & \hat{d}^\dagger \\ \hat{d} & 0 \end{pmatrix}, \tag{3.17}$$
$$\hat{d} = \frac{-2}{\sqrt{3}} \left[\partial_{x_1} e^{i\frac{2\pi}{3}} + (\partial_{x_2} + i\sqrt{3}eBx_1/2) e^{-i\frac{2\pi}{3}} \right],$$

where operator $\hat{d}$ is the non-orthogonal version of operator $\hat{\pi}$. Then, the basis of LL states for Dirac electrons is transformed from Eqs. (2.35) and (2.33) to

$$\psi_0^{k_2} = \frac{e^{ik_2x_2}}{\sqrt{L}} \begin{pmatrix} \frac{1+\beta}{2}\varphi_0 \\ \frac{1-\beta}{2}\varphi_0 \end{pmatrix} \qquad \psi_{n\neq 0}^{k_2} = \frac{e^{ik_2x_2}}{\sqrt{2L}} \begin{pmatrix} \varphi_{|n|+\frac{\beta-1}{2}} \\ c_n\varphi_{|n|-\frac{\beta+1}{2}} \end{pmatrix}, \tag{3.18}$$
$$\varphi_m = A_m e^{-\frac{z^2}{2}} e^{-\frac{iz^2}{2\sqrt{3}}} \mathbb{H}_m(z), \qquad A_m = \frac{1}{\sqrt{m!2^{(m-1)}\lambda_B\sqrt{\pi}}},$$
$$E_n = \frac{n}{|n|}\frac{v}{\lambda_B}\sqrt{2|n|}, \qquad z = \frac{\sqrt{3}x_1}{2\lambda_B} - k_2\lambda_B, \qquad c_n = -\frac{n}{|n|}e^{-i\frac{2\pi}{3}}\beta.$$

Here, $\beta = B/|B|$ (B can be negative), $\mathbb{H}_n$ is the Hermite polynomial and $\lambda_B = 1/\sqrt{|eB|}$ is the magnetic length.

3.3.2 Magnetic translational symmetry and magnetic Bloch wave function

An electron in a square lattice crystal in a magnetic field must satisfy both the constraint of the periodic lattice potential and the magnetic vector potential. Just like the simple model introduced in the beginning of this chapter, for an electron in a hexagonal moiré superlattice in a magnetic field, once the magnetic field satisfies the relation $BS/\phi_0 = p/q$, where $S = \sqrt{3}a^2/2$ is the area of a super unit cell, the translational symmetry of the electron will be recovered but in a reduced way [82, 107]. To rigorously investigate this, consider an electron that exists in a periodic potential environment in the absence of a magnetic field $\boldsymbol{B}$.

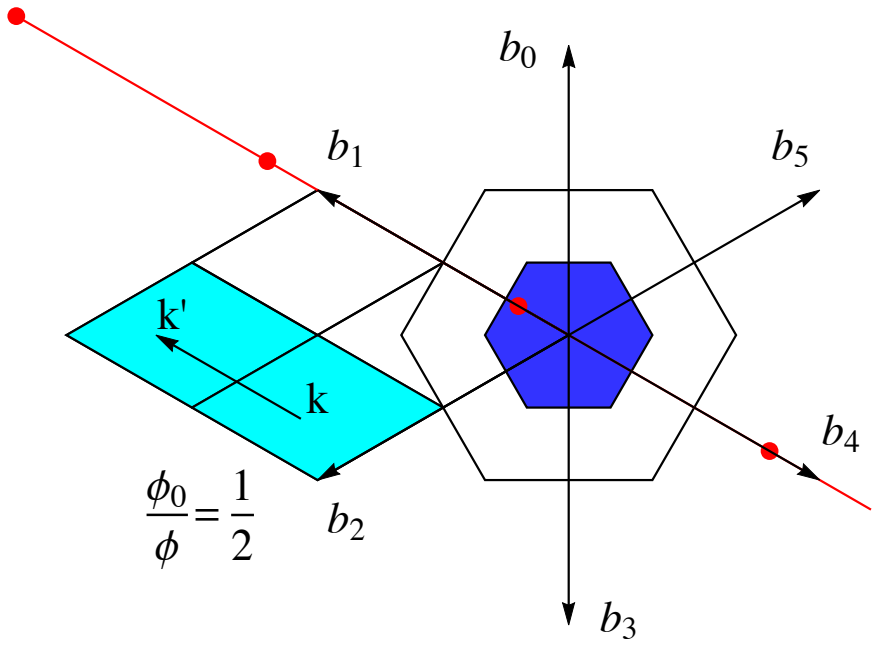

Figure 3.7: An example of the moiré superlattice Brillouin zone (i.e. the larger hexagon with area $\sqrt{3}b^2/2$, and reciprocal lattice vectors $\boldsymbol{b}_m$) and two smaller magnetic Brillouin zones (shaded blue). Red dots show the k_2 values used to construct Bloch states $|^{n,j}_{t,\boldsymbol{k}}\rangle$.

The Hamiltonian of the electron follow the translational symmetry

$$\hat{T}_{\boldsymbol{X}}\hat{H}(\boldsymbol{r}) = \hat{H}(\boldsymbol{r}+\boldsymbol{X}) = \hat{H}(\boldsymbol{r}), \quad \hat{T}_{\boldsymbol{X}}\varphi(\boldsymbol{r}) = e^{i\boldsymbol{k}\cdot\boldsymbol{X}}\varphi(\boldsymbol{r}), \tag{3.19}$$

where $\boldsymbol{X} = m_1\boldsymbol{a}_1 + m_2\boldsymbol{a}_2$, and $\hat{T}_{\boldsymbol{X}}$ describe the geometrical translations. In the presence of a magnetic field, however, as the vector potential of a magnetic field $\boldsymbol{A}(\boldsymbol{r})$ depends on the coordinate; the Hamiltonian $\hat{H}(\boldsymbol{r})$ after a translation $\boldsymbol{a}$, $\hat{H}(\boldsymbol{r}+\boldsymbol{a})$, is not necessarily the same as $\hat{H}(\boldsymbol{r})$, i.e. $[\hat{T}_{\boldsymbol{X}}, \hat{H}] \neq 0$. In this case, we must introduce a "magnetic translation operator" $\hat{\Theta}_{\boldsymbol{X}}$, which generates the magnetic translational group

$$G_M = \{\hat{\Theta}_{\boldsymbol{X}} = e^{ieBm_1 a\frac{\sqrt{3}}{2}x_2}\hat{T}_{\boldsymbol{X}}, \boldsymbol{X} = m_1\boldsymbol{a}_1 + m_2\boldsymbol{a}_2\}. \tag{3.20}$$

Here, $\hat{\Theta}_{\boldsymbol{X}}$ satisfies $[\hat{\Theta}_{\boldsymbol{X}}, \hat{H}] = 0$, but it does not self-commute, i.e.

$$\hat{\Theta}_{\boldsymbol{X}}\hat{\Theta}_{\boldsymbol{X}'} = e^{i2\pi\frac{p}{q}m_1'm_2}\hat{\Theta}_{\boldsymbol{X}+\boldsymbol{X}'}, \quad \hat{\Theta}_{\boldsymbol{X}}\hat{\Theta}_{\boldsymbol{X}'} = e^{i2\pi\frac{p}{q}(m_1'm_2 - m_1m_2')}\hat{\Theta}_{\boldsymbol{X}'}\hat{\Theta}_{\boldsymbol{X}}. \tag{3.21}$$

To avoid this problem, we consider the subgroup of G_M consisting of translations

$$G'_M = \{\hat{\Theta}_{\boldsymbol{R}} = e^{ieBm_1 a\frac{\sqrt{3}}{2}x_2}\hat{T}_{\boldsymbol{R}}, \boldsymbol{R} = m_1 q\boldsymbol{a}_1 + m_2 q\boldsymbol{a}_2\}, \tag{3.22}$$

on a $(q \times q)$-enlarged superlattice [9] . All reciprocal lattice vectors are shrunk by $1/q$, i.e. folding the momentum space on a magnetic Brillouin zone with area $\sqrt{3}b^2/(2q^2)$, as shown in Fig. 3.7. In this new group, all translations commute, i.e.

$$\hat{\Theta}_{\boldsymbol{R}}\hat{\Theta}_{\boldsymbol{R}'} = \hat{\Theta}_{\boldsymbol{R}+\boldsymbol{R}'}, \quad \hat{\Theta}_{\boldsymbol{R}}\hat{\Theta}_{\boldsymbol{R}'} = \hat{\Theta}_{\boldsymbol{R}'}\hat{\Theta}_{\boldsymbol{R}}.$$

Furthermore, subgroup G'_M is isomorphic to the simple group of translations, $\hat{T}_{\boldsymbol{R}}$ such that the eigenstates of $\hat{\Theta}_{\boldsymbol{R}}$ form a plane-wave basis.

The Bloch wave function can be constructed as

$$|^{n,j}_{t,\boldsymbol{k}}\rangle = \frac{1}{\sqrt{N}}\sum_s e^{ik_1 qas}\psi_n^{k_2+\frac{\sqrt{3}}{2}\frac{b}{q}(pqs+jq+tp)}, \tag{3.23}$$

where the sum runs over $s = -N/2, \cdots, N/2$, $j \in [0, p-1]$ and $t \in [0, q-1]$. This Bloch wave function has the following properties:

$$\begin{aligned}
&\hat{\Theta}_{sq\boldsymbol{a}_1}|^{n,j}_{t,\boldsymbol{k}}\rangle = e^{ik_1 qas}|^{n,j}_{t,\boldsymbol{k}}\rangle, \quad \hat{\Theta}_{rq\boldsymbol{a}_2}|^{n,j}_{t,\boldsymbol{k}}\rangle = e^{ik_2 qar}|^{n,j}_{t,\boldsymbol{k}}\rangle, \quad s, r \in \mathbb{Z}, \\
&\hat{\Theta}_{\boldsymbol{a}_1}|^{n,j}_{t,\boldsymbol{k}}\rangle = |^{n,j}_{t+1,\boldsymbol{k}}\rangle, \quad \hat{\Theta}_{\boldsymbol{a}_2}|^{n,j}_{t,\boldsymbol{k}}\rangle = e^{i\frac{2\pi pt}{q}}e^{i\boldsymbol{k}\cdot\boldsymbol{a}_2}|^{n,j}_{t,\boldsymbol{k}}\rangle.
\end{aligned} \tag{3.24}$$

This basis is similar to the set of Bloch states for a one-dimensional chain with p sites per elementary unit cell, and multiple atomic orbitals on each site labelled by the LL index, n. Details about the magnetic translational operator and the construction of the Bloch wave function can be found in Appendix H.

[9] One point to be emphasized here is the subgroup of G_M is not unique, another simple definition is $G''_M = \{\hat{\Theta}_{\boldsymbol{R}} = e^{ieBm_1 a\frac{\sqrt{3}}{2}x_2}\hat{T}_{\boldsymbol{R}}, \boldsymbol{R} = m_1\boldsymbol{a}_1 + m_2 q\boldsymbol{a}_2\}$, i.e. only enlarge the unit cell along $\boldsymbol{a}_1$ direction by q times. This choice will cancel the q-fold degenerate in that of G'_M, but will lead to a difficulty that one has to distinguish between odd number q and even number q [72], and one lose the symmetry of point group.

3.3.3 The Heisenberg matrix on a basis of magnetic Bloch states

To calculate the eigenenergies of the Hamiltonian of moiré perturbed graphene in magnetic field, we expand eigen functions of that on the basis of wave function of graphene in magnetic field. The coefficient of the basis is the element of matrix, which generates the same eigen energies by diagonalization. In practical, using the Bloch wave function, Eq. (3.23), to sandwich the Hamiltonian including the moiré perturbation Eq. (3.6), we obtain a general expression for the elements of the matrix, i.e.

$$\begin{aligned}\langle {}^{n,j}_{t,\boldsymbol{k}}|\hat{H}|{}^{\tilde{n},\tilde{j}}_{\tilde{t},\tilde{\boldsymbol{k}}}\rangle &= \frac{1}{N}\sum_{s,\tilde{s}} e^{-ik_1qas}e^{i\tilde{k}_1qa\tilde{s}}\langle\psi_n^{k_2+\frac{\sqrt{3}}{2}\frac{b}{q}(pqs+jq+tp)}|\hat{H}|\psi_{\tilde{n}}^{\tilde{k}_2+\frac{\sqrt{3}}{2}\frac{b}{q}(pq\tilde{s}+\tilde{j}q+\tilde{t}p)}\rangle \\ &= \delta_{t,\tilde{t}}\delta_{\boldsymbol{k},\tilde{\boldsymbol{k}}}\sum_{\Delta s} e^{-ik_1qa\Delta s}\mu_{n\tilde{n}}^{k_2+\frac{\sqrt{3}}{2}bj,\,k_2+\frac{\sqrt{3}}{2}b(p\Delta s+\tilde{j})}, \end{aligned} \tag{3.25}$$

where $\Delta s = \tilde{s} - s$ and

$$\begin{aligned}\mu_{n\tilde{n}}^{k_2\tilde{k}_2} &= \delta_{n,\tilde{n}}E_n + \xi\beta v\sum_m (u_1^+(-1)^m - iu_1^-) \\ &\times [e^{i2\pi/3}\frac{\tilde{n}}{|\tilde{n}|}(ib_m^1 + b_m^2)M_m^{n^-,\tilde{n}^+} + e^{-i2\pi/3}\frac{n}{|n|}(-ib_m^1 + ib_m^2)M_m^{n^+,\tilde{n}^-}] \\ &+ vb\sum_m (u_0^+ + i(-1)^m u_0^-)[M_m^{n^-,\tilde{n}^-} + \frac{n}{|n|}\frac{\tilde{n}}{|\tilde{n}|}M_m^{n^+,\tilde{n}^+}] \\ &+ \xi vb\sum_m (u_3^- + i(-1)^m u_3^+)[M_m^{n^-,\tilde{n}^-} - \frac{n}{|n|}\frac{\tilde{n}}{|\tilde{n}|}M_m^{n^+,\tilde{n}^+}], \end{aligned} \tag{3.26}$$

$$\begin{aligned} M_0^{n_1,n_2} &= e^{i\beta\lambda^2\sqrt{3}}\delta^- W_{1,\text{-}1,\text{-}1}^{n_1,n_2}, \quad M_1^{n_1,n_2} = \delta^- W_{\text{-}1,1,0}^{n_1,n_2}, \quad M_2^{n_1,n_2} = \delta^0 W_{\text{-}1,0,1}^{n_1,n_2}, \\ M_3^{n_1,n_2} &= e^{i\beta\lambda^2\sqrt{3}}\delta^+ W_{\text{-}1,\text{-}1,1}^{n_1,n_2}, \quad M_4^{n_1,n_2} = \delta^+ W_{1,1,0}^{n_1,n_2}, \quad M_5^{n_1,n_2} = \delta^0 W_{1,0,\text{-}1}^{n_1,n_2}, \\ W_{c_1,c_2,c_3}^{n_1,n_2} &= \frac{N_{n_1,n_2}}{3}\lambda_B A_{n_1}A_{n_2}2^{\bar{n}}\sqrt{\pi}\underline{n}!L_{\underline{n}}^{|\delta n|}(2\lambda^2)\,e^{\text{-}\lambda^2}\lambda^{|\delta n|} \\ &\times e^{i|\delta n|(c_1\frac{\pi}{2}+c_2\frac{\delta n}{|\delta n|}\beta\frac{\pi}{3})}e^{i\beta c_3\lambda^2 4k_2/b}. \end{aligned}$$

Here $L_n^{\alpha}(x)$ is the associated Laguerre polynomial, $\lambda = b\lambda_B/2$, $\delta^{\pm} = \delta_{\tilde{k}_2,k_2\pm\sqrt{3}b/2}$, $\delta^0 = \delta_{\tilde{k}_2,k_2}$, $\bar{n} = \max[n_1,n_2]$, $\underline{n} = \min[n_1,n_2]$, $\delta n = n_1 - n_2$, and $N_{n_1,n_2} = (1-\delta_{n_1,\text{-}1})(1-$

$\delta_{n_2,-1})\sqrt{1+\delta_{n_1,0}}\sqrt{1+\delta_{n_2,0}}$. Furthermore, we make use of the integral

$$\int_{-\infty}^{\infty} e^{-x^2}\mathbb{H}_n(x+y)\mathbb{H}_m(x+z)dx = 2^n\sqrt{\pi}m!y^{n-m}L_m^{n-m}(-2yz), \quad n \geq m, \quad (3.27)$$

which can be found in Ref. [196].

Therefore, the entire Hamiltonian is described by a big matrix. For a given flux ratio p/q and momentum $\boldsymbol{k}$ and $\tilde{\boldsymbol{k}}$ in the magnetic Brillouin zone, this matrix contains all cross-terms between different LLs n, indices j and t as well as a summation of s and $\tilde{s}$. Since Hamiltonian Eq. (3.6) contains only the simplest moiré harmonics, i.e., $\boldsymbol{b}_m$, the cross term between $|_{t,\boldsymbol{k}}^{n,j}\rangle$ and $|_{\tilde{t},\tilde{\boldsymbol{k}}}^{\tilde{n},\tilde{j}}\rangle$ is limited to the difference between $k_2+\frac{\sqrt{3}}{2}b(ps+j)$ and $\tilde{k}_2+\frac{\sqrt{3}}{2}b(p\tilde{s}+\tilde{j})$, which prescribes the value of $|\tilde{s}-s| \leq 1$. For simplicity, we set $\Delta s = \tilde{s}-s = 0, \pm 1$. Because $[\hat{\Theta}_{\boldsymbol{X}}, \hat{H}] = 0$ and index t are conserved, t is q-fold degenerate as well. We will later set $t = 0$ to reduce the dimension of the Heisenberg matrix by $1/q$ times.

3.3.4 Calculation and programing details

Given the momentum position $\boldsymbol{k}$ in the Brillouin zone, the flux ratio $\phi/\phi_0 = p/q$ and the number of included LLs, n_{max}, a matrix containing all elements $\langle_{t,\boldsymbol{k}}^{n,j}|\hat{H}|_{\tilde{t},\tilde{\boldsymbol{k}}}^{\tilde{n},\tilde{j}}\rangle$ can be constructed, and after diagonalization, we obtain a set of eigenenergies. By varying the magnetic field ϕ/ϕ_0 at the given $\boldsymbol{k}$, we can obtain the magnetic energy spectrum. By varying $\boldsymbol{k}$ in the Brillouin zone, we can obtain the magnetic band structure for the given ϕ/ϕ_0.

To obtain an accurate description of the spectrum up to energy E, we must include LLs up to a cutoff energy E_c to guarantee that $(E_c - E)/|V^{\pm}| \gg 1$. The number of matrix elements and hence the computational time thus scale as E_c^4. By using practical calculations, we determine an empirical formula suggesting that the inclusion of a number of LLs $n_{max} \simeq c_N\phi_0/\phi + d_N$ (where $c_N = 10$ and $d_N = 2$) is sufficient for convergence in the energy range $-0.85vb < \epsilon < 0.85vb$ ($vb \sim 350$meV) when $\sum_i |u_i| = 0.15$, i.e. $V^+ = 22$meV. The software we used is Mathematica.

Each unperturbed LL can hold $g\phi/\phi_0 = gp/q$ electrons per unit cell where $g = 4$ accounts for spin and valley degeneracy. After applying the perturbation, each LL splits into p minibands, so each magnetic miniband holds g/q electrons per unit cell.

3.4 Results and discussion

3.4.1 Magnetic spectrum of moiré perturbed SLG

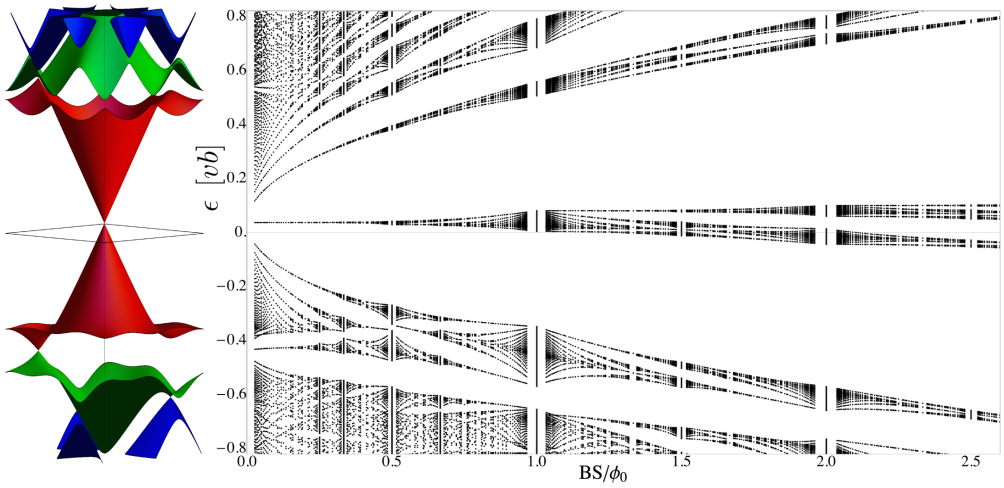

Figure 3.8: (Right panel) A typical fractal energy spectrum found by exact numerical diagonalization. It is calculated for an inversion-symmetric superlattice perturbation with $V^+ = 0.063vb$ and $V^- = 0$, $\theta = 0$ from Eq. (3.11) (i.e. $u_0 = 0.032$, $u_1 = -0.063$ and $u_3 = -0.055$). The fractal dimension of the butterfly spectrum is $D = 1.71567$. (Left panel) The $B = 0$ minibands with a distinct secondary DP in the valence band.

Fig. 3.8 shows a typical fractal spectrum of magnetic minibands as a function of the magnetic flux $\phi = SB$ per moiré supercell [10]. The plot shown is calculated for an inversion-symmetric superlattice perturbation with $V^+ = 0.063vb$, $V^- = 0$ and $\theta = 0$ from Eq. (3.11) (i.e. $u_0 = 0.032$, $u_1 = -0.063$ and $u_3 = -0.055$) by diagonalizing the Heisenberg matrix in the basis $|^{n,j}_{t,\boldsymbol{k}}\rangle$. The $B = 0$ miniband

[10] One may notice that this plot is not so symmetric as Fig. 3.1. It is because that: (1) Once the inversion symmetry holds, the spectrum in the magnetic field with an opposite direction ($B < 0$) is simply the mirror reflection of the counter part, so it is omitted for simplicity. (2) The magnetic spectrum of Fig. 3.1 is periodic in the aspect of integer α, but Fig. 3.8 is not. Because the system described by the latter has a moiré perturbation coupled with magnetic field, the increasing of magnetic field leads to more asymmetric feature in Fig. 3.8. Besides, this is also the reason for a "rescaled butterfly" pattern.

spectrum is displayed on the left side of Fig. 3.8, with the main DP and a secondary DP in the valence band. For $\phi \lesssim 0.2\phi_0$, the magnetic miniband spectra can be traced to the analytically-calculated sequence of LLs associated with the two DPs as shown by the red lines on the far left of Fig. 3.9. At a higher flux, the LLs are fractured into a hierarchy of bands and gaps, which can be understood by analyzing the dispersion of electrons at the simplest flux fractions. In the vicinity of each simple fraction, the miniband spectrum also resembles a spectrum of Dirac-like LLs. The splitting of the zero energy LL can be viewed as an effective broadening of it which is proportional to $e^{-\frac{\phi_0}{\phi}}$, so it goes fast when $\phi \leq \phi_0$, and slows down when $\phi \geq \phi_0$.

3.4.2 Hierarchy of the Dirac-like spectrum

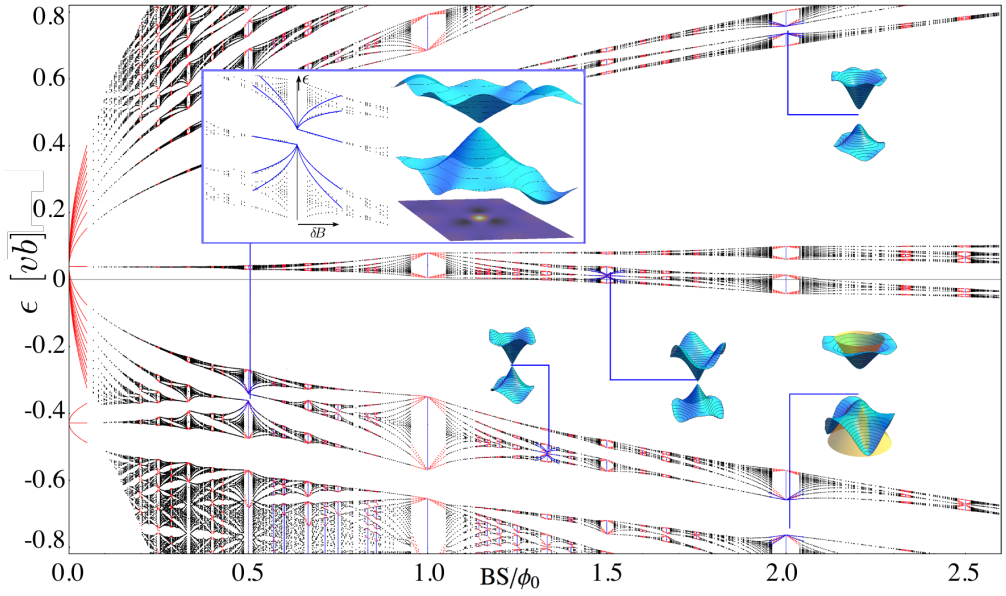

Figure 3.9: The hierarchy of the Dirac-like spectrum, which is found by exact numerical diagonalization, with $u_0 = 0.032$, $u_1 = -0.063$ and $u_3 = -0.055$. Note that only the minibands generated from the lowest ten "LLs" are shown. The numerical data (black) is the same as shown in the right panel of Fig. 3.8. The red lines in the vicinity of zero magnetic field are the LLs of the first and secondary DP, which are calculated from Eq. (3.18), Eq. (3.8) and Eq. (3.10). The insets show examples of magnetic minibands, at simple fractions $B_{p/q} = \frac{p}{q}\phi_0/S$, and their fit (shown in yellow, from Eq. (3.28)) with Dirac spectra used to calculate the energies of the effective Dirac LLs. The red lines in the vicinity of each simple fraction are also fit to LLs via Eq. (3.28) as well. For the Dirac-like spectrum in $\phi/\phi_0 = 1/2$, the Berry curvature of the lower magnetic miniband is shown as a colour map inset, in which lighter colours represent higher values of Berry curvature.

In a strong perpendicular magnetic field (i.e. $\phi \gtrsim 0.2\phi_0$), the edges of many of the consecutive magnetic bands can be described in terms of a weakly gapped Dirac-like spectrum [40, 49], i.e.

$$H_D = \begin{pmatrix} \frac{1}{2}\xi\Delta & v\hat{\pi}^\dagger \\ v\hat{\pi} & -\frac{1}{2}\xi\Delta \end{pmatrix}. \tag{3.28}$$

Then, the basis of LL states for the gapped Dirac-like electrons are described by

$$\begin{aligned} E_0 &= \frac{\xi\beta\Delta}{2}, \qquad E_{n\neq 0} = \frac{n}{|n|}\sqrt{\frac{\Delta^2}{4} + \frac{2|n|v^2}{\lambda_B^2}}, \\ \psi_0 &= \frac{e^{ik_y y}}{\sqrt{L}} \begin{pmatrix} \frac{1+\beta}{2}\varphi_0 \\ \frac{1-\beta}{2}\varphi_0 \end{pmatrix}, \qquad \psi_{n\neq 0} = \frac{e^{ik_y y}}{\sqrt{2L}} \begin{pmatrix} \varphi_{|n|+\frac{\beta-1}{2}} \\ c_n\varphi_{|n|-\frac{\beta+1}{2}} \end{pmatrix}, \\ \varphi_m &= A_m e^{-\frac{z^2}{2}} \mathbb{H}_m(z), \qquad A_m = \frac{1}{\sqrt{m!2^m\lambda_B\sqrt{\pi}}}, \\ z &= \frac{x}{\lambda_B} - k_y\lambda_B, \qquad c_n = -\beta\lambda_B\frac{E_n - \xi\Delta/2}{v\sqrt{2|n|}}. \end{aligned} \tag{3.29}$$

Here, $\beta = B/|B|$, $\mathbb{H}_n$ is a Hermite polynomial and $\lambda_B = 1/\sqrt{|eB|}$ is the magnetic length. Then, the largest gaps in the surrounding fractal spectrum at $B = B_{p/q} + \delta B$ can be interpreted [89] in terms of weakly broadened LLs of these next generation Dirac electrons, which are evaluated using Eq. (3.29) and parameters Δ and $B \to \delta B$. In Fig. 3.9, the analytically calculated effective LLs are shown in red in the vicinity of the corresponding rational flux values. They interpolate the groups of minibands into the interval within which the exact diagonalization fails, due to the basis set size. This correspondence can be best seen in cases when the gap Δ between consecutive minibands is small, and the largest gaps are around the broadened "$n = 0$" LL of the corresponding effective Dirac-like model.

One example is shown as an inset in Fig. 3.9 with the Berry curvature of the lower magnetic miniband shown as a colour map. Most of the Berry curvature concentrates on the tip of the cone, confirming that the magnetic minibands of moiré-perturbed graphene are Dirac-like but not a quadratic dispersion $\hat{H} = \hat{p}^2/2m$.

Furthermore, for some parameters, there will be a real DP without any gap in the magnetic minibands, thus yielding an exact π Berry phase. The calculation details of the Berry curvature of the magnetic Bloch wave functions are presented in Appendix I.

3.4.3 Incompressible states of moiré perturbed SLG

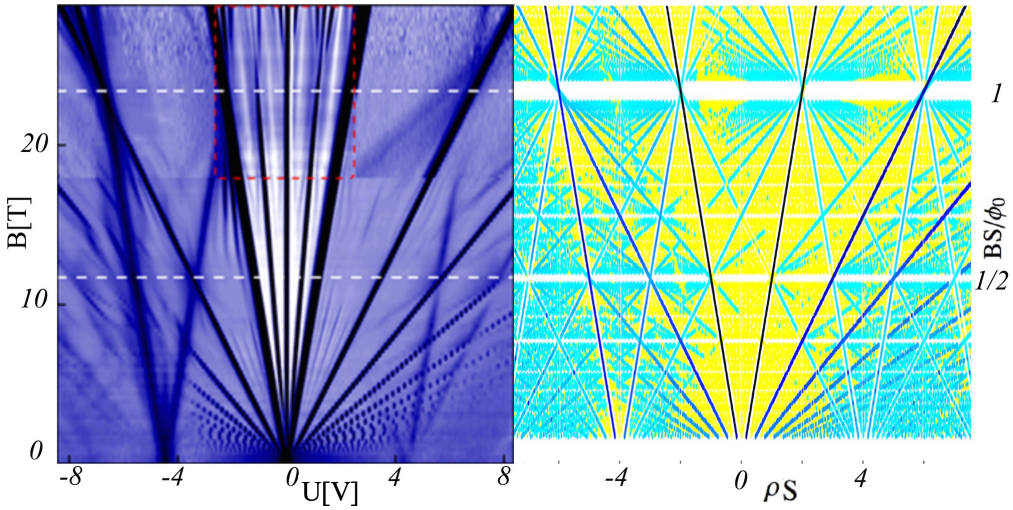

Figure 3.10: The experimental (left) and theoretical (right) carrier density-magnetic field diagram. The experimental diagram is from [50]. It is measured from a capacitance experiment, in which a top gate (gold lead) on graphene-*h*-BN heterostructure is used. By tuning the gate voltage as well as magnetic field, the capacitance of the setup can be measured and mapped onto the plot. The darker, the capacitance smaller. Therefore, a significant black stripe represents a continuous big gap. The theoretical plot maps the gaps in the magnetic spectrum Fig. 3.8 onto the carrier density per super unit cell ρS-magnetic field diagram. Larger gaps are shown using a darker colour.

A sample in which the Fermi level is located at a gap acts as an insulator. This state is called an "incompressible state" because an incoming electron does not have an energy level to occupy. If we vary the carrier density ρ of the moiré perturbed graphene at a given value of magnetic field, the conductivity of the sample will alternatively display both conducting and insulating behavior depending on whether the carrier density is located in a miniband or a gap. Varying the magnitude of the magnetic field generates a similar phenomena.

Because each Bloch wave function can hold $g_s g_v$ electrons and splits into q minibands, each miniband can hold $g_s g_v/q$ electrons [11] . Here, g_s and g_v are spin

[11] As a reminder, each LL holds $g_s g_v \phi_0/\phi$ electrons, and splits into p minibands; besides, each

and valley degeneracy. At the zeroth LL, the carrier has 50% possibility of being an electron or a hole, so the largest gaps above (below) the broadened "$n = 0$" LL have carrier density per unit cell $\rho S = g_s g_v p/2q$ ($\rho S = -g_s g_v p/2q$). Using the largest gap as a reference for tracing the main DP in graphene, we can understand the carrier density for a given magnetic field by counting how many minibands are filled. The filling factor is defined as the gradient of density with respect to magnetic field, i.e.

$$\nu = \frac{d(\rho S)}{d(BS/\phi_0)}. \tag{3.30}$$

The reason of the weird definition is to adopt the label of axis of Fig. (3.10). Noticeably, the filling factor is constant when the Fermi level is in a gap. By filling the minibands in Fig. 3.8 up to the Fermi level, we can map the gap size as a function of carrier density and magnetic field, resulting in the so-called "fan diagram", in which the "bone of the fan" is the filling factor describing the big gaps, as shown in the right panel of Fig. 3.10.

The darkest lines in Fig. 3.10 correspond to filling factors $\nu = \pm 2$, which radiates from $\rho S = 0$, $BS/\phi_0 = 0$. Furthermore, dark lines radiate from $\rho S = -4$, $BS/\phi_0 = 0$ track the LLs of the valence band secondary DP. Other dark lines correspond to the large gaps surrounding the "$n = 0$" LLs in the next generation of Dirac electrons, e.g. in the vicinity of B_1, $B_{1/2}$. From Eq. (3.30), we can derive the change in the filling factor when the Fermi level crosses a miniband, i.e. the change of gradients at these inter-crossings is

$$\delta\nu = g_s g_v q. \tag{3.31}$$

This reflects the additional q-fold degeneracy of states in magnetic minibands at $B_{p/q}$ [12] . These same qualitative features are also presented in the left panel of

original BZ holds $g_s g_v$ electrons, and the magnetic BZ is $1/q^2$ smaller but q-fold degenerates, so each each miniband can hold $g_s g_v/q$ electrons.

[12]Eq. (3.31) can be derived by solving the cross point of two straight lines. One needs to notice that crossing point between the horizontal axis and the filling factor line is not arbitrary, but

Fig. 3.10, which displays the results of experimental capacitance measurements performed on the graphene-h-BN heterostructure in Ref. [50]. Fig. 3.10 shows both the experimental [50] and theoretical results for the density-magnetic field diagram of moiré-perturbed SLG. Both of the fan diagrams show explicit radiating structures, which originates from the biggest gap between the zeroth LL and the $\pm$1st LL of the main DP and the secondary DP in the valence band. The comparison shown in Fig. 3.10 demonstrates that even the super unit cell is big ($S = \frac{\sqrt{3}}{2}14^2\,\mathrm{nm}^2$), it still requires a significantly strength of magnetic field, i.e. $B \simeq 25\mathrm{T}$, to achieve a flux quantum $\phi = \phi_0$.

One may notice that there are 3 additional black lines (3 additional gaps, i.e., 4 additional energy levels) between $\nu = 2$ and $\nu = -2$ in the left panel of Fig. 3.10, and there is no counterpart in the theoretical predication. This phenomenon originates from the fact that the state around zero energy is relatively near, the 4-fold spin and valley degeneracy is lifted by many-body effect. The plot in the right panel of Fig. 3.10 is based on the single-electron picture. So to explain this feature, a further calculation including many-body effect is needed.

3.4.4 The lifting of valley degeneration using an inversion asymmetric perturbation

To study the effect of the addition of a weak inversion-asymmetric perturbation in Eqs. (3.6-3.11), we set $V^- = V^+/10 = 0.015$ in Eq. (3.11). Given this, the final parameter set is $u_0^+ = 0.032$, $u_1^+ = -0.063$, $u_3^+ = -0.054$, $u_0^- = -0.0032$, $u_1^- = -0.0063$ and $u_3^- = -0.0054$.

Fig. 3.11 provides an example of the magnetic miniband spectrum and incompressibility map calculated for an inversion-asymmetric perturbation. The degeneracy of $\boldsymbol{K}$ and $\boldsymbol{K}'$ is lifted due to the inversion-asymmetric perturbation. The Dirac-like features and corresponding hierarchy of gaps in the magnetic minibands persist, but the fan diagram acquires additional lines, intercrossing with

$g_s g_v n$, $n \in \mathbb{Z}$.

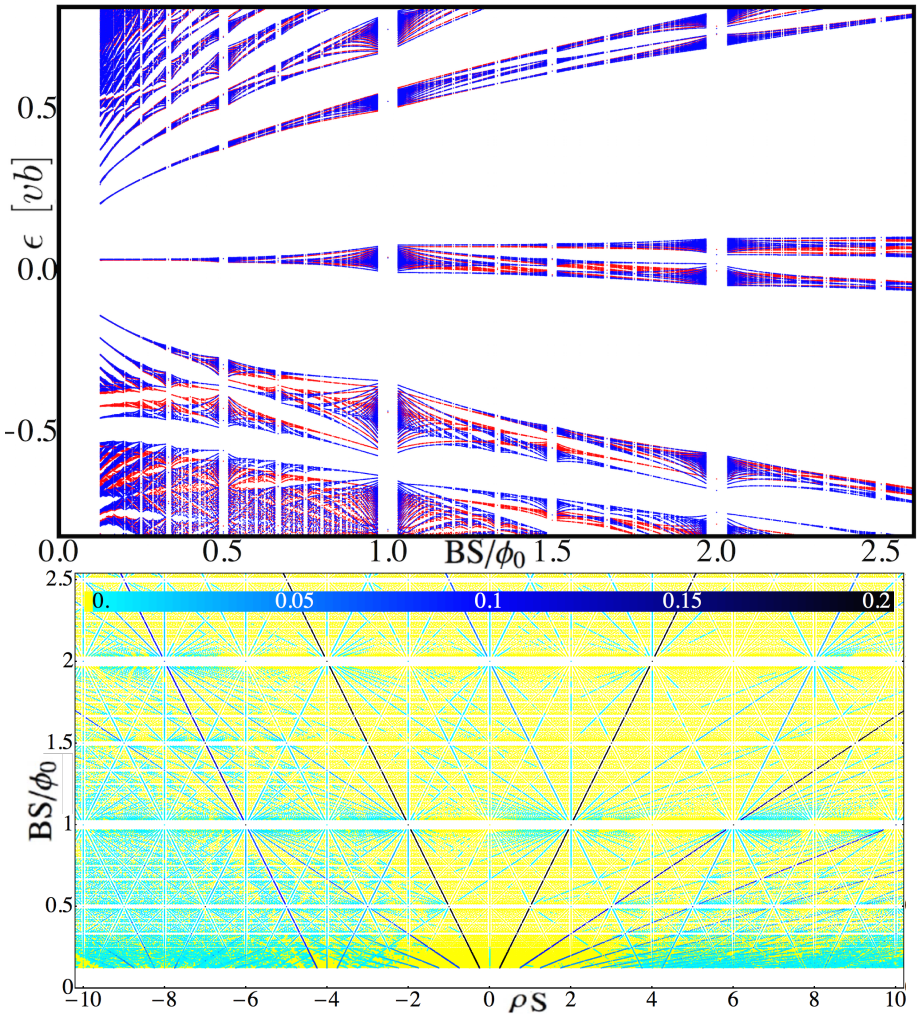

Figure 3.11: (Upper) The magnetic spectrum of the valley $\boldsymbol{K}$ (blue dots) and $\boldsymbol{K}'$ (red dots) of inversion asymmetric moiré perturbed SLG, with parameter set $u_0^+ = 0.032$, $u_1^+ = -0.063$, $u_3^+ = -0.054$, and $u_0^- = -0.0032$, $u_1^- = -0.0063$, $u_3^- = -0.0054$. (Lower) The corresponding density-magnetic field diagram, which shows the incompressible electron state in the fractal spectrum of magnetic minibands. Here, larger gaps are shown with a darker colour; furthermore, yellow points indicate a trivially small gap with the gap size in units of vb.

$\delta[d\rho/dB] = g_v q/\phi_0$, indicating that a combination of inversion and time inversion asymmetry lifts the valley degeneracy [13] of the fractal spectra.

3.4.5 Magnetic spectra of various superlattice perturbations

By varying u_i^+, the spectrum can be classified into three groups depending on the mutual arrangement of the first and second minibands in the valence band [88]. These groups and corresponding figures are: (a) the first and second bands do not overlap and are connected by a single isotropic secondary DP as shown in the valence band of the left panel of Fig. 3.8; (b) the first and second bands do not overlap and are connected by a triplet of anisotropic secondary DPs as shown in the upper left panel of Fig. 3.12; and (c) the first and second bands overlap as shown in the conduction band in Fig. 3.8. Note that, while a purely inversion-symmetric moiré superlattice perturbation generates both a gapless primary DP and a gapless secondary DP, the addition of a finite inversion-asymmetric component opens gaps at both DPs.

The examples of model-dependent values for parameters u_i, listed in Table 3.1, indicate that the combination of several factors can strongly shift the resulting moiré perturbation across the parameter space [88]. Here we systematically investigate the effect of several different choices of parameters for the moiré perturbation.

We choose three representative situations, each with only one non-zero parameter, i.e. $u_0^+ = 0.15$, $u_1^+ = 0.15$ and $u_3^+ = 0.15$. Similarly to Fig. 3.8, the left side of each panel in Fig. 3.12 displays the $B = 0$ miniband structure, whereas the right side displays the fractal magnetic miniband spectrum. Fig. 3.12 shows the band structures as the yellow transparent bands for several simple fractions $\frac{1}{2}$, $\frac{1}{1}$, $\frac{3}{2}$ and

[13] For $u_i^- = 0$, the spatial inversion symmetry, $H(\boldsymbol{r}, \zeta) = \sigma_z H(-\boldsymbol{r}, -\zeta)\sigma_z$, prescribes the relation $\epsilon_{\boldsymbol{K}+\boldsymbol{k}} = \epsilon_{\boldsymbol{K}'-\boldsymbol{k}}$ between spectra in graphene's two valleys. For $B = 0$, time reversal symmetry prescribes the same relation, however when both $B \neq 0$ and $u_i^- \neq 0$ the spectra in the two valleys are unrelated.

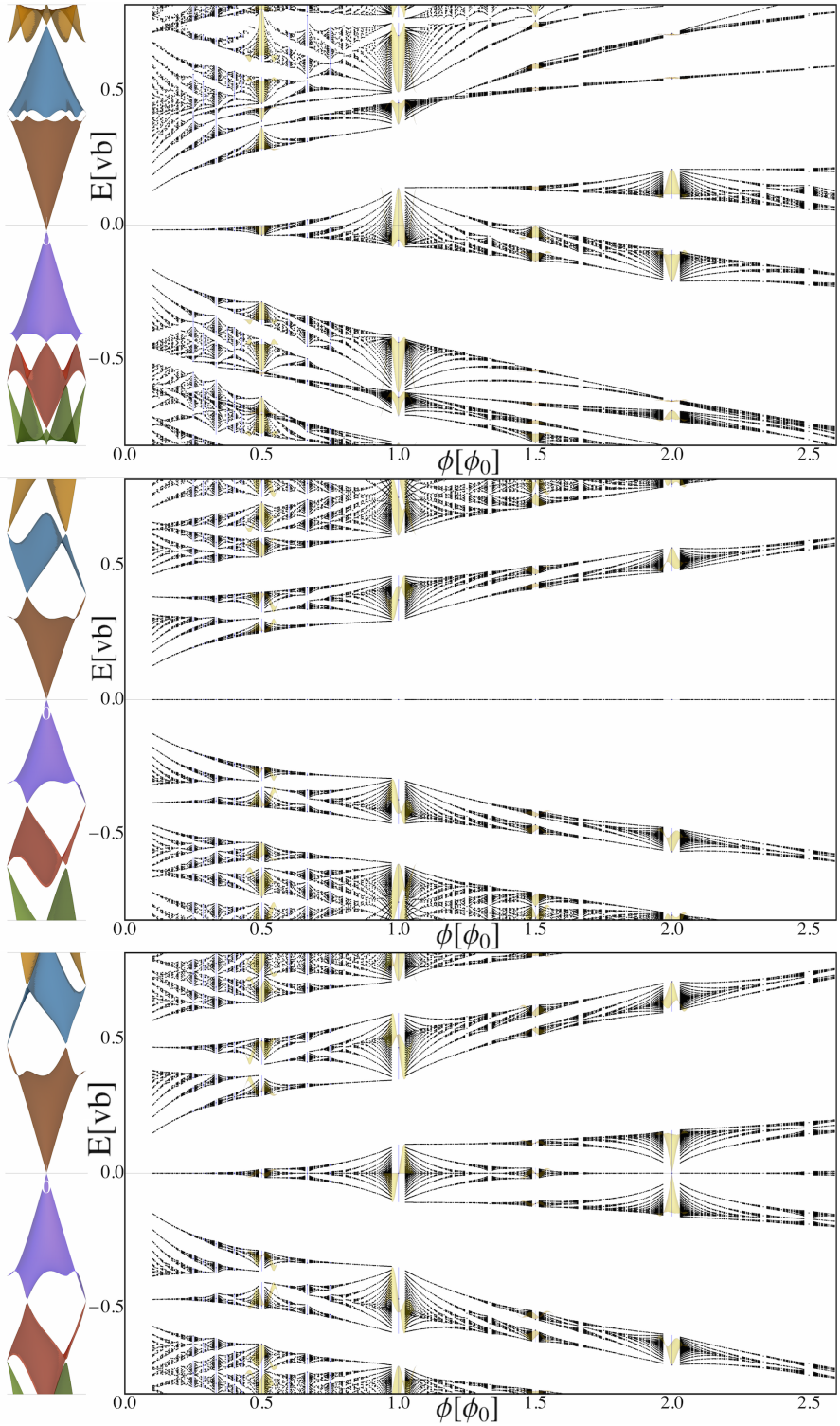

Figure 3.12: Magnetic minibands for $u_0^+ = 0.15$ (top), $u_1^+ = 0.15$ (middle) and $u_3^+ = 0.15$ (bottom). The panel on the left shows the $B = 0$ band structures, whereas the right panels show the magnetic spectra. For the simple fraction $\phi/\phi_0 = 1/2, 1/1/, 3/2, 2/1$, the full dispersion of the magnetic minibands structures is given.

$\frac{2}{1}$. From the magnetic spectra shown in Fig. 3.12 and Fig. 3.8, we note that the LL structure of the main DP is relatively robust.

For the simple potential modulation, i.e. $u_0^+ = 0.15$, the spectrum obeys the "inversion symmetry" $\epsilon_{\boldsymbol{K}+\boldsymbol{p}} = \epsilon_{\boldsymbol{K}-\boldsymbol{p}}$, which follows from the 4th equality in Eq. (3.7) with $u_1^+ = u_3^+ = 0$. The valence band of this spectrum provides an example of a spectrum with three secondary DPs, which is in sharp contrast to the other spectra - which display only a single secondary DP.

For $u_1^+ = 0.15$, the spectrum obeys electron-hole symmetry $\epsilon_{\boldsymbol{K}+\boldsymbol{p}} = -\epsilon_{\boldsymbol{K}+\boldsymbol{p}}$, which follows from the 3rd equality in Eq. (3.7) with $u_0^+ = u_3^+ = 0$. Note that the zeroth LL is completely degenerate.

For $u_3^+ = 0.15$, the spectrum obeys the semi-electron-hole symmetry $\epsilon_{\boldsymbol{K}+\boldsymbol{p}} = -\epsilon_{\boldsymbol{K}-\boldsymbol{p}}$, which follows from the 2nd equality in Eq. (3.7) with $u_0^+ = u_1^+ = 0$. This symmetry is manifested in the magnetic minibands of the "zeroth LL" in the magnetic spectrum for simple fractions, shown as the yellow bands in the bottom panel of Fig. 3.12. As an example, $\phi/\phi_0 = 2/1$ in the vicinity of $E = 0$ displays a completely gapless third-generation Dirac cone, so the Berry phase can be evaluated exactly as π.

3.5 Conclusion

To conclude this chapter, we found a systematic reappearance of Dirac-like features at the edges of consecutive minibands formed in magnetic fields $B_{p/q} = \frac{p}{q}\phi_0/S$ that provides rational magnetic flux through a unit cell of the moiré superlattice created by a hexagonal substrate for electrons in graphene. The Dirac-type features in the minibands at $B = B_{p/q}$ determine a hierarchy of gaps in the surrounding fractal spectrum. Using the additional q-fold degeneracy of magnetic minibands at $B_{p/q}$, we traced the hierarchy of the gaps to their manifestation in the form of incompressible states based on variation in carrier density and magnetic field.

Chapter 4

Valley asymmetry and zero-energy modes in the Hofstadter spectrum of a BLG van der Waals heterostructure with hexagonal boron nitride

4.1 Introduction

In the previous chapter, we presented moiré-perturbed SLG in a magnetic field. In this chapter, we repeat the analysis for BLG and study the moiré superlattice (mSL) perturbation on a BLG-hexagonal boron nitride (h-BN) heterostructure.

Apart from the quantum Hall effect of SLG superlattices described in the previous chapter, there has also been significant work on aligned heterostructures of BLG with h-BN, including the observation of Hofstadter's butterfly in transport measurements [41]. Theoretically, the mSL perturbation of this heterostructure can be modeled in a similar manner to the monolayer-graphene/h-BN heterostructure, except that the perturbation is felt much more strongly for the graphene

layer closest to the h-BN [174, 175]. Because of this, the inversion symmetry of this heterostructure is broken, typically leading to gaps both at zero energy and at the edge of the first miniband [174]. In a magnetic field, the broken inversion symmetry is manifested as a strongly broken valley symmetry in the magnetic miniband structure [175]. Other systems in which the miniband structure is generated by an mSL include twisted BLG [48, 132, 176–181], graphene with almost commensurate $\sqrt{3} \times \sqrt{3}$ hexagonal crystals [186], and graphene on metal catalysts such as Ir(111) [185].

In this chapter, we focus on the fractal magnetic minibands in BLG, where the sublattice composition of the electron states at the edge between the conduction and valence bands produces specific features in the Hofstadter butterfly spectra. We show that the low-energy Hofstadter butterfly spectrum of BLG, dominated by the bands composed of zero-energy LL states $n = 0$ and $n = 1$, which are degenerate in unperturbed BLG [68], is a superposition of two very different miniband spectra associated with electrons in opposite valleys of graphene's band structure. The miniband spectrum in one valley is only slightly broadened by the superlattice potential, incorporating one completely unperturbed $n = 0$ LL. However, the miniband spectrum in the other valley is substantially broadened by the superlattice potential. This valley asymmetry results from the interplay between inversion symmetry breaking produced by a moiré perturbation applied to only one of the two BLG layers and the sublattice composition of the electron LL states $n = 0$ and $n = 1$, which reside on different sublattice/layers in the opposite valleys, i.e. $\boldsymbol{K}$ and $\boldsymbol{K}'$.

4.2 Theoretical framework

4.2.1 Introduction to the Hamiltonian

To describe the sublattice (A/B) and top/bottom (1/2) layer composition of electron states in BLG with Bernal-stacking of the layers on boron nitride, we start

from the clean BLG Hamiltonian represented in Eq. (2.22) and then add moiré perturbation $\hat{M}_\xi$ from Eq. (3.6) into the top layer, resulting in a 4×4 matrix

$$\hat{H}_\xi = \begin{pmatrix} v\hat{p}\cdot\boldsymbol{\sigma} + M_\xi & \gamma_1(\xi\sigma_1 - i\sigma_2)/2 \\ (\gamma_1(\xi\sigma_1 - i\sigma_2)/2)^\dagger & v\hat{p}\cdot\boldsymbol{\sigma} \end{pmatrix}, \tag{4.1}$$

$$M_\xi = vbu_0^+ f_+ + \xi vb\sigma_3 u_3^+ f_- + \xi v\boldsymbol{\sigma}\cdot\left[\boldsymbol{l}_z \times \nabla\left(u_1^+ f_-\right)\right],$$

where we use the basis of Bloch functions $(\phi_{A_1}, \phi_{B_1}, \phi_{A_2}, \phi_{B_2})$ for valley $\boldsymbol{K}$ ($\xi = 1$) and $(\phi_{B_1}, -\phi_{A_1}, \phi_{B_2}, -\phi_{A_2})$ for valley $\boldsymbol{K'}$ ($\xi = -1$). The 2×2 Pauli matrices $\sigma_{1,2,3}$ act in the space of sublattice components. The off-diagonal parts of this Hamiltonian account for $\gamma_1 \simeq 0.4\,\text{eV}$, which describes interlayer hopping between A_2 and B_1 sublattices. The diagonal entries consider the electrons' Dirac spectrum within each layer (i.e. $v \simeq 10^8\,\text{cm/s}$ [105] and $\boldsymbol{p} = -i\nabla + e\boldsymbol{A}$) with a perturbation $\hat{M}_\xi$ produced by the h-BN substrate crystallographically aligned with the bottom layer [49, 88]. Here, $f_\pm = \sum_m (\pm 1)^{m+\frac{1}{2}} e^{i\boldsymbol{b}_m\cdot\boldsymbol{r}}$, where $m = 0, 1, ..., 5$, $\boldsymbol{b}_m = \hat{R}_{m\pi/3}[1 - (1+\delta)^{-1}\hat{R}_\theta](0, \frac{4\pi}{\sqrt{3}a})$, and $\hat{R}_\varphi$ is the anti-clockwise rotation by angle φ. For highly oriented van der Waals heterostructures, with a small misalignment angle $\theta \ll 1$, the Bragg vectors $\boldsymbol{b}_m$ of the moiré superlattice potential, satisfy $|\boldsymbol{b_m}| = b \approx \frac{4\pi}{\sqrt{3}a_g}\sqrt{\delta^2 + \theta^2}$, where $a_g = 2.46\mathring{A}$ is the lattice constant of graphene. The moiré pattern period $a = a_g\sqrt{\delta^2 + \theta^2}$, $\delta = 1.8\%$ considers the relative lattice mismatch between graphene and h-BN [37], and θ is the misalignment angle between the two hexagonal lattices. A moiré perturbation applied to only one of the two graphene layers in BLG breaks its inversion symmetry [174], which, in conjunction with time-inversion symmetry breaking due to a magnetic field, causes the energy spectra to be different for electrons in the $\boldsymbol{K}$ and $\boldsymbol{K'}$ valleys [68]. This feature of BLG-h-BN heterostructures persists even if BLG is covered on top by another h-BN film since the perturbation for BLG electrons at low energies will be dominated by only one h-BN layer, i.e. the one better aligned with graphene. Because the inversion symmetry in the BLG/h-BN heterostructure is broken from the beginning, it is

unnecessary to introduce inversion asymmetric properties. Therefore, we use $u_i = u_i^+$ for simplicity.

4.2.2 Low-energy effective Hamiltonian for moiré-perturbed BLG

Low-energy electron states in BLG can be described [68] using a simplified 2-band Hamiltonian, which can be obtained from Eq. (4.1) by using the Schrieffer-Wolff projection [61, 62] on the basis of Bloch states residing on A_1 and B_2 sublattices. To study the low energy behavior of moiré-perturbed BLG, the projection results are presented in [174]. The simplified 2 band Hamiltonian is

$$\tilde{H}_\xi = -\xi\frac{v^2}{\gamma_1}\begin{pmatrix} 0 & \left(\hat{\pi}^\dagger\right)^2 \\ \hat{\pi}^2 & 0 \end{pmatrix} + \tilde{M}_\xi, \tag{4.2}$$

$$\tilde{M}_1 = \begin{pmatrix} vbg_+(r) & \frac{bv^2}{\gamma_1}h_+^*(r)\hat{\pi}^\dagger \\ \frac{bv^2}{\gamma_1}\hat{\pi}h_+(r) & \frac{v^3b}{\gamma_1^2}\hat{\pi}g_-(r)\hat{\pi}^\dagger \end{pmatrix},$$

$$\tilde{M}_{-1} = \begin{pmatrix} \frac{v^3b}{\gamma_1^2}\hat{\pi}^\dagger g_-(r)\hat{\pi} & \frac{bv^2}{\gamma_1}\hat{\pi}^\dagger h_-(r) \\ \frac{bv^2}{\gamma_1}h_-^*(r)\hat{\pi} & vbg_+(r) \end{pmatrix},$$

$$g_\pm(r) = \sum_m e^{i\boldsymbol{b}_m\cdot\boldsymbol{r}}(u_0 \pm iu_3(-1)^m),$$

$$h_\pm(r) = \pm iu_1\sum_m(-1)^m e^{i\boldsymbol{b}_m\cdot\boldsymbol{r}}\left(b_m^x \pm ib_m^y\right)/b.$$

Hamiltonian $\hat{H}_\xi$ is written in the basis of Bloch states (ϕ_{A_1}, ϕ_{B_2}) for the $\boldsymbol{K}$ valley and $(\phi_{B_2}, -\phi_{A_1})$ for the $\boldsymbol{K}'$ valley. In the absence of a magnetic field, the first term in Eq. (4.2) describes gapless massive chiral fermions with quadratic dispersion $\epsilon = \alpha p^2/2m$, where $\alpha = +1$ ($\alpha = -1$) denotes the conduction (valence) band. The symmetry-broken perturbation leads to a gap in the main DP [88, 174]. In moiré-perturbed BLG, the gap size at the neutrality point can be calculated by third order perturbation, $\Delta_0 \simeq 12vb|u_1u_3| + 6bv|u_0(u_0^2 + 2u_1^2 + u_3^2)|$ (see Appendix E).

4.3 Secondary DP of moiré-perturbed BLG

Similarly to moiré-perturbed SLG discussed in Chapter 3, the moiré perturbation leads to secondary DP formation in the valence band. Using $\boldsymbol{k}\cdot\boldsymbol{p}$ theory to describe the vicinity of each moiré Brillouin zone corner $|\zeta\boldsymbol{\kappa}\rangle$, $|\zeta(\boldsymbol{\kappa}+\boldsymbol{b}_2)\rangle$, and $|\zeta(\boldsymbol{\kappa}+\boldsymbol{b}_1)\rangle$ ($\zeta=\pm1$), the corresponding effective Hamiltonian can be written in a basis of the above three plane wave states Eq. (2.25) as

$$\begin{aligned}
\hat{H}_{\zeta\boldsymbol{\kappa}} &= \begin{pmatrix} \hat{\epsilon}_0+2\tilde{v}\hat{p}_x & W^* & W \\ W & \hat{\epsilon}_0-\tilde{v}(\hat{p}_x+\sqrt{3}\hat{p}_y) & W^* \\ W^* & W & \hat{\epsilon}_0-\tilde{v}(\hat{p}_x-\sqrt{3}\hat{p}_y) \end{pmatrix}, \\
W &\approx \frac{vb}{2}(u_0+i\zeta u_3)+\frac{v^3b^3}{6\gamma_1^2}e^{\frac{2i\pi}{3\xi}}(u_0-i\zeta u_3)+\frac{\alpha\zeta v^2b^2}{\xi\sqrt{3}\gamma_1}e^{\frac{-2i\pi}{3\xi}}u_1, \\
\hat{\epsilon}_0 &= \frac{\alpha v^2b^2}{3\gamma_1}+\frac{\alpha v^2}{\gamma_1}\hat{p}^2, \quad \tilde{v}=\zeta\alpha\frac{bv^2}{\sqrt{3}\gamma_1}.
\end{aligned} \tag{4.3}$$

Time-reversal symmetry prescribes that $\hat{H}(\xi,\zeta,\boldsymbol{p},\boldsymbol{B})=\hat{H}^*(\text{-}\xi,\text{-}\zeta,\text{-}\boldsymbol{p},\text{-}\boldsymbol{B})$[1] . Therefore, we focus on $\hat{H}(1,\zeta,\boldsymbol{p},\boldsymbol{B})$ from now on. For the exact moiré Brillouin zone corner, because of the three-fold rotational symmetry of the above Hamiltonian[2], we can diagonalize using

$$\varphi_1=\frac{1}{\sqrt{3}}\begin{pmatrix}1\\1\\1\end{pmatrix}, \quad \varphi_2=\frac{1}{\sqrt{3}}\begin{pmatrix}e^{i\xi\pi}\\e^{-i\xi\frac{\pi}{3}}\\e^{i\xi\frac{\pi}{3}}\end{pmatrix}, \quad \varphi_3=\frac{1}{\sqrt{3}}\begin{pmatrix}e^{-i\xi\pi}\\e^{i\xi\frac{\pi}{3}}\\e^{-i\xi\frac{\pi}{3}}\end{pmatrix}.$$

[1] As a reminder: $\xi,\zeta=\pm1$, ξ identifies the valley of the Brillouin zone of graphene, and ζ identifies the valley of the moiré Brillouin zone.

[2] After applying a coordinate rotation $\hat{R}_{2\pi/3}$ as well as a basis rotation:

$$\hat{\mathbb{R}}_3=\begin{pmatrix}0&1&0\\0&0&1\\1&0&0\end{pmatrix}, \tag{4.4}$$

the Hamiltonian is invariant, i.e., it is three-fold rotational symmetric.

Then, using a basis of $(\varphi_1, \varphi_2, \varphi_3)$, the effective Hamiltonian can be written as:

$$\hat{H}_3 = \begin{pmatrix} \hat{\epsilon}_0+\epsilon_1 & \tilde{v}\hat{\Pi}^\dagger & \tilde{v}\hat{\Pi} \\ \tilde{v}\hat{\Pi} & \hat{\epsilon}_0+\epsilon_2 & -\tilde{v}\hat{\Pi}^\dagger \\ \tilde{v}\hat{\Pi}^\dagger & -\tilde{v}\hat{\Pi} & \hat{\epsilon}_0+\epsilon_3 \end{pmatrix} + \frac{k^2v^2}{\gamma_1}\begin{pmatrix} s_1+s_2 & 0 & 0 \\ 0 & -s_1 & 0 \\ 0 & 0 & -s_2 \end{pmatrix}$$
$$+\tilde{v}\begin{pmatrix} 0 & -(s_1+s_2+s_3)\hat{\Pi}^\dagger & (s_2-s_3)\hat{\Pi} \\ -(s_1+s_2+s_3)\hat{\Pi} & 0 & -(s_1+2s_3)\hat{\Pi}^\dagger \\ (s_2-s_3)\hat{\Pi}^\dagger & -(s_1+2s_3)\hat{\Pi} & 0 \end{pmatrix}, \tag{4.5}$$

where the energy shift of the bands resulting from the moiré perturbation is

$$\begin{aligned} \epsilon_1 &= 2\Re W = s_1\gamma_1 + s_2(\gamma_1 - \frac{b^2v^2}{3\gamma_1}) + s_3\frac{2b^2v^2}{3\gamma_1}, \\ \epsilon_2 &= -\Re W + \sqrt{3}\Im W = s_1\frac{b^2v^2}{3\gamma_1} - s_2(\gamma_1 - \frac{b^2v^2}{3\gamma_1}) + s_3\frac{2b^2v^2}{3\gamma_1}, \\ \epsilon_3 &= -\Re W - \sqrt{3}\Im W = -s_1(\gamma_1 + \frac{b^2v^2}{3\gamma_1}) - s_3\frac{4b^2v^2}{3\gamma_1}, \\ s_1 &= \frac{bv\left(\mu_0+\sqrt{3}\zeta\mu_3\right)}{2\gamma_1}, \quad s_2 = \frac{bv\left(\mu_0-\sqrt{3}\zeta\mu_3\right)}{2\gamma_1}, \quad s_3 = \frac{1}{2}\sqrt{3}\zeta\mu_1, \end{aligned} \tag{4.6}$$

where $\Re$ and $\Im$ denote the real and imaginary parts, respectively, and $\hat{\Pi} = \hat{p}_x + i\hat{p}_y$. The onsite energy shifts ϵ_1, ϵ_2 and ϵ_3 fulfill the relation $\epsilon_3 = -(\epsilon_1+\epsilon_2)$ and the gap is given by

$$\Delta_\kappa = \epsilon_1 - \epsilon_2 = -\frac{bv}{\gamma_1}(b^2v^2 - 3\gamma_1^2)(3u_0 - \zeta\sqrt{3}u_3), \tag{4.7}$$

which shows that the gap size of secondary DP depends on the difference between u_0 and u_3 values. Interestingly, a pair of simple microscopic models [88] predict the same ratio for the moiré potential parameters of Eq. (3.11), which, for $\alpha = -1$ and $\xi = -\zeta$, result in gap Δ_κ vanishing, i.e $\epsilon_1 = \epsilon_2$ are degenerate in the lowest order of zone folding.

4.4 Heisenberg matrix of moiré-perturbed BLG in a magnetic field

Similarly to Eq. (3.23) in Chapter 3, we can build a magnetic Bloch wave function of moiré-perturbed BLG, but the only difference is that the LLs of SLG are replaced by those of BLG:

$$\psi_{n=0,1}(k_2)=\frac{e^{ik_2x_2}}{\sqrt{L}}\begin{pmatrix}\frac{1-\beta}{2}\varphi_{|n|}(k_2)\\ \frac{1+\beta}{2}\varphi_{|n|}(k_2)\end{pmatrix},\ \psi^{\alpha}_{|n|\geq 2}(k_2)=\frac{e^{ik_2x_2}}{\sqrt{2L}}\begin{pmatrix}\varphi_{|n|-1-\beta}(k_2)\\ -\frac{n}{|n|}\tau\varphi_{|n|-1+\beta}(k_2)\end{pmatrix},$$

$$\epsilon_{n=0,1}=0,\qquad \epsilon_{n\geq 2}=\frac{n}{|n|}\frac{1}{m\lambda_B^2}\sqrt{|n|(|n|-1)},\quad \varphi_m(k_2)=\frac{\sqrt{3}e^{-\frac{z^2}{2}-\frac{iz^2}{2\sqrt{3}}}}{\sqrt{m!2^{(m+1)}\lambda_B\sqrt{\pi}}}\mathbb{H}_m(z)$$

$$z=\frac{\sqrt{3}x_1}{2\lambda_B}-k_2\lambda_B,\quad \lambda_B=1/\sqrt{|eB|},\quad \hat{\pi}\varphi_n(k_2)=-\tau\lambda_B^{-1}\sqrt{2n}\varphi_{n-1}(k_2), \tag{4.8}$$

where $\beta=B/|B|$, $\tau=e^{i\frac{2\pi}{3}}$ and $\mathbb{H}_n(z)$ are the Hermite polynomials.

By the same technique presented in Chapter 3, the expression of an element of the Heisenberg matrix of BLG is

$$\begin{aligned}\mu^{k_2\tilde{k}_2}_{n\tilde{n}}=&\,\delta_{n,\tilde{n}}\delta_{k_2,\tilde{k}_2}E_n+vb(\frac{n}{|n|}\frac{\tilde{n}}{|\tilde{n}|})^{\delta_{\xi,\text{-}1}}\sum_m\left(u_0+i(\text{-}1)^m u_3\right)M_m^{|n|-\xi\beta\text{-}1,|\tilde{n}|-\xi\beta\text{-}1}\\
&+\frac{v^2b}{\gamma_1}\frac{e^{-i\pi/3}\frac{\tilde{n}}{|\tilde{n}|}\beta}{\lambda_B}\sqrt{2(|\tilde{n}|\,\delta_{\xi,1}+|n|\delta_{\xi,\text{-}1})+\xi\beta-1}\,(-iu_1)\\
&\times\sum_m(\text{-}1)^m\left(b^1_m-ib^2_m\right)M_m^{|n|\text{-}1-\beta\delta_{\xi,1},|\tilde{n}|\text{-}1+\beta\delta_{\xi,\text{-}1}}\\
&+\frac{v^2b}{\gamma_1}\frac{e^{i\pi/3}\frac{n}{|n|}\beta}{\lambda_B}\sqrt{2(|n|\delta_{\xi,1}+|\tilde{n}|\delta_{\xi,\text{-}1})+\xi\beta-1}\,(iu_1)\\
&\times\sum_m(\text{-}1)^m\left(b^1_m+ib^2_m\right)M_m^{|n|\text{-}1+\beta\delta_{\xi,\text{-}1},|\tilde{n}|\text{-}1-\beta\delta_{\xi,1}}\\
&+\frac{v^3b}{\gamma_1^2}\frac{(\frac{n}{|n|}\frac{\tilde{n}}{|\tilde{n}|})^{\delta_{\xi,1}}}{\lambda_B^2}\sqrt{2|n|+\xi\beta-1}\sqrt{2\,|\tilde{n}|+\xi\beta-1}\\
&\times\sum_m\left(u_0-i(\text{-}1)^m u_3\right)M_m^{|n|\text{-}1,|\tilde{n}|\text{-}1},\end{aligned} \tag{4.9}$$

where

$$
\begin{aligned}
M_0^{n_1,n_2} &= e^{i\beta\lambda^2\sqrt{3}}\delta^- W_{1,\text{-}1,\text{-}1}^{n_1,n_2},\ M_1^{n_1,n_2} = \delta^- W_{\text{-}1,1,0}^{n_1,n_2},\ M_2^{n_1,n_2} = \delta^0 W_{\text{-}1,0,1}^{n_1,n_2},\\
M_3^{n_1,n_2} &= e^{i\beta\lambda^2\sqrt{3}}\delta^+ W_{\text{-}1,\text{-}1,1}^{n_1,n_2},\ M_4^{n_1,n_2} = \delta^+ W_{1,1,0}^{n_1,n_2},\ M_5^{n_1,n_2} = \delta^0 W_{1,0,\text{-}1}^{n_1,n_2},\\
W_{c_1,c_2,c_3}^{n_1,n_2} &= \frac{N_{n_1,n_2}}{3}\lambda_B A_{n_1} A_{n_2} 2^{\bar{n}}\sqrt{\pi}\underline{n}! L_{\underline{n}}^{|\delta n|}(2\lambda^2)\, e^{\text{-}\lambda^2}\lambda^{|\delta n|}\\
&\quad\times e^{i|\delta n|(c_1\frac{\pi}{2}+c_2\frac{\delta n}{|\delta n|}\beta\frac{\pi}{3})} e^{i\beta c_3\lambda^2 4k_2/b},
\end{aligned}
$$

Here, $\xi = \pm 1$ is the valley index, $L_n^{\alpha}(x)$ is the associated Laguerre polynomial, $\lambda = b\lambda_B/2$, $\delta^{\pm} = \delta_{\tilde{k}_2,k_2\pm\sqrt{3}b/2}$, $\delta^0 = \delta_{\tilde{k}_2,k_2}$, $\bar{n} = \max[n_1,n_2]$, $\underline{n} = \min[n_1,n_2]$, $\delta n = n_1 - n_2$ and $N_{n_1,n_2} = (1-\delta_{n_1,\text{-}1})(1-\delta_{n_2,\text{-}1})\sqrt{1+\delta_{n_1,0}}\sqrt{1+\delta_{n_2,0}}(1-\delta_{n_1,\text{-}2})(1-\delta_{n_2,\text{-}2})\sqrt{1+\delta_{n_1,1}}\sqrt{1+\delta_{n_2,1}}$.

4.5 Magnetic butterfly spectra of moiré-perturbed BLG

The most interesting feature of electrons in clean BLG in strong magnetic fields is the degeneracy of the two orbital LLs, with $n = 0$ and $n = 1$, which appear at $\epsilon = 0$, the edge between the valence and conduction bands. As shown in Fig. 4.1, the mixing of these degenerate LLs by the moiré superlattice potential determines the main features of the lower-energy portion of the magnetic miniband spectrum.

Figure 4.1 shows both the band structure in the absence of a magnetic field (the left panels) and the magnetic spectrum of the $\boldsymbol{K}$ and $\boldsymbol{K}'$ valleys of the BLG/h-BN heterostructure (the right panels) for different parameter sets. For small flux, the magnetic miniband spectra can be traced to the sequence of LLs for (gapped) BLG. At a higher flux, these LLs broaden and split, forming a fractal pattern, with the most striking features formed around zero energy. Because of the large energy spacing between the zero-energy and next LL, i.e. $\Delta\epsilon \simeq \frac{1}{m\lambda_B^2}$ in Eq. (2.36), the qualitative features of the spectrum around zero energy can be explained by considering only the coupling between the two zero-energy states, i.e. $n = 0$ and $n = 1$.

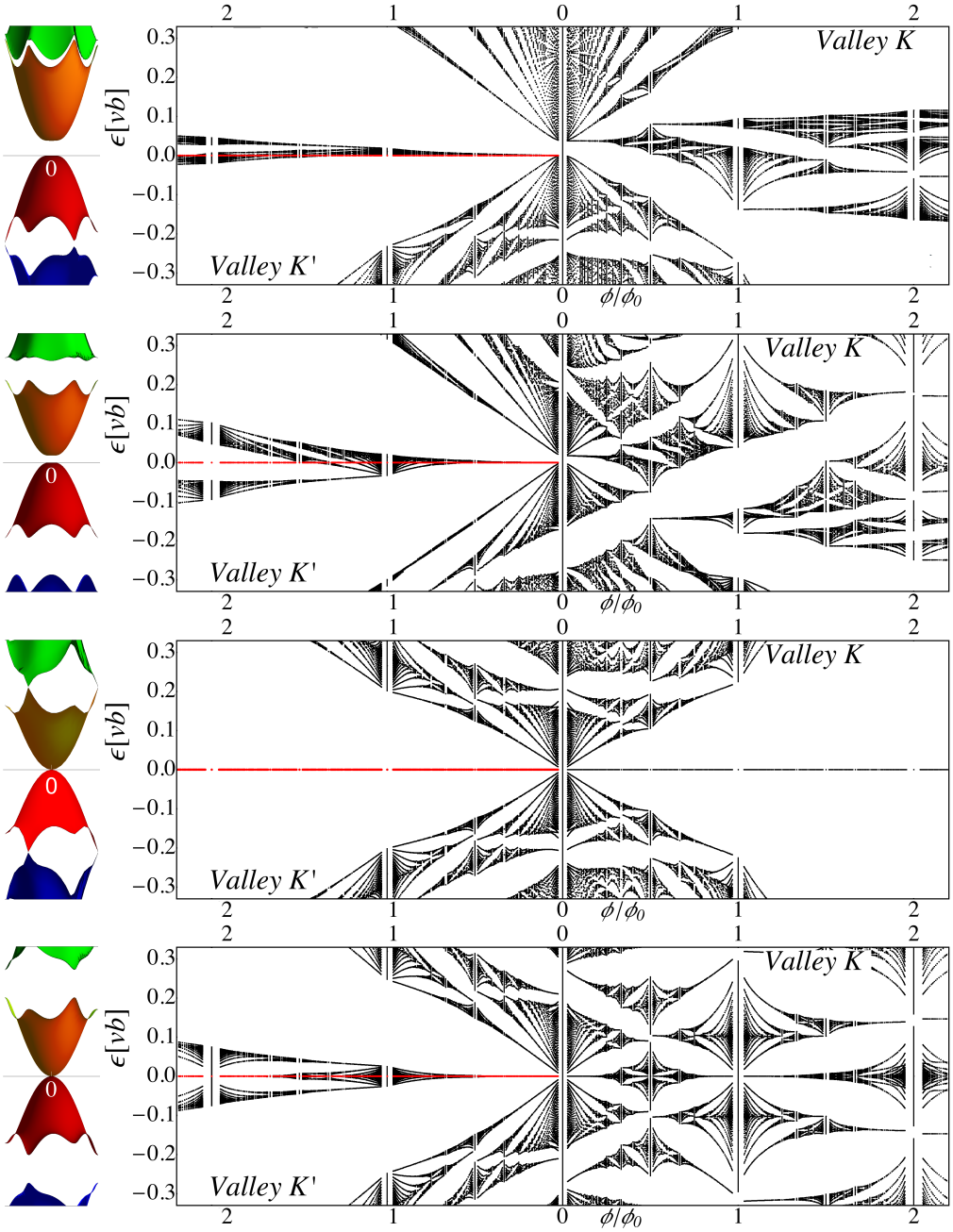

Figure 4.1: The fractal energy spectrum of the moiré pattern for (from top to bottom) parameters $u_{0,1,3} = \{0.032, -0.063, -0.055\}$, $u_0 = -0.15$, $u_1 = 0.15$ and $u_3 = 0.15$. The left inset shows the band structure of moiré perturbed BLG in the absence of a magnetic field, which illustrates the generically gapped original DP and the secondary gapped DP in the valence band. The middle and right subplots show the magnetic spectrum of BLG/h-BN in the $\boldsymbol{K}$ ($\boldsymbol{K}'$) valley, where the vertical lines represent the band width for simple fractions of flux.

Beyond the features of SLG discussed in Chapter 3, including traceable LLs, the hierarchy of DP and incompressible electron states, we note that the valley symmetry of the spectrum of moiré perturbed BLG, preserved in the absence of a magnetic field, is broken. This occurs because, in the absence of the perturbation, the distribution of the wave function among the layers is, for a given LL, exactly inverted in the two valleys. The moiré potential primarily affects the wave function component in the top layer, which is directly below *h*-BN, breaking the layer symmetry and leading to valley-asymmetric spectra with gaps. As shown in Fig. 2.14, the zero-energy LL are localized, depending on the valley, either completely on the bottom ($\boldsymbol{K}'$) or on the top ($\boldsymbol{K}$) layer in the absence of perturbation. The spectrum in the valley in which the wave function sits on the layer furthest from the substrate, contains a zero-energy LL completely decoupled from the rest of the spectrum. This is highlighted in red in the left-hand side of the main panel of Fig. 4.1.

As discussed in [174], we note that the Hamiltonian of Eq. (4.2) has the property $\epsilon^{u_0,u_1,u_3}_{\boldsymbol{K}+\boldsymbol{p}} = -\epsilon^{-u_0,u_1,-u_3}_{\boldsymbol{K}+\boldsymbol{p}}$. In particular, for the situation $u_0 = u_3 = 0$ and $u_1 \neq 0$, we find that the Hamiltonian of Eq. (4.2) obeys $\sigma_z \hat{H}_\xi \sigma_z = -\hat{H}_\xi$, which prescribes an "electron-hole" symmetry in the resulting spectrum. This relation also suggests that

$$\langle^{n,j}_{t,\boldsymbol{k}}|\tilde{H}_\xi|^{\tilde{n},\tilde{j}}_{\tilde{t},\boldsymbol{k}}\rangle = -\langle^{-n,j}_{t,\boldsymbol{k}}|\tilde{H}_\xi|^{-\tilde{n},\tilde{j}}_{\tilde{t},\boldsymbol{k}}\rangle, \qquad \langle^{0/1,j}_{t,\boldsymbol{k}}|\tilde{H}_\xi|^{0/1,\tilde{j}}_{\tilde{t},\boldsymbol{k}}\rangle = -\langle^{0/1,j}_{t,\boldsymbol{k}}|\tilde{H}_\xi|^{0/1,\tilde{j}}_{\tilde{t},\boldsymbol{k}}\rangle,$$

such that the Heisenberg matrix has $2p$-fold degenerate eigenvalues $\epsilon = 0$. Hence in such a moiré superlattice, the zero-energy LL remains completely unperturbed.

4.6 Summary

In summary, we have shown that the presence of the *h*-BN substrate lifts the valley degeneracy of BLG in a magnetic field, which in turn leads to a different magnetic Hofstadter's butterfly in each of the valleys. Furthermore, the zero-energy LL

located on the top layer remains unaffected by the moiré perturbation, making the BLG/*h*-BN spectra unique in comparison to other known magnetic spectra, in which all LLs split into sub-bands.

Chapter 5

Influence of a parallel magnetic field on the electronic properties of multilayer graphene

In this chapter, we study how a magnetic field parallel to the graphene layers impacts the low-energy electronic dispersion of BLG and TLG-ABC [19]. Based on the tight-binding model, we derive the parallel-field-induced term in the Hamiltonian [20] and describe its influence on both the low-energy electronic band structure and the Lifshitz transition [63]. Depending on the magnitude and angle of the magnetic field, the low-energy dispersion splits into several different phase regions. Our results show that the effect of a parallel field on BLG is similar to that of uniaxial homogeneous strain [110, 111]. However, in TLG-ABC, results are more complicated due to the presence of next-nearest layer hopping (γ_2 of the Slonczewski-Weiss-McClure parameters [55–57]) which has a strong effect on the low-energy band structure.

5.1 Introduction

The effects of a perpendicular magnetic field on graphene and the corresponding LLs have been widely studied [19] in addition to the role of a tilted field in BLG

[21–26]. To our knowledge, the effect of a parallel magnetic field on BLG and multilayer graphene has to date been overlooked, because the flux is limited by the small distance between layers. The manifestation of any effect requires a huge field $\simeq$ 100T, which is why interest in this subject is limited [20]. However, the Lifshitz transition in BLG and TLG-ABC only occurs in the low-energy regime, so its interplay with a parallel field may reveal new features that have yet to be studied.

In this chapter, we study the influence of a parallel field on the Lifshitz transition in BLG and TLG-ABC, comparing our results with the effect of strain [110]. First, BLG is initially described within the tight-binding model, and a parallel magnetic field is introduced by Peierls substitution [83, 109, 112]. Next, the model is reduced to a two-component low-energy effective Hamiltonian. The band structure of BLG with a parallel field is comprehensively analyzed, and the phase diagram is compared with that of strained BLG. Next, TLG-ABC with a parallel field is studied in a similar manner. In addition, after deriving the effective two-component Hamiltonian for TLG, we study its low-energy band structure without the effect of skewed hopping γ_3, then discuss the interplay between γ_3 and γ_2 in the presence of a parallel field.

5.2 BLG with a parallel magnetic field

5.2.1 Low-energy Hamiltonian of BLG with a parallel magnetic field

In a parallel magnetic field, the degeneracy of electron spin will be lifted by Zeeman effect, for $B = 10$T, the Zeeman energy is $E_{\text{Zeeman}} = \mu_e B = -0.58$meV where the magnetic momentum of an electron is $\mu_e = -9.3 \times 10^{-24}$J/T.

Although the Zeeman energy scale is comparable with the trigonal warping of BLG, $E = \gamma_1 v_3^2/4v^2 \simeq 1$meV. and the interaction between the Zeeman effect and trigonal warping is complicated. However, in the vicinity of zero energy, the

dominant impact Zeeman effect has on the band structure is in lifting the spin degeneracy, duplication and shifting the location of Dirac cone. Note that this does not affect the shape and dispersion of the Dirac cone, due to the coupling between spin and orbit is weak [113]. In other words, the Zeeman effect is almost irrelevant in comparison to the effect the parallel field has on the shape of the electronic bands. Therefore, we only focus on the orbital effect of the magnetic field and disregard possible spin effects [20, 141].

In the tight binding model, the electromagnetic interaction is induced by the Peierls substitution [83, 109, 112]. Any two operators located at different sites, i.e. $\boldsymbol{n}$ and $\boldsymbol{n}+\boldsymbol{\delta}$, are connected by an additional phase factor that represents the effect of parallel transport along the magnetic field direction, as shown in Fig. 2.4),

$$f(\boldsymbol{k}) = \sum_{i=1}^{3} \exp\left(i\boldsymbol{k}\cdot\boldsymbol{\delta}_i - ie\int_{\boldsymbol{n}}^{\boldsymbol{n}+\boldsymbol{\delta}_i} \boldsymbol{A}\, d\boldsymbol{x} \right). \tag{5.1}$$

Here, $\boldsymbol{k}$ is the vector momentum and $\boldsymbol{\delta}_i$ is the relative vector between atomic sites. Applying a Taylor expansion in the vicinity of the $\boldsymbol{K}$ point, we can obtain an expression for the shift momentum, which is different for each hopping path. Considering a BLG sheet with a parallel field, the vector potential is chosen such that the magnetic field can be evaluated as follows

$$\begin{aligned} \boldsymbol{A} &= z(B_y\hat{i} - B_x\hat{j}) = Bz(\sin(\theta)\hat{i} - \cos(\theta)\hat{j}), \\ \boldsymbol{B} &= B_x\hat{i} + B_y\hat{j} = B(\cos(\theta)\hat{i} + \sin(\theta)\hat{j}). \end{aligned} \tag{5.2}$$

Using the mid-point between the bottom and top layer as the zero point for coordinate z and applying the transformation $\boldsymbol{k} \to \boldsymbol{k} + e\boldsymbol{A}$, the Hamiltonian of BLG

(2.22)

$$\hat{H}_{\mathrm{BLG}} = \begin{pmatrix} 0 & v\hat{\pi}^\dagger & v_4\hat{\pi}^\dagger & v_3\hat{\pi} \\ v\hat{\pi} & 0 & \gamma_1 & v_4\hat{\pi}^\dagger \\ v_4\hat{\pi} & \gamma_1 & 0 & v\hat{\pi}^\dagger \\ v_3\hat{\pi}^\dagger & v_4\hat{\pi} & v\hat{\pi} & 0 \end{pmatrix},$$

will be transformed into

$$\hat{H}_b = \begin{pmatrix} \hat{D}_{-\frac{1}{2}} & \hat{V}_0 \\ \hat{V}_0^\dagger & \hat{D}_{\frac{1}{2}} \end{pmatrix}, \quad \hat{D}_n = \begin{pmatrix} 0 & v\tilde{\hat{\pi}}_n^\dagger \\ v\tilde{\hat{\pi}}_n & 0 \end{pmatrix}, \quad \hat{V}_n = \begin{pmatrix} v_4\tilde{\hat{\pi}}_n^\dagger & v_3\tilde{\hat{\pi}}_n \\ \gamma_1 & v_4\tilde{\hat{\pi}}_n^\dagger \end{pmatrix}.$$

Here $\tilde{\hat{\pi}}_n = \hat{\pi} + n\beta i e^{-i\theta}$ ($\tilde{\hat{\pi}}_0 = \hat{\pi}$), and $\beta = Bed$ represents the momentum modification due to parallel field B, where e is the electron charge and θ describes the angle of the field. When $B = 1\mathrm{T}$, $\beta \simeq 3 \times 10^{-5}\gamma_0/v$.

Based on [20], we consider the situation in which the energy is much lower than γ_1. Using the Schrieffer-Wolff transformation and assume that $\gamma_1 \gg \epsilon, vk, v\beta, v_3k$, we can obtain a new low-energy effective Hamiltonian in the basis of orbitals on $A1$ and $B2$ sites as follows:

$$\hat{H} = \hat{H}_1 + \hat{H}_2 + \hat{H}_3, \quad \hat{H}_1 = -\frac{1}{2m}\begin{pmatrix} 0 & \hat{\pi}^{\dagger 2} \\ \hat{\pi}^2 & 0 \end{pmatrix},$$
$$\hat{H}_2 = v_3\begin{pmatrix} 0 & \hat{\pi} \\ \hat{\pi}^\dagger & 0 \end{pmatrix} \quad \hat{H}_3 = \frac{\beta^2}{8m}\begin{pmatrix} 0 & -e^{-2i\theta} \\ -e^{2i\theta} & 0 \end{pmatrix}. \tag{5.3}$$

Here, the effective mass of the electron in BLG is $m = \gamma_1/(2v^2)$. This new low-energy Hamiltonian has one additional term, $\hat{H}_3$, which describes the parallel field effect. The term $\hat{H}_1$ results in a parabolic dispersion within a relatively high-energy region [68]. Both of the $\hat{H}_2$ and $\hat{H}_3$ terms tend to modify the topology of the low-energy band structure when their corresponding energy magnitude is comparable to that of $\hat{H}_1$. If $|\boldsymbol{k}| \lesssim mv_3$, then the second term, $\hat{H}_2$, will have a significant effect

on the low-energy band structure, and lead to the appearance of trigonal warping [68]. The term $\hat{H}_3$, which will become important when the magnitude of β is as large as $\boldsymbol{k}$, causes two-fold splitting.

5.2.2 Lifshitz transition in BLG with a parallel field

In the extreme situation of $\beta \gg mv_3$, where v_3 can be ignored, the dispersion relation is

$$E^2 = \frac{k^4}{4m^2} + \frac{\beta^4}{64m^2} + \frac{k^2\beta^2}{8m^2}\cos(2\theta - 2\varphi),$$

where φ is the polar angle of momentum k. In the scenario $\theta - \varphi = n\pi$ and $k = \beta/2$, the field splits the low-energy dispersion into two pockets with two new DPs along the direction of the parallel field direction located at $\beta^2 v^2/(2\gamma_1)$ [20].

There is a strong interplay between the parallel field effect and skewed hopping γ_3. To simplify the process of analyzing this interplay, and as there are only two variables β and v_3 aside from momentum k, it is convenient to define a dimensionless variable to eliminate one of these variables. We therefore choose $\mathbb{K}_b = mv_3$ as a new momentum unit and consequently $\mathbb{E}_b = mv_3^2/2 \simeq 2.53\text{meV}$ as new energy unit. Thus, $\hat{k} = k/\mathbb{K}_b$, $\hat{\beta} = \beta/\mathbb{K}_b$ (when $B = 55\text{T}$ then $\beta = \mathbb{K}_b$), $\hat{E} = E/\mathbb{E}_b$ and the dispersion relation given by the Hamiltonian in Eq. (5.3) is

$$\begin{aligned}\hat{E}^2 = {} & (-2+\hat{k}_x)^2\hat{k}_x^2 + 4\hat{k}_y^2 + 2\hat{k}_x(6+\hat{k}_x)\hat{k}_y^2 + \hat{k}_y^4 + \hat{\beta}^4 \\ & + 2\hat{\beta}^2\left[\left((-2+\hat{k}_x)\hat{k}_x - \hat{k}_y^2\right)\cos(2\theta) + 2(1+\hat{k}_x)\hat{k}_y\sin(2\theta)\right].\end{aligned}$$

The first limiting case we consider regarding the dispersion is for $\beta = 0$ in Eq.(5.3); we obtain a dispersion with the usual trigonal warping and three DPs located around the central DPs at a distance of $2mv_3$ from the centre in momentum space and with the Lifshitz transition occurring at $v_3^2\gamma_1/(4v^2)$, as shown in Fig. 2.5. For $\theta = 0$ (i.e. the field is in the direction of one of the three outer DPs) and when $\hat{\beta} < 1$, the band structure has four DPs, as shown in Fig. 5.1(a). Increasing $\hat{\beta}$,

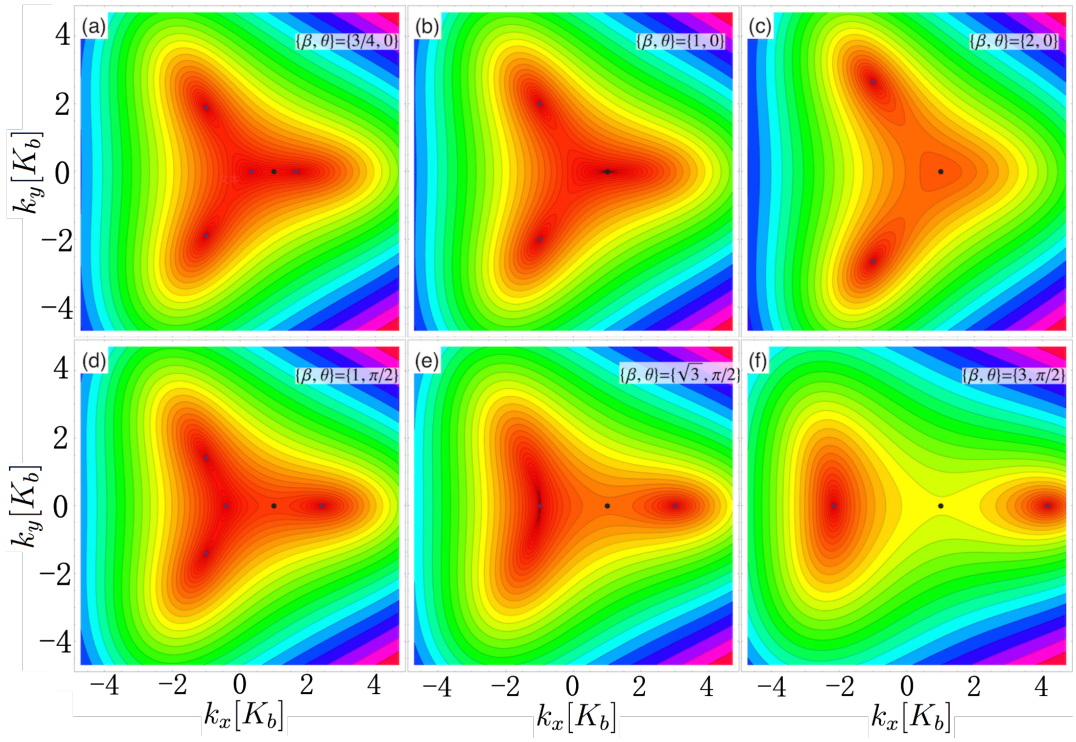

Figure 5.1: Contour plots for the valence band structures of BLG with different parallel fields. The longer wavelength of the colour light, the higher the energy. The unit of momentum is $\mathbb{K}_b = mv_3 \sim 1/300\gamma_0/v$. Panels along the top correspond to $\theta = 0$ with strengths as follows: (a) $\hat{\beta} = 3/4\mathbb{K}_b$; (b) $\hat{\beta} = \mathbb{K}_b$ and (c) $\hat{\beta} = 2\mathbb{K}_b$. Panels along the bottom correspond to $\theta = \pi/2$, with strengths as follows: (d) $\hat{\beta} = \mathbb{K}_b$; (e) $\hat{\beta} = \sqrt{3}\mathbb{K}_b$ and (f) $\hat{\beta} = 3\mathbb{K}_b$. The point locates $(1, 0)$ is always an extreme point (but not necessary a Dirac point).

the two DPs on the x-axis move towards each other, and coalesce at $\hat{\beta} = 1$, as shown in Fig. 5.1(b). When $1 < \hat{\beta} < 3$, the two combined DPs have an increase in energy and form a local minimum, as shown in Fig. 5.1 (c). As $\hat{\beta} \geq 3$, the magnetic field effect overwhelms the trigonal warping effect of v_3, and the band structure has only two DPs. In general, $\hat{\beta} = 1$ and $\hat{\beta} = 3$ are critical values for phase transitions for the $\theta = 0$ case. For $\theta = \pi/2$ (i.e. the field does not cross the outer DP) and when $\hat{\beta} < \sqrt{3}$, there are four DPs, as shown in Fig. 5.1(d). With increasing $\hat{\beta}$, three DPs move towards each other and coalesce at $\hat{\beta} = \sqrt{3}$, as shown in Fig. 5.1(e). When $\sqrt{3} < \hat{\beta}$, two of the three coalesced DPs vanish and the band structure is left with only two DPs, as shown in Fig. 5.1(f). The effect of the field overwhelms the effect of v_3 from this point onwards. Here, in the case of $\theta = \pi/2$, $\hat{\beta} = \sqrt{3}$ is the critical condition for a phase transition. For both $\theta = 0$ and $\theta = \pi/2$, point $(k_x, k_y) = (1, 0)\mathbb{K}_b$ is a constant extreme point.

To determine the phase diagram of BLG in a parallel field, we first distinguish the phase I (i.e. with four DPs) from the other phases. This can easily be achieved by requiring that the off-diagonal component of the Hamiltonian in Eq. (5.3) be zero, i.e.

$$-\frac{1}{2m}\hat{\pi}^2 + v_3\hat{\pi}^\dagger - \frac{\beta^2}{8m}e^{2i\theta} = 0. \tag{5.4}$$

This equation can be solved analytically for simple values of θ or generally solved by a numerical method. By counting the number of real solutions in the momentum space and for various field strengths, the first phase can be determined. To determine the remaining phases, which may include a local minimum, we need some additional criteria. For a continuous function, the determinant of the Hessian matrix (i.e. a matrix of second derivatives) $\mathbb{H}$ of the function (i.e. dispersion E) can be used to determine the property the point (k_x, k_y) [114], i.e.

$$\mathbb{H} = \begin{vmatrix} \frac{\partial^2 E}{\partial k_x^2} & \frac{\partial^2 E}{\partial k_x \partial k_y} \\ \frac{\partial^2 E}{\partial k_y \partial k_x} & \frac{\partial^2 E}{\partial k_y^2} \end{vmatrix}. \tag{5.5}$$

If $\mathbb{H}(k_x, k_y) > 0$, then the point (k_x, k_y) is a local minimum or maximum depending on whether $\partial_{k_x}\hat{E}^2 > 0$ or $\partial_{k_x}\hat{E}^2 < 0$. If $\mathbb{H}(k_x, k_y) < 0$, then the point (k_x, k_y) is a saddle point. In addition, if $\mathbb{H}(k_x, k_y) = 0$, then we need to include higher order derivatives. By counting different types of points, we construct the phase diagram shown in Fig. 5.2, which is six-fold and consists of three phases, and these distinct phase regions are as follows: (I) Four DPs corresponding to the contour plots shown as subplots (a) and (d) in Fig. 5.1; (II) Two DPs and one local minimum, shown as subplots (b) and (e) in Fig. 5.1 and (III) Two DPs shown as subplots (c) and (f) in Fig. 5.1.

5.2.3 Comparing the effect of parallel field with homogeneous strain

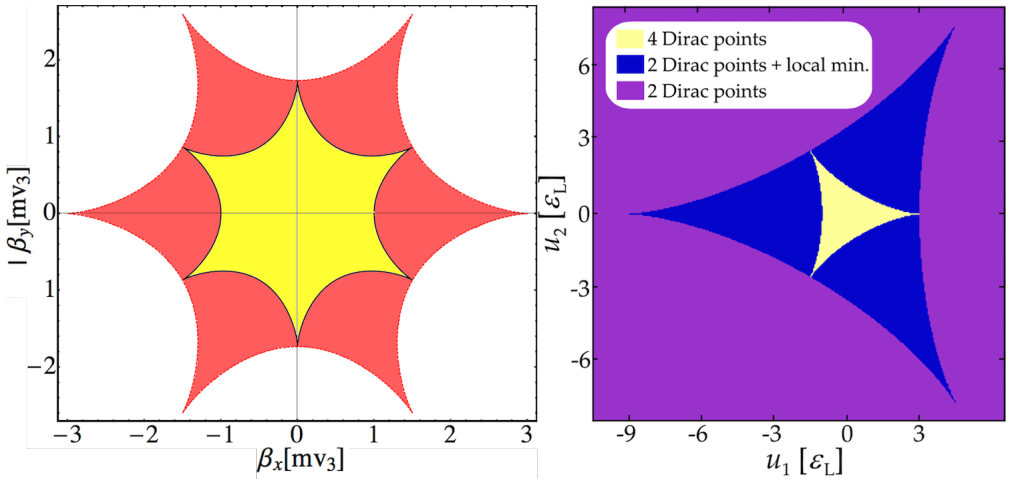

Figure 5.2: The phase diagram of BLG in a parallel magnetic field (left) and with homogeneous strain (right) [110]. u_1 and u_2 is the real and imaginary part of the complex number ω, respectively. In the left panel, the phase shown in yellow corresponds to the regime with four DPs, the phase shown in red corresponds to the regime with two DPs and one local minimum and the phase in white corresponds to the regime with only two DPs.

To describe the effect of homogeneous strain on BLG in the low-energy regime, the following term is used [110]:

$$\hat{H}_s = \begin{pmatrix} 0 & \omega \\ \omega^* & 0 \end{pmatrix}, \tag{5.6}$$

where ω is a complex number. Both terms in $\hat{H}_s$ (i.e. homogeneous strain) and $\hat{H}_3$ (i.e. parallel field) do not interact with momentum, so their effect will not generate three equidistant new DPs as skewed hopping γ_3 does. In the extreme case of $v_3 \to 0$, they only provide a quadratic splitting with two new DPs. Similar to the phases for a parallel magnetic field, the additional terms of $\hat{H}_s$ lead to a three-fold rotational symmetric phase diagram with the following three distinct phases, (a) four DPs, (b) two DPs and one local minimum point and (c) two DPs only.

In Fig. 5.2, both the parallel field and homogeneous strain phase diagrams have three phases, illustrating the competition between the external effect (i.e. either parallel magnetic field or homogeneous strain) and the intrinsic trigonal warping effect due to skewed hopping γ_3. In general, in the regime of weak external fields, the trigonal warping effect dominates, so the band structure has four DPs. With increasing external fields, the double warping effect gradually becomes comparable. At certain critical points in the parametric regime, the external fields overwhelm the intrinsic trigonal warping effect in BLG and the dispersion changes dramatically.

The difference here arises because strain is not a vector so two opposite strain directions are identical, but the magnetic field is an axial-vector, so the two opposite field directions are not identical. Therefore, the phase diagram is three-fold symmetric for strain and six-fold symmetric for a parallel magnetic field.

As for the magnitude of the field, $\beta^2/8m \simeq 0.7$meV for $B = 100$T is still smaller than $\omega = 5$meV, which is estimated for 1% strain effect in BLG [111]. Because of the small distance between the different layers of graphene, the magnetic flux is limited. Therefore, from the point of view of the band structure, the parallel field effect on BLG is a weaker version of uniaxial homogeneous strain. For practical use, a common magnitude of magnetic field in a laboratory is about $B = 10$T, $\hat{\beta} = 0.06[mv_3]$ is still in the region of $\hat{\beta} < 1$, so the dominant effect is still γ_3 and the low-energy band structure always has four DPs, as in the normal clean BLG.

5.3 TLG-ABC with a parallel field

5.3.1 Low-energy Hamiltonian of TLG-ABC with a parallel field

By applying a Peierls substitution, we can study the effect of a parallel field in TLG-ABC Hamiltonian Eq. (2.28). Choosing the same gauge transformation Eq. (5.2) as in the last section, we can obtain $\hat{H}_C$ for TLG-ABC with a parallel field as follows

$$\hat{H}_C = \begin{pmatrix} \hat{D}_{-1} & \hat{V}_{-1/2} & W \\ \hat{V}^{\dagger}_{-1/2} & \hat{D}_0 & \hat{V}_{1/2} \\ W & \hat{V}^{\dagger}_{1/2} & \hat{D}_1 \end{pmatrix}, \quad W = \begin{pmatrix} 0 & \frac{\gamma_2}{2} \\ 0 & 0 \end{pmatrix}. \tag{5.7}$$

Using a Schrieffer-Wolff transformation, we can project the effect of high-energy atomic sites on low-energy sites, and obtain a two-component effective low-energy Hamiltonian as

$$\hat{H}_C = \hat{H}_{C1} + \hat{H}_{C2} + \hat{H}_{C3}, \qquad \hat{H}_{C1} = \frac{v^3}{\gamma_1^2} \begin{pmatrix} 0 & \hat{\pi}^{\dagger 3} \\ \hat{\pi}^3 & 0 \end{pmatrix}, \tag{5.8}$$

$$\hat{H}_{C2} = \left(\frac{\gamma_2}{2} + \frac{v v_3}{\gamma_1} \left(\beta^2 - 2\hat{k}^2 \right) \right) \begin{pmatrix} 0 & 1 \\ 1 & 0 \end{pmatrix}, \quad \hat{H}_{C3} = \frac{\beta^2 v^3}{\gamma_1^2} \begin{pmatrix} 0 & e^{-2i\theta} \hat{\pi}^{\dagger} \\ e^{2i\theta} \hat{\pi} & 0 \end{pmatrix}.$$

In addition to the Hamiltonian considered in Ref. [19], the trigonal warping term $\hat{H}_{C2}$ includes a magnetic field dependent part, and there is a double-warping term $\hat{H}_{C3}$. Because the underlying dispersion relation changes from square to cubic, the parallel-field-induced term behaves differently from that of BLG. Trigonal warping in TLG-ABC has three origins, i.e. the skewed hopping parameter γ_3, next-nearest interlayer hopping parameter γ_2 and the parallel field β. In $\hat{H}_{C2}$, the parallel field term is independent of electronic momentum, and it becomes one of the joint origins of trigonal warping.

The Lifshitz transition in TLG-ABC in the absence of an external field occurs at $(v^3k^3/\gamma_1^2)^2 \simeq (\gamma_2/2 - 2vv_3k^2/\gamma_1)^2$, i.e. $k \simeq 0.037\gamma_0/v$. Below this energy, γ_2 is the dominant term. In a parallel magnetic field, the magnetic field effect is comparable with $vv_3\beta^2/\gamma_1 \simeq \gamma_2$, i.e. $B \simeq 166$T. Below this magnitude of the magnetic field, the dominant term of changing the shape of band is γ_2.

5.3.2 TLG-ABC band structure in a parallel magnetic field with $\gamma_3 = 0$

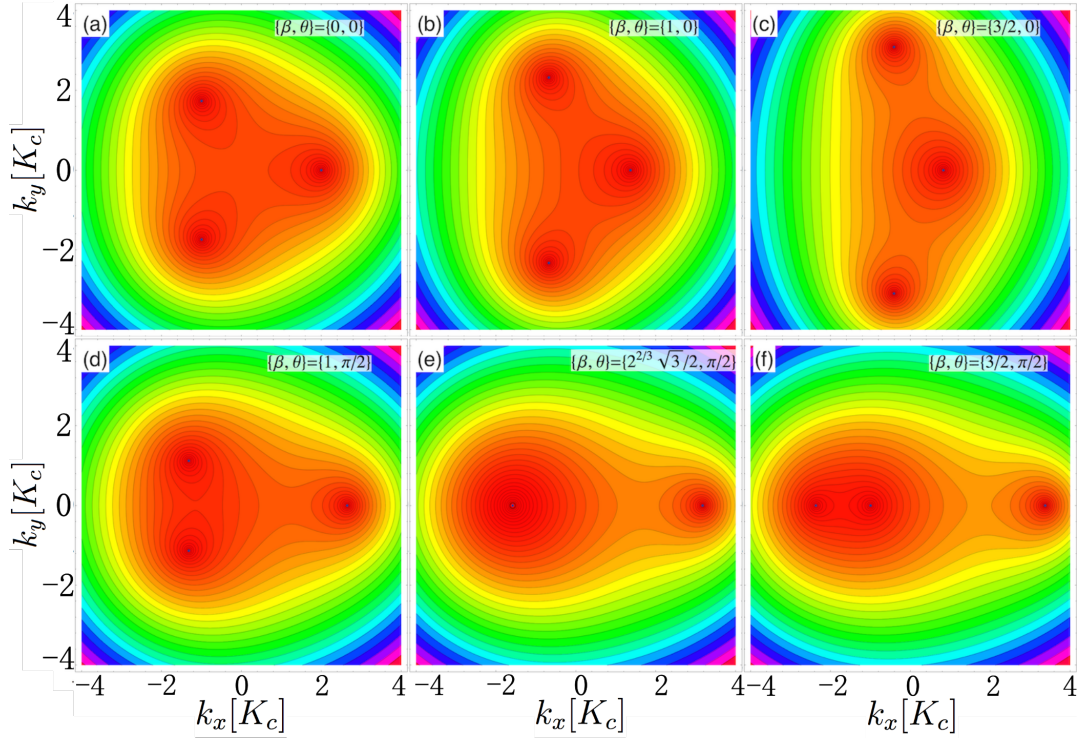

Figure 5.3: Contour plots for the energy bands of TLG-ABC in a parallel field with $\gamma_3 = 0$. All momenta are in the units of $\mathbb{K}_c = \gamma_1^{2/3}(-\gamma_2/2)^{1/3}/v \sim 1/50\gamma_0/v$. The longer wavelength of colour light are for the higher energy. Panels along the top correspond to the $\theta = 0$ field with strengths as follows: (a) $\hat{\beta} = 0\mathbb{K}_c$; (b) $\hat{\beta} = 1\mathbb{K}_c$ and (c) $\hat{\beta} = 3/2\mathbb{K}_c$. Panels along the bottom corresponds to $\theta = \pi/2$ with strengths as follows: (d) $\hat{\beta} = 1\mathbb{K}_c$; (e) $\hat{\beta} = \sqrt{3}/2^{1/3}\mathbb{K}_c$ and (f) $\hat{\beta} = 3/2\mathbb{K}_c$.

As in the discussion of Ref. [19], the trigonal warping in TLG-ABC is dominated by the presence of next-nearest layer hopping γ_2, as discussed in conjunction with Eq.(2.29), with magnitude $\gamma_2/2 = -10$meV$\sim -1/400\gamma_0$, much higher than the magnitude of k^2vv_3/γ_1 in $\hat{H}_{C2}$. Therefore, we begin TLG-ABC analysis with a parallel magnetic field from $v_3 = 0$, which still holds most of the essential features.

With new units $\mathbb{K}_c = \gamma_1^{2/3}(-\gamma_2/2)^{1/3}/v \sim 0.02\gamma_0/v$ and $\mathbb{E}_c = v_3^3\gamma_1/v^3 \sim 0.3$meV, the physical quantities change to $\hat{k} = k/\mathbb{K}_c$ and $\hat{\beta} = \beta/\mathbb{K}_c$, $\hat{E} = E/\mathbb{E}_c$. Furthermore, the dispersion is given as

$$\begin{aligned}\hat{E}^2_{\gamma_3=0} = 1 - 2\hat{k}_x^3 + \hat{k}_x^6 + 6\hat{k}_x\hat{k}_y^2 + 3\hat{k}_x^4\hat{k}_y^2 + 3\hat{k}_x^2\hat{k}_y^4 + \hat{k}_y^6 + (\hat{k}_x^2 + \hat{k}_y^2)\hat{\beta}^4 \\ + 2\hat{\beta}^2\left[(-\hat{k}_x + \hat{k}_x^4 - \hat{k}_y^4)\cos(2\theta) + \hat{k}_y\left(1 + 2\hat{k}_x(\hat{k}_x^2 + \hat{k}_y^2)\right)\sin(2\theta)\right].\end{aligned} \tag{5.9}$$

Using the above dispersion, we calculated the contour plots shown in Fig. 5.3 for different magnitudes and directions of the parallel magnetic field.

In the case of $\hat{\beta} = 0$, the dispersion reduces to $\hat{E}^2 = \hat{k}^6 + 1 - 2\hat{k}^3\cos(3\varphi)$, and the DPs spread around the central local minimum at a distance of $\hat{k} = 1$, as shown in Fig. 5.3(a). When $\theta = 0$, the TLG-ABC band structure in a parallel magnetic field always has three DPs, and the distance between each of them increases with the increase of magnetic field, as shown in Figs. 5.3(b) and 5.3(c). When $\theta = \pi/2$, the band structure still has three DPs, as shown in Figs. 5.3(d) and 5.3(f), except for one scenario in which it has only two DPs, as shown in Fig. 5.3(e). The origin of this phenomenon is that two of the three DPs become superimposed when the parallel magnetic field effect overwhelms the trigonal warping effect, which occurs at $\hat{\beta} = \sqrt{3}/2^{1/3}\mathbb{K}_c$ (i.e. $B \simeq 900$T).

In the extreme case of $\hat{\beta} \gg \mathbb{K}_c$, the effect of γ_2 can be neglected, so the parallel magnetic field will lead to a three-fold splitting. All three DPs are on the same axis which is perpendicular to the magnetic field direction, which is similar to that of Fig. 5.3(f). The monotonic phase diagram for $\gamma_3 = 0$ is shown in Fig. 5.6(a).

5.3.3 Lifshitz transition in the presence of γ_2 and v_3

Given that we already have three parameters γ_2, γ_3 and β together with momentum k, it is not possible to only keep one parameter and eliminate the other two by simply introducing a new dimensionless unit as in BLG or TLG-ABC (without γ_3). Therefore, we employ a new unit to simplify and eliminate γ_3, $\mathbb{K}_d = v_3\gamma_1/v^2 \simeq$

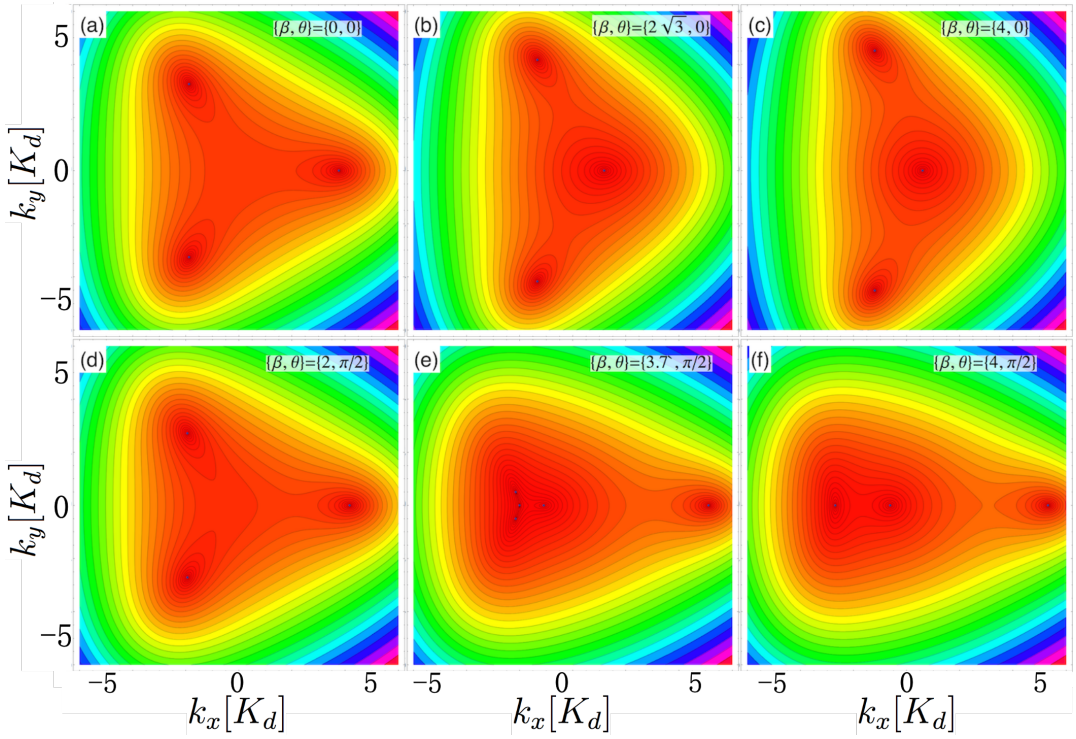

Figure 5.4: Contour plots for TLG-ABC in a parallel field, with $\gamma_3 \neq 0$ and $\gamma_2 \neq 0$. All momenta are in the units of $\mathbb{K}_d = v_3\gamma_1/v^2 \sim 1/150\gamma_0/v$. The longer wavelength of colour light are for the higher energy. Panels along the top correspond to $\theta = 0$ with strengths of the fields as follows (a) $\hat{\beta} = 0$; (b) $\hat{\beta} = 2/\sqrt{3}\mathbb{K}_d$ and (c) $\hat{\beta} = 4\mathbb{K}_d$. Panels along the bottom correspond to $\theta = \pi/2$ with strengths of the fields as follows (d) $\hat{\beta} = 2\mathbb{K}_d$; (e) $\hat{\beta} = 3.7\mathbb{K}_d$ and (f) $\hat{\beta} = 4\mathbb{K}_d$. Given that $\mathbb{K}_d = 1/150\gamma_0/v$ is 1/3 of $\mathbb{K}_c \sim 1/50\gamma_0/v$, i.e. the scale of the axis in Fig. 5.3 and Fig. 5.5.

$0.01\gamma_0/v$ with $\mathbb{E}_d = v_3^3\gamma_1/v^3 \simeq 0.3$meV and leave γ_2 and β for the analysis. Thus, we have $\hat{k} = k/\mathbb{K}_d$, $\hat{\beta} = \beta/\mathbb{K}_d$, $\hat{E} = E/\mathbb{E}_d$ and $\hat{\gamma}_2 = \gamma_2/\mathbb{E}_d$. The new regularized dispersion is:

$$
\begin{aligned}
E_A^2 &= E_{A1}^2 + E_{A2}^2, \qquad (5.10)\\
E_{A1}^2 &= 4\hat{k}^4 + \hat{k}^6 + \hat{\beta}^4 + \hat{k}^2\hat{\beta}^2(-4+\hat{\beta}^2) + 2\hat{k}^3(-2\hat{k}^2+\hat{\beta}^2)\cos(3\varphi)\\
&\quad + 2\hat{k}\hat{\beta}^2\left(\hat{k}^3\cos(2\varphi-2\theta) + (-2\hat{k}^2+\hat{\beta}^2)\cos(\varphi+2\theta)\right),\\
E_{A2}^2 &= \frac{1}{4}\hat{\gamma}_2\left(-8\hat{k}^2 + 4\hat{\beta}^2 + \hat{\gamma}_2 + 4\hat{k}^3\cos(3\varphi) + 4\hat{k}\hat{\beta}^2\cos(\varphi+2\theta)\right).
\end{aligned}
$$

By analytically evaluating the parallel-magnetic field dispersion with v_3 and γ_2, we can finally recognize that there are 19 extreme points. Among them, nine are potential DPs. Although analytical expressions for $\hat{k}_x$ and $\hat{k}_y$ are obtainable, expressions are along and complicated, and not particularly useful.

Since the presence of $\gamma_2/2 = -50\mathbb{E}_d$ completely overwhelms the effect of γ_3 for $\beta = 0$, the dispersion becomes

$$
\hat{E}^2 = (\hat{k}^3 - 2\hat{k}^2 - 25)^2 + 4\hat{k}^3(25 + 2\hat{k}^2)\sin(3\varphi/2)^2. \qquad (5.11)
$$

Compared with the situation in which $\gamma_3 = 0$, we note that when $\theta = 0$, the band structure will be similar to that of Fig. 5.3. When $\theta = \pi/2$, the presence of γ_3 generates additional DPs and a new phase within the regime of small β values. With increasing β, the parallel field effect overwhelms the effect of v_3, so the topology of the two band structures is qualitatively identical with or without γ_3. As for the phase diagram, which is shown in Fig. 5.6(b), the presence of γ_3 causes it to become anisotropic. Only in a specific window of β and θ are there additional phases.

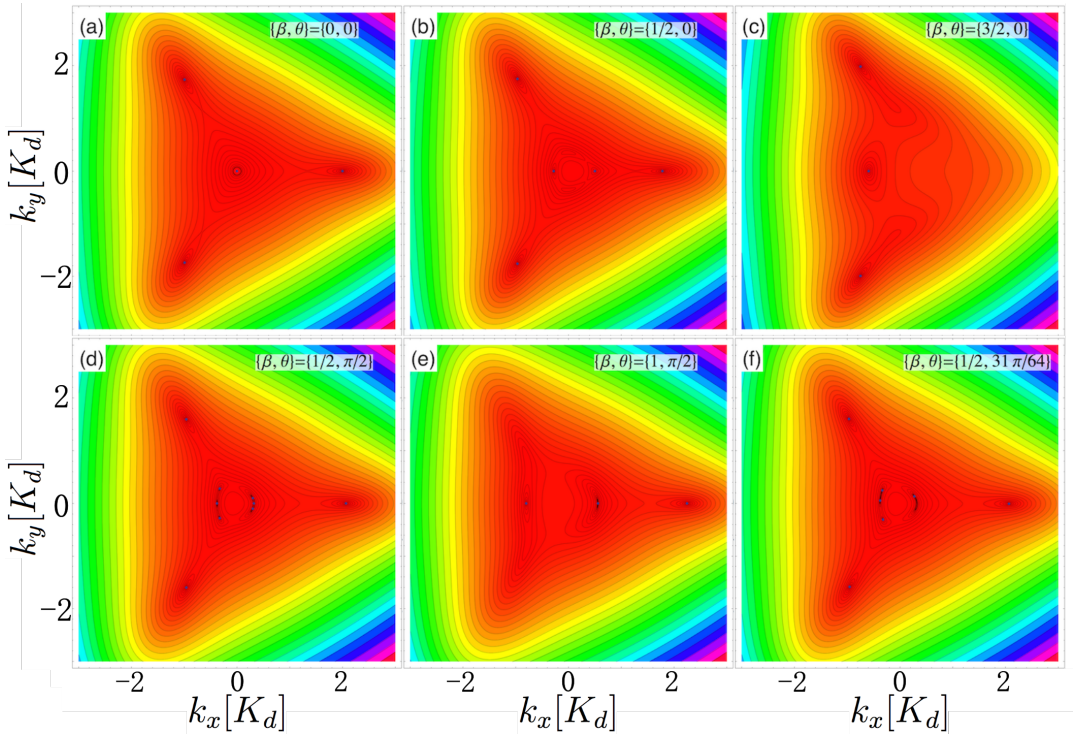

Figure 5.5: Contour plot of TLG-ABC band structure in a parallel field with $\gamma_2 = 0$. The axes are $\hat{k}_x$ and $\hat{k}_y$. All momenta are in units of $\mathbb{K}_d = v_3\gamma_1/v^2 \sim 1/150\gamma_0/v$. The longer wavelength of colour light, the higher the energy. Panels along the top correspond to $\theta = 0$ with strengths as follows: (a) $\hat{\beta} = 0$; (b) $\hat{\beta} = 1/2\mathbb{K}_d$ and (c) $\hat{\beta} = 3/2\mathbb{K}_d$. Panels along the bottom correspond to $\theta = \pi/2$ and (d) $\hat{\beta} = 1/2\mathbb{K}_d$; (e) $\theta = \pi/2$ $\hat{\beta} = 1\mathbb{K}_d$ and (f) $\theta = 31\pi/64$, $\hat{\beta} = 1/2\mathbb{K}_d$. Finally, the scaling of the axes in Fig. 5.5 is the same as in Fig. 5.3 and Fig. 5.4.

5.3.4 TLG-ABC band structure in a parallel field and the absence of γ_2

In Eq. (5.7), we employed γ_2 as half of the value in bulk graphite, but the exact value of γ_2 in TLG-ABC is still unknown. Therefore, for completeness, we discuss different input values of γ_2 for the dispersion.

First, consider the extreme situation in which $\hat{\gamma}_2 = 0$. Following the same procedure of counting DPs as before, we can distinguish the following four different major phases, as shown in Fig. 5.5: (I) three DPs shown in subplots (a), (c) and (e); (II) five DPs shown in subplot (b); (III) seven DPs shown in subplot (f) and (IV) 9 DPs shown in subplot (d).

By comparing this set of band structures (i.e. Fig. 5.5) with the former band structures obtained in Figs. 5.1, 5.3 and 5.4, we note that the extremely low-energy band structure becomes more complicated due to the existence of γ_3. The maximum number of DPs achieved is nine points as shown as Fig. 5.5(d). The existence of $\hat{\gamma}_2$ simplifies the complicated band structure given by γ_3. The corresponding phase diagram, which is anisotropic, is shown in Fig. 5.6(f); as evident from the figure, the number of DPs monotonically decreases with increasing β.

5.3.5 TLG-ABC phase diagram with a parallel magnetic field

If $\gamma_3 = 0$, then the phase always has three DPs and is isotropic, as shown in Fig. 5.6(a). If $\gamma_2 = 0$, then there will be four different phases with three, five, seven and nine DPs, as shown in Fig. 5.6(c). Between these two extremes, the interplay between γ_2 and γ_3 leads to a shift between the one and four phase situations. When γ_2 equals half the value of that of in bulk graphite, the phase diagram consists of five DPs and three DPs, and the five DPs phase only exist in six small triangular regions, as shown in Fig. 5.6(b).

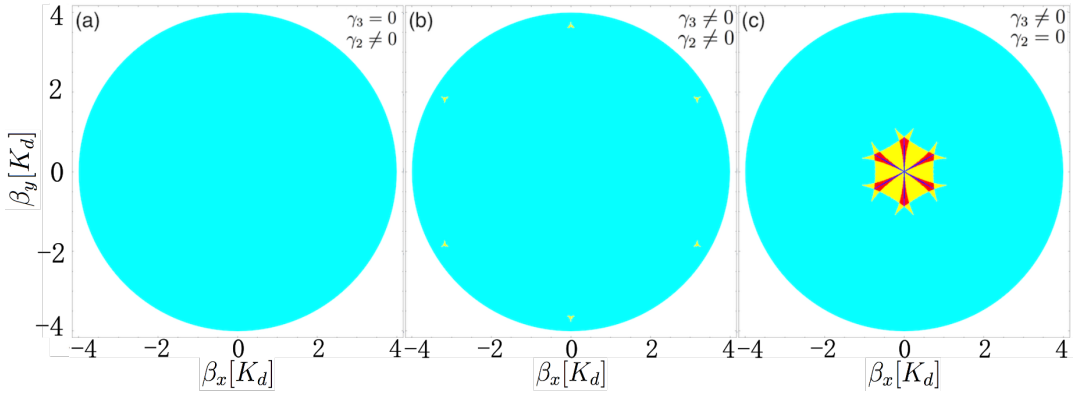

Figure 5.6: TLG-ABC phase diagram with a parallel field. All momenta are in units of $\mathbb{K}_d = v_3\gamma_1/v^2 \sim 1/100\gamma_0/v$. For $\beta = \mathbb{K}_d$, $B \simeq 300$T. The left subplot corresponds to $\gamma_3 = 0$ and γ_2 equal to half the value of that of bulk graphite. The middle subplot corresponds to for $\gamma_3 = 0.1\gamma_0$ and γ_2 equal to half the value of that of bulk graphite. The right subplot corresponds to $\gamma_3 = 0.1\gamma_0$ and $\gamma_2 = 0$. The colour represents the different number of DPs, cyan corresponds to three DPs, yellow corresponds to five DPs, red corresponds to seven DPs and blue corresponds to nine DPs.

5.4 Conclusion

In this chapter, we discussed the influence of a parallel magnetic field on BLG, and we then compared our results with the effect of homogeneous strain in BLG. As shown in this chapter, these two influences are similar: both phase diagrams consist of three phases and a maximum of four DPs. The difference between the parallel magnetic field and homogeneous strain is that the phase diagram of the latter is three-fold, whereas it is six-fold for the former. Furthermore, the effect of a parallel magnetic field is as small as that of a 1% strain. In addition, we investigated the effect of a parallel magnetic field on TLG-ABC, finding that γ_3 solely provides sophisticated phases and γ_2 generally overwhelms the effect of γ_3. Finally, we obtained a diagram consisting of two phases.

Chapter 6

Electronic transport properties of multilayer graphene

6.1 Introduction

As noted in Chapter 2, interactions between different layers in multilayer graphene may be described by additional hopping parameters in the tight-binding model, and their effect is manifested in band structure and transport properties [31, 34]. For example, trigonal warping, which is the distortion of the band structure in the low-energy region, is caused by skew hopping γ_3 in BLG and next-nearest-layer hopping γ_2 in TLG-ABC. Such a change in the band structure will alter the transport properties in the low-energy region [33]. The minimum conductivity σ_m of finite-size multilayer graphene [1] is still an open and interesting question [7, 32].

Snyman and Beenakker [29] calculated σ_m for BLG in the absence of γ_3 using an analytical mode matching (MM) method, finding that it is $\sigma_m = 2\sigma_0$, where $\sigma_0 = g_s g_v e^2/h\pi$ is minimum conductivity of SLG [128], and g_s and g_v are the degeneracy of spin and valley, respectively. Then, Cserti [30] calculated σ_m, including the effect of γ_3, using Kubo's formula. His results suggest that σ_m of BLG will increase three-fold when γ_3 is considered, i.e. $\sigma_m = 6\sigma_0$. The transport properties of this

[1] The minimum conductivity is the characteristic of the system. In experiment, one may not be necessary to know where DP is; however, with the equipment of this information, one can tune the gate voltage to the minimum conductivity to approach DP.

system have also been calculated by Gao using a Green Function (GF) method [115]. Experimental measurement on minimum conductivity of BLG is studied by NovoSelov et al [93].

In this chapter, the transport properties of multilayer graphene, especially BLG, and TLG-ABA and TLG-ABC, are studied using analytical as well as numerical methods and the results of these methods are compared. We also discuss the impact of using different parameter values. This chapter is organized as follows. In Section 6.2, we introduce the main concepts for calculating transport properties and the setup used in our study. In Section 6.3, we describe the analytical mode matching method. Next, in Section 6.4, we show and discuss the results of this method. In Section 6.5, we describe the numerical method used, i.e. the recursive GF method is described. In Section 6.6, we describe the numerical results of the recursive GF approach and compare them with the results of the mode matching method.

6.2 Theoretical framework of transport

6.2.1 Sketch of setup

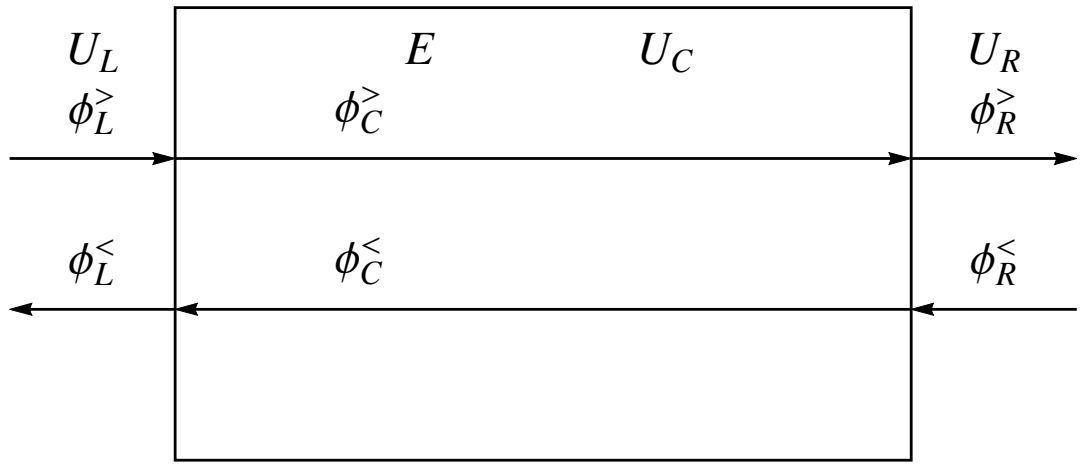

Figure 6.1: Sketch of the transport setup. The black arrow represents the propagating modes of the wave function.

In this section, we describe the conceptual setup used in later calculations. A

sketch of the setup used in our study is shown in Fig. 6.1. The setup models a two-probe conductance measurement with a central conductor (a graphene ribbon) sandwiched between two leads. Here, U_L, U_C and U_R are the gate voltages applied to the left lead, central conductor and right lead, respectively, and E is the incident electron energy. In the left lead, $\phi_L^>$ and $\phi_L^<$ are the rightwards incident wave and leftwards reflected wave, respectively. On the right-hand side, $\phi_R^>$ and $\phi_R^<$ are the rightwards outgoing wave and leftwards incident wave, respectively. The waves in the conductor are denoted by ϕ_C.

6.2.2 Landauer-Büttiker formalism

The fundamental equation describing the transport properties of mesoscopic systems is the Landauer-Büttiker (LB) formula. A further discussion of electronic transport in mesoscopic systems can be found in Appendix. J.1 LB formula transforms the transmission problem into a scattering problem [117] as follows:

$$I = \frac{2e^2}{h}\frac{\mu_R - \mu_L}{e}\bar{T}. \tag{6.1}$$

Here, I is the current, $\mu_{L/R}$ is the chemical potential, the left-right transmission probability (flux), $\bar{T} = \sum_{n,m} |s_{nm}|^2$, s_{nm} is the element of scattering matrix $S = [s_{nm}]$ and n/m is the index of the transverse mode of the wave function [133]. The LB formula is the mesoscopic version of Ohm's rule, $I = U/\mathcal{R}$, where $\mathcal{R}$ is the macroscopic resistance, and $1/\mathcal{R}$ can be considered as a generalization of different scattering channels. A further discussion about scattering matrix can be found in Appendix J.3.

Thus, the Landau conductance and conductivity are

$$G = g\frac{e^2}{h}\bar{T}, \quad \sigma = \frac{L}{W}G. \tag{6.2}$$

Here, g is degeneracy, for graphene it is the product of spin and valley degeneracy, i.e. 4. The expression of the other transport properties can be found in

Appendix J.2.

6.3 Mode matching method

6.3.1 Theoretical introduction

The basis of the mode matching method is to match the incident wave to the outgoing waves at each interface. This method can be used to calculate the transmission coefficients and also other transport properties. A further discussion can be found in Appendix J.4.

At the interface between the left lead and conductor, the matching equation is

$$\begin{pmatrix} \phi^{>}_{L_1} & \phi^{>}_{L_2} & \phi^{<}_{L_1} & \phi^{<}_{L_2} \end{pmatrix} \begin{pmatrix} 1 \\ 0 \\ r_{11} \\ r_{12} \end{pmatrix} = \begin{pmatrix} \phi^{>}_{C1} & \phi^{>}_{C2} & \phi^{<}_{C1} & \phi^{<}_{C2} \end{pmatrix} \begin{pmatrix} t_{11} \\ t_{12} \\ 0 \\ 0 \end{pmatrix}. \quad (6.3)$$

Here, transmission coefficients t_{11} and t_{12} and reflection coefficients r_{11} and r_{12} construct the t-matrix and the r-matrix, respectively, i.e.

$$t = \begin{pmatrix} t_{11} & t_{12} \\ t_{21} & t_{22} \end{pmatrix}, \quad r = \begin{pmatrix} r_{11} & r_{12} \\ r_{21} & r_{22} \end{pmatrix}. \quad (6.4)$$

Note that "1" represents the unit incident wave amplitude. We also consider mode matching at the right interface and the phase factor e^{ikL} acquired by each wave while propagating within the conductor.

6.3.2 Wave function of BLG at zero energy

In this section, we calculate the minimum conductivity σ_m of multilayer graphene of finite size at zero temperature, zero energy, zero external field and zero impurity, which is a well-defined system [184].

We first need to find the wave functions for both conductor and leads. For the former, Eq. (2.22) can be solved at $U_C = E = 0$ in the absence of γ_3 and γ_4 from

$$\begin{aligned} v\hat{\pi}^\dagger B1 = 0, \\ v\hat{\pi}A1 + \gamma_1 A2 = 0, \\ \gamma_1 B1 + v\hat{\pi}^\dagger B2 = 0, \\ v\hat{\pi}A2 = 0. \end{aligned} \tag{6.5}$$

These equations separate, so exact analytical solutions for the $E = 0$ wave function are (not normalized) calculated as [2]

$$\chi_1 = \begin{pmatrix} 0 \\ 0 \\ 0 \\ 1 \end{pmatrix}, \chi_2 = \begin{pmatrix} 0 \\ 1 \\ 0 \\ \frac{x}{l_1} \end{pmatrix}, \chi_3 = \begin{pmatrix} 1 \\ 0 \\ 0 \\ 0 \end{pmatrix}, \chi_4 = \begin{pmatrix} -\frac{x}{l_1} \\ 0 \\ 1 \\ 0 \end{pmatrix}. \tag{6.6}$$

Here, $l_1 = v/\gamma_1$ is the characteristic length and x represents the coordinate. We observe that the peculiar form of the wave functions depend on x, which means that in the process of propagation the electron density shifts from the dimer to the non-dimer site. Since the corresponding dispersion relation related to the dimer site is at higher energy, it can only have a virtual state at zero energy. In the leads, the gate voltage and the Fermi level should be large enough to provide a sufficient number of transverse modes to guarantee that a reduction in conductivity is not due to the leads. For this reason, we can solve the equation at E=∞ to guarantee that the leads act as a source. In this case, the wave functions are (not normalized) calculated as [3]

[2] In the solving process, one will encounter equation $\hat{\pi}^2 A1 = 0$. This equation can be solved by an ansatz $\phi = xe^{ik_x x}e^{ik_y y}$.

[3] This set of wave function can be derived by solving Eq. (2.22) in the absence of v_3 and v_4. The four eigen energies can be expressed as: $E_{a_1,a_2} = (a_1\gamma_1 + a_2\sqrt{4v^2p^2 + \gamma_1^2})/2$, and four corresponding eigen functions are: $\psi_{a_1,a_2} = \big(-a_1(p_x + ip_y)^2/p^2, -ia_1a_2E_{a_1,a_2}(p_x + ip_y)/(vp^2), -ia_2E_{a_1,a_2}(p_x + ip_y)/(vp^2), 1\big)$. In the ex-

$$\tau_1 = \begin{pmatrix} -i \\ 1 \\ 0 \\ 0 \end{pmatrix}, \tau_2 = \begin{pmatrix} 0 \\ 0 \\ -i \\ 1 \end{pmatrix}, \tau_3 = \begin{pmatrix} i \\ 1 \\ 0 \\ 0 \end{pmatrix}, \tau_4 = \begin{pmatrix} 0 \\ 0 \\ i \\ 1 \end{pmatrix}. \tag{6.7}$$

In this situation, infinite energy overwhelms the interlayer hopping effect, therefore, the layers are essentially separate.

6.3.3 Minimum conductivity contributed by evanescent modes

As shown in Eq. (2.26), at zero energy, there is no non-zero real solution for the dispersion relation of BLG, i.e., propagating modes are prohibited in this region, there is only evanescent modes [4] . For a wide and narrow conductor ($W \gg L$) in which W is the width of the conductor, there are many evanescent modes that contribute appreciably to the conductance. This is somewhat counter-intuitive, because an evanescent mode should only contribute towards transport over a small length before vanishing. In an undoped clean graphene sheet at zero energy, all modes are evanescent, and σ_m is dominated by transport due to evanescent modes [128].

For a wide and short conductor ($W \gg L$), the boundary condition in the y direction is irrelevant, so in the $\gamma_1 \gg \epsilon$ region, the summation of the discretized transverse momentum $k_{y,n} = 2\pi n/W$, $n = 0, \pm 1, \pm 2, \ldots$, determined by periodic boundary condition, can be replaced by an integral over k_y, i.e.

$$\mathrm{tr}[t.t^\dagger] \to \frac{W}{\pi} \int_0^\infty dk_y \sum_{s=\pm} T_s(0, k_y). \tag{6.8}$$

treme of $E \gg \gamma_1, vp_y$, $p^2 \simeq p_x^2$, the wave function can be simplified as $\psi_{a_1,a_2} = (-a_1, -ia_1a_2p_x/|p_x|, -ia_2p_x/|p_x|, 1)$. Here, we take $a_2 = 1$ (conduction band), then the different signs of a_1 and p_x will generate four wave functions.

[4] For a plain wave, $e^{ik_x x}$, if $k_x \in \mathbb{R}$, it will not decay in propagation, so it is called "propagating modes". However, if $k_x \notin \mathbb{R}$, it will decay (or explode) in propagation, so it is called "evanescent modes". A detailed discussion can be found in Appendix. J.5.

Then, the conductance can be calculated from the Landauer-Büttiker formula, i.e. Eq. (J.10).

6.4 Numerical results of the mode matching method

6.4.1 Minimum conductivity of BLG at $E = 0$ with γ_1 only

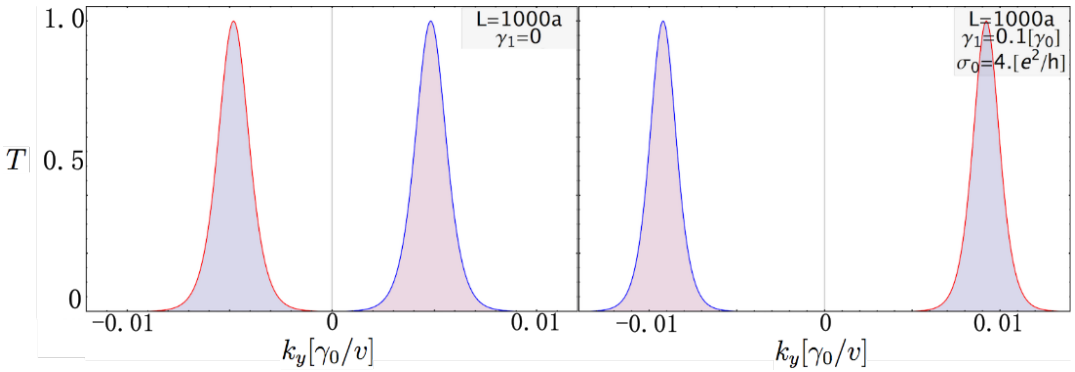

Figure 6.2: Transmission coefficients for BLG at zero energy for a system with $L = 1000a_g$ and $\gamma_3 = 0$; the calculation for $\gamma_1 = 0$ is shown on the left, whereas the calculation for $\gamma_1 \neq 0$ is shown on the right.

First we study the minimum conductivity of BLG, at zero energy in the simplest parametric region, and therefore, we only include γ_0 and γ_1 in this model [29]. The distribution of transmission coefficients along k_y is shown in Fig. 6.2.

The transmission coefficients $T_{\pm}(\epsilon, ky)$ for BLG, in the absence of γ_3, are given by the eigenvalues of $t.t^{\dagger}$, i.e.

$$\begin{aligned} T_{\pm}(\epsilon, k_y) &= \cosh^{-2}(k_y L \pm k_c L), \\ k_c &= L^{-1} \log\left(\frac{L}{2l_1} + \sqrt{1 + \frac{L^2}{4l_1^2}}\right), \end{aligned} \tag{6.9}$$

Here, the characteristic length is $l_1 = v/\gamma_1$. $\pm k_c$ is the location of the peak of the right panel of Fig. 6.2. The value of peak is unit. Then, from Eq. (J.10) and Eq. (6.8), the minimum conductivity of the simplest BLG model [29] is

$$\sigma_m = 2\sigma_0, \quad \sigma_0 = \frac{g_s g_v}{\pi}\frac{e^2}{h}. \tag{6.10}$$

This is two times the minimum conductivity of SLG [7, 135]. Note that γ_1 by itself does not influence the transport properties of BLG, but shifts the distribution of transmission coefficients along the k_y axes.

6.4.2 Minimum conductivity of BLG at $E = 0$, with γ_3 only

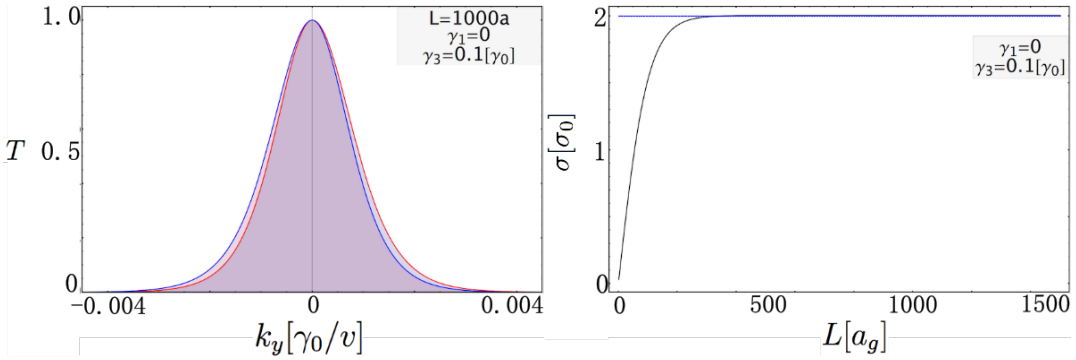

Figure 6.3: Transport properties of BLG at zero energy for $\gamma_3 = 0.1\gamma_0$ and $\gamma_1 = 0$. In the left plot, the horizontal axis k_y is in unit of γ_0/v and vertical axis represents transmission coefficients T. The length of the example setup is $L = 1000a_g$. The blue horizontal line is reference conductivity $\sigma_m = 2\sigma_0$.

For completeness, we also calculated the transmission probability of BLG with $\gamma_3 = 0.1\gamma_0$ and $\gamma_1 = 0$, obtaining the results shown in Fig. 6.3. As shown in Fig. 6.3, the existence of γ_3 changes the minimum conductivity to be a function of system length. If the length of system is too short, the minimum conductivity can even be zero, which is counter-intuitive because the shorter the length of system, the easier it is to penetrate for evanescent modes. When system length $L > 200a_g$, we have $\sigma_{E=0} \simeq 2.005\sigma_0$, i.e. two times the minimum conductivity obtained for the simplest BLG model in the previous subsection.

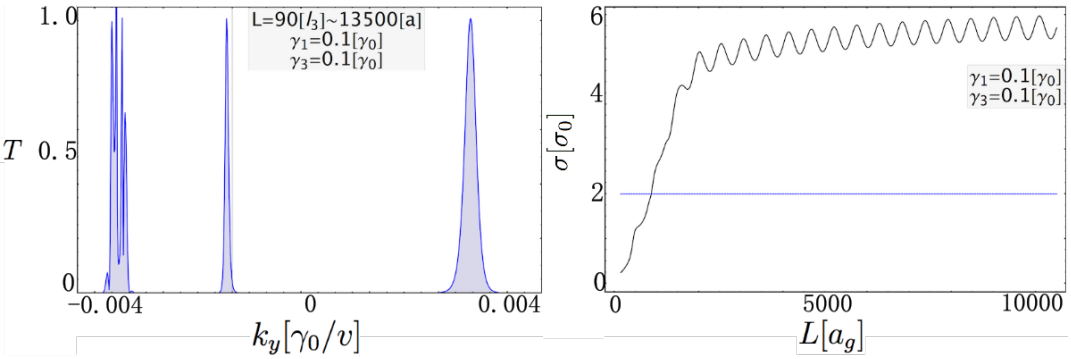

Figure 6.4: Transport properties of BLG for $E = 0$ and $\gamma_1 = \gamma_3 = \gamma_0/10$. The left plot shows the probability distribution as a function of k_y for $L = 13500a_g = 90l_3$. The right plot shows σ_m as a function of L. The blue horizontal line is reference conductivity $\sigma_m = 2\sigma_0$.

6.4.3 Minimum conductivity of BLG at $E = 0$ with γ_3 and γ_1

The eigen wave functions of Eq. (2.22) when $\gamma_4 = 0$ and $E = 0$ are

$$\chi_1 = \begin{pmatrix} 1 \\ 0 \\ \beta_p \\ 0 \end{pmatrix}, \chi_2 = \begin{pmatrix} 1 \\ 0 \\ \beta_n \\ 0 \end{pmatrix}, \chi_3 = \begin{pmatrix} 0 \\ \beta_p \\ 0 \\ 1 \end{pmatrix}, \chi_4 = \begin{pmatrix} 0 \\ \beta_n \\ 0 \\ 1 \end{pmatrix}, \tag{6.11}$$

Here, $\beta_p = (1+\rho)l_1/2l_3$, $\beta_n = (1-\rho)l_1/2l_3$ and $\rho = \sqrt{1+8k_y l_3}$. An analytical expression we calculated for the transmission probability for BLG with $\gamma_1 = \gamma_0/10$ and $\gamma_3 = \gamma_0/10$ is

$$T_{\pm}(\epsilon, k_y) \tag{6.12}$$
$$= \frac{\lambda^2\rho^2\left(\lambda^2\cosh(\alpha_t)(\rho^2\cosh^2(\alpha_\rho)+\sinh^2(\alpha_\rho))+\sinh^2(\alpha_\rho)(\cosh(2\alpha_\rho)(\tau^4+1)+2\tau^2)\right)}{(\cosh(2\alpha_\rho)(\tau^2-1)^2+\lambda^2\rho^2\cosh(2\alpha_t)-(\tau^2+1)^2+\lambda^2)^2}.$$

Here, $\alpha_t = -Lk_y - L/2l_3$, $\alpha_\rho = -L\rho/2l_3$, $l_3 = l_1 v/v_3 \sim 150a_g$, $\lambda = l_1/l_3$ and $\tau^2 = \lambda^2(1-\rho^2)/2$. From the above, the transport probability depends on variables L, k_y and l_3, the latter being the characteristic length given by γ_3. The left panel of Fig. 6.4 shows transmission probability as a function of k_y.

The behaviour of minimum conductivity σ_m as a function of L is also shown in Fig. 6.4. In the region of $L < l_3 = 150a_g$, the effect of γ_3 lowers the value of σ_m, even to zero. With an increase of L, σ_m increases quickly, and at $L \simeq 2000a_g$, it starts to oscillate. This oscillatory behaviour is due to the resonance of evanescent modes at certain lengths. Once $L \simeq 10l_3$, conductivity becomes almost stable at $5\sigma_0$; beyond this value, the increase of σ_m slows down, gradually approaching the expected analytical value of $6\sigma_0$ [30].

From Eq. (6.12), the ratio between the system length L and the characteristic length l_3 changes the resonance conditions for the evanescent modes, therefore revealing the manifestation of γ_3 in the transport properties of BLG. The smaller the value of γ_3, the larger length L is required to reveal the influence of γ_3.

6.4.4 Minimum conductivity of TLG-ABC at $E = 0$

To study the minimum conductivity of TLG-ABC at zero energy, zero external field and zero temperature, we investigate the effect of each of the parameters from most important to least important.

The simplest model for TLG-ABC only includes intralayer hopping γ_0 and vertical interlayer hopping γ_1, which together capture the features of the cubic dispersion of the TLG-ABC band structure in Eq. (2.29). The next parameter in order of importance that we consider is γ_2. As discussed in the Section 2.5.1 and expressed in Eq. (2.29), γ_2 induces the trigonal warping effect in TLG-ABC and therefore causes significant modifications in the band structure [19].

Finally, skewed hopping γ_3 is considered as it has a weaker impact on the band structure. The other skewed interlayer hopping γ_4 is omitted in this calculation, as it is relatively small compared to the other parameters and only induces an electron-hole asymmetry in the band structure.

6.4.5 Minimum conductivity of TLG-ABC at $E = 0$ with γ_1 and γ_2

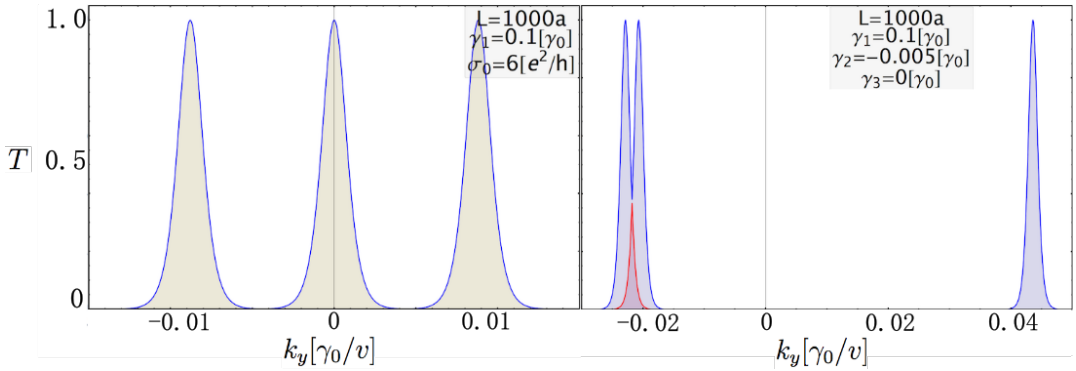

Figure 6.5: Regarding the transmission probability for TLG-ABC at zero energy, for the result in the left plot, we only considered the effect of γ_1, i.e. $\gamma_3 = 0$, whereas for the right plot includes the effect of $\gamma_2 = -0.005\gamma_0$. Both situations yield $\sigma_m = 3\sigma_0$. In both the subplots, the horizontal axis k_y is in units of γ_0/v and the vertical axis shows the transmission amplitude T. The length of the setup is $L = 1000a_g$.

If only γ_1 is considered in TLG-ABC, then $\sigma_m = 3\sigma_0$, which is the same as the conductivity of three separate layers of SLG. As shown in Fig. 6.5, the transmission coefficients in this case are

$$T_\alpha(\epsilon, k_y) = \cosh^{-2}(k_y L + \alpha k_c L), \quad \alpha \in [-1, 0, 1]. \tag{6.13}$$

The eigenfunctions for $\gamma_2 = -0.005\gamma_0$ and $\gamma_1 = 0.1\gamma_0$ are

$$\chi_1 = \begin{pmatrix} 0 \\ \beta_1 \\ 0 \\ \alpha_1 \\ 0 \\ 1 \end{pmatrix}, \chi_2 = \begin{pmatrix} 0 \\ \beta_2 \\ 0 \\ \alpha_2 \\ 0 \\ 1 \end{pmatrix}, \chi_3 = \begin{pmatrix} 0 \\ \beta_3 \\ 0 \\ \alpha_3 \\ 0 \\ 1 \end{pmatrix}, \chi_4 = \begin{pmatrix} 1 \\ 0 \\ \alpha_1 \\ 0 \\ \beta_1 \\ 0 \end{pmatrix}, \chi_5 = \begin{pmatrix} 1 \\ 0 \\ \alpha_2 \\ 0 \\ \beta_2 \\ 0 \end{pmatrix}, \chi_6 = \begin{pmatrix} 1 \\ 0 \\ \alpha_3 \\ 0 \\ \beta_3 \\ 0 \end{pmatrix}, \tag{6.14}$$

Here, $\alpha_m = |\gamma_2/\gamma_1|^{2/3}(i\eta_m)^{-1}$, $\beta_m = |\gamma_2/\gamma_1|^{1/3}(i\eta_m)$, and $\eta_m = e^{i\pi(2m-1)/3}$. Although the influence of γ_2 on the band structure of TLG-ABC is much stronger

than that of γ_3 in BLG, from Eq. (2.29), we note that the presence of γ_2 does not affect σ_m.

6.4.6 Minimum conductivity of TLG-ABC at $E = 0$, with γ_0, γ_1 and γ_3

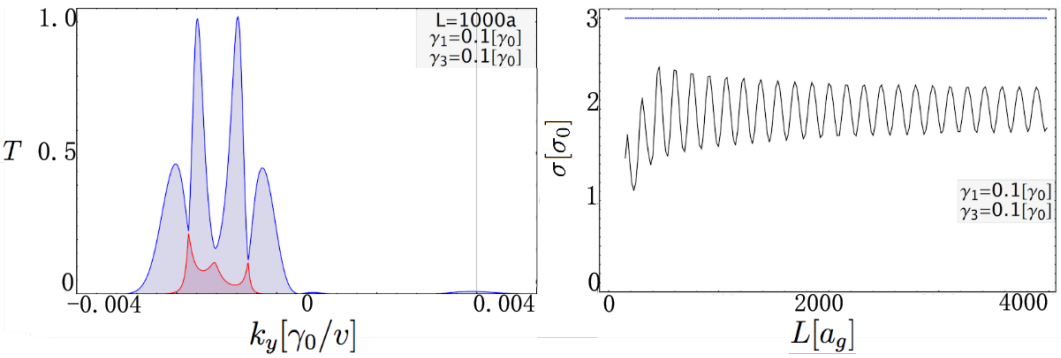

Figure 6.6: Regarding the transport properties of TLG-ABC for $E = 0$, $\gamma_1 = \gamma_3 = \gamma_0/10$ and $\gamma_2 = 0$, the left plot shows the distribution of the transmission coefficients as a function of k_y for $L = 1000a_g = 6.6l_3$. In the right plot, σ_m is calculated as a function of L. The blue horizontal line is reference conductivity $\sigma_m = 3\sigma_0$.

To study the interplay between γ_1 and γ_3 considering the transport properties of TLG-ABC, we first set γ_2 to zero. As shown in Fig. 6.6, γ_3 reduces the value of minimum conductivity σ_m in TLG-ABC, after which σ_m stabilizes at $\sigma_m \simeq 2.125\sigma_0$.

6.4.7 Minimum conductivity of TLG-ABC at $E = 0$, with γ_0, γ_1, γ_2 and γ_3

As shown in Fig. 6.7, the interplay between γ_2 and γ_3 slightly increases σ_m to $3.25\sigma_0$, which is slightly higher than that of three separate SLG, i.e. $3\sigma_0$. Note that this is still much lower than the minimum conductivity of BLG which is $6\sigma_0$. We observe that the oscillations shown in Fig. 6.6 are much weaker than those of Fig. 6.7 because the presence of γ_2 increases the distance between the peaks of the evanescent modes, therefore causing the resonance between different evanescent modes to be much weaker.

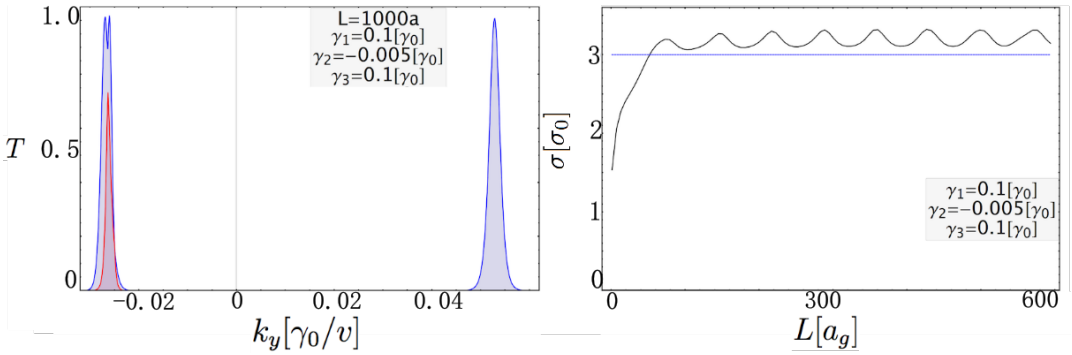

Figure 6.7: Regarding the transport properties of TLG-ABC in the case of incident energy $E = 0$ and both $\gamma_1 = \gamma_3 = \gamma_0/10$ and $\gamma_2 = -0.005\gamma_0$, the left plot shows the distribution of transmission coefficients as a function of k_y, for conductor length $L = 1000a_g = 6.6l_3$. In the right plot, σ_m is calculated through L. The blue horizontal line is reference conductivity $\sigma_m = 3\sigma_0$.

6.4.8 Conclusions of the mode matching calculation

In this section, we calculated the minimum conductivity σ_m of multilayer graphene, BLG and TLG-ABC. We found that the role each hopping parameters plays is not as intuitive as in the band structures. Our analytical evaluation suggests that vertical hopping such as γ_1 and γ_2, does not influence σ_m. In addition, skewed hopping γ_3 changes σ_m to be a function of length L with a behaviour approximating a limit. Furthermore, given the interplay between γ_3 and γ_1, γ_2 significantly modifies σ_m in a non-monotonical manner. In BLG, the interplay between γ_3 and γ_1 increases σ_m. However, in TLG-ABC, given the interplay between γ_3 and γ_1, γ_2 decreases σ_m below the value obtained using BLG. Moreover, the numerical values of γ_1 and γ_2 do not affect the minimum conductivity. Conversely, the exact value of γ_3 affects the minimum conductivity, as shown in Eq. (6.12), which depends on the characteristic length l_3. Finally, the mode matching method also induces a dependency on length L. The completed manifestation of the effect of γ_3 can only be observed for $L \gg l_3$, such as $L \simeq 90l_3 \simeq 2\mu m$.

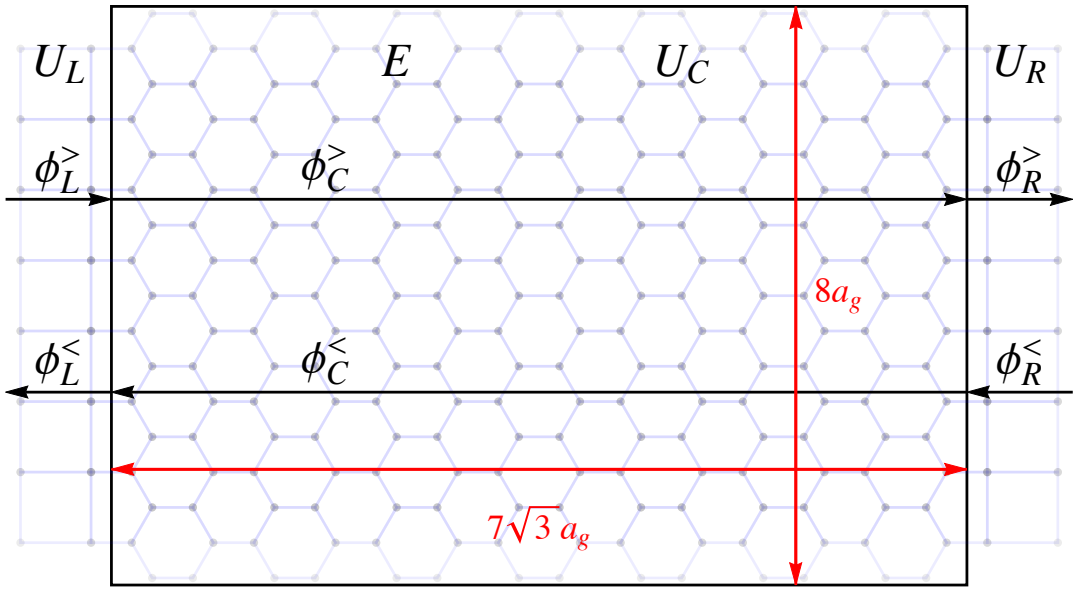

Figure 6.8: Sketch of the transport setup of Green function Calculation. The central conductor has a hexagonal lattice to represent graphene and is sandwiched between square lattices (representing normal metal) on the left and right. The edges of the graphene nano-ribbon are armchair style. The size of this setup is $L = 7\sqrt{3}a_g$ and $W = 8a_g$, (i.e. 7 hexagons long and 8 hexagons wide). The black arrow represents the propagating modes of the wave function, and the red arrows define the total length and width of the ribbon.

6.5 Theory of the recursive GF

6.5.1 Sketch of setup

Because we need to switch from continuous model describing infinite-size sample to discretized model describing finite-size sample, so here we need to redefine our conceptual setup. A sketch of the setup used in Green function calculation study is shown in Fig. 6.8. The idea of this setup is similar to that of Fig. 6.1: two-probe, conductance measurement and varying gate voltage. However, there are some details need to be emphasized. In Green function study, the leads adopted are either normal metal (i.e. square lattice), or graphene (i.e. hexagonal lattice). The typical size of the setup is $L = 30\sqrt{3}a_g$ and $W = 150a_g$, (i.e. 30 hexagons long and 150 hexagons wide), with armchair [116] top and bottom edges [5] . All

[5]The reason that we do not calculate the nano-ribbon with a zigzag edge is the electron in it will have a non-binding edge state, which features very different electronic, magnetic as well as chemical properties. We are not interested in these weird behavior caused by edge state, we would like to understand the system as a whole. So in the study of a finite-size setup, we will

Green function calculations reported here will model systems of this size unless otherwise stated.

6.5.2 Definition of Green function

Following [117], Green function (GF) is a general name for functions with the specific mathematical structure

$$G = (E - \hat{H})^{-1}, \tag{6.15}$$

which are usually used for describing the distant response to a source. The GF can be expanded in a basis of eigenfunctions as [6]

$$G(\vec{r}, \vec{r}') = \sum_{\alpha} \frac{\psi_\alpha(\vec{r})\,\psi_\alpha^*(\vec{r}')}{E - \epsilon_\alpha + i\eta}. \tag{6.16}$$

Here ϵ_α is the eigen energy of state α, and η is an infinitesimal value used to avoid a singularity. The alternative form of GF, i.e. Eq. (6.16) is more suitable for a system with solvable wave functions.

6.5.3 Tight binding model and GF

Within the tight-binding model, since the wave functions of the electrons can be described by the superposition of the atomic orbitals, the Hamiltonian of the system can be expressed as a matrix in which diagonal elements are the on-site energies of the atomic orbitals, and off-diagonal elements describe the interactions

keep our study in armchair-edge. If we have a infinite-width setup, we can use continuous model and we will not observe edge state, which is the reason we did not emphasize this point in the calculation of mode matching method.

[6] This expression can be simply obtained by expanding GF on the orthogonal basis of eigen function of Hamiltonian. In Eq. (6.16), there is a "$+i\eta$" in the denominator, which indicates it is 'Retarded" GF. Its counterpart is "Advanced" GF, which features a "$-i\eta$" in the denominator. The origin of the two kinds of GF is that Eq. (6.15) has two solutions. One describes an excitation generating two waves traveling outwards, i.e. distant responses chronologically happen after a excitation, which is named by retarded GF. Oppositely, the other one describes two waves traveling inwards and colliding to generate an excitation, i.e. distant responses chronologically happen before a excitation, which is named by advanced GF. In the following discussion of this thesis, we will only discuss retarded GF unless stated otherwise.

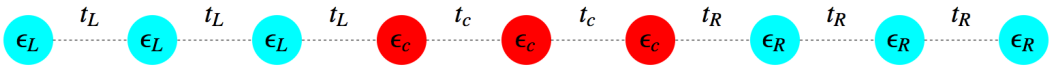

Figure 6.9: Diagram of a one-dimensional chain of atoms sandwiched between two one-dimensional leads. The red/blue dots represents the atomic sites of conductor/leads. The on-site energies are denoted as $\epsilon_c/\epsilon_L/\epsilon_R$ with the dashed lines between the dots representing the hopping between different sites, denoted as $t_c/t_L/t_R$, respectively.

between different atomic sites.

As an example, the discretized Hamiltonian of a one-dimensional wire connected by two different one-dimensional leads, shown in Fig. 6.9, is

$$\left(\begin{array}{cc|ccc|cc} \epsilon_L & t_L & 0 & 0 & 0 & 0 & 0 \\ t_L & \epsilon_L & t_L & 0 & 0 & 0 & 0 \\ \hline 0 & t_L & \epsilon_c & t_c & 0 & 0 & 0 \\ 0 & 0 & t_c & \epsilon_c & t_c & 0 & 0 \\ 0 & 0 & 0 & t_c & \epsilon_c & t_R & 0 \\ \hline 0 & 0 & 0 & 0 & t_R & \epsilon_R & t_R \\ 0 & 0 & 0 & 0 & 0 & t_R & \epsilon_R \end{array}\right) \rightarrow \left(\begin{array}{ccc} \hat{H}_L & \hat{H}_{Lc} & 0 \\ \hat{H}_{cL} & \hat{H}_c & \hat{H}_{cR} \\ 0 & \hat{H}_{Rc} & \hat{H}_R \end{array}\right).$$

Because only nearest neighbour interactions are allowed, the off-diagonal block (elements) are zero. Therefore, this matrix is able to be block-diagonalized.

6.5.4 Self energy

At the interface between the leads and the conductor, as shown in Fig. 6.8, the GF method can be expressed as (6.15), i.e.

$$\left(\begin{array}{cc} G_L & G_{Lc} \\ G_{cL} & G_c \end{array}\right)\left(\begin{array}{cc} E-\hat{H}_L & -\hat{H}_{Lc} \\ -\hat{H}_{Lc}^{\dagger} & E-\hat{H}_c \end{array}\right)=\left(\begin{array}{cc} I & 0 \\ 0 & I \end{array}\right).$$

Here, G_c and $\hat{H}_c$ are the GF and Hamiltonian of the conductor, respectively, G_L and $\hat{H}_L$ are the GF and Hamiltonian on the left lead, respectively, and G_{Lc}, G_{cL} and $\hat{H}_{Lc}$ are the off-diagonal block of GF and Hamiltonian.

The matrix describing the lead is considered to be semi-infinite, so $\hat{H}_L$ and $\hat{H}_R$ are of infinite order. A common way to treat this infinite dimensional matrix is to describe the influence of a lead on the conductor using an effective term called the self energy (SE), denoted by Σ, with

$$\begin{aligned} G_c &= (E - \hat{H}_c - \Sigma_L)^{-1}, \\ \Sigma_L &= \hat{H}_{Lc}^{\dagger} g_L \hat{H}_{Lc}, \\ g_L &= [E - \hat{H}_L]^{-1}. \end{aligned} \tag{6.17}$$

For general types of crystal lattice, the self energy is difficult to calculate [120, 122–127]. In Appendix L, we present several methods for calculating the self energy.

As an example, the self energy of a semi infinite normal metal (i.e. a square lattice) can be calculated using Eq. (6.16) together with the fact that the eigenfunctions of square lattices can be expressed in the form of standing waves $\sin(ak)$, where $\boldsymbol{k}$ is the wave vector. The self energy of the left lead obtained with this method is $\Sigma = -e^{ika} t_L/a$ [117], where t_L is the hopping parameter between the nearest-neighbour atoms in the left lead.

6.5.5 Fisher-Lee relation and transmission probability

The Fisher-Lee relation [118] is the bridge that relates the response at a certain position to inputs at a different position in the ribbon by using various scattering matrix components. An element of this relation can be expressed as follows [7]:

$$s_{nm} = -\delta_{nm} + i\sqrt{v_n v_m} \sum_{q}^{W_R} \sum_{p}^{W_L} \chi_n(q)\, G_{RL}(q;p)\, \chi_m(p)\,. \tag{6.18}$$

Here $q \in W_R$ and $p \in W_L$ are the indices of atomic sites in real space, $W_{L/R}$ is the width, (i.e. the total amount of sites), n and m are mode indices, G_{qp} is the

[7] This can be simply understood as transforming the distant response in real space into the response in momentum space, and modifying obtained "probability amplitude" to "current amplitude". In other words, the transmission coefficients s_{nm} is obtained by using the eigenfunction of different modes χ_n to extract corresponding probability amplitude from GF, then modulate it with velocity. Another way of deriving Fisher-Lee relation can be found in Appendix L.1.

(retarded) GF relating sites q and p, $v_{n/m}$ and $\chi_{n/m}$ are the the velocity and the transverse wave function of mode n/m.

Furthermore, we can use this information to obtain the total transmission probability [8]

$$\bar{T}_{RL} = \mathrm{tr}\left[\Gamma_R G \Gamma_L G^\dagger\right], \quad \Gamma_{L/R} = i\left[\Sigma_{L/R} - \Sigma_{L/R}^\dagger\right]. \tag{6.19}$$

For a graphene conductor, evanescent modes must be included into the self energy calculation, as they may penetrate into the finite-size conductor and contribute towards transport. However, in the semi-infinite leads, the evanescent cannot penetrate the infinite-size lead, this manifests as these modes have zero group velocity, so the corresponding elements of the transmission matrix vanish [119].

6.5.6 Generalization of the GF method

Below is a brief procedure for applying the GF method to a transport problem. A further discussion can be found in Appendix ch:GFacceleration.

(1) Discretize the Hamiltonian for both the leads as well as the conductor.

(2) Based on the Hamiltonian of the lead, obtain the eigenfunction, all modes (i.e. propagating and evanescent modes), the dispersion relation, the velocity and the self energy of the lead.

(3) With the self energy describing the effect of the leads on the conductor, the proper method of dividing the system into slices, and the proper auxiliary technique (i.e. recursive method or matrix decimation), we can invert the big matrix and obtain the necessary blocks of the GF.

(4) From the necessary blocks, e.g. G_{RL} and so on, calculate the S-matrix, and all the other physical quantities.

The most complicated step in the above GF method is the self energy calculation, the central conductor region can be easily simulated by a Hamiltonian matrix

[8] This expression can be simply obtained by deriving the square of Fisher-Lee relation.

regardless of how complicated its structure is. The self energy calculation involves finding the eigenfunctions of the lead (especially the relative phase difference between different sites in one cell), the velocity, (which might be directed opposite to the momentum), and the contour integral (if the eigenfunction expansion method is used to obtain the self energy).

6.6 Numerical results of the GF

As the multilayer graphene conductor is connected to the leads, the transport properties of the system depend on the nature of the leads. However, it is imperative to distinguish physical effects of the conductor from those of the lead and to minimize any particular effects of the lead. To this end, two different types of leads are chosen and compared. The first is a normal metal, (i.e. a square lattice), which is the simpler of the two. The second is the same material as the conductor itself. The gate voltage is fixed such that the lead has a large number of modes and the robustness of electronic transport properties at these points is confirmed. Note that the details of how different lattices are connected at the interface have no significant influence on the transport properties [129]. In the following subsections, we present various transport results obtained for multilayer graphene for different parametric regions.

6.6.1 Transport properties of the BLG conductor

Investigation of lead properties

As shown in Fig. 6.10, there is a deep cusp in the centre of the curve for the BLG lead, but there is no counterpart in the curve corresponding normal metal leads. Zero conductivity at $U_L = 0$ arises from the presence of the DP of graphene, in which both U_L and U_C are zero. The central conductor together with the leads form an infinitely long and homogeneous system in which the evanescent modes do not contribute towards transport.

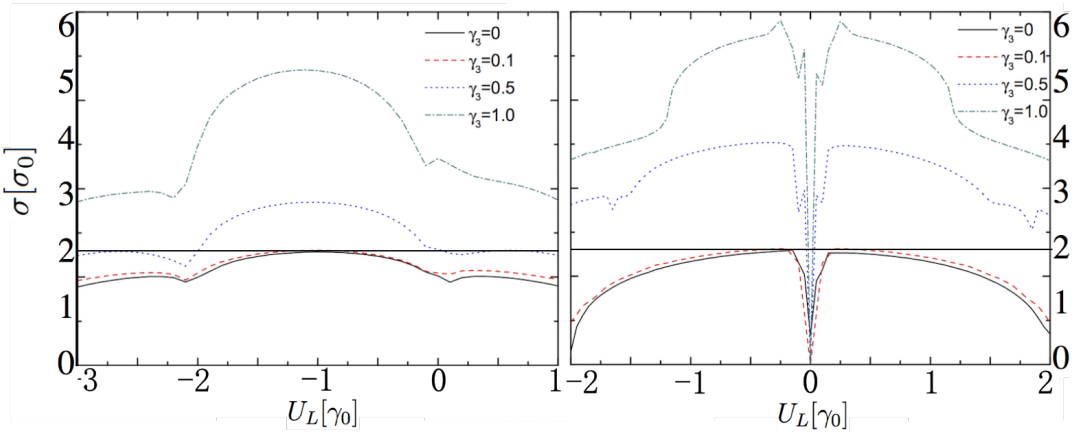

Figure 6.10: Conductivity of BLG as a function of gate voltage on lead U_L with $U_C = E = 0$. The left panel shows results for the normal metal (i.e. a square lattice) leads, whereas the right panel shows results for BLG leads (hexagonal lattice). The different lines represent different values of γ_3. The horizontal line is reference conductivity $\sigma_m = 2\sigma_0$.

In the case of $U_L = -\gamma_0$ for square lattice leads or $U_L = 0.24\gamma_0$ for hexagonal lattice leads, the lead will have a large number of modes and minimum resistance. In the latter calculations of this thesis, the gate voltages on the leads are fixed to the above two values. To keep the matrix inversion stable, a very small complex value is added to the energy input, which is the source of the asymmetry in the figure.

Initially, for slowly increasing γ_3, σ increases slowly, but at large values of γ_3, σ drastically changes because the characteristic length of γ_3, i.e. $l_3 = v\gamma_0/(\gamma_1\gamma_3)$, decreases when γ_3 increases, as shown in Fig. 6.4. When L is comparable to l_3, the effect of γ_3 gradually emerges.

Investigating the robustness of the central conductor

In this subsection, we investigate the robustness of the transport properties of the central conductor in the parametric region in which the leads have minimum resistance. As discussed above, minimum resistance in the leads is achieved for $U_L = -\gamma_0$ for the square lattice leads and $U_L = 0.24\gamma_0$ for graphene leads. Our results, depicted in Fig. 6.11 for various values of γ_3 (i.e. $\gamma_3 = 0$, $0.1\gamma_0$, $0.3\gamma_0$ and $0.5\gamma_0$), show little change in the conductivity with increasing γ_3 values. These

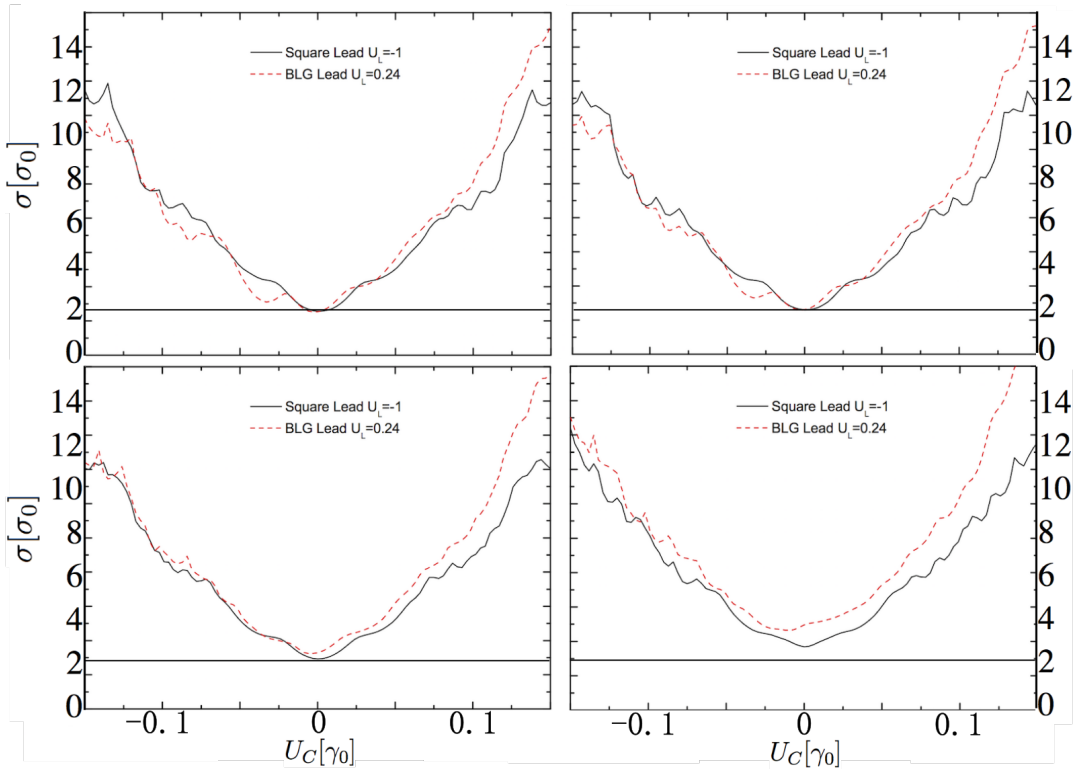

Figure 6.11: Conductivity of the BLG conductor as a function of the gate voltage in the leads U_c. The four plots are for $\gamma_3 = 0$, $\gamma_3 = 0.1\gamma_0$, $\gamma_3 = 0.3\gamma_0$ and $\gamma_3 = 0.5\gamma_0$, respectively. The gate voltages of the leads are $U_L = -\gamma_0$ and $U_L = 0.24\gamma_0$ for the square lattice (i.e. black solid line) and hexagonal lattice (i.e. red dashed line) respectively. The incident energy is $E = 0$. The horizontal line is reference conductivity $\sigma_m = 2\sigma_0$.

observations confirm that for small values of γ_3, the transport properties of the device are robust and uncover the low importance of γ_3 in this parametric region.

Transport properties of the central BLG conductor

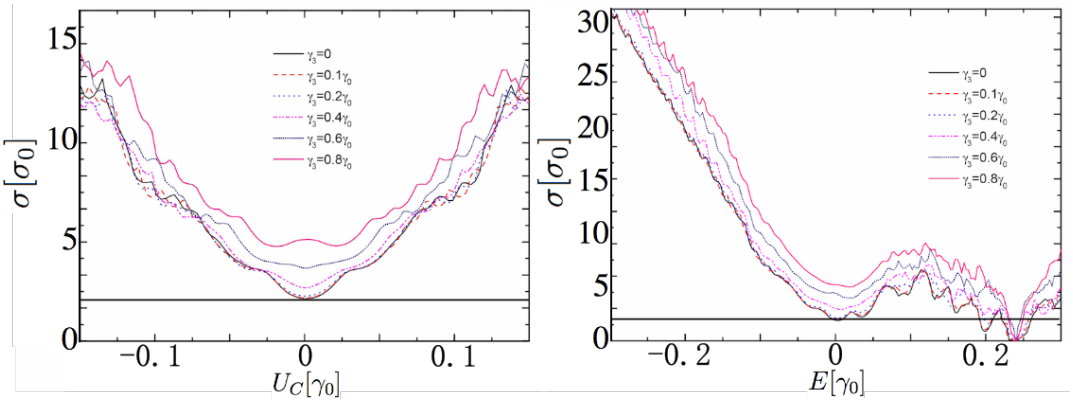

Figure 6.12: Regarding the conductivity of BLG as a function of incident energy, the left plot shows square leads with gate voltage $U_L = -\gamma_0$, whereas the right plot shows for BLG leads with $U_L = 0.24\gamma_0$. Different lines represent results for various values of γ_3. The horizontal line is reference conductivity $\sigma_m = 2\sigma_0$.

By varying overall energy E, the transport properties of the conductor can be studied, as shown in Fig. 6.12. The conductance in the vicinity of $E = 0$, which corresponds to the position of the DP, exhibits a minimum without becoming zero, because in the parametric region, evanescent modes are strong and can penetrate through the central conductor, contributing towards transport. The second local minimum is the conductance that occurs at $E = 0.24\gamma_0$, in which σ falls to almost zero. This feature occurs because at this energy, we are close to the DP in the leads, where the evanescent modes are weak and cannot penetrate through the conductance and do not contribute towards transport.

As shown in Fig. 6.12, conductivity increases with increasing γ_3. Furthermore, the minimum conductivity in the absence of γ_3 confirms the theoretical prediction, i.e. $\sigma_m = 2\sigma_0$. However, the minimum conductivity of BLG with γ_3 effect, i.e., $\sigma_m = 6\sigma_0$, can be only approached by a very high value of $\gamma_3' \simeq 0.8\gamma_0 \gg \gamma_3 = 0.1\gamma_0$. This confirms our theoretical prediction that the interplay between $l_3 = v^2/v_3\gamma_1 \simeq 150a_g$ and length of conductor L determines the minimum conductivity. Once l_3 is comparable with $L = 30\sqrt{3}a_g$, (for $\gamma_3' = 0.8\gamma_0$, $l_3 \simeq 20a_g$) the trigonal warping

effect on transport will be explicit. The completely manifestation of that effect require much longer sample. Additionally, we need $W \gg L$ [128], (here $W/L \simeq 5$) so this is the reason that a $\sigma_m = 6\sigma_0$ is not shown.

Transport properties of the central BLG conductor with biased voltage

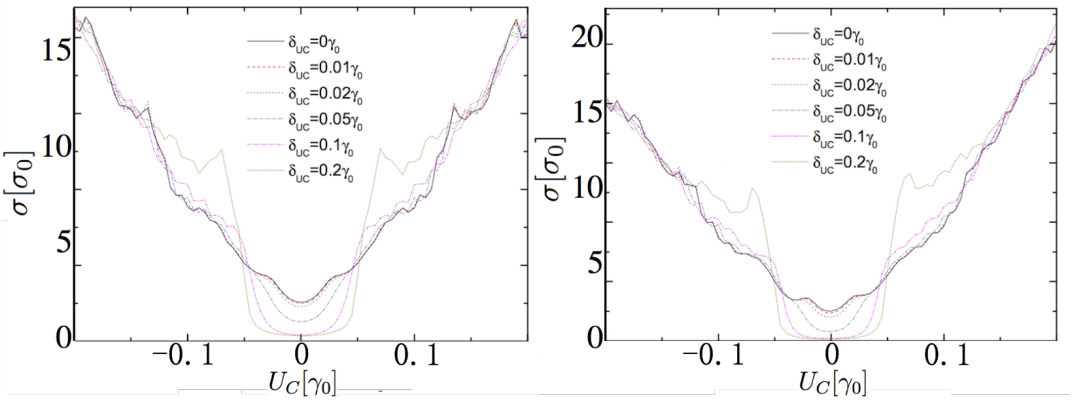

Figure 6.13: The conductivity of BLG as a function of gate voltage on conductor U_C, the left plot represents square leads with gate voltage $U_L = -\gamma_0$, whereas the right plot represents BLG leads with $U_L = 0.24\gamma_0$. Different lines represent results for various values of biased gate voltage δ_{UC}.

The biased voltage is defined as $\delta_{UC} = (U_{top} - U_{bottom})/2$, which opens a gap in the band structure. By applying the biased gate voltage to the conductor, BLG behaves like a semiconductor [69], as shown in Fig. 6.13.

6.6.2 Transport properties of TLG-ABA and TLG-ABC

Influence of different parameters on the conductivity of TLG-ABC and TLG-ABA

Our previous calculation from Section 6.4 suggests that the minimum conductivity σ_m of TLG-ABA and TLG-ABC should be approximately three times that of SLG, but a small constraint to width W can hinder the numerical calculation. The non-linear behaviour of σ_m with respect to variations in γ_3 is because of the oscillations that occur by varying l_3 while maintaining constant length L.

As shown in Fig. 6.16, the effect of γ_2 generally follows the prediction of the mode matching method, i.e. the value of γ_2 does not affect the σ_m.

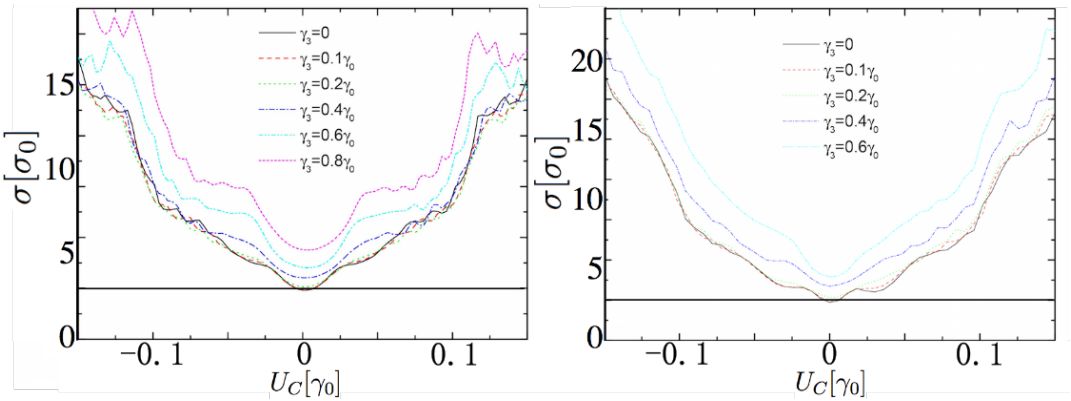

Figure 6.14: The transport properties of TLG-ABC. In the left panel, a TLG-ABC ribbon is sandwiched between square lattice leads, with $U_L = -\gamma_0$ and $U_C = 0$. In the right panel, a TLG-ABC ribbon is sandwiched between TLG-ABC leads with $U_L = 0.5\gamma_0$ and $U_C = 0$. Different lines represents different values of γ_3. The horizontal line is reference conductivity $\sigma_m = 3\sigma_0$.

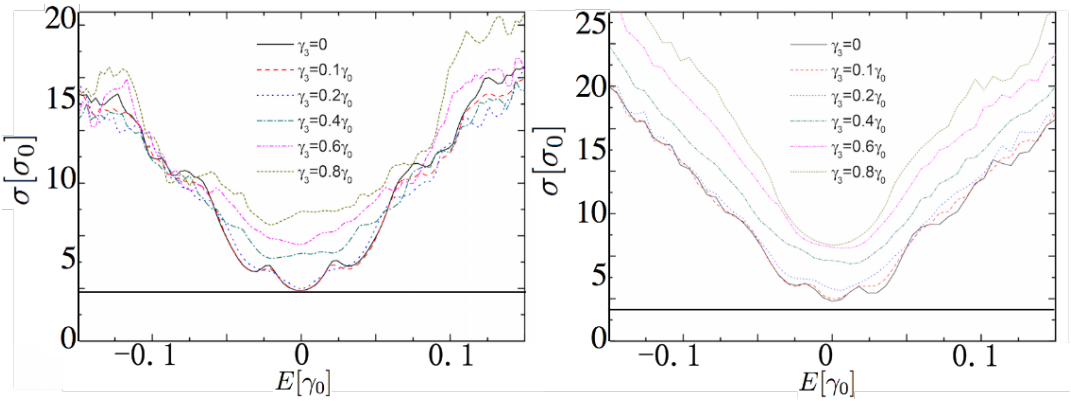

Figure 6.15: Regarding the transport properties of TLG-ABA. In the left panel, a TLG-ABA ribbon is sandwiched between square lattice leads with $U_L = -\gamma_0$ and $U_C = 0$. In the right panel, a TLG-ABA ribbon is sandwiched between TLG-ABA leads with $U_L = 0.5\gamma_0$ and $U_C = 0$. Different lines represents different values of γ_3. The horizontal line is reference conductivity $\sigma_m = 3\sigma_0$.

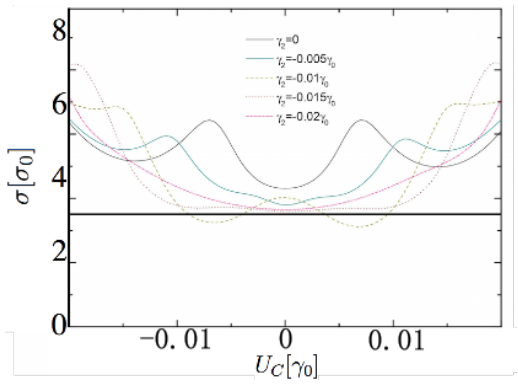

Figure 6.16: Regarding the transport properties of a TLG-ABC ribbon sandwiched between square lattice leads with $U_L = -\gamma_0$, $E = 0$ and $\gamma_3 = 0$. Different lines present different value of γ_2. The horizontal line is reference conductivity $\sigma_m = 3\sigma_0$.

6.6.3 Conclusion of the GF investigation

Our analytical expressions are based on the continuous situation in which the transverse wave vector k_y has infinitely high resolution. However, in the GF calculations, the resolution of k_y is determined by the width of the conductor. This relation suggests that if the width of the system is not large enough, low-energy conductivity will be decreased or may even be zero. Note that the required computing memory for the GF calculation is proportional to the square of the width. In addition, the calculation time is dominated by the matrix inversion, which is proportional to the cube of the matrix dimension. For example, consider an armchair nano-ribbon of BLG, with modest size $L = 30a_g \simeq 73$Å and at least $W = 10L \simeq 730$Å(to guarantee $W \gg L$), which suggests approximately 300 hexagon arranged transversely. The required memory to save each slice is $(300 \times 12)^2 \times 8 \times 2 \simeq 207$MB (i.e. 12 atomic sites for one slice of BLG, 8×2 digits for one complex number).

Therefore, to observe the effect of γ_3, the setup needs to fulfill $W \gg L$ as $L \gg 90l_3 = 13500a_g \simeq 2\mu m$, so we must take $W = 10L_{Min} \simeq 20\mu m$ [128]. In addition to the aforementioned cubic relation of time, this calculation requires approximately $16,000$GB of memory for one block of the calculation (and needs at least four similarly sized blocks to complete the calculation). This computational requirement is the current difficulty in the numerical GF calculation approach.

Nevertheless, to study the electronic transport properties of multilayer graphene, especially in the low-energy region and in the presence of skew hopping parameter γ_3, the GF method is applied. Due to the limitations of memory and time, we did not achieve the condition of $L \gg l_3$, and therefore, our results do not reveal the complicated behaviour discussed in Fig. 6.4, or the analytic predictions in the low-energy region discussed in Ref.[30, 128]. The measurement of minimum conductivity requires very clean sample in zero temperature, zero gate voltage and zero energy, this is not a easy condition. To our knowledge, there have not been any experiments to date that have directly proven the results presented in this chapter.

Chapter 7

Conclusion

This thesis covered the following topics:

(1) We focussed on the butterfly spectrum of moiré perturbed SLG in a perpendicular magnetic field. Beyond the secondary DP of the moiré perturbed graphene, the magnetic spectrum demonstrates a hierarchy of third-order DPs with LL structures. By mapping the size of the gap on the plot of carrier density and magnetic field strength, the fan diagram provides a theoretical analysis comparable with experimental results. Moreover, the inversion asymmetry effect lifted valley degeneracy and exhibited some new filling factors. In addition, magnetic spectra involving different types of parameter sets were systematically studied.

(2) Based on the work of the previous chapter, we then focussed on the magnetic spectrum of moiré perturbed BLG in a perpendicular magnetic field. As the inversion symmetry is broken from the beginning, the magnetic spectra of moiré perturbed BLG shows two very different spectra in the two valleys and also features a non-perturbed zeroth LL. Finally, we focussed on the zeroth and first "fractured LL" in a simple fraction; the simplified 2×2 Hamiltonian can be a basis for further study of the many-body problem around the zero energy of moiré perturbed BLG.

(3) Next, we focussed on the impact of a parallel magnetic field on BLG and TLG-ABC. The band structure of BLG in a parallel magnetic field may acquire different shapes depending on the direction and strength of the applied field. These shapes can be generally classified into three distinct phases based on the number

of DPs and/or extreme points contained in the spectrum. The phase diagram of BLG in parallel magnetic field is similar to that of homogeneously strained BLG. However, the overall effect of the former is much weaker than that of the latter. Next, we investigated the impact of a parallel magnetic field on the band structure of TLG-ABC and found that next-nearest layer hopping γ_2 overwhelms the trigonal warping effect caused by skewed hopping γ_3.

(4) We studied the transport properties of multilayer graphene, by using both a continuous analytical and a discrete numerical model. The analytical calculations of minimum conductivity of BLG and TLG-ABC revealed that the vertical hoppings (i.e. γ_1 and γ_2) did not qualitatively affect the transport properties. However, the skewed hopping (i.e. γ_3) had a sophisticated effect on electronic transmission in multilayer graphene. The study suggested that the conductivity of multilayer graphene depends on the system size in the sense that a complete manifestation of the influence of γ_3 can only be seen with a relatively long sample.

Our numerical simulations, using the recursive GF method, seemed to confirm our analytical results. However, significant restrictions in terms of memory and computational time limited our numerical calculations. Therefore, we were unable to obtain a definitive confirmation of the analytical results.

Appendix A

An introduction to fractal patterns

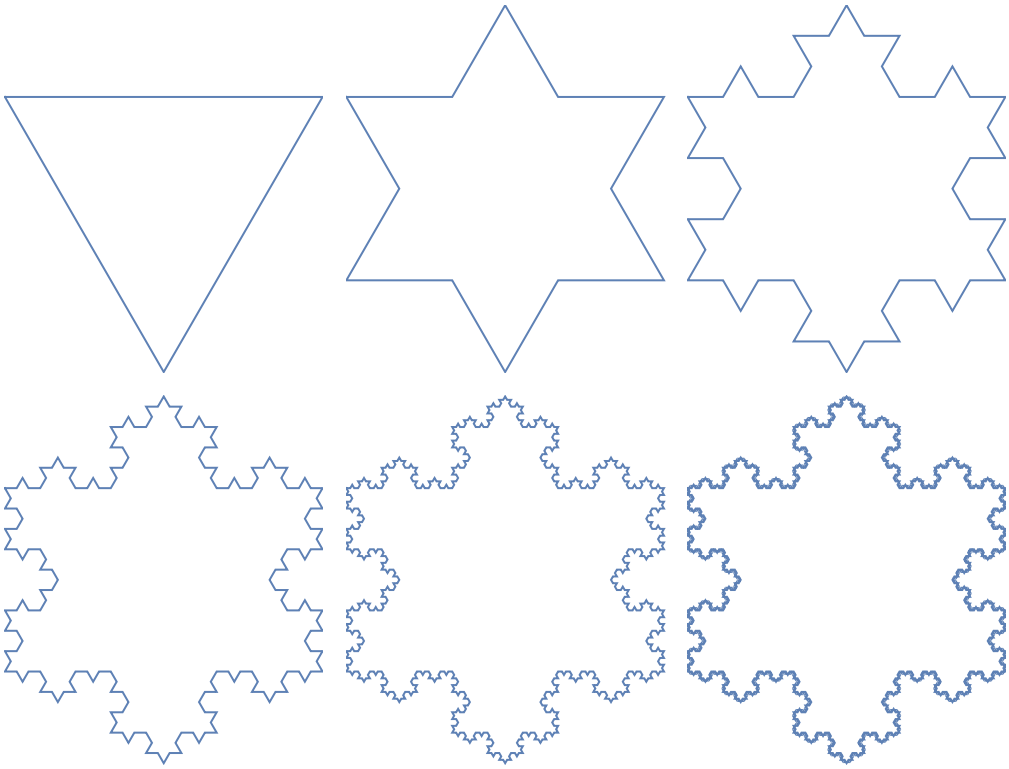

Figure A.1: The procedure to generate a Koch snowflake fractal pattern up to the $5th$ recursion.

A fractal is usually defined as a "Fragmented geometric shape, which can be divided into several parts, and each part (at least approximately) has the shrunk overall shape" [201]. That is to say, that a fractal pattern is self-similar. This

idea was first proposed in the 17th century, but the word "fractal" was coined by Benoít B. Mandelbrot in 1975.

Typically, a fractal pattern has the following features:

1. It always has a fine structure on any small scale;

2. It is very irregular, and can be described neither entirely nor partly by traditional Euclidean geometric language;

3. It has a (at least approximate or statistical) self-similar form;

4. In some cases, it has a simple recursive definition.

As an example of a two-dimensional fractal pattern, the Koch snowflake (also known as the Koch curve) is shown in Fig. A.1 (a algorithm for the generation of this pattern is given at the end of this chapter in Mathematica language). The initial perimeter is 1, and the area is $s_0 = \sqrt{3}/6$. Each step increases the perimeter by 1/3 over its previous value, and the unit of the length increase is $\epsilon = 1/3^n$, where n is the number of recursions. Its area limit is $s_0 8/5$. Infinite recursive steps lead to an infinite perimeter, with an infinitesimal unit of increased length but finite area. On can notice that this recursively-defined fractal pattern has some unique features as compared to a normal line: its length is infinite, and since it has a fine and irregular structure on any small scale no matter how small, one cannot define a gauge small enough to describe it. Thus, a Koch curve is not a one-dimensional pattern. Some new language is needed to describe this type of pattern.

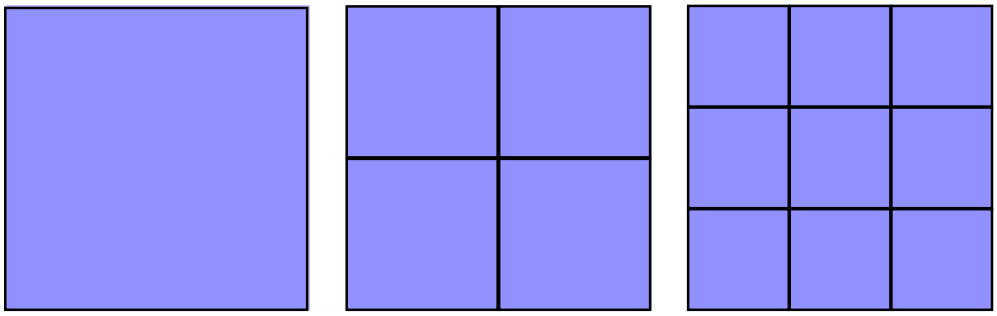

Figure A.2: The fractal dimension of a square. By defining a smaller scale $\epsilon = 1$, 1/2, 1/3, the number of tiles for filling this unit square is $N = 1$, 4, 9, so that the fractal dimension of the square is $D = -\log n/\log \epsilon \equiv 2$.

One of the commonly used characteristics of a fractal is"fractal dimension".

This describes how complex the fractal patterns are when measured at different scales and their capability of "space-filling". If we define a small "tile" with a scale is ϵ, and use it to measure the number of the tiles N needed to fill the geometrical pattern, so from the equation

$$\left(\frac{1}{\epsilon}\right)^D = N, \tag{A.1}$$

the fractal dimension is defined as $D = -\log n/\log \epsilon$. For example, the fractal dimension of a square is constantly at $D = 2$, no matter how small a tile is used, as shown in Fig. A.2. The same applies to all simple geometrical objects, i.e. straight line ($D = 1$), rectangles ($D = 2$) and cubes ($D = 3$).

However, this quantity is not necessarily an integer for fractal patterns. Considering the Koch snowflake as shown in Fig. A.1, in the nth recursive step, the small tile is the unit of $\epsilon = 1/3^n$. The perimeter of nth recursive is $(1 + 1/3)^n$. There are $N = (1 + 1/3)^n 3^n$ tiles. Thus, the fractal dimension of the Koch snowflake is given as follows:

$$D = -\frac{\log N}{\log \epsilon} = -\frac{\log[(1 + 1/3)^n 3^n]}{\log[1/3^n]} = \frac{\log 4}{\log 3} \sim 1.26186,$$

i.e. the dimension of the Koch snowflake is higher than that of a one dimensional line but lower than that of a two-dimensional square.

The exact value of fractal dimension quantity D is not always easy to evaluate. In fact, most of time it is quite difficult to find, and one can only estimate its upper and lower limits.

A program for generating the Koch snowflake is given as following, where the function "KochFractal" determines how change to the fractal, if recursively generated, will generate new fractal patterns:

```
KochFractal[x_]:={x[[1]],(2 x[[1]]+x[[2]])/3,RotationMatrix[[Pi]/3]
.((x[[1]]+2 x[[2]])/3-(2 x[[1]]+x[[2]])/3)+(2 x[[1]]+x[[2]])/3,
(x[[1]]+2 x[[2]])/3,x[[2]]};
```

```
Kochsnowflake[PointSet0_,nD_]:=Nest[Flatten[KochFractal/@
Partition[#,2,1],1]&, PointSet0,nD];
Graphics[Polygon[Kochsnowflake[{{0,0},{1,0},{1/2,-Sqrt[3]/2},{0,0}},3]]]
```

Appendix B

The origin of Hofstadter butterfly spectrum

The fractal Hofstadter butterfly spectrum, as show in Fig. 3.1, can be generated considering a two-dimensional square lattice with lattice constant a, as shown in the top panel of Fig. 3.2. This system can be described by a simple Hamiltonian of the tight-binding model applied to derive the graphene Hamiltonian in Chap. 2.

If one unit cell has q atomic orbitals, then each atomic orbital can be denoted by ϕ_l, $l \in [1, q]$. Because of the translational symmetry of a crystal, we can build a tight-binding Bloch wave function Φ_l of one unit cell which depends on position vector, $\boldsymbol{r}$, and the wave vector, $\boldsymbol{k}$, as follows:

$$\Phi_l(\boldsymbol{r}, \boldsymbol{k}) = \frac{1}{\sqrt{N}} \sum_{i=1}^{N} e^{i\boldsymbol{k}\cdot\boldsymbol{R}_{i,l}} \phi_l(\boldsymbol{r} - \boldsymbol{R}_{i,l}), \tag{B.1}$$

where $\boldsymbol{R}_{i,l}$ represents the position of the lth atomic orbital in the ith unit cell, and N is number of unit cells. Then, the electron wave function $\Psi_j(\boldsymbol{r}, \boldsymbol{k})$ of each unit cell can be expressed as a linear superposition of Bloch wave functions as follows:

$$\Psi_j(\boldsymbol{r}, \boldsymbol{k}) = \sum_{l=1}^{q} c_{j,l} \Phi_l(\boldsymbol{r}, \boldsymbol{k}), \tag{B.2}$$

where $c_{j,l}$ are the coefficients of the expansion. Based on the electron wave func-

tion $\Psi_j(\boldsymbol{r}, \boldsymbol{k})$, we can formally express the jth energy eigenvalue $E_j(\boldsymbol{k})$ of the Hamiltonian of the system $\hat{\mathcal{H}}$, as follows:

$$E_j(\boldsymbol{k}) = \frac{\left\langle \Psi_j | \hat{\mathcal{H}} | \Psi_j \right\rangle}{\langle \Psi_j | \Psi_j \rangle} = \frac{\sum_{i,l}^{q} c_{ji}^* c_{jl} \left\langle \Phi_i | \hat{\mathcal{H}} | \Phi_l \right\rangle}{\sum_{i,l}^{q} c_{ji}^* c_{jl} \langle \Phi_i | \Phi_l \rangle}. \tag{B.3}$$

To minimize the energy E_j, we calculate the derivative of E_j with respect to the coefficient c_{ji}^*, and set $\partial E_j / \partial c_{ji}^* = 0$. Thus, we obtain the following equation:

$$\begin{aligned} &\sum_{l=1}^{q} H_{il} c_{jl} = E_j \sum_{l=1}^{q} S_{il} c_{jl}, \\ &H_{il} = \left\langle \Phi_i | \hat{\mathcal{H}} | \Phi_l \right\rangle, \quad S_{il} = \langle \Phi_i | \Phi_l \rangle, \end{aligned}$$

which can be transformed into a matrix form.

As each unit cell contains q atomic orbitals, the $q \times q$ matrix equation is given as follows:

$$\hat{H}\psi_j = E_j S \psi_j, \quad \psi_j = \begin{pmatrix} c_{j1} & c_{j2} & \cdots & c_{jq-1} & c_{jq} \end{pmatrix}^T,$$

$$H = \begin{pmatrix} H_{11} & H_{12} & \cdots & H_{1q-1} & H_{1q} \\ H_{21} & H_{22} & \cdots & H_{2q-1} & H_{2q} \\ \cdots & \cdots & \cdots & \cdots & \cdots \\ H_{q-11} & H_{q-12} & \cdots & H_{q-1q-1} & H_{q-1q} \\ H_{q1} & H_{q2} & \cdots & H_{qq-1} & H_{qq} \end{pmatrix} \tag{B.4}$$

$$S = \begin{pmatrix} S_{11} & S_{12} & \cdots & S_{1q-1} & S_{1q} \\ S_{21} & S_{22} & \cdots & S_{2q-1} & S_{2q} \\ \cdots & \cdots & \cdots & \cdots & \cdots \\ S_{q-11} & S_{q-12} & \cdots & S_{q-1q-1} & S_{q-1q} \\ S_{q1} & S_{q2} & \cdots & S_{qq-1} & S_{qq} \end{pmatrix} \tag{B.5}$$

and the energy E_j can be obtained by solving the determinant of the secular

equation as follows:

$$\det(H - ES) = 0 \tag{B.6}$$

We will use the following assumptions to simplify Eq. (B.6): The dominant contribution of the diagonal entries H_{ll} arises from the same site $\boldsymbol{R}_i = \boldsymbol{R}_j$ as well as the nearest neighboring sites $|\boldsymbol{R}_i - \boldsymbol{R}_j| = a$. The off-diagonal entries $H_{ll'}$ arise from the nearest neighboring sites $|\boldsymbol{R}_i - \boldsymbol{R}_j| = a$. The contribution of other further sites is omitted. Therefore, for the diagonal entry,

$$\begin{aligned}
H_{ll} &= \frac{1}{N}\sum_{i=1}^{N}\left\langle \phi_l(\boldsymbol{r}-\boldsymbol{R}_{l,i})|\hat{\mathcal{H}}|\phi_l(\boldsymbol{r}-\boldsymbol{R}_{l,i})\right\rangle \\
&\quad + \frac{1}{N}\sum_{i}^{N}\sum_{j \text{ near } i}^{N} e^{i\boldsymbol{k}\cdot(\boldsymbol{R}_{l,j}-\boldsymbol{R}_{l,i})}\left\langle \phi_l(\boldsymbol{r}-\boldsymbol{R}_{l,i})|\hat{\mathcal{H}}|\phi_l(\boldsymbol{r}-\boldsymbol{R}_{l,j})\right\rangle \\
&= \epsilon_{\text{ao}} + \sum_{j \text{ near } i}^{N} t e^{i\boldsymbol{k}\cdot(\boldsymbol{R}_{l,j}-\boldsymbol{R}_{l,i})} \\
\epsilon_{\text{ao}} &= \left\langle \phi_l(\boldsymbol{r}-\boldsymbol{R}_{l,i})|\hat{\mathcal{H}}|\phi_l(\boldsymbol{r}-\boldsymbol{R}_{l,i})\right\rangle \\
t &= \left\langle \phi_l(\boldsymbol{r}-\boldsymbol{R}_{l,i})|\hat{\mathcal{H}}|\phi_l(\boldsymbol{r}-\boldsymbol{R}_{l,j})\right\rangle,
\end{aligned} \tag{B.7}$$

where ϵ_{ao} is the onsite energy of atomic orbitals in the absence of a magnetic field. Because its only effect is to shift the global on-site energy, here we simply set it to zero. t is the transfer integral of the two atomic orbitals in the absence of a magnetic field, which only depends on the difference between $\boldsymbol{R}_{l,i}$ and $\boldsymbol{R}_{l,j}$ for the nearest neighboring sites of the square lattice. For off-diagonal entries,

$$\begin{aligned}
H_{ll'} &= \frac{1}{N}\sum_{i}^{N}\sum_{j \text{ near } i}^{N} e^{i\boldsymbol{k}\cdot(\boldsymbol{R}_{l,j}-\boldsymbol{R}_{l',i})}\left\langle \phi_l(\boldsymbol{r}-\boldsymbol{R}_{l,i})|\hat{\mathcal{H}}|\phi_{l'}(\boldsymbol{r}-\boldsymbol{R}_{l',j})\right\rangle \\
&= \sum_{j \text{ near } i}^{N} t e^{i\boldsymbol{k}\cdot(\boldsymbol{R}_{l,j}-\boldsymbol{R}_{l',i})}
\end{aligned} \tag{B.8}$$

Furthermore, we assume that the dominant contribution of each entry of S arises from the same site $\boldsymbol{R}_i = \boldsymbol{R}_j$, and that all wave functions are orthogonal and

normalized, such that matrix S becomes a unitary matrix. Thus, the eigenenergy can be obtained by diagonalizing matrix $\hat{H}$.

In the case of zero magnetic field, the lattice constant is a, the unit cells are not enlarged, and each unit cell contains only one atomic orbital, as shown in the top panel of Fig. 3.2. In this case, matrix H in Eq. (B.5) is a 1×1 matrix,

$$\begin{aligned}\hat{H}_{11} &= t \sum_{j \text{ near } i}^{N} e^{i\boldsymbol{k}\cdot(\boldsymbol{R}_{l,j}-\boldsymbol{R}_{l,i})} \\ &= t(e^{ik_x a} + e^{-ik_x a} + e^{ik_y a} + e^{-ik_y a}) \\ &= 2t\left[\cos(k_x a) + \cos(k_y a)\right]\end{aligned}$$

In finite magnetic field $\boldsymbol{A} = B(0, x, 0)$, the Peierls substitution $\boldsymbol{k} \to \boldsymbol{k} - e\boldsymbol{A}$ suggests that the exponential term, $e^{i\boldsymbol{k}\cdot(\boldsymbol{R}_{l,j}-\boldsymbol{R}_{l',i})}$, which describes hopping between nearest neighboring sites in Eq. (B.8) and (B.7) becomes coordinate dependent,

$$e^{i\boldsymbol{k}\cdot(\boldsymbol{R}_{l,j}-\boldsymbol{R}_{l',i})} \to e^{i\boldsymbol{k}\cdot(\boldsymbol{R}_{l,j}-\boldsymbol{R}_{l',i})-ie\boldsymbol{A}\cdot(\boldsymbol{R}_{l,j}-\boldsymbol{R}_{l',i})} = e^{i\boldsymbol{k}\cdot(\boldsymbol{R}_{l,j}-\boldsymbol{R}_{l',i})} e^{\pm i2\pi m\phi/\phi_0} \tag{B.9}$$

where $\boldsymbol{R}^x_{l',i} = ma$ and the nearest sites are $\boldsymbol{R}_{l,j} - \boldsymbol{R}_{l',i} = (\pm a, 0)$ or $(0, \pm a)$ for a square lattice. $\phi = Ba^2$ is the magnetic flux threading a unit cell, and $\phi_0 = h/e$ is the flux quantum, $\hbar = 1$.

For example, if $\frac{\phi}{\phi_0} = \frac{1}{2}$, the phase factor in Eq. (B.9) $e^{\pm i2\pi m\frac{\phi}{\phi_0}} = e^{\pm i2\pi(m+2)\frac{\phi}{\phi_0}}$, will be periodic for length $2a$, as shown in the middle panel of Fig. 3.2. The translational symmetry is reduced by 2 times, and each unit cell contains two atomic orbitals. The matrix in Eq. (B.5) is of 2×2 order now:

$$H = 2t \begin{pmatrix} \cos(k_y a) & \cos(k_x a) \\ \cos(k_x a) & \cos(k_y a - \pi) \end{pmatrix}$$

One can find that the translational symmetry of the electron in the square lattice in the magnetic field can be recovered if the ratio between magnetic flux

and flux quanta ϕ/ϕ_0 in $e^{\pm i2\pi m\phi/\phi_0}$ is a rational number (like 1/2 or 2/3 etc):

$$\alpha = \frac{p}{q} = \frac{\phi}{\phi_0}, \quad p, q \in \mathbb{Z} \tag{B.10}$$

In this case, the magnetic unit cell is enlarged q times, as shown in the bottom panel of Fig. 3.2. The form of the matrix containing the eigen energies is

$$H = 2t \begin{pmatrix} \cos(k_y a - 2\pi\alpha \times 0) & \cos(k_x a) & 0 & \cos(k_x a) \\ \cos(k_x a) & \cos(k_y a - 2\pi\alpha \times 1) & \cos(k_x a) & 0 \\ 0 & \cos(k_x a) & \cdots & \cos(k_x a) \\ \cos(k_x a) & 0 & \cos(k_x a) & \cos(k_y a - 2\pi\alpha \times (q-1)) \end{pmatrix}. \tag{B.11}$$

The eigenenergies of the bands can be obtained by diagonalizing the matrix for a given point in the magnetic Brillouin zone. By mapping the bandwidth on the rational value p/q, the butterfly spectrum can be built as shown in Fig. 3.1.

Appendix C

The description of moiré pattern

Two super-positioned lattices with the same Bravais lattice structure generate a supercell with the same lattice structure and a much larger lattice constant, and the pattern formed by the supercell is called a moiré pattern.

To describe this pattern, we firstly define difference between the two lattice constants δ as,

$$a_{BN} = (1 + \delta)a_g, \tag{C.1}$$

where $a_g \simeq 2.46\,\text{Å}$ and $a_{BN} \simeq 2.50\,\text{Å}$ are the primitive lattice constants of graphene and h-BN, respectively. So $\delta = 1.8\%$. Here, both a_g and a_{BN} are not necessary rational number, which means that the exact superlattice constant a does not exist, i.e. one can not find two integer n_1 and n_2 to commensurate the two lengths,

$$n_1 a_g \neq n_2 a_{BN}, \quad n_1,\ n_2 \in \mathbb{Z}. \tag{C.2}$$

In other words, the moire pattern in real space does not have exact translational invariance once if the two lattice constants are not exactly commensurate. Therefore, we alternatively utilize the concept of "beat" to describe this pattern.

Consider that we have two stasis wave with wave number g and g' respectively.

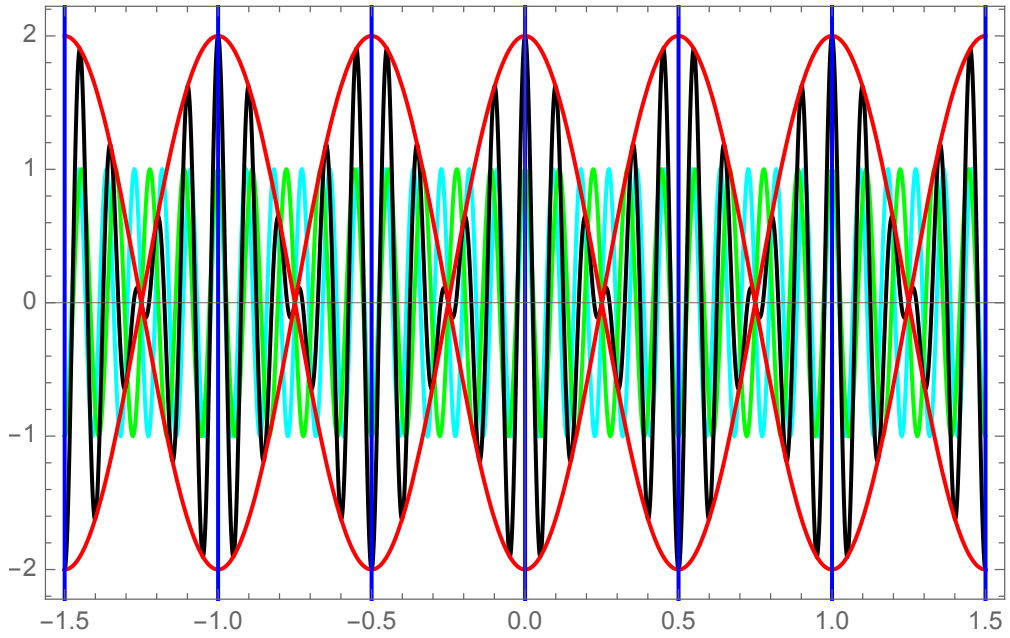

Figure C.1: The superposition of two stasis waves. The cyan line represents $\cos(gx)$, and the green line represents $\cos(g'x)$. Their superposition generates a fast oscillation wave $\cos(x(g+g')/2)$, as the black line shown, as well as a slow oscillation wave $\cos(x(g-g')/2)$, as the red line shown. If we are only interested in "the period of the amplitude of envelop wave", but not "the period of phase", then the periodical envelop wave can be described by wave number $b = g - g'$.

The triangular equation suggests that their superposition can be expressed as following form,

$$\cos(gx) + \cos(g'x) = 2\cos(\frac{g+g'}{2}x)\cos(\frac{g-g'}{2}x). \tag{C.3}$$

On the right hand side of Eq. (C.3), the first term represents a fast oscillation wave with wave number $(g + g')/2$, and the second term represents a slow oscillation envelop wave with a wave number $(g - g')/2$. As shown in Fig. C.1, "the period of the amplitude" of envelop wave can be described by wave number $b = g - g'$.

Extend this concept of beat to two-dimensional situation, we can define the reciprocal vectors of the moiré superlattice. Consider that two substrates of 2D materials, the difference of reciprocal lattice constant is $g' = (1+\delta)^{-1}g$, and a finite misalignment angle θ, where $g(g')$ is the module of reciprocal vector $\boldsymbol{g}_m$ ($\boldsymbol{g}'_m$). We

can build following relation

$$\boldsymbol{g}'_m = (1+\delta)^{-1}\hat{R}_\theta \boldsymbol{g}_m, \quad m \in [0, ..., 5], \tag{C.4}$$

where $\hat{R}_\theta$ is the rotational operator. For hexagonal lattice, the six (i.e. $m = 0, \cdots 5$) shortest reciprocal vectors of the moiré superlattice are shown in Fig. 3.5.

In the case of small misalignment angle $\theta \simeq 0$, the reciprocal vectors of the moiré superlattice are defined as

$$\boldsymbol{b}_m = \boldsymbol{g}_m - \boldsymbol{g}'_m \simeq \begin{pmatrix} \delta & \theta \\ -\theta & \delta \end{pmatrix} \boldsymbol{g}_m. \tag{C.5}$$

Here, $b = |\boldsymbol{b}_m|$ is the module of reciprocal superlattice vector. Then the moiré superlattice is defined as

$$\boldsymbol{a}_m = \frac{\boldsymbol{b}_{m+1} \times \hat{l}_z}{\boldsymbol{b}_{m+1} \cdot (\boldsymbol{b}_m \times \hat{l}_z)} \simeq \frac{1}{\delta^2 + \theta^2} \begin{pmatrix} \delta & \theta \\ -\theta & \delta \end{pmatrix} \boldsymbol{a}_g, \tag{C.6}$$

where $\boldsymbol{a}_g$ is the lattice vector of the material with shorter lattice constant, here, being graphene. In the case of $\theta = 0$,

$$\begin{aligned} \boldsymbol{b}_m &= \delta * \boldsymbol{g}_m, \quad \boldsymbol{a}_m = \boldsymbol{a}_g/\delta, \\ \boldsymbol{g}_m &= \hat{R}_{2\pi m/6}(0, 4\pi/\sqrt{3}a_g). \end{aligned} \tag{C.7}$$

The superlattice vectors $\boldsymbol{a}_1$ and $\boldsymbol{a}_2$ are shown in Fig. 3.4.

In general, we utilize the concept of beat to overcome the problem of non-commensuration. Opposite to normal sequence of defining lattice of a system, we define reciprocal superlattice vector firstly, then we define superlattice vector in real space. One point need to be emphasized is that the "superlattice constant" $a = |\boldsymbol{a}_m|$ defined here does not describe the "exact translational invariance of moiré pattern in real space", as it only exists for commensurate lattice constants.

Appendix D

Construction of Hamiltonian of moiré perturbed graphene

This Hamiltonian Eq. (3.6) is not microscopically derived, but phenomenologically derived based on symmetric analysis argument. It can be understood as a kinetic term and potential terms. We take the Dirac Hamiltonian of clean graphene, i.e., Eq. (2.19), as the dominant part of Hamiltonian of moiré perturbed graphene [1] . The rest of Eq. (3.6) can be considered as terms due to the moiré potential.

Let's consider the second term $vbu_0^+ f_+$, this diagonal term has no σ matrices, it simply describes the potential arising from the moiré perturbation. The vb is the magnitude of energy scale. Furthermore, we assume moiré perturbation is translational invariant, and we can represent the periodic moiré potential as a Fourier series, and relate the scattering process of electron due to moiré potential with the reciprocal superlattice vectors. Although different reciprocal lattice vectors may have different coefficients in the Fourier series, we assume this perturbation should bear the same symmetric properties as the system, such as rotational symmetry, so the reciprocal lattice vectors of same module will have the same numerical values. If we only keep the lowest order of reciprocal lattice (reason is given below), then we can truncate Fourier series and represent it by $f_+ = \sum_m e^{i\boldsymbol{b}_m \cdot \boldsymbol{r}}$, and use u_0^+ to

[1] Because that h-BN has a large band gap (i.e. $\Delta_{h\text{-BN}} \sim 6\,\text{eV}$ [45]), its influence to low-energy band structure can be counted in by Schrieffer-Wolff transformation, but it is not necessary as it is trivial.

describe the size of the potential. So this is the simplest potential term $vbu_0^+ f_+$.

Moreover, because the difference between boron and nitride atom sites, the inversion symmetry and six-fold rotational symmetry are broken in *h*-BN, so we need an additional term to describe this "asymmetric effect". Similarly, we represent the "asymmetric" potential by Fourier series, generalize the size of potential as u_0^-, and absorb the minus sign into the phase factor term, so we get the term $f_- = \sum_m i(-1)^m e^{i\boldsymbol{b}_m \cdot \boldsymbol{r}}$. This f_- will get a minus sign if coordinate is inverted $\boldsymbol{r} \to -\boldsymbol{r}$. So this is the potential term $vbu_0^- f_-$.

The further two terms in Eq. (3.6), $\xi vb\sigma_3(u_3^+ f_- + u_3^- f_+)$ describe the difference of sublattices caused by moiré perturbation. The reason that u_3^+ accompanies with f_- but not f_+ is following: The Dirac Hamiltonian of graphene we use here is not a normal "Hamiltonian", but actually a matrix of coefficient of Bloch wave function on sublattices space. When we rotate the coordinate $\pi/3$ (or inverse) in real space, the sublattice space as well as valley space will change too, we use σ and ξ to notify sublattice and valley. So we need to include this effect into the symmetric operation $\hat{C}_6$. The detail of this symmetric operation can be found in Ref. [88]. Anyway, by applying symmetric operation, the term $\xi vb\sigma_3 u_3^+ f_-$ holds six-fold rotational invariance but $\xi vb\sigma_3 u_3^- f_+$ not.

The last two terms $\xi v\boldsymbol{\sigma} \cdot \left[\boldsymbol{l}_z \times \nabla \left(u_1^+ f_- + u_1^- f_+\right)\right]$ in Eq. (3.6), which has an additional ∇ operator, describe the modulation of the hopping amplitude between the nearest atomic sties, . This comes from the fact that σ_1 and σ_2 are mixed together after the symmetric operation $\hat{C}_6$. We need to build a vector matrix $\boldsymbol{\sigma}$ including these two matrices simultaneously. So we need another vector term to be the counter part of $\boldsymbol{\sigma}$. By applying simple rotation to $f_\pm$, one can discover that the simplest form of this counter part can be constructed as $(-b_m^y + b_m^x,\, b_m^x + b_m^y)$. The vector $(-b_m^y, b_m^x)$ can be transformed into $\nabla \times f_\pm$, associated with $u_1^\pm$. The other vector (b_m^x, b_m^y) can be transformed into $\nabla f_\pm$, associated with $u_2^\pm$.

The reason of absence of $u_2^\pm$ in Eq. (3.6) is that its effect can be removed by a gauge transformation, $\psi' = \exp[-i\xi(u_2^+ f_- + u_2^- f_+)]\psi$, so we can omit this term for

simplicity. Due to symmetric operation requirement, there is no more valid term, so we construct the Hamiltonian of moiré perturbation.

The validity of discarding higher order of reciprocal superlattice in Fourier series comes from a numerical investigation [88]. It turns out that higher order is ten times smaller than lower order, so they can be neglected without too much compromise of accuracy. This fact can be understood by the following physical picture. To describe the effect of atomic sites of h-BN to sublattices of graphene, we can calculate it by the electric quadrupole of point charge. Due to the system is translation-invariant, we can represent this by Fourier series. Then the integral of the potential depends on the module reciprocal superlattice vector. If we treat this heterostructure as a two-dimensional system, then the higher order of reciprocal superlattice vectors are not trivial and can not be discarded at will. However, if we treat this system as three-dimensional, i.e. count in the interlayer distance between graphene and h-BN ($d = 3.22$ Å). This distance is much larger than the Bohr radius of $2p_z$ atomic orbital of graphene ($0.27\,\text{Å} \leq a_{p_z} \leq 0.53\,\text{Å}$). The higher order effect of reciprocal superlattice in Fourier series will decay very fast, therefore we can neglect them.

This approximation also suggests that the inter-valley scattering is trivial. Because an inter-valley scattering needs the momentum transferred $\delta k \simeq g_m$, where g_m is the reciprocal lattice of graphene. From Eq. (C.5), one knows that $g_m \simeq 55b$ ($\delta = 0.18\%$ and $\theta = 0$), which means that inter-valley scattering is a 55th order effect or moiré perturbation, so it is obviously trivial.

The formal procedures of constructing this Hamiltonian based on symmetric analysis argument is following:

1. Determine the dominant term, the Dirac Hamiltonian describing the electron in clean graphene, which also corresponds to the kinetic energy part.

2. We need to describe the effect of moiré perturbation, but we do not know the exact form or size of the potential, and we want to include effects corresponding to all different symmetries. So we start our analysis from several symmetric

requirements:

(a) We assume that the moiré pattern is translation-invariant, so we can represent the periodic moiré potential by Fourier series.

(b) We assume that the Hamiltonian has the same symmetric properties (rotational invariant, or etc) as the system. The detailed form of this symmetric operator (and time-reversal operator below) can be found in Ref. [88].

(c) We assume that the Hamiltonian is time-reversal invariant in the absence of magnetic field.

(d) We do not consider inter-valley scattering, this can be understood from the fact that only the lowest reciprocal superlattice vector dominates the perturbation.

3. Because that the Dirac Hamiltonian is written on the basis of sublattices and dependent on valley, so we need to distinguish valid matrix structure from sublattices space and valley space. From the symmetric requirements and assumptions above, we can rule out all invalid matrix forms. Finally, one can get four potential matrices: I, $\xi\sigma_3$, (mixed) $\xi\sigma_1$ and $\xi\sigma_2$.

4. To account in coordinate inversion-symmetric and inversion-asymmetric terms, we can construct two different Fourier series, f_+ and f_-.

5. Therefore, we can have four matrices multiply two Fourier series, i.e. eight different symmetric terms, and we use eight parameters $u^{\pm}_{0,1,2,3}$ to describe the corresponding size of potential respectively. Furthermore, $u^{\pm}_2$ can be gauged away, so finally we have six terms to describe the moiré perturbation.

Appendix E

The degenerate perturbation calculation using Green function

Using perturbation theory, one can analytically calculate the nth-order self energy at the main DP of the moiré perturbed SLG Eq. (3.6), or BLG, Eq. (4.2). Because that there are two states locating at zero energy, therefore in principle, we need to use degenerate perturbation theory; however, because the perturbation term only includes non-zero reciprocal lattice, so the coupling term between the two zero energy states actually vanishes. The modification comes from the higher orders, that is the reason the second order perturbation but not first order dominates in Eq. (3.8).

Assume that a system can be described by a Hamiltonian, $\hat{H}_0$, and a perturbation, $\hat{M}$:

$$\hat{H} = \hat{H}_0 + \hat{M}. \tag{E.1}$$

To derive the energy modification of energy valley at $E = 0$, we can consider this problem as obtaining an effective Hamiltonian from the original Hamiltonian containing all necessary momentum states that are coupled. Because that the perturbation term only includes the lowest reciprocal lattice vector, so we can only project the effects of these states onto the zero-energy zero-momentum states

by Schrieffer-Wolff transformation.

In practice, we utilize Green function to express the effect from couple states. Green function is defined by Eq. (6.15) and can be Taylor expanded at zero energy as follows:

$$\begin{aligned} G &= (E - \hat{H})^{-1} \\ &= G_0 + G_0\hat{M}G_0 + G_0\hat{M}G_0\hat{M}G_0 + \mathbb{O}(\hat{M}^3) \\ &\simeq G_0(1 + \hat{M}G_0 + \hat{M}G_0\hat{M}G_0), \end{aligned}$$

where

$$G_0 = (E - \hat{H}_0)^{-1}. \tag{E.2}$$

By inverting this expression, we obtain the following:

$$\begin{aligned} E - \hat{H} &= (1 + \hat{M}G_0 - \hat{M}G_0\hat{M}G_0)^{-1}G_0^{-1} \\ &\simeq (1 - \hat{M}G_0 - \hat{M}G_0\hat{M}G_0)G_0^{-1} \\ &= G_0^{-1} - \hat{M} - \hat{M}G_0\hat{M} \\ &= E - \hat{H}_0 - \hat{M} - \hat{\Sigma}^{(2)}, \end{aligned}$$

where the second-order self energy is

$$\hat{\Sigma}^{(2)} = \hat{M}G_0\hat{M}. \tag{E.3}$$

$\hat{\Sigma}$ contains the effect of coupled states. To understand this process, we use the moiré perturbation of SLG, Eq. (3.6) to exemplify this procedure. One can consider right hand side of Eq. (E.3) as following procedures:

(1) an electron (of zero momentum) is moiré perturbed, and the change of its momentum is $\boldsymbol{b}_m$;

(2) the propagation of this electron can be described by zeroth order Green

function G_0;

(3) this electron is scattered again by moiré perturbation, and gets an additional change of momentum $\boldsymbol{b}'_m$.

After (3), if $\boldsymbol{b}_m + \boldsymbol{b}'_m \neq 0$, then this term will not generate a modification to the diagonal term (onsite energy), but an off-diagonal term, i.e., a higher order modification we are not interested in.

In practice, one can find the combination of reciprocal superlattice with a sum of zero $\boldsymbol{b}_{m_1}+\boldsymbol{b}_{m_2} = 0$, i.e. (b_0, b_3), (b_1, b_4) and (b_2, b_5). The second-order self-energy at the exact DP is as follows:

$$\begin{aligned}\hat{\Sigma}^{(2)} = \lim_{\epsilon\to 0,\boldsymbol{p}\to 0} & \hat{M}_{\boldsymbol{b}_0} G_0(\epsilon, \boldsymbol{p}+\boldsymbol{b}_3)\hat{M}_{\boldsymbol{b}_3} + \hat{M}_{\boldsymbol{b}_3} G_0(\epsilon, \boldsymbol{p}+\boldsymbol{b}_0)\hat{M}_{\boldsymbol{b}_0} \\ & + \hat{M}_{\boldsymbol{b}_1} G_0(\epsilon, \boldsymbol{p}+\boldsymbol{b}_4)\hat{M}_{\boldsymbol{b}_4} + \hat{M}_{\boldsymbol{b}_4} G_0(\epsilon, \boldsymbol{p}+\boldsymbol{b}_1)\hat{M}_{\boldsymbol{b}_1} \\ & + \hat{M}_{\boldsymbol{b}_2} G_0(\epsilon, \boldsymbol{p}+\boldsymbol{b}_5)\hat{M}_{\boldsymbol{b}_5} + \hat{M}_{\boldsymbol{b}_5} G_0(\epsilon, \boldsymbol{p}+\boldsymbol{b}_2)\hat{M}_{\boldsymbol{b}_2}.\end{aligned}$$

Here, $\hat{M}_{\boldsymbol{b}_i}$ is the component of $\hat{M}$ that includes only the Bragg vector, $\boldsymbol{b}_i$.

Appendix F

Microscopic model for the moiré perturbation

To describe the interlayer coupling in graphene/*h*-BN heterostructure, several studies [87, 175, 189, 190] have made use of the similarity between this system and twisted BLG. In the latter system [176–179], the electronic structure can be described by a bilayer-like Hamiltonian, in which the intralayer blocks are given by the Dirac Hamiltonian and the interlayer blocks describe the modulation of the interlayer coupling as a function of the position within the mSL [178]. Applied to the K valley of the graphene/*h*-BN heterostructure, such a Hamiltonian takes the form

$$\hat{H}_{\text{2layer}} = \begin{pmatrix} v\boldsymbol{\sigma}\cdot\boldsymbol{p} & \hat{T}(\boldsymbol{r}) \\ \hat{T}^{\dagger}(\boldsymbol{r}) & \hat{H}_{\text{hBN}} \end{pmatrix}, \quad \hat{H}_{\text{hBN}} = \begin{pmatrix} \epsilon_N & 0 \\ 0 & \epsilon_B \end{pmatrix},$$
$$\hat{T}(\boldsymbol{r}) = \frac{1}{3}\sum_{j=0,1,2} e^{-i(\hat{R}_{2\pi j/3}\boldsymbol{\kappa})\cdot\boldsymbol{r}} \begin{pmatrix} \gamma_N & \gamma_B e^{-i\frac{2\pi}{3}j} \\ \gamma_N e^{i\frac{2\pi}{3}j} & \gamma_B \end{pmatrix}.$$

As mentioned above, the Dirac Hamiltonian is used for the graphene layer, $\hat{H}_{\text{hBN}}$ describes the *h*-BN layer with ϵ_B and ϵ_N characterizing the on-site energy of the boron and nitrogen sublattices, respectively, and $\hat{T}(\boldsymbol{r})$ describes the spatially varying interlayer coupling, with γ_B and γ_N being the hopping integrals from

graphene to the boron and nitrogen sites, respectively. For the energies of interest, $|\epsilon| \ll |\epsilon_N|, |\epsilon_B|$, the Hamiltonian can be projected onto the Hilbert space of the graphene layer using a Schrieffer-Wolff transformation [61, 62], so that the perturbation can be parametrized by Eq. (3.6) with,

$$\{U^{\pm}_{i=0,1,3}\} = V^{\pm}\left\{\frac{\pm 1}{2}, -1, \frac{-\sqrt{3}}{2}\right\}, \tag{F.1}$$

where

$$V^{+} = \frac{1}{18}\left(\frac{\gamma_N^2}{\epsilon_N} + \frac{\gamma_B^2}{\epsilon_B}\right), \quad V^{-} = \frac{\sqrt{3}}{18}\left(\frac{\gamma_N^2}{\epsilon_N} - \frac{\gamma_B^2}{\epsilon_B}\right).$$

Appendix G

Vectors in non-orthogonal coordinates

The word "covariant" and "contra-variant" describes "how the quantitative description of certain geometric or physical entities changes with a change of basis" [202] . When an orthogonal basis is rotated into another orthogonal basis, the distinction between co- and contra-variant vectors is invisible, but in skew coordinate or, curvilinear coordinates, the differences are clear.

Definition: Let V be a vector space of dimension N over the field of scalar S, and let each of $f = (x_1, x_2, ..., x_n)$, $f' = (y_1, y_2, ..., y_n)$ (a row array with basis vector entries) be a basis of V, then the change of basis from f to f' is given by the following:

$$f \to f' = (\sum_i a_{1i}x_i, ..., \sum_i a_{ni}x_i) = fA, \tag{G.1}$$

where a_{1i} is a scalar without an array structure. A is an invertible $n \times n$ matrix with entries a_{ji}, each vector x_i of f and y_i of f' is a linear combination $y_j = \sum_i a_{ji}x_i$. Based on the transformation matrix A and a fundamental transformation equation of basis $f' = fA$ ($f'A^{-1} = f$), we can define two different types of vector by comparing their form with the form of the transformation of the basis.

G.1 Contra-variant vector

First, the contra - variant vectors are defined as follows: One vector "v"(a column array with vector entries) in V is expressed as one linear combination of the elements of the f basis as $v = \sum_i v^i[f]x_i$, where $v^i[f]$ are scalars without array structure in S (e.g. coordinates), known as the components of v in the f basis. Denote the column vector of components of v by $v[f]$ (the column array with a scalar entry $v^i[f]$) as follows:

$$v[f] = \begin{pmatrix} v^1[f] & ... & v^n[f] \end{pmatrix}^T.$$

To ensure that the above equation can be expressed as the matrix product of one row vector and one column vector, start from the equality that a position vector in any arbitrary coordinate system is identical

$$fv[f] = f'v[f']. \tag{G.2}$$

One obtains $v[fA] = A^{-1}v[f]$. The method for transforming v is opposite to the method of transforming basis f; thus, v are called "contra-variant vectors".

For a vector, such as a velocity or direction vector, to be basis-independent, the component of the vector must contra-vary with the change of basis to compensate. That is, the components must vary with the inverse transformation to that of the change of basis. Examples of contra-variance include the position of an object relative an observer, or any derivative of position with respect to time, such as velocity and acceleration.

G.2 Covariant vector

Covariant vectors are defined as follows: One linear functional α (row array with vector entries) on V is uniquely expressed in terms of its components $\alpha(x_i)$ (scalar in S without array structure) in the f basis as $\alpha(x_i) = \alpha_i[f]$, $\alpha(y_i) = \alpha_i[f']$. These

components are the result of α acting on the basis vector x_i of f basis under change of basis $f' = fA$.

$$\alpha_i[f'] = \alpha(y_i) = \alpha\left(\sum_i a_{ji}x_i\right) = \sum_i a_{ji}\alpha(x_i) = \sum_i a_{ji}\alpha_i[f].$$

The last two steps apply the properties of linear functional. Then, rewriting in the matrix form, we obtain the following: $\alpha[fA] = \alpha[f]A$. Because the components of the linear functional α transform with the matrix A, these components are said to transform covariantly under a change of basis.

For a dual-vector to be basis-independent, it must covary with a change of basis (i.e. it must be subject to the same transformation as the change of basis). Thus, these dual-vectors (or co-vectors, as opposed to the vectors) are said to be covariant. In general, covariant vectors appear when taking the gradient of a function.

In physics, contra-variant vectors often have units including a distance unit, whereas covariant vectors often have units including an inverse-distance unit.

G.3 Practical calculations in the Thesis

From the expression above, it can be determined that

$$\alpha[f']v[f'] = \alpha[f']AA^{-1}v[f'] = \alpha[f]v[f]. \tag{G.3}$$

This means that the dot product between corresponding coordinate of contra-variant and covariant vector is identical. Alongside Eq. (G.2), all properties of non-coordinates can be evaluated. But one needs to ensure that the following relation does not hold:

$$f\alpha[f] \neq f'\alpha[f']. \tag{G.4}$$

For example, the common orthogonal basis f, corresponding column vector

$v[f]$ and linear functional vector $\alpha[f]$ are

$$f = (\hat{\boldsymbol{x}}, \hat{\boldsymbol{y}}), \quad v[f] = (x, y)^T, \quad \alpha[f] = (k_x, k_y). \tag{G.5}$$

In addition, we introduce a new non-orthogonal basis f',

$$f' = (\hat{\boldsymbol{x}}_1, \hat{\boldsymbol{x}}_2), \quad \hat{\boldsymbol{x}}_1 = \frac{1}{2}\hat{\boldsymbol{x}} + \frac{\sqrt{3}}{2}\hat{\boldsymbol{y}}, \quad \hat{\boldsymbol{x}}_2 = -\frac{1}{2}\hat{\boldsymbol{x}} + \frac{\sqrt{3}}{2}\hat{\boldsymbol{y}}. \tag{G.6}$$

In this new basis, the column vector $v[f']$ and linear functional vector $\alpha[f']$ are notified as

$$v[f'] = (x_1, x_2)^T, \quad \alpha[f'] = (k_1, k_2). \tag{G.7}$$

From Eq.(G.2) and Eq.(G.3), we can get the following equations,

$$\begin{aligned} x\hat{\boldsymbol{x}} + y\hat{\boldsymbol{y}} &= x_1\hat{\boldsymbol{x}}_1 + x_2\hat{\boldsymbol{x}}_2, \\ xk_x + yk_y &= x_1k_1 + x_2k_2. \end{aligned}$$

Their solutions are

$$\begin{aligned} x_1 &= x + \frac{1}{\sqrt{3}}y, \quad x_2 = -x + \frac{1}{\sqrt{3}}y, \\ k_1 &= \frac{1}{2}k_x + \frac{\sqrt{3}}{2}k_y, \quad k_2 = -\frac{1}{2}k_x + \frac{\sqrt{3}}{2}k_y. \end{aligned}$$

As shown in Fig. G.1, one can notice the coordinates of reciprocal superlattice vectors in non-orthogonal coordinate system are much simplified, all components of momentum can be expressed by integer times $\sqrt{3}b/2$.

Furthermore, Eq. (G.4) suggests that

$$k_x\hat{\boldsymbol{x}} + k_y\hat{\boldsymbol{y}} \neq k_1\hat{\boldsymbol{x}}_1 + k_2\hat{\boldsymbol{x}}_2.$$

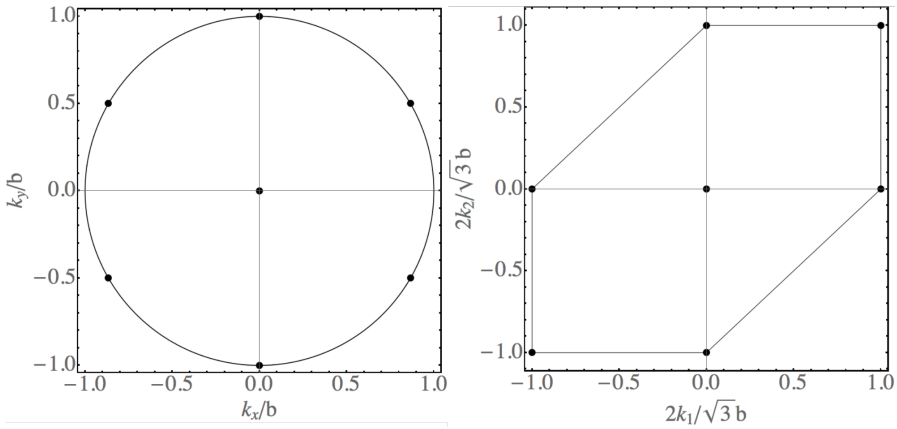

Figure G.1: Momentum in orthogonal and non-orthogonal coordinates. (Left) The first order of reciprocal superlattice vectors (shown in Fig. 3.5) in Cartesian coordinate system. (Right) The first order of reciprocal superlattice vectors in non-orthogonal coordinate system.

Therefore, we define two new vectors $\boldsymbol{c}_1$ and $\boldsymbol{c}_2$ to fulfill the identity of vector

$$k_x\hat{\boldsymbol{x}} + k_y\hat{\boldsymbol{y}} = k_1\boldsymbol{c}_1 + k_2\boldsymbol{c}_2.$$

This suggests that

$$\boldsymbol{c}_1 = \hat{\boldsymbol{x}} + \frac{1}{\sqrt{3}}\hat{\boldsymbol{y}}, \quad \boldsymbol{c}_2 = -\hat{\boldsymbol{x}} + \frac{1}{\sqrt{3}}\hat{\boldsymbol{y}}, \tag{G.8}$$

Note that $\boldsymbol{c}_1$ and $\boldsymbol{c}_2$ are not unit vector, but they fulfills

$$\hat{\boldsymbol{x}}_i \cdot \boldsymbol{c}_j = \delta_{ij}. \tag{G.9}$$

If one choose gauge for letting vector potential along $\boldsymbol{c}_1$ or $\boldsymbol{c}_2$ direction, this choice can simplify the solution of LLs, so

$$\boldsymbol{A} = -\frac{\sqrt{3}}{2}Bx_1\boldsymbol{c}_2. \tag{G.10}$$

Therefore, in a magnetic field, the momentum changes to

$$\hat{\boldsymbol{p}} \to \hat{\boldsymbol{p}} + e\boldsymbol{A} = k_1\boldsymbol{c}_1 + k_2\boldsymbol{c}_2 - e\frac{\sqrt{3}}{2}Bx_1\boldsymbol{c}_2, \tag{G.11}$$

So the operator $\hat{\pi}$ transforms into

$$\begin{aligned}
\pi &= (\hat{\boldsymbol{x}} + i\hat{\boldsymbol{y}}) \cdot (\hat{\boldsymbol{k}} + e\boldsymbol{A}) \\
&= \left[(\hat{\boldsymbol{x}}_1 - \hat{\boldsymbol{x}}_2) + \frac{i}{\sqrt{3}} (\hat{\boldsymbol{x}}_1 + \hat{\boldsymbol{x}}_2) \right] \cdot \left[k_1 \boldsymbol{c}_1 + k_2 \boldsymbol{c}_2 - e\frac{\sqrt{3}}{2} B x_1 \boldsymbol{c}_2 \right] \\
&= \frac{2}{\sqrt{3}} \left[e^{i\frac{\pi}{6}} k_1 + e^{i\frac{5\pi}{6}} (k_2 - \frac{\sqrt{3}}{2} eBx_1) \right].
\end{aligned}$$

Appendix H

The magnetic translational group and magnetic Bloch wave function

H.1 The magnetic translational symmetry

We know that an electron in a square lattice crystal in a magnetic field will be subject to both the periodic lattice potential as well as the magnetic vector potential. For an electron in a hexagonal moiré superlattice in a magnetic field, once the magnetic field fulfills the relation $BS/\phi_0 = p/q$, where S is the area of unit cell and $p, q \in \mathbb{Z}$, the translational symmetry of the electron will be recovered but in a reduced way [82, 107]. To investigate this further, we start from the gauge invariance of the Hamiltonian. Consider an electron existing in a periodic potential environment in the absence of a magnetic field $\boldsymbol{B}$. The Hamiltonian of the electron obeys translational symmetry as follows:

$$\hat{T}_{\boldsymbol{X}}\hat{H}(\boldsymbol{r}) = \hat{H}(\boldsymbol{r}+\boldsymbol{X}) = \hat{H}(\boldsymbol{r}),$$
$$\hat{T}_{\boldsymbol{X}}\varphi(\boldsymbol{r}) = e^{i\boldsymbol{k}\cdot\boldsymbol{X}}\varphi(\boldsymbol{r}),$$

where $\boldsymbol{X} = m_1\boldsymbol{a}_1 + m_2\boldsymbol{a}_2$, and $\hat{T}_{\boldsymbol{X}}$ are geometrical translations. However, when a magnetic field is present, its vector potential $\boldsymbol{A}(\boldsymbol{r})$, depends on the coordinate. Therefore, the Hamiltonian, $\hat{H}(\boldsymbol{r})$, after a translation $\boldsymbol{a}$ is $\hat{H}(\boldsymbol{r}+\boldsymbol{a})$, which is

not necessarily the same as $\hat{H}(\boldsymbol{r})$. To preserve the translational symmetry of the Hamiltonian, one can apply gauge invariance so that the vector potential $\boldsymbol{A}(\boldsymbol{r})$ and the eigenfunction of a Hamiltonian ψ to fulfill the relation [82]:

$$\boldsymbol{A} \to \boldsymbol{A} + \nabla f(\boldsymbol{r}), \qquad \psi \to \psi e^{ief(\boldsymbol{r})},$$

where $f(\boldsymbol{r})$ is an arbitrary function that depends on the coordinates. To describe the transformation of the wave function in a magnetic field, one can define a "magnetic translation operator" $\hat{\Theta}_{\boldsymbol{X}} = e^{ief}\hat{T}_{\boldsymbol{X}}$, where

$$f(\boldsymbol{r}) = -B\hat{z} \cdot \boldsymbol{r} \times (m_1\boldsymbol{a}_1) = Bm_1ax_2\sqrt{3}/2.$$

This operator generates a magnetic translational group as follows:

$$G_M = \{\hat{\Theta}_{\boldsymbol{X}} = e^{ieBm_1a\frac{\sqrt{3}}{2}x_2}\hat{T}_{\boldsymbol{X}}, \boldsymbol{X} = m_1\boldsymbol{a}_1 + m_2\boldsymbol{a}_2\},$$

where $\hat{\Theta}_X$ is known as the "magnetic translational operator".

$$\hat{\Theta}_{\boldsymbol{X}}\hat{\Theta}_{\boldsymbol{X}'} = e^{i2\pi\frac{p}{q}m_1'm_2}\hat{\Theta}_{\boldsymbol{X}+\boldsymbol{X}'}, \quad \hat{\Theta}_{\boldsymbol{X}}\hat{\Theta}_{\boldsymbol{X}'} = e^{i2\pi\frac{p}{q}(m_1'm_2-m_1m_2')}\hat{\Theta}_{\boldsymbol{X}'}\hat{\Theta}_{\boldsymbol{X}}.$$

The subgroup of G_M is comprised of translations

$$G_M' = \{\hat{\Theta}_{\boldsymbol{R}} = e^{ieBm_1a\frac{\sqrt{3}}{2}x_2}\hat{T}_{\boldsymbol{R}}, \boldsymbol{R} = m_1q\boldsymbol{a}_1 + m_2q\boldsymbol{a}_2\},$$

on a $(q \times q)$-enlarged superlattice. In subgroup G_M', the additional phase factor induced by commutation of magnetic translational operators automatically vanishes:

$$\hat{\Theta}_{\boldsymbol{R}}\hat{\Theta}_{\boldsymbol{R}'} = \hat{\Theta}_{\boldsymbol{R}+\boldsymbol{R}'}, \quad \hat{\Theta}_{\boldsymbol{R}}\hat{\Theta}_{\boldsymbol{R}'} = \hat{\Theta}_{\boldsymbol{R}'}\hat{\Theta}_{\boldsymbol{R}},$$

This subgroup, G'_M, is isomorphic to the simple group of translations, $\hat{T}_{\boldsymbol{R}}$, so that the eigenstates of $\hat{\Theta}_{\boldsymbol{R}}$ form a plane wave basis,

$$\hat{\Theta}_{\boldsymbol{R}}\psi_{\boldsymbol{k}}(\boldsymbol{r}) = e^{i\boldsymbol{k}\cdot\boldsymbol{R}}\psi_{\boldsymbol{k}}(\boldsymbol{r}).$$

Moreover, all reciprocal lattices shrink by $1/q$, i.e. the momentum space is folded onto a magnetic BZ (mBZ) with area $\sqrt{3}b^2/(2q^2)$.

Furthermore, because the translation operator $\hat{\Theta}_{\boldsymbol{a}_2}$ commutes with $\hat{\Theta}_{\boldsymbol{R}}$, one can define a new quantum number $t \in [0, \cdots, q-1]$ to index this q-fold degeneracy as follows:

$$\begin{aligned}
&\hat{\Theta}_{q\boldsymbol{a}_2}\psi_{\boldsymbol{k}}(\boldsymbol{r}) = (\hat{\Theta}_{\boldsymbol{a}_2})^q\psi_{\boldsymbol{k}}(\boldsymbol{r}) = e^{i\boldsymbol{k}\cdot q\boldsymbol{a}_2}\psi_{\boldsymbol{k}}(\boldsymbol{r}),\\
&\hat{\Theta}_{\boldsymbol{a}_2}\psi_{\boldsymbol{k}}(\boldsymbol{r}) = e^{i2\pi t/q}e^{i\boldsymbol{k}\boldsymbol{a}_2}\psi_{\boldsymbol{k}}(\boldsymbol{r}), \quad t \in [0, q-1],
\end{aligned} \tag{H.1}$$

Note that the operator $\hat{\Theta}_{\boldsymbol{a}_2}$ does not commute with $\hat{\Theta}_{\boldsymbol{a}_1}$, so that one cannot use $\hat{\Theta}_{\boldsymbol{a}_1}$ to define another new quantum number.

H.2 Magnetic Bloch wave function

Below, we attempt to build a Bloch wave function based on the LL wave function Eq. (3.18). The result of applying a magnetic translation operator to the LL wave function is:

$$\hat{\Theta}_{n_1\boldsymbol{a}_1}\psi_n^{k_2} = \psi_n^{k_2+n_1\frac{\sqrt{3}b}{2}\frac{p}{q}}, \quad \hat{\Theta}_{n_2\boldsymbol{a}_2}\psi_n^{k_2} = e^{in_2ak_2}\psi_n^{k_2+n_1\frac{\sqrt{3}b}{2}\frac{p}{q}}.$$

Moreover, the Bloch wave function $|X\rangle$ needs to satisfy the requirement of group theory, where X are quantum numbers, which will be determined later,

$$\hat{\Theta}_{sq\boldsymbol{a}_1}|X\rangle = e^{ik_1qas}|X\rangle, \quad \hat{\Theta}_{rq\boldsymbol{a}_2}|X\rangle = e^{ik_2qar}|X\rangle, \quad s, r \in \mathbb{Z}. \tag{H.2}$$

The summation of the nth LL wave function all over sites is given by the following:

$$\sum_{r,s} \hat{\Theta}_{sq\boldsymbol{a}_1} \hat{\Theta}_{rq\boldsymbol{a}_2} \psi_n^{k_2} = \sum_{r,s} e^{iqark_2} \psi_n^{k_2 + \frac{\sqrt{3}b}{2q} pqs}.$$

To satisfy the requirement, one can multiply the additional phase factor, e^{-ik_2qar} and e^{iqask_1} to complement the two equations of Eq. (H.2) respectively. Furthermore, the argument $k_2 + \frac{\sqrt{3}b}{2q} pqs$ can not cover the entire k_2 axis, because that the magnetic Brillouin zone is $k_2 \in \frac{\sqrt{3}b}{2q}[-\frac{1}{2}, \frac{1}{2}]$; therefore further quantum numbers are needed. It is intuitively to take $v \in [0, pq-1]$, so

$$|n, v, \boldsymbol{k}\rangle = \frac{1}{N^{\frac{3}{2}}} \sum_s e^{i(k_1 qs + k_2 sr)a} \hat{\Theta}_{-qs\boldsymbol{a}_1} \hat{\Theta}_{-rs\boldsymbol{a}_2} \psi_n^{k_2 + \frac{\sqrt{3}b}{2q}(qps+v)},$$

However, considering that there is one additional q-fold degeneracy as given by Eq. (H.1), it is more convenient to set two separate quantum numbers $j \in [0, p-1]$ and $t \in [0, q-1]$ (with the coprime property between p and q guaranteeing that there will be no superposition points), so that the final Bloch wave function is given as follows:

$$\begin{aligned} |^{n,j}_{t,\boldsymbol{k}}\rangle =& \frac{1}{N^{\frac{3}{2}}} \sum_{r,s} e^{i(k_1 qs + k_2 sr)a} \hat{\Theta}_{-qs\boldsymbol{a}_1} \hat{\Theta}_{-rs\boldsymbol{a}_2} \psi_n^{k_2 + \frac{\sqrt{3}b}{2q}(qj+pt)} \\ =& \frac{1}{\sqrt{N}} \sum_s e^{ik_1 qas} \psi_n^{k_2 + \frac{\sqrt{3}}{2}\frac{b}{q}(pqs+jq+tp)}, \end{aligned} \tag{H.3}$$

where the sum runs over $s = -N/2, \cdots, N/2$. This basis is similar to the set of Bloch states for a one-dimensional chain with p sites per elementary unit cell, and multiple atomic orbitals on each site are labelled by the LL index, n. It is easy to confirm that Eq. (H.3) fulfills the magnetic translational group requirement, and has the following properties:

$$\hat{\Theta}_{\boldsymbol{a}_1} |^{n,j}_{t,\boldsymbol{k}}\rangle = |^{n,j}_{t+1,\boldsymbol{k}}\rangle, \quad \hat{\Theta}_{\boldsymbol{a}_2} |^{n,j}_{t,\boldsymbol{k}}\rangle = e^{i\frac{2\pi pt}{q}} e^{i\boldsymbol{k}\cdot\boldsymbol{a}_2} |^{n,j}_{t,\boldsymbol{k}}\rangle.$$

Appendix I

The Berry phase

I.1 Origin and definition of Berry phase

Assuming that an eigenstate, $|n(\boldsymbol{R})\rangle$, of a Hamiltonian $\hat{H}(\boldsymbol{R})$, evolves adiabatically in a circle in a parameter space, $\boldsymbol{R}$, the state evolves in the circle such that it differs by a phase factor from the initial state. This phase factor is the so-called Berry phase Γ_n, which can be expressed as a path integral in the parameter space as follows:

$$\Gamma_n = \int_C d\boldsymbol{R} \cdot \mathbb{A}_n(\boldsymbol{R}), \tag{I.1}$$

where the vector-valued function

$$\mathbb{A}_n(\boldsymbol{R}) = i \langle n(\boldsymbol{R})| \frac{\partial}{\partial \boldsymbol{R}} |n(\boldsymbol{R})\rangle , \tag{I.2}$$

is called the Berry vector potential. Eq. (I.1) shows that, in addition to the dynamical phase, the quantum state will acquire an additional phase Γ_n.

In a two-dimensional parameter space (such as momentum space), one can derive the Berry curvature $\Omega_n(\boldsymbol{k})$ from the Berry vector potential, $\mathbb{A}_n(\boldsymbol{k})$ as follows:

$$\Omega_n(\boldsymbol{k}) = [\boldsymbol{\nabla}_{\boldsymbol{k}} \times \mathbb{A}_n(\boldsymbol{k})]_{k_z}. \tag{I.3}$$

Berry phase can be expressed as a form of flux,

$$\Gamma_n = \oint_S d\boldsymbol{S} \cdot \boldsymbol{\Omega}_n(\boldsymbol{k}). \tag{I.4}$$

In this form, the Berry curvature $\boldsymbol{\Omega}_n(\boldsymbol{k})$ and Berry vector potential $\mathbb{A}_n(\boldsymbol{k})$ resemble a magnetic field $\boldsymbol{B}$ and a magnetic vector potential $\boldsymbol{A}$. The difference is that real space changes to parameter space.

I.2 Berry phase and LLs of graphene

To introduce the impact of Berry phase on the vanishing of the "zero point energy" of LL, following the discussion in reference [92], we consider a normal electron in a magnetic field, with a vector potential $\boldsymbol{A}$. The canonical momentum is replaced by $\boldsymbol{p} = \boldsymbol{k} - e\boldsymbol{A}$, and the semiclassical model of electrons in a magnetic field suggests that $\dot{\boldsymbol{k}} = -e\dot{\boldsymbol{r}} \times \boldsymbol{B}$. Then, coordinate $\boldsymbol{r}$ and momentum $\boldsymbol{p}$ are prescribed by the Bohr-Sommerfeld quantization rule (to ensure a single valued wave function),

$$\oint d\boldsymbol{r} \cdot \boldsymbol{p} = 2\pi \left(n + \frac{1}{2}\right), \tag{I.5}$$

where n is an integer, and the additional fraction $1/2$ accounts for the Maslov Index [187]. Substituting the expression for $\boldsymbol{k}$ into Eq. (I.5) and applying Stokes' theorem, we obtain the following:

$$\frac{\phi}{\phi_0} = n + \frac{1}{2}, \tag{I.6}$$

where $\phi = BS = B\pi r^2$ is the magnetic flux threading the orbit of electron, and $\phi_0 = h/e$ is the flux quantum. One can translate this from real space into momentum space with the relation $\boldsymbol{k} = -e\boldsymbol{r} \times \boldsymbol{B}+$ constant, which is the integral

of the acceleration equation of an electron in a magnetic field.

$$\frac{k^2}{2eB} = n + \frac{1}{2}. \tag{I.7}$$

Now that the momentum is quantized, accordingly, the energy can also be evaluated. Let us consider the free electron gas,

$$E_n = \frac{k^2}{2m} = \left(n + \frac{1}{2}\right)\omega_C, \tag{I.8}$$

where $\omega_C = eB/m$ is the frequency of a cyclotron. Note that the Maslov index is the origin of the "zero point energy" of two-dimensional electron gas.

The vanishing of zero point energy for the LL of graphene occurs because of the existence of the π Berry phase. One Bloch electron cycle in graphene will attain an extra π factor, so the Bohr-Sommerfeld rule for graphene is given as follows:

$$\oint d\boldsymbol{r} \cdot \boldsymbol{p} + \pi = 2\pi\left(n + \frac{1}{2}\right), \tag{I.9}$$

Obviously, the π Berry phase cancels the effect of the Maslov Index and zero point energy. Thus, the LL spectrum of graphene features a zeroth LL independent of the strength of the magnetic field as follows:

$$E_n = vk = v\sqrt{2neB}, \qquad n = 0, 1, 2, \cdots \tag{I.10}$$

I.3 Berry phase in Bloch bands

An electron in a crystal can be described by the Bloch wave function $\psi_{n\boldsymbol{q}}(\boldsymbol{r})$, where $\boldsymbol{q}$ is the crystal momentum, located in the first Brillouin zone. Following the discussion in reference [91], we use the transformed eigenstate

$$u_{n\boldsymbol{q}}(\boldsymbol{r}) = e^{-i\boldsymbol{q}\cdot\boldsymbol{r}}\psi_{n\boldsymbol{q}}(\boldsymbol{r}), \tag{I.11}$$

to satisfy the strict periodic boundary condition, $u_{n\boldsymbol{q}}(\boldsymbol{r}+\boldsymbol{a}) = u_{n\boldsymbol{q}}(\boldsymbol{r})$, where $\boldsymbol{a}$ is a lattice vector. Following Eq. (I.11), the Bloch state's Berry phase, Berry curvature and Berry vector potential are given as follows:

$$\Gamma_n = \oint_C d\boldsymbol{q} \cdot \mathbb{A}_n, \quad \Omega_n(\boldsymbol{q}) = \boldsymbol{\nabla}_{\boldsymbol{q}} \times \mathbb{A}_n, \quad \mathbb{A}_n = \langle u_n(\boldsymbol{q})| \, i\boldsymbol{\nabla}_{\boldsymbol{q}} \, |u_n(\boldsymbol{q})\rangle \, . \tag{I.12}$$

I.4 The calculation of Berry phase for the magnetic minibands of the graphene/h-BN heterostructure

The Berry phase Γ_m, Berry vector potential $\mathbb{A}_m$ and Berry curvature $\boldsymbol{\Omega}_m(\boldsymbol{k})$, Eq. (I.12), of the third generation of DPs of moiré perturbed graphene, for a circular contour, are expressed in terms of non-orthogonal momenta k_1 and k_2, at $k_1 = k_2 = 0$:

$$\begin{aligned}
&\Gamma_m = i\int_0^{2\pi} d\theta[\cos(\theta+\frac{\pi}{6})\langle u_m(\boldsymbol{k})|\partial_{k_1}u_m(\boldsymbol{k})\rangle - \cos(\theta-\frac{\pi}{6})\langle u_m(\boldsymbol{k})|\partial_{k_2}u_m(\boldsymbol{k})\rangle],\\
&\mathbb{A}_m = i\hat{i}\langle u_m(\boldsymbol{k})|\partial_{k_1}u_m(\boldsymbol{k})\rangle + i\hat{j}\langle u_m(\boldsymbol{k})|\partial_{k_2}u_m(\boldsymbol{k})\rangle,\\
&\boldsymbol{\Omega}_m(\boldsymbol{k}) = -2\mathrm{Im}[\langle\partial_{k_1}u_m(\boldsymbol{k})|\partial_{k_2}u_m(\boldsymbol{k})\rangle],
\end{aligned}$$

where

$$\begin{aligned}
u_m(\boldsymbol{k}) &= e^{-i\boldsymbol{k}\cdot\boldsymbol{r}}\sum_n C_m^{n,j}(\boldsymbol{k})|_{0,k}^{n,j}\rangle\\
&= \sum_{njs} C_m^{n,j}(\boldsymbol{k})\frac{e^{ik_1(qas-x_1)}e^{x_2\frac{\sqrt{3}}{2}b(ps+j)}}{\sqrt{NL(2-\delta_{0n})}}\begin{pmatrix}\varphi_{|n|}(z(s,j))\\ -e^{i\frac{2\pi}{3}}\frac{n}{|n|}\varphi_{|n|-1}(z(s,j))\end{pmatrix},
\end{aligned}$$

with $z(s,j) = \frac{\sqrt{3}}{2}\frac{x_1}{\lambda_B} - (k_2 + \frac{\sqrt{3}}{2}b(ps+j))$, $C_m^{n,j}(\boldsymbol{k})$ being the coefficient of the mth bands, which comes from the eigenvector of the Heisenberg matrix.

One can calculate the distribution of the Berry curvature in the Brillouin zone

using

$$\langle\partial_{k_1}u_m(\boldsymbol{k})|\partial_{k_2}u_m(\boldsymbol{k})\rangle = \frac{1}{N}\frac{1}{\sqrt{3}}\sum_{n_1,n_2,j,s}\frac{1}{\sqrt{(2-\delta_{n_10})(2-\delta_{n_20})}}$$
$$\times[\mathbb{G}^{j,s}_{m,n_1}(\partial_{k_2}C^{n_2,j}_m(\boldsymbol{k}))\sqrt{3}\delta_{|n_1|,|n_2|}(1+\frac{n_1n_2}{|n_1n_2|})$$
$$-\mathbb{G}^{j,s}_{m,n_1}C^{n_2,j}_m(\boldsymbol{k})\lambda_B\sqrt{3}\delta_{|n_1|,|n_2|-1}(\sqrt{2|n_2|}+\frac{n_1n_2}{|n_1n_2|}\sqrt{2(|n_2|-1)})$$
$$+\mathbb{G}^{j,s}_{m,n_1}C^{n_2,j}_m(\boldsymbol{k})\lambda_B(1+\frac{i}{\sqrt{3}})\sqrt{\frac{3}{2}}(\mathbb{F}^{|n_2|,1}_{|n_1|}+\frac{n_1n_2}{|n_1n_2|}\mathbb{F}^{|n_2|-1,1}_{|n_1|-1})$$
$$+\frac{i2\lambda_B}{\sqrt{3}}C^{n_1,j*}_m(\boldsymbol{k})(\partial_{k_2}C^{n_2,j}_m(\boldsymbol{k}))\sqrt{\frac{3}{2}}(\mathbb{F}^{|n_2|,1}_{|n_1|}+\frac{n_1n_2}{|n_1n_2|}\mathbb{F}^{|n_2|-1,1}_{|n_1|-1})$$
$$-\frac{i2\lambda_B}{\sqrt{3}}C^{n_1,j*}_m(\boldsymbol{k})C^{n_2,j}_m(\boldsymbol{k})\lambda_B\sqrt{\frac{3}{2}}(\sqrt{2|n_2|}\mathbb{F}^{|n_2|-1,1}_{|n_1|}+\frac{n_1n_2}{|n_1n_2|}\sqrt{2(|n_2|-1)}\mathbb{F}^{|n_2|-2,1}_{|n_1|})$$
$$+\frac{i2\lambda_B^2}{\sqrt{3}}C^{n_1,j*}_m(\boldsymbol{k})C^{n_2,j}_m(\boldsymbol{k})(1+\frac{i}{\sqrt{3}})\sqrt{\frac{3}{2}}(\mathbb{F}^{|n_2|,2}_{|n_1|}+\frac{n_1n_2}{|n_1n_2|}\mathbb{F}^{|n_2|-1,2}_{|n_1|-1})$$
$$+\frac{i2\lambda_B^2}{\sqrt{3}}C^{n_1,j*}_m(\boldsymbol{k})C^{n_2,j}_m(\boldsymbol{k})(1+\frac{i}{\sqrt{3}})\frac{1}{2}\delta_{|n_1|,|n_2|}(1+\frac{n_1n_2}{|n_1n_2|})],$$

where

$$\mathbb{G}^{j,s}_{m,n_1} = (\partial_{k_1}C^{n_1,j}_m)^* - iC^{n_1,j*}_m(qas-\frac{2\lambda_B^2}{\sqrt{3}}(k_2+\frac{\sqrt{3}}{2}b(ps+j))),$$
$$\mathbb{F}^{n_2,n_3}_{n_1} = \begin{cases}\frac{\sqrt{n_1!n_2!n_3!}}{(\frac{n_1+n_2-n_3}{2})!(\frac{n_2+n_3-n_1}{2})!(\frac{n_3+n_1-n_2}{2})!} & \text{For } n_1+n_2+n_3=\text{even}\\ 0 & \text{For } n_1+n_2+n_3=\text{odd}\end{cases}$$

In the case of a small gap induced by $u_0 = 1/1000$, the Berry phase is approximately π. With the increasing of the size of the gap, the Berry phase rapidly decreases, but still occupies at least half of π in the region of the tip of the cone. This confirms that the LL structure shown in Fig. 3.8 is a manifestation of (gapped) Dirac Hamiltonian. In the ideal case, where $u_0 = u_1 = 0$, $u_3 = 0.15$, as shown in the zeroth LL in the bottom panel of Fig. 3.12, the Berry phase of an electron in a finite magnetic field in a moiré superlattice will be exactly π.

For practical numerical calculation of the Berry phase, there are some points that need to be mentioned. First, the gauge choice for $C^{n,j}_m(\boldsymbol{k})$ should be continuous in $\boldsymbol{K}$. Otherwise, in the procedure for the diagonalization of the matrix, the

eigenfunctions corresponding to degenerate eigenvalues may cause an artificial discontinuity in the derivatives of the eigenstates because they appear in the wrong sequence.

Secondly, because most of the Berry phase is concentrated at the very centre of the secondary DP, the numerical calculation of derivatives needs to evaluate the difference in the eigenstates in a very small step. One could appeal to the numerical method of multi-points interpolation to increase the accuracy in the vicinity of the secondary DP.

Appendix J

Electronic transport in mesoscopic systems

J.1 Landauer-Büttiker (LB) formula

Consider an one-dimensional conductor of length L, there is only one transverse mode of electron with wave number k, and the probability density per unit length is $n = 1/L$. So the corresponding electronic current (the charge of electron is $-e$) is

$$I = -\sum_k env_k = -\frac{2e}{h}\int dE, \tag{J.1}$$

where the velocity of the electron $v_k = dE/(dk\hbar)$, factor 2 comes from the spin degeneracy, and relation $\sum_k(\cdots) = (L/2\pi)\int(\cdots)dk$ used.

Next, let us consider that two conductors are connected, we label them as left and right side of the interface, and all states in left (right) conductor are filled to chemical potential μ_L (μ_R). Thus, the current flow is due to the electrons with energies in the range between μ_L and μ_R (and linear response holds [117]). The

injected current from left side is

$$I_L^{\text{in}} = -\frac{2e}{h}\int_{\mu_R}^{\mu_L} dE = \frac{2e^2}{h}\frac{\mu_R - \mu_L}{e}. \tag{J.2}$$

If the contact is not reflectless, the electron has a probability to be reflected, thus we use transmission probability T to describe this. Thus, the outgoing current in the right side and the reflected current in the left side are

$$I_R^{\text{out}} = \frac{2e^2}{h}\frac{\mu_R - \mu_L}{e}T, \quad I_L^{\text{out}} = \frac{2e^2}{h}\frac{\mu_R - \mu_L}{e}(1-T). \tag{J.3}$$

The total current flow though the interface is

$$I = I_L^{\text{in}} - I_L^{\text{out}} = \frac{2e^2}{h}\frac{\mu_R - \mu_L}{e}T. \tag{J.4}$$

This is the origin of Eq. (6.1).

Since the electronic voltage drop across the conductor is $V = (\mu_L - \mu_R/(-e)$, and the conductance is $G = I/V$, thus,

$$G = \frac{2e^2}{h}T. \tag{J.5}$$

This is the Landauer-Büttiker (LB) formula for a single-mode wire at zero temperature.

If there are multiple transverse modes in the conductor, and the temperature is not zero, then the transmission probability of each channel, will be a function of transverse momentum(k_y), temperature $\mathbb{T}$, Fermi level ϵ_F, energy ϵ or other variables, $T(k_y, \mathbb{T}, \epsilon_F, \epsilon, \cdots)$, and the conductance is

$$G = \frac{2e^2}{h}\bar{T}, \quad \bar{T} = \sum_{k_y} T(k_y, \mathbb{T}, \epsilon_F, \epsilon, \cdots), \tag{J.6}$$

where $\bar{T}$ is total transmission probability for all channels.

If there are more than two terminals, then the current flow going out from the

terminal p is the summation of pure current from all the other terminals:

$$I_L = \frac{2e}{h} \sum_M [\bar{T}_{ML}\mu_L - \bar{T}_{LM}\mu_M]. \tag{J.7}$$

Here, $\bar{T}_{LM}$ is the total transmission probability from terminal M to terminal L. The conductance between two terminals from L to R is

$$G_{RL} = \frac{2e}{h}\bar{T}_{RL}. \tag{J.8}$$

In the calculation of this thesis, the LB formula of multi-terminal and finite temperature is not referred. Further detailed discussion can be found in [117].

J.2 Important physical properties in transport problem

In order to use the Landauer formula, it is necessary to calculate the total transmission probability $\bar{T}$, and this can be archived by using scattering theory [117]. Basically, total transmission probability $\bar{T}_{RL}$ (suppose here we have only left and right two terminals) is the summation over all transmission probability between transverse modes in different terminals, i.e.

$$\bar{T}_{RL} = \sum_{m\in L}\sum_{n\in R} T_{nm}, \quad T_{nm} = |s_{nm}|^2 . \tag{J.9}$$

Here, n and m are indexes of different transverse modes in left and right side, respectively. T_{nm} is the transmission probability between transverse modes n in right contact and m in left contact. s_{nm} is the transmission coefficients between transverse modes n in right contact and m in left contact, which is also the element of scattering matrix $S_{RL} = [s_{nm}]$.

Thus, the Landau conductance and conductivity are

$$G = g_s g_v \frac{e^2}{h} \mathrm{tr}\left[S_{RL}^\dagger S_{RL}\right], \quad \sigma = \frac{L}{W} G. \tag{J.10}$$

Here, g_s and g_v are degeneracy indices for spin and valley, respectively. L and W is the length and width of two-dimensional materials. The noise in electronic transport problem can be understood as the interference between different channels, so it can not be expressed by conductivity, and it is given by

$$P = \mathrm{tr}\left[S_{RL}^\dagger S_{RL}(1 - S_{RL}^\dagger S_{RL})\right]. \tag{J.11}$$

The Fano factor [134] measures the shot noise [1]. Fano factor is given by

$$F = 1 - \frac{\mathrm{tr}\left[S_{RL}^\dagger S_{RL} S_{RL}^\dagger S_{RL}\right]}{\mathrm{tr}\left[S_{RL}^\dagger S_{RL}\right]}. \tag{J.12}$$

The Fano factor of clean graphene (and BLG) is the same as diffusive metal, 1/3 [29]. Both Fano factor and conductivity are important parameters for a material of a detector.

So the key to solve the problem is generalized into obtaining the scattering matrix S_{RL}.

J.3 Scattering matrix

In quantum mechanics, an electron is described by a wave function. Using the superposition principle, one can solve the scattering problem of an electron incident on a scatterer [133].

Consider an incident electron wave function, Ψ^{in}, and outgoing electron wave

[1] Shot noise is the noise caused by fluctuation that a detector receives. Once the signal is weak, amount of incoming particles is few, and the fluctuation matters. We use shot noise to describe this noise and Fano factor to describe the distribution of related events, which is different from Poisson distribution, as these events in Poisson distribution are not related to each other. It can be understood as noise to signal ratio.

function, Ψ^{out}, which can be expressed as follows:

$$\Psi^{in} = \sum_m a_m \psi_m^{in}, \quad \Psi^{out} = \sum_n b_n \psi_n^{out}, \tag{J.13}$$

where a_m and b_n are coefficients and ψ_m^{in} and ψ_n^{out} are the basis functions constituting the full orthogonal basis. For a simple incident wave

$$\Psi^{in} = \psi_1^{in}, \tag{J.14}$$

where a_1 is constant, the quantum-mechanical transition amplitude from state ψ_1^{in} to the state ψ_n^{out} is denoted using s_{n1} by

$$\psi_1^{in} = \sum_n \left\langle \psi_n^{out} | \psi_1^{in} \right\rangle \psi_n^{out} = \sum_n s_{n1} \psi_n^{out}. \tag{J.15}$$

The (first-indexed) outgoing wave is,

$$\Psi_1^{out} = \sum_n s_{n1} \psi_n^{out}. \tag{J.16}$$

Therefore, for an arbitrary incident wave,

$$\begin{aligned} \Psi^{in} &= \sum_m a_m \psi_m^{in}, \quad \Psi_m^{out} = \sum_n s_{nm} \psi_n^{out}, \\ \Psi^{out} &= \sum_m a_m \Psi_m^{out} = \sum_m a_m \sum_n s_{nm} \psi_n^{out} \equiv \sum_n \psi_n^{out}, \end{aligned} \tag{J.17}$$

where a_m is the coefficient of the basis. Thus,

$$b_n = \sum_m s_{nm} a_m. \tag{J.18}$$

If the coefficients b_n and a_m are collected into vector columns,

$$\hat{b} = \begin{pmatrix} b_1 \\ b_2 \\ \cdots \end{pmatrix} \quad \hat{a} = \begin{pmatrix} a_1 \\ a_2 \\ \cdots \end{pmatrix}, \tag{J.19}$$

then the quantities s_{nm} can be treated as a matrix:

$$S = [s_{nm}], \tag{J.20}$$

which is the so-called scattering matrix. Note that a summation over each line and each column of the transmission probability matrix $T_{nm} = |s_{nm}|^2$ are equal to unity, because of flux conservation. In other words, the summation of the amplitude probability of reflected and transmitted wave equals that of incident wave, i.e. unit. This can be used to check the validity of our numerical calculations.

Depending on the different arrangements of the coefficient columns $\hat{a}$ and $\hat{b}$, the scattering matrices can be divided into an s-matrix or a t-matrix. In each scatterer, if all coefficients (both inwards and outwards) of each side are gathered into coefficient columns, this scattering matrix is the so-called "t-matrix". On the other hand, if the coefficients are classified as inwards and outwards to the scatterer (irrespective of their sides), the scattering matrix is the so-called "s-matrix". The advantage of the t-matrix is that it is analytically friendly and can easily conjoins successive transmission process, but it is numerically unstable because of the potential propagation of evanescent modes. In contrast, the use of the s-matrix is more complicated, but it is generally stable.

As shown in Fig. 6.1, there are four wave functions at the left interface between the left lead and nano ribbon (the incident wave function is leftward). If the $\hat{a}$ comprises the coefficients of $\psi_L^>$ and $\psi_L^<$ (left side), and $\hat{b}$ comprises the coefficients of $\psi_C^>$ and $\psi_C^<$ (right side), then the constructed matrix $[S_{CL}]$ is the t-matrix. If $\hat{a}$ comprises the coefficients of $\psi_L^>$ and $\psi_C^<$ (inward to the surface), and $\hat{b}$ comprises

the coefficients of $\psi_C^>$ and $\psi_L^<$ (outward from the surface), then the constructed matrix $[S_{CL}]$ is the s-matrix.

J.4 Mode matching

Because the probability of electron is continuous everywhere, one can match the outgoing wave function and the incident wave function to solve the scattering problem of an electron at an interface [133]. .

Commonly, the Schrödinger equation is second-order derivative equation. Because that the electronic probability is continuous, the wave function and its first-order derivates are continuous (one can integrate Schrödinger equation to get a first-order derivative equation). One can get two equations at each interface. For Dirac equation of graphene, it is first-order derivates equation. We do not necessarily get the continuous condition of first-order derivates. So the number of equations we get is halved. However, Dirac equation Eq. (2.19) has 2×2 matrix structure, which provides additional boundary condition. Furthermore, The effective Hamiltonian of BLG in low energy Eq. (2.24) is second order. In principle, we can apply the continuous condition of first-order derivates. An alternative way of matching wave function of BLG is to use the 4×4 Hamiltonian, Eq. (2.22). We replace the continuous condition of first-order derivates by continuous condition of wave function of more sites. In practice, (discontinuous) potential that in the interface may be important to the wave function of dimer sites, so a first-order derivates condition may not be the best choice. That is the reason we chose 4×4 Hamiltonian and corresponding to wave function in our calculation.

J.5 Evanescent and propagating modes

A fundamental equation of mesoscopic transport problem is "Single-band effective mass equation". Its basic idea is to consider necessary band only (normally conduction band), absorb the lattice potential into the effective mass (by expan-

sion at the extreme point in BZ), and discretize the continuous band into several minibands.

Anyway, one can easily extend these ideas into Dirac equation of graphene.

$$[v(i\hbar\nabla + e\boldsymbol{A}) \cdot \sigma\Psi(\boldsymbol{r})] = E\Psi(\boldsymbol{r}). \tag{J.21}$$

Here, $\boldsymbol{A}$ is vector potential and m is the effective mass of quasi electron. The solution (with $\boldsymbol{A} = 0$) can be written in the form

$$\Psi(\boldsymbol{r}) = \begin{pmatrix} \phi_A \\ \phi_B \end{pmatrix} e^{ik_x x} e^{ik_y y}. \tag{J.22}$$

By applying the periodic boundary condition on the wave function along transverse direction, the transverse momentum is given by,

$$k_y = n_y \frac{2\pi}{W}, \tag{J.23}$$

where W is the width of the nano-ribbon. The momentum along longitudinal direction, k_x, is continuous. Thus the continuous band is discretized into several sub-bands,

$$E^2(k_x, n_y) = v^2 \left(k_x^2 + n_y^2 \frac{4\pi^2}{W^2} \right). \tag{J.24}$$

Thus, each wave function referring a discretized k_y is a "transverse mode" or a "channel".

From this point of view, we can distinguish "evanescent mode" and "propagating modes". In Eq. (J.24), if $E^2 < v^2 n_y^2 4\pi^2/W^2$, then we get $k_x^2 < 0$, and this will leads to an imaginary momentum $k_x = i\kappa_x$. Correspondingly, longitudinal plain wave $e^{ik_x x} = e^{-\kappa_x x}$. This wave will decay (or explode, depends on the sign of κ_x) with the increase of length, so it is called evanescent mode. The existence of evanescent mode is the reason of numerical instability of t-matrix. The group

velocity of evanescent mode wave function is zero. Depends on the absolute value of κ_x, evanescent mode may travel through a certain length before it vanishes, but it can not penetrate an infinite length system. Oppositely, the plain wave referring to a real number of k_x is "propagating modes" as it will not decay in propagation.

Appendix K

Methods of accelerating the GF calculation

K.1 Recursive Method and Gauss elimination

The recursive Green function (GF) method [117, 121] follows from the practical demand for efficiently inverting a matrix. It relies on the fact that interactions between atoms are dominated by the nearest neighboring atomic orbitals. It is possible to build a GF atom by atom though a recursive procedure. If the Hamiltonian can be block diagonalized into the following form:

$$H = \begin{pmatrix} H_{11} & V_{12} & 0 & 0 & 0 \\ V_{21} & H_{22} & V_{23} & 0 & 0 \\ 0 & V_{32} & H_{33} & ... & 0 \\ 0 & 0 & ... & ... & V_{m-1m} \\ 0 & 0 & 0 & V_{mm-1} & H_{mm} \end{pmatrix}, \tag{K.1}$$

then the corresponding GF can be derived recursively to have the following form:

$$G = \begin{pmatrix} \begin{pmatrix} G_{11}^{(m)} & ... & ... & G_{1m-1}^{(m)} \\ ... & G_{22}^{(m)} & ... & ... \\ ... & ... & ... & ... \\ G_{m-11}^{(m)} & ... & ... & G_{m-1m-1}^{(m)} \end{pmatrix} & \begin{pmatrix} G_{1m}^{(m)} \\ ... \\ ... \\ G_{m-1m}^{(m)} \end{pmatrix} \\ \begin{pmatrix} G_{m1}^{(m)} & ... & ... & G_{mm-1}^{(m)} \end{pmatrix} & \left(G_{mm}^{(m)}\right) \end{pmatrix}, \tag{K.2}$$

where elements can be recursively expressed as follows:

$$\begin{aligned} G_{mm}^{(m)} &= \left((E - H_{mm}) - V_{mm-1} G_{m-1m-1}^{(m-1)} V_{m-1m}\right)^{-1}, \\ G_{1m}^{(m)} &= -G_{1m-1}^{(m-1)} V_{m-1m} G_{mm}^{(m)}, \\ G_{m1}^{(m)} &= -G_{mm}^{(m)} V_{mm-1} G_{m-11}^{(m-1)}, \\ G_{ab}^{(m)} &= G_{ab}^{(m-1)} + G_{am-1}^{(m-1)} V_{m-1m} G_{mm}^{(m)} V_{mm-1} G_{m-1b}^{(m-1)}. \end{aligned} \tag{K.3}$$

Here, the impact from the $m-1$th slice to the mth slice can be calculated using the GF $G_{m-1,m-1}^{(m-1)}$, where the superscript denotes the $(m-1)$ recursive step, and the subscript indicates the block of the $m-1$th line and $m-1$th column. All expressions start from the first-order GF, $G_{11}^{(1)} = (E - H_{11})^{-1}$. At the mth step, the first evaluated block is $G_{mm}^{(m)}$, which requires the Hamiltonian of the slice m $(E - H_{mm})$, the two corresponding neighboring interaction matrices (V_{1m}, V_{m1}) and the block GF of the $m-1$th slice of the $m-1$ slices system ($G_{m-1m-1}^{(m-1)}$). Once the $G_{mm}^{(m)}$ is obtained, the other block is achievable.

From the perspective of practical application, the most essential block is G_{RL}, in particular, the $G_{m1}^{(m)}$. Less important blocks are G_{11}, G_{1m} and G_{mm}. One can use them to check correctness via the unitary relation of the transmission probability matrix and the transmission function. The next most useful blocks are the diagonal matrices, which will be needed in the calculation of density of states. The rest of the block matrices are useless, calculating them all will drastically slow the calculation. We should necessarily store the very end slice, $G_{m-1m-1}^{(m-1)}$ for $G_{mm}^{(m)}$,

and the other three corner blocks $G^{(m-1)}_{1m-1}$, $G^{(m-1)}_{m-11}$, and $G^{(m-1)}_{11}$ (or even only the left-lower corner if one only need S_{RL}). If one wants the density of states, the diagonal block should be stored, too.

The physical meaning of recursive GF method is intuitive. For our current sliced system, each Hamiltonian matrix block represents the dynamical property of each slice in real space. We know that the $G(\boldsymbol{r}, \boldsymbol{r}')$ represent the response at $\boldsymbol{r}$ to the source at $\boldsymbol{r}'$. For our current sliced situation, $G^{(m)}_{ab}$ represents the response at b to source at a. From this perspective, let us reconsider the expression: $G^{(m)}_{m1} = -G^{(m)}_{mm} V_{mm-1} G^{(m-1)}_{m-11}$. The first one, $G^{(m)}_{m1}$, which represents the response of the right lead to the excitation in the left lead, consists of $G^{(m-1)}_{m-11}$, V_{mm-1} and $G^{(m)}_{mm}$; they represent the excitation generated at the 1st slice; this excitation spreads to the entire conductor until the $m-1$th slice and generates a response at the $m-1$th ($G^{(m-1)}_{m-11}$); then, the excitation affects the next slice mth via the interaction matrix, V_{mm-1}. Finally, the mth slice generates a response to the excitation in itself, in particular, namely $G^{(m)}_{mm}$. Furthermore, we can transform $G^{(m)}_{m1}$ as follows:

$$\begin{aligned} G^{(m)}_{m1} &= -G^{(m)}_{mm} V_{mm-1} G^{(m-1)}_{m-11} \\ &= G^{(m)}_{mm} V_{mm-1} G^{(m-1)}_{m-1m-1} V_{m-1m-2} G^{(m-2)}_{m-21} \\ &= (-1)^m G^{(m)}_{mm} V_{mm-1} G^{(m-1)}_{m-1m-1}. \end{aligned} \tag{K.4}$$

Then, the physical meaning is clearer. A source of excitation at the 1st slice, via V_{21}, it spreads to 2nd slice, then transports on and on, until the very last slice mth, where we denote the response at mth to the source 1st with $G^{(m)}_{m1}$. The second expression is as follows:

$$G^{(m)}_{ab} = G^{(m-1)}_{ab} + G^{(m-1)}_{am-1} V_{m-1m} G^{(m)}_{mm}. \tag{K.5}$$

With the interpretation above, the latter term $G^{(m-1)}_{am-1} V_{m-1m} G^{(m)}_{mm} V_{mm-1} G^{(m-1)}_{m-1b}$ can be understood as the excitation from the bth slice spreading to the mth (which is the new slice) via V_{mm-1}, then spreading from the new mth slice back to the

$m-1$th slice via V_{m-1m}, so we can reasonably understand it as the reflection due to a new slice. The first term in the right hand side of Eq. (K.5), $G_{ab}^{(m-1)}$, obviously represents the response at the bth slice to an excitation at the ath slice without mth slice, so we can understand $G_{ab}^{(m)}$ as a superposition of the old response in the $1 \sim m-1$ slices and the new response generates from the reflection by the new mth slice.

K.2 Matrix decimation

Both the recursive GF technique and the to-be-introduced matrix decimation method originate from the Gauss elimination, which eliminates unnecessary dimensions of a matrix for calculating the transport properties. The recursive technique discussed above only calculates and saves the necessary blocks of GF, so as to avoid the immense computational effort of inverting a huge matrix.

Matrix decimation directly decimates the unnecessary freedom of a huge matrix of a Hamiltonian, but its numerical stability is not as good as that of the recursive technique.

Consider an $N \times N$ matrix $H = E - \hat{H}$. If the lth dimension needs to be decimated, its influence can be effectively expressed as a modification of all elements H_{ij} in this matrix:

$$H_{ij}^{(1)} = H_{ij} + H_{il}(H_{ii} - H_{ll})^{-1} H_{lj}, \tag{K.6}$$

where $H_{ij}^{(1)}$ is the element of a new decimated matrix $H^{(n-1)}$, all related elements will be transformed into an effective form. It is very suitable to treat elements or blocks with only nearest-slice-interactions. The recursive form of this decimation expression is as follows:

$$H_{ij}^{(n)} = H_{ij}^{(n-1)} - \frac{H_{il}^{(n-1)} H_{li}^{(n-1)}}{H_{ll}^{(n-1)}}. \tag{K.7}$$

Because of the fact that decimation is arbitrarily available to any diagonal block (slice) in the matrix, and it does not need to involve the self-energy from the very beginning, as in the recursive GF. Thus, we can decimate all of the extra freedom from the Hamiltonian, i.e. all blocks describing the atomic sites inside the conductor, only leave the blocks describing the atomic sites at the interface. Then, we can connect the effective decimated Hamiltonian to the lead, then calculate the GF with the self-energy of the lead. Finally, if the Hamiltonian of a crystal has longitudinal translational symmetry, then the decimation process can be accelerated.

Appendix L

Several methods of self energy calculation

L.1 Analytical treatment of the self energy of a hexagonal lattice

Because of the contour path integration of the surface GF of graphene, the form of the eigenfunction is hard to determine; therefore, another method is applied [119].

Consider a periodic lead coupled to a central region, which is described by the following Hamiltonian and corresponding eigenfunction as follows:

$$H_{All}\psi_{All} = \begin{pmatrix} ... & ... & 0 & 0 & 0 \\ B_L^\dagger & A_L & V_L & 0 & 0 \\ 0 & V_L^\dagger & H & V_R^\dagger & 0 \\ 0 & 0 & V_R & A_R & B_R^\dagger \\ 0 & 0 & 0 & ... & ... \end{pmatrix} \begin{pmatrix} \psi_L e^{-ik} a_{in} + \tilde{\psi}_L e^{ik} a_{out} \\ \psi_L a_{in} + \tilde{\psi}_L a_{out} \\ \phi \\ \psi_R b_{in} + \tilde{\psi}_R b_{out} \\ \psi_R e^{-ik} b_{in} + \tilde{\psi}_R e^{ik} b_{out} \end{pmatrix}, \quad \text{(L.1)}$$

where A_X is the diagonal block representing each slice of lead, B_X is the interaction between slices of lead, V_X is the interaction between lead and conductor, H itself represents the Hamiltonian of conductor, $a_{in,out}$ and $b_{in,out}$ are the coefficients of wave function, e^{ink} is the longitudinal wave function that provides a phase fac-

tor for each additional slice, ψ_X and $\tilde{\psi}_X$ are the transverse wave function. The corresponding eigenfunction of each slice is in the same line of the vector array. ϕ is the wave function for the conductor, however, it has no particular form because the situation inside the conductor not necessarily known; therefore, we will use the surface wave function to express it.

Let us simplify to collect the terms including a_{in}, a_{out}, b_{in} and b_{out}, which can be expressed using the following:

$$G_{ab}^{(0)} = V_a(E - H)^{-1}V_b^{\dagger}. \tag{L.2}$$

We obtain the following form

$$\begin{pmatrix} a_{out} \\ b_{out} \end{pmatrix} = S \begin{pmatrix} a_{in} \\ b_{in} \end{pmatrix}, \tag{L.3}$$

where the S-matrix is

$$\begin{aligned} S &= -1 + i \begin{pmatrix} \left(-e^{-ik}t_L - G_{LL}^{(0)}\right)\psi_L & -G_{LR}^{(0)}\psi_R \\ -G_{RL}^{(0)}\psi_L & \left(-e^{-ik}t_R - G_{RR}^{(0)}\right)\psi_R \end{pmatrix}^{-1} v_A\Psi_A \\ &= -1 + i\Psi \left(g^{-1} - \begin{pmatrix} G_{LL}^{(0)} & G_{LR}^{(0)} \\ G_{RL}^{(0)} & G_{RR}^{(0)} \end{pmatrix} \right)^{-1} v_A\Psi_A, \end{aligned} \tag{L.4}$$

where $g_X = -\frac{1}{t}\psi_X e^{ik}\psi_X$, and notify:

$$\begin{aligned} v_A &= \begin{pmatrix} v_L & 0 \\ 0 & v_R \end{pmatrix}, \; g_A = \begin{pmatrix} g_L & 0 \\ 0 & g_R \end{pmatrix}, \\ \Psi_A &= \begin{pmatrix} \psi_L & 0 \\ 0 & \psi_R \end{pmatrix}, \; V_A = \begin{pmatrix} V_L \\ V_R \end{pmatrix}. \end{aligned} \tag{L.5}$$

Therefore, in the space of lead,

$$\begin{pmatrix} G_{LL}^{(0)} & G_{LR}^{(0)} \\ G_{RL}^{(0)} & G_{RR}^{(0)} \end{pmatrix} = V_A(E-H)^{-1}V_A^\dagger \tag{L.6}$$

Then,

$$\begin{aligned} S &= -1 + i\Psi_A \left(g_A^{-1} - V_A(E-H)^{-1}V_A^\dagger \right)^{-1} v\Psi_A \\ &= -1 + i\Psi_A g_A \Psi_A v_A + i\Psi_A g_A V_A \left(E - H - V_A^\dagger g_A V_A \right)^{-1} V^\dagger g \Psi v \\ &= -1 + i\Psi_A \frac{V_A}{t} \left(E - H - V^\dagger g_A V_A \right)^{-1} \frac{V_A^\dagger}{t} \Psi_A v_A. \end{aligned} \tag{L.7}$$

Finally, the self energy part is given as follows:

$$\Sigma = V_A^\dagger g_A V_A. \tag{L.8}$$

L.2 Amplitude transfer matrix method

This section will involve the amplitude transfer matrix (ATM). Based on its fundamental idea, we will discuss the accelerated amplitude transfer matrix (AATM) as our main application. If the reader wants to know more about this numerical method, we recommend an excellent review [127].

Define the amplitude transfer matrix T_+, T_- which represents the amplitude of a unit source ($G_{n,m}$) to the right ($G_{n+1,m}$) or left ($G_{n-1,m}$) as follows:

$$\begin{aligned} G_{n+1,m} &= T_+ G_{n,m} \quad \text{for} \quad n \geq m, \\ G_{n-1,m} &= T_- G_{n,m} \quad \text{for} \quad n \leq m, \end{aligned} \tag{L.9}$$

where $G_{n,m}$ is the matrix block at n, m. Thus, the definition of the GF in the form of the multiplication of matrix $G\tilde{H} = I$, where $\tilde{H} = E - H$, yields the following:

$$\tilde{H}_1 G_{10} + \tilde{H}_0 G_{00} + \tilde{H}_{-1} G_{-10} = -1, \tag{L.10}$$

where $\tilde{H}_1 = \tilde{H}_{n,n+1}$, $\tilde{H}_0 = \tilde{H}_{n,n}$ and $\tilde{H}_{-1} = \tilde{H}_{n,n-1}$, so

$$G_{00} = -(\tilde{H}_1 T_+ + \tilde{H}_0 + \tilde{H}_{-1} T_-)^{-1}. \tag{L.11}$$

Furthermore, in the case of left and right end surfaces, the T_+ and T_- matrices will vanish. Therefore we obtain the boundary condition as the right surface GF, G_{00}^{RS}, and the left surface GF, G_{00}^{LS} respectively (the superscripts "RS" and "LS" denote the right surface and the left surface, and are not to be confused with the "retarded" GF) as follows:

$$\begin{aligned} G_{00}^{RS} &= -\left(\tilde{H}_1 T_+ + \tilde{H}_0\right)^{-1}, \\ G_{00}^{LS} &= -\left(\tilde{H}_0 + \tilde{H}_{-1} T_-\right)^{-1}, \end{aligned} \tag{L.12}$$

if one sets $n' = 0$ and $n \neq 0$,

$$\begin{aligned} \tilde{H}_0 G_{n,0} &= -\tilde{H}_{-1} G_{n-1,0} - \tilde{H}_1 G_{n+1,0} \\ G_{n,0} &= -\tilde{H}_0^{-1}\left(\tilde{H}_{-1} G_{n-1,0} + \tilde{H}_1 G_{n+1,0}\right) \end{aligned} \tag{L.13}$$

Let us apply the definition of T_+ (T_-) in the case of $n > 0$ ($n < 0$), so that the recursive expression can be given as follows:

$$\begin{aligned} T_+^{(n+1)} &= \left(1 - \nu_0 T_+^{(n)}\right)^{-1} \mu_0, \\ T_-^{(n+1)} &= \left(1 - \mu_0 T_-^{(n)}\right)^{-1} \nu_0, \end{aligned} \tag{L.14}$$

where $\mu_0 = -\tilde{H}_0^{-1}\tilde{H}_{-1}$ and $\nu_0 = -\tilde{H}_0^{-1}\tilde{H}_1$. The initial input can be given as $T_+^{(0)} = T_-^{(0)} = 0$. Thus, the transfer matrices T_+ and T_- can be evaluated for as many slices as possible to simulate the effect of a semi-infinite lead. After we obtain the T_+ and T_- that fulfills our precise demand, we can substitute them into (L.12) to obtain the surface GF that we want.

There is one critical point in the general numerical calculation, in particular,

we know that the entire matrix of the conductor is real, but after many inversions, the real matrix will diverge. Therefore, we have to add a small imaginary part to the energy as $E + i\eta$ to avoid the divergence of the inverted matrix. The bigger η is, the faster convergence but the lower precision will be and vice versa.

L.3 The accelerated amplitude transfer matrix method

The ATM method is not difficult to understand, and it has a clearly physical meaning [127]; however it has the downside of low convergent speed. Therefore, the accelerated amplitude transfer matrix (AATM) is developed, on the basis of the same concept as ATM. Substituting μ_0 ν_0 into (L.13), one can obtain the following:

$$G_{n,0} = \mu_0 G_{n-1,0} + \nu_0 G_{n+1,0}. \tag{L.15}$$

Applying (L.9), this becomes

$$G_{n,0} = \mu_0 T_- G_{n-2,0} + \nu_0 T_+ G_{n+2,0}. \tag{L.16}$$

Therefore, $G_{n,0}$ is related to $G_{n\pm2,0}$ now. Now, if we continue this process to relate the $G_{n,0}$ to $G_{n\pm i,0}$, one can evaluate the recursive expression as follows:

$$G_{n,0} = \mu_i G_{n-2^i,0} + \nu_0 G_{n+2^i,0}. \tag{L.17}$$

where

$$\begin{aligned} \mu_i &= \left(1 - \mu_{i-1}\nu_{i-1} - \mu_{i-1}\nu_{i-1}\right)^{-1} \mu_{i-1}^2, \\ \nu_i &= \left(1 - \mu_{i-1}\nu_{i-1} - \mu_{i-1}\nu_{i-1}\right)^{-1} \nu_{i-1}^2, \end{aligned} \tag{L.18}$$

For (L.17), let us take $n = 2^i$; then we can write each expression for $i = 1, 2, ...n$:

$$\begin{aligned}
i = 0 \quad & G_{1,0} = \mu_0 G_{0,0} + \nu_0 G_{2,0}, \\
i = 1 \quad & G_{2,0} = \mu_1 G_{0,0} + \nu_0 G_{4,0}, \\
i = 2 \quad & G_{4,0} = \mu_2 G_{0,0} + \nu_0 G_{8,0}, \\
& \quad ... \qquad\qquad ... \\
i = j \quad & G_{2^j,0} = \mu_j G_{0,0} + \nu_0 G_{2^{j+1},0}.
\end{aligned} \tag{L.19}$$

Now, we plug each equation in reverse order, i.e. plug ith into $i-1$th, in ith which makes the Matrix ν_i is arbitrarily small, so that we can obtain expressions for $G_{1,0}$ and $G_{0,0}$ as follows:

$$\begin{aligned}
G_{1,0} &= T_+ G_{0,0}, \\
T_+ &= \mu_0 + \nu_0\mu_1 + \nu_0\nu_1\mu_2 + ... + \nu_0\nu_1...\nu_{i-1}\mu_i + ...
\end{aligned} \tag{L.20}$$

If one takes $n = -2^i$, after a similar process,

$$\begin{aligned}
G_{-1,0} &= T_- G_{0,0}, \\
T_- &= \nu_0 + \mu_0\nu_1 + \mu_0\mu_1\nu_2 + ... + \mu_0\mu_1...\mu_{i-1}\nu_i + ...
\end{aligned} \tag{L.21}$$

Combining (L.20), (L.21) and (L.18), we can calculate T_+ and T_- in a more efficient way.

L.4 Pre-basis semi-analytical method

Following the discussion in [122, 123], for the given two-terminal setup, in the case of the preservation of time-reversal symmetry, the entire matrix can be given as,

$$\mathbb{H} = \begin{pmatrix} ... & H_1 & 0 & 0 & 0 \\ H_{-1} & H_0 & H_{ML} & 0 & 0 \\ 0 & H_{ML}^{\dagger} & H_M & H_{MR} & 0 \\ 0 & 0 & H_{MR}^{\dagger} & H_0 & H_1 \\ 0 & 0 & 0 & H_{-1} & ... \end{pmatrix}, \tag{L.22}$$

where H_M is the Hamiltonian of the conductor, H_{MR} and H_{ML} are the interaction matrices between the conductor and the first slice on the right and left hand side lead. H_0 and $H_{\pm 1}$ are the blocks for the lead and the interaction between other slices and the lead, respectively. For an orthogonal basis set, the overlap matrix $\mathbb{S}$ has the same structure as $\mathbb{H}$, but in the following discussion, we will remain in the region of the orthogonal basis, so that all diagonal blocks S in $\mathbb{S}$ are I and the rest are 0.

From the Schródinger equation, $(\mathbb{H} - E\mathbb{S})\Phi = 0$, in the region of the lead, we define $\mathbb{K}_0 = H_0 - E$, $\mathbb{K}_1 = H_1$, $\mathbb{K}_{-1} = H_{-1}$ and $\Phi = (..., n_k^{1/2} e^{ikz}\phi_k, ...)$.

We construct a new $2N \times 2N$ matrix,

$$\mathbb{M} = \begin{pmatrix} -K_1^{-1}K_0 & -K_1^{-1}K_0 \\ I_N & 0 \end{pmatrix}. \tag{L.23}$$

For its $2N$ $1 \times 2N$ eigenvectors, the first N-lines of each eigenvectors are simply the eigenvectors, ϕ_k, of H_0, and the $2N$ eigenvalues, $e^{ik(E)}$, give the wave vector $k(E)$ in the lead for a given E. Therefore, once K_1 becomes invertible, this method can be used. If it is not, an extra decimation step is needed, and then we can perform the next step. But for now, we will consider K_1 to be invertible.

Based on the $2N$ eigenvalues, $e^{ik_n(E)}$, where $n \in [1, ..., 2N]$ and the $2N$ eigen-

vectors ψ_{k_n}, we can obtain the velocity of the waves and distinguish their propagation directions, and, based on the complexity of k_n, know whether the waves are evanescent. This can be expressed as follows:

$$v_{k_n} = i\phi_{k_n}^{\dagger}(H_1 e^{ik_n} - H_{-1}e^{-ik_n})\phi_{k_n}, \tag{L.24}$$

where ϕ_{k_n} are the first N components of ψ_{k_n}. Based on whether $v < 0$ or $v > 0$, the $2N$ wave can be divided into left-going ($<$) and right-going ($>$) groups.

The surface GF is given as follows:

$$\begin{aligned} G_L &= [I_N - \sum_{n_<,n_>}^{N,N} \phi_{k_n^<} e^{-ik_n^<} \phi_{k_n^<}^{\dagger} \phi_{k_n^>} e^{ik_n^>} \phi_{k_n^>}^{\dagger}]\mathbb{V}^{-1}, \\ G_R &= [I_N - \sum_{n_<,n_>}^{N,N} \phi_{k_n^>} e^{ik_n^>} \phi_{k_n^>}^{\dagger} \phi_{k_n^<} e^{-ik_n^<} \phi_{k_n^<}^{\dagger}]\mathbb{V}^{-1}, \\ \mathbb{V} &= K_1^{\dagger}[\sum_{n_>}^{N} \phi_{k_n^>} e^{-ik_n^>} \phi_{k_n^>}^{\dagger} - \sum_{n_<}^{N} \phi_{k_n^<} e^{-ik_n^<} \phi_{k_n^<}^{\dagger}]. \end{aligned} \tag{L.25}$$

Then, one can obtain the self-energy simply from the surface GF.

If K_1 is non-invertible, one needs to apply singular value decomposition to H_1 to squeeze the unnecessary dimensions of the matrix. In LAPACK, this command is "zggsvd"; in Mathematica, it is "SingularValueDecomposition". If the dimension of H_1 is N, and the dimension of full rank block of H_1 is R, then this routine will be given as follows:

$$H_{1<N\times N>} = U_{<N\times N>}\Lambda_{1<N\times R>}[0_{<R\times(N-R)>}, W_{<R\times R>}]Q_{<N\times N>}^{\dagger}, \tag{L.26}$$

where $< X \times Y >$ is the dimension of the matrix. The matrix Q is the rotation

matrix we need, we construct a global rotation matrix as follows:

$$\mathbb{Q} = \begin{pmatrix} ... & 0 & 0 & 0 & 0 \\ 0 & Q & 0 & 0 & 0 \\ 0 & 0 & I_M & 0 & 0 \\ 0 & 0 & 0 & Q & 0 \\ 0 & 0 & 0 & 0 & ... \end{pmatrix}. \tag{L.27}$$

The matrix of the entire Hamiltonian can be rotated into the form as follows:

$$\mathbb{Q}^\dagger \mathbb{H} \mathbb{Q} = \begin{pmatrix} ... & Q^\dagger H_1 Q & 0 & 0 & 0 \\ Q^\dagger H_{-1} Q & Q^\dagger H_0 Q & Q^\dagger H_{\mathrm{ML}} & 0 & 0 \\ 0 & H_{\mathrm{ML}}^\dagger Q & H_M & H_{\mathrm{MR}} Q & 0 \\ 0 & 0 & Q^\dagger H_{\mathrm{MR}}^\dagger & Q^\dagger H_0 Q & Q^\dagger H_1 Q \\ 0 & 0 & 0 & Q^\dagger H_{-1} Q & ... \end{pmatrix}. \tag{L.28}$$

Each block will transform into:

$$\begin{aligned} Q^\dagger H_0 Q &= \begin{pmatrix} C_{<(N-R)\times(N-R)>} & B_{<(N-R)\times R>} \\ B^\dagger_{<R\times(N-R)>} & D_{<R\times R>} \end{pmatrix}, \\ Q^\dagger H_1 Q &= \begin{pmatrix} 0_{<N\times(N-R)>} & \tilde{H}_{1<N\times R>} \end{pmatrix}, \\ Q^\dagger H_{-1} Q &= \begin{pmatrix} 0_{<(N-R)\times N>} \\ \tilde{H}^\dagger_{1<R\times N>} \end{pmatrix}. \end{aligned} \tag{L.29}$$

Because the diagonal block, $C_{<(N-R)\times(N-R)>}$, is only semi-connected to block $B_{<(N-R)\times R>}$, but not connected to the block $\tilde{H}_{1<N\times R>}$, it is ideal for decimation. Applying the Eq. (K.7), all C blocks can be decimated, and the smaller

block will be expressed as follows:

$$\begin{pmatrix} Q^\dagger H_0 Q & Q^\dagger H_1 Q \\ Q^\dagger H_{-1} Q & Q^\dagger H_0 Q \end{pmatrix} \overset{\text{All C}}{\rightarrow} \begin{pmatrix} D_{2<R\times R>} & \Theta_{<R\times R>} \\ \Theta^\dagger_{<R\times R>} & \Delta_{<R\times R>} \end{pmatrix},$$
$$\begin{pmatrix} Q^\dagger H_0 Q & Q^\dagger H_1 Q \\ Q^\dagger H_{-1} Q & Q^\dagger H_0 Q \end{pmatrix} \overset{\text{Upper C}}{\rightarrow} \begin{pmatrix} D_{2<R\times R>} & T_{1<R\times N>} \\ T^\dagger_{1<N\times R>} & D_{1<N\times N>} \end{pmatrix},$$
$$\begin{pmatrix} 0 & H_{MR} Q \\ Q^\dagger H^\dagger_{MR} & Q^\dagger H_0 Q \end{pmatrix} \overset{\text{Lower C}}{\rightarrow} \begin{pmatrix} 0_{<N\times N>} & \Theta_{MR<N\times R>} \\ \Theta^\dagger_{MR<R\times N>} & D_{2<N\times N>} \end{pmatrix}. \tag{L.30}$$

Thus, after decimation of all the blocks C, the entire matrix will become

$$\mathbb{Q}^\dagger \mathbb{H} \mathbb{Q} = \begin{pmatrix} ... & \Theta & 0 & 0 & 0 & 0 & 0 \\ \Theta^\dagger & \Delta & T_1 & 0 & 0 & 0 & 0 \\ 0 & T_1^\dagger & D_1 & Q^\dagger H_{LM} & 0 & 0 & 0 \\ 0 & 0 & H^\dagger_{LM} Q & K_M & \Theta_{MR} & 0 & 0 \\ 0 & 0 & 0 & \Theta^\dagger_{MR} & D_2 & \Theta & 0 \\ 0 & 0 & 0 & 0 & \Theta^\dagger & \Delta & \Theta \\ 0 & 0 & 0 & 0 & 0 & \Theta^\dagger & ... \end{pmatrix}. \tag{L.31}$$

Thus, this is a new matrix of the entire Hamiltonian, for which the hopping matrix of the lead Θ is invertible. Using the same technique, the corresponding surface GF is obtained as G_L and G_R in Eq. (L.25), and the self-energy is given as follows:

$$\begin{aligned} \Sigma_L &= H^\dagger_{LM} Q \left(-D_1 - T_1^\dagger G_L T_1 \right)^{-1} Q^\dagger H_{LM}, \\ \Sigma_R &= \Theta_{MR} \left(G_R^{-1} - (D_2 - \Delta) \right)^{-1} \Theta^\dagger_{MR}. \end{aligned} \tag{L.32}$$

Bibliography

[1] P. R. Wallace, Phys. Rev. **71**, 622 (1947).

[2] K. S. Novoselov and A. H. Castro Neto, Phys. Scr. **7**, 014006 (2012).

[3] K. S. Novoselov, A. K. Geim, S. V. Morozov, D. Jiang, Y. Zhang, S. V. Dubonos, I. V. Grigorieva and A. A. Firsov, Science **306**, 666 (2004).

[4] http://www.nobelprize.org.

[5] M. J. Allen, V. C. Tung and R. B. Kaner, Chem. Rev. **110**, 132 (2010).

[6] A. H. Castro Neto, F. Guinea, N. M. R. Peres, K. S. Novoselov and A. K. Geim, Rev. Mod. Phys. **81**, 109 (2009).

[7] M. I. Katsnelson, K. S. Novoselov and A. K. Geim, Nature Physics **2**, 620 (2006).

[8] A. K. Geim and K. S. Novoselov, Nature Materials **6**, 183 (2007).

[9] A. A. Balandin, Nature Materials **10**, 569 (2011).

[10] F. Menges, H. Riel, A. Stemmer, C. Dimitrakopoulos and B. Gotsmann, Phys. Rev. Lett. **111**, 205901 (2013).

[11] R. J. Younga, I. A. Kinlocha, L. Gonga and K. S. Novoselov, Composites Science and Technology **72**, 1459 (2012).

[12] K. M. F. Shahil and A. A. Balandin, Solid State Communications **152**, 1331 (2012).

[13] F. Bonaccorso, Z. Sun, T. Hasan and A. C. Ferrari, Nature Photonics **4**, 611 (2010).

[14] C. Chung, Y. Kim, D. Shin, S. Ryoo, B. Hong and D. Min. Acc. Chem. Res. **46** (10), 2211 (2013).

[15] T. Kuilaa, S. Bosea, A. K. Mishrab, P. Khanraa, N. H. Kimc and J. H. Lee, Progress in Materials Science, **57**(7), 1061, (2012).

[16] K. S. Novoselov, V. I. Fal'ko, L. Colombo, P. R. Gellert, M. G. Schwab and K. Kim, Nature **490**, 192 (2012).

[17] G. W. Semenoff, Phys. Rev. Lett. **53**, 2449 (1984).

[18] P. Avouris, Z. Chen and V. Perebeinos, Nature Nanotechnology **2**, 605 (2007).

[19] M.Koshino and E. McCann, Phys. Rev. B **80**, 165409 (2009).

[20] S. S. Pershoguba and V. M. Yakovenko, Phys. Rev. B **82**, 205408 (2010).

[21] L. Nunes, A.L. Mota and E.C. Marino, Solid State Communications **152**, 2082 (2012).

[22] Y. Hyun, Y. Kim, C. Sochichiu and M. Choi, Journal of Physics: Condensed Matter **24**, 045501 (2012).

[23] N. A. Goncharuk and L. Smĉka, Journal of Physics: Condensed Matter **24**, 185503 (2012).

[24] S. Pershoguba and V. Yakovenko, Phys. Rev. B **86**, 165404 (2012).

[25] N. A. Goncharuk, L. Nádvorník, C. Faugeras, M. Orlita and L. Smĉka, Phys. Rev. B **86**, 155409 (2012).

[26] M. Choi, Y. Hyun and Y. Kim, Phys. Rev. B **84**, 195437 (2011).

[27] M. I. Katsnelson, Eur. Phys. J. B **52**, 151 (2006).

[28] M. I. Katsnelson, Eur. Phys. J. B **51**, 157 (2006).

[29] I. Snyman and C. W. J. Beenakker, Phys. Rev. B. **75**, 045322 (2007).

[30] J. Cserti, A. Csordás and G. Dávid, Phys. Rev. Lett. **99**, 066802 (2007).

[31] K. Kechedzhi, E. H. Hwang and S. Das Sarma, Phys. Rev. B. **86**, 165442 (2012).

[32] M. Koshino and T. Ando, Phys. Rev. B. **73**, 245403 (2006).

[33] S. J. Yuan, H. De Raedt and M. I. Katsnelson, Phys. Rev. B. **82**, 235409 (2010).

[34] H. Xu and T. Heinzel, Phys. Rev. B. **77**, 245401 (2008).

[35] A. Kara, et al, Surface Science Reports **67**, 1, **1**, (2012).

[36] C. R. Dean, A. F. Young, I. Meric, C. Lee, L. Wang, S. Sorgenfrei, K. Watanabe, T. Taniguchi, P. Kim, K. L. Shepard and J. Hone, Nature Nanotech. **5**, 722 (2010).

[37] J. Xue, J. Sanchez-Yamagishi, D. Bulmash, P. Jacquod, A. Deshpande, K. Watanabe, T. Taniguchi, P. Jarillo-Herrero and B. J. LeRoy, Nat. Mater. **10**, 282 (2011).

[38] D. Chen, et al, Chem. Rev., 2012, **112** 11, 6027 (2012).

[39] S. Z. Butler and et al, ACS Nano, **7** (4) 2898, (2013).

[40] L. A. Ponomarenko, R. V. Gorbachev, G. L. Yu, D. C. Elias, R. Jalil, A. A. Patel, A. Mishchenko, A. S. Mayorov, C. R. Woods, J. R. Wallbank, M. Mucha-Kruczynski, B. A. Piot, M. Potemski, I. V. Grigorieva, K. S. Novoselov, F. Guinea, V. Fal'ko and A. K. Geim, Nature **497**, 594 (2013).

[41] C. R. Dean, L. Wang, P. Maher, C. Forsythe, F. Ghahari, Y. Gao, J. Katoch, M. Ishigami, P. Moon, M. Koshino, T. Taniguchi, K. Watanabe, K. L. Shepard, J. Hone and P. Kim, Nature **497**, 598 (2013).

[42] B. Hunt, J. D. Sanchez-Yamagishi, A. F. Young, M. Yankowitz, B. J. LeRoy, K. Watanabe, T. Taniguchi, P. Moon, M. Koshino, P. Jarillo-Herrero and R. C. Ashoori, Science **340**, 1413 (2013).

[43] D. S. L. Abergel, J. R. Wallbank, Xi Chen, M. Mucha-Kruczyński and Vladimir. I. Fal'ko, New Journal of Physics **15** (2013) 123009.

.

[44] S. J. Haigh, et al, Nature Materials **11**, 764 (2012).

[45] K. Watanabe, T. Taniguchi and H. Kanda, Nature Mater. **3**, 404 (2004).

[46] R. Decker, Y. Wang, V. W. Brar, W. Regan, H.-Z. Tsai, Q. Wu, W. Gannett, A. Zettl and M. F. Crommie, Nano Lett. **11**, 2291 (2011).

[47] M. Yankowitz, J. Xue, D. Cormode, J. D. Sanchez-Yamagishi, K. Watanabe, T. Taniguchi, P. Jarillo-Herrero, P. Jacquod and B. J. LeRoy, Nature Phys. **8**, 382 (2012).

[48] R. Bistritzer and A. H. MacDonald, Phys. Rev. B **84** 035440 (2011).

[49] X. Chen, J. R. Wallbank, A. A. Patel, M. Mucha-Kruczyński, E. McCann and V. I. Fal'ko, Phys. Rev. B **89**, 075401 (2014).

[50] G. L. Yu, R. V. Gorbachev, J. S. Tu, A. V. Kretinin, Y. Cao, R. Jalil, F. Withers, L. A. Ponomarenko, B. A. Piot, M. Potemski, D. C. Elias, X. Chen, K. Watanabe, T. Taniguchi, I. V. Grigorieva, K. S. Novoselov, V. I. Fal'ko, A. K. Geim and A. Mishchenko, Nat. Phys **10**, 525 (2014).

[51] K. S. Novoselov, A. K. Geim, S. V. Morozov, D. Jiang, M. I. Katsnelson, I. V. Grigorieva, S. V. Dubonos and A. A. Firsov, Nature (London) **438**, 197 (2005).

[52] Y. Zhang, Y.-W. Tan, H. L. Stormer and P. Kim, Nature (London) **438**, 201 (2005).

[53] R.Z Saito, G. Dresselhaus and M. S. Dresselhaus, *Physical Properties of Carbon Nanotubes* (Imperial College Press, 1998).

[54] F. Guinea, A. H. Castro Neto and N. M. R. Peres, Phys. Rev. B **73**, 245426 (2006).

[55] A. Grúneis, C. Attaccalite, L. Wirtz, H. Shiozawa, R. Saito, T. Pichler and A. Rubio, Phys. Rev. B **78**, 205425 (2008).

[56] R. Saito, M. Fujita, G. Dresselhaus and M. S. Dresselhaus, Phys. Rev. B **46**, 1804 (1992).

[57] M. S. Dresselhaus and G. Dresselhaus, Adv. Phys. **51**, 1 (2002).

[58] N. B. Brandt, S. M. Chudinov and Y. G. Ponomarev, Modern Problems in Condensed Matter Sciences **20**, 1 (1988).

[59] M. S. Dresselhaus, G. Dresselhaus, K. Sugihara, I. L. Spain and H. A. Goldberg, *Graphite Fibers and Filaments*, **5** (Springer-Verlag, Berlin, 1988).

[60] B. Partoens and F. M. Peeters, Phys. Rev. B **74**, 075404 (2006).

[61] S. Bravyi, D. DiVincenzo and D. Loss, Annals of Physics, **326** (10), 2793 (2011).

[62] J. R. Schrieffer and P. A. Wolff, Physical Review **149** (2), 491, (1966).

[63] L. M. Lifshitz, Zh. Exp. Teor. Fiz. **38**, 1565 (1960); Sov. Phys. JETP **11**, 1130 (1960).

[64] A. L. Rakhmanov, A. V. Rozhkov, A. O. Sboychakov and F. Nori, prl **109**, 206801 (2012).

[65] J. Hass, F. Varchon, J. E. Millán-Otoya, M. Sprinkle, N. Sharma, W. A. de Heer, C. Berger, P. N. First, L. Magaud and E. H. Conrad, Phys. Rev. Lett. **100**, 125504 (2008).

[66] F. Varchon, P. Mallet, L. Magaud and J.-Y. Veuillen, Phys. Rev. B **77**, 165415 (2008).

[67] J. Berashevich and T. Chakraborty, Phys. Rev. B **84**, 033403 (2011).

[68] E. McCann and V. I. Fal'ko, Phys. Rev. Lett. **96**, 086805 (2006).

[69] E. McCann, Phys. Rev. B **74**, 161403 (2006).

[70] E. McCann, D.S.L. Abergel and V.I. Fal'ko, Eur. Phys. J. Special Topics **148**, (91) 103 (2007).

[71] H. Raza (eds), etc, *Graphene Nanoelectronics Metrology, Synthesis, Properties and Applications*, (Springer, 2012).

[72] L. D. Landau, Z. Phys. **64**, 629 (1930).

[73] K. von Klitzing, G. Dorda and M. Pepper, Phys. Rev. Lett. **45**, 494 (1980).

[74] R.E. Prange and S.M. Girvin (eds.), *The Quantum Hall Effect*, (Springer-Verlag, New York, 1986).

[75] A.H. MacDonald (ed.), *Quantum Hall Effect: A Perspective*, (Kluwer, Boston, 1989).

[76] J. Nilsson, A. H. Castro Neto, F. Guinea and N. M. R. Peres, Phys. Rev. Lett. **97**, 266801 (2006).

[77] D.S.L. Abergel and V.I. Fal'ko, Phys. Rev. B **75**, 155430 (2007).

[78] T. Ohta, A. Bostwick, J. L. McChesney, T. Seyller, K. Horn and E. Rotenberg, Phys. Rev. Lett. **98**, 206802 (2007).

[79] J. Guettinger, C. Stampfer, F. Molitor, D. Graf, T. Ihn and K. Ensslin, New J. Phys. **10**, 125029 (2008).

[80] M.Koshino and E. McCann, Phys. Rev. B **79**, 125443 (2009).

[81] E. Brown, Phys. Rev. **133**, 1038 (1964).

[82] L. D. Landau and E. M. Lifshitz, *Statistical Physics* (Pergamon Press Ltd., 1980), **9**, part 2, Sec. 60.

[83] D. R. Hofstadter, Phys. Rev. B **14**, 2239 (1976).

[84] D. K. Ferry, Prog. Quant. Electr. **16**, 251 (1992); C. Albrecht, J. H. Smet, D. Weiss, K. von Klitzing, R. Hennig, M. Langenbuch, M. Suhrke, U. Rössler, V. Umansky and H. Schweizer, Phys. Rev. Lett. **83**, 2234 (1999); T. Schlösser, K. Ensslin, J. P. Kotthaus and M. Holland, Europhys. Lett. **33**, 683 (1996); C. Albrecht, J. H. Smet, K. von Klitzing, D. Weiss, V. Umansky and H. Schweizer, Phys. Rev. Lett. **86**, 147 (2001); M. C. Geisler, J. H. Smet, V. Umansky, K. von Klitzing, B. Naundorf, R. Ketzmerick and H. Schweizer, Phys. Rev. Lett. **92**, 256801 (2004).

[85] A. T. N'Diaye, S. Bleikamp, P. J. Feibelman and T. Michely, Phys. Rev. Lett. **97**, 215501 (2006); S. Marchini, S. Günther and J. Wintterlin, Phys. Rev. B **76**, 075429 (2007); P. Sutter, J. T. Sadowski and E. Sutter, Phys. Rev. B **80**, 245411 (2009); M. Sicot, P. Leicht, A. Zusan, S. Bouvron, O. Zander, M. Weser, Y. S. Dedkov, K. Horn and M. Fonin, ACS Nano **6**, 151 (2012) M. Batzill, Surface Science Reports **67**, 83 (2012).

[86] C. Ortix, L. Yang and J. van den Brink, Phys. Rev. B **86**, 081405 (2012).

[87] M. Kindermann, B. Uchoa and D. L. Miller, Phys. Rev. B **86**, 115415 (2012).

[88] J. R. Wallbank, A. A. Patel, M. Mucha-Kruczyński, A. K. Geim and V. I. Fal'ko, Phys. Rev. B, **87**, 245408 (2013).

[89] M. C. Chang and Q. Niu, Phys. Rev. Lett. **75**, 1348 (1995).

[90] D. S. L. Abergel, J. R. Wallbank, X. Chen, M. Mucha-Kruczyński and V. I. Fal'ko, New. J. Phys. **15**, 123009 (2013).

[91] D. Xiao, M. C. Chang and Q. Niu, Rev. Mod. Phys. **82**, 3, (2010).

[92] J. Xue, arXiv:1309.6714v1 (2013).

[93] K. S. Novoselov, E. McCann, S. V. Morozov, V. I. Fal'ko, M. I. Katsnelson, U. Zeitler, D. Jiang, F. Schedin and A. K. Geim, Nature Phys. **2**, 177 (2006).

[94] B. E. Feldman, J. Martin and A. Yacoby, Nature Phys. **5**, 889 (2009).

[95] R. T. Weitz, M. T. Allen, B. E. Feldman, J. Martin and A. Yacoby, Science **330**, 812 (2010).

[96] Y. Zhao, P. Cadden-Zimansky, Z. Jiang and P. Kim, Phys. Rev. Lett. **104**, 066801 (2010).

[97] J. Martin, B. E. Feldman, R. T. Weitz, M. T. Allen and A. Yacoby, Phys. Rev. Lett. **105**, 256806 (2010).

[98] A. S. Mayorov, D. C. Elias, M. Mucha-Kruczyński, R. V. Gorbachev, T. Tudorovskiy, A. Zhukov, S. V. Morozov, M. I. Katsnelson, V. I. Fal'ko, A. K. Geim and K. S. Novoselov, Science **333**, 860 (2011).

[99] J. Velasco Jr, L. Jing, W. Bao, Y. Lee, P. Kratz, V. Aji, M. Bockrath, C. N. Lau, C. Varma, R. Stillwell, D. Smirnov, F. Zhang, J. Jung and A. H. MacDonald, Nature Nanotech. **7**, 156 (2012).

[100] W. Bao, J. Velasco, Jr., F. Zhang, L. Jinga, B. Standleye, D. Smirnov, M. Bockratha, A. H. MacDonald and C. N. Lau, P. Natl Acad. Sci. USA **109**, 10802 (2012).

[101] F. Freitag, J. Trbovic, M. Weiss and C. Schönenberger, Phys. Rev. Lett. **108**, 076602 (2012).

[102] H. J. van Elferen, A. Veligura, E. V. Kurganova, U. Zeitler, J. C. Maan, N. Tombros, I. J. Vera-Marun and B. J. van Wees, Phys. Rev. B **85**, 115408 (2012).

[103] F. Freitag, M. Weiss, R. Maurand, J. Trbovic and C. Schönenberger, Sol. St. Commun. **152**, 2053 (2012).

[104] F. Freitag, M. Weiss, R. Maurand, J. Trbovic and C. Schönenberger, Phys. Rev. B **87**, 161402 (2013).

[105] R. S. Deacon, K.-C. Chuang, R. J. Nicholas, K. S. Novoselov and A. K. Geim, Phys. Rev. B **76**, 081406 (2007).

[106] A. B. Kuzmenko, I. Crassee, D. van der Marel, P. Blake and K. S. Novoselov, Phys. Rev. B **80**, 165406 (2009).

[107] J. Zak, Phys. Rev. **134**, 1602 (1964).

[108] J. Zak, Phys. Rev. **134**, 1607 (1964).

[109] G. Y. Oh, J. Phys.: Condens. Matter **12**, 1539 (2000).

[110] M. Mucha-Kruczyński, Igor L. Aleiner and Vladimir I. Fal'ko, Solid State Communications **151**, 1088 (2011).

[111] D. A. Gradinar, H Schomerus and V. I. Fal'ko, Phys. Rev. B **85**, 165429 (2012).

[112] R. E. Peierls, Z. Phys. **80**, 763 (1933).

[113] C. L. Kane and E. J. Mele Phys. Rev. Lett. **95**, 226801 (2005).

[114] K. Binmorem and J. Davies, *Calculus Concepts and Methods* (Cambridge University, 2007).

[115] M. Gao, G. P. Zhang and Z. Y. Lu, Computer Physics Communications **185**, 856 (2014).

[116] L. Brey and H. A. Fertig, Phys. Rev. B. **73**, 235411 (2006).

[117] S. Datta, *Electronic Transport in Mesoscopic Systems* (Cambridge university, 1995).

[118] D. S. .Fisher and P. A. Lee, Phys. Rev. B **23**, 6851 (1981).

[119] H. .Schomerus, Phys. Rev. B **76**, 045433 (2007).

[120] M. B. Nardelli, Phys. Rev. B **60**, 7828 (1999).

[121] B. A. McKinnon and T. C. Choy, Australian Journal of Physics, **46** 601(1993).

[122] I. Rungger and S. Sanvito, Phys. Rev. B **78**, 035407 (2008).

[123] S. Sanvito, C. J. Lambert, J. H. Jefferson and A. M. Bratkovsky, Phys. Rev. B **59**, 11936 (1999).

[124] M. G. Reuter, T. Seideman and M. A. Ratner, Phys. Rev. B **83**, 085412 (2011).

[125] M. P. López Sancho, J. M. López Sancho and J. Rubio, J. Phys. F: Met. Phys. **14**, 1205 (1984).

[126] M. P. López Sancho, J. M. López Sancho and J. Rubio, J. Phys. F: Met. Phys. **15**, 851 (1985).

[127] J. Velev and W. Butler, J. Phys.: Condens. Matter **16**, 637 (2004).

[128] J. Tworzydo, B. Trauzettel, M. Titov, A. Rycerz and C. W. J. Beenakker, Phys. Rev. Lett. **96**, 246802 (2006).

[129] Y. M. Blanter and I. Martin, Phys. Rev. B **76**, 155433 (2007).

[130] W. Bao, L. Jing, J. Velasco Jr, Y. Lee, G. Liu, D. Tran, B. Standley, M. Aykol, S. B. Cronin, D. Smirnov, M. Koshino, E. McCann, M. Bockrath and C. N. Lau. Nature Physics **7**, 948 (2011).

[131] J. M. B. Lopes dos Santos, N. M. R. Peres and A. H. Castro Neto, Phys. Rev. Lett. **99**, 256802 (2007); Phys. Rev. B **86**, 155449 (2012); R. Bistritzer and A. H. MacDonald, Phys. Rev. B **81**, 245412 (2010); **84**, 035440 (2011); P. Moon and M. Koshino, Phys. Rev. B **85**, 195458 (2012); Z. F. Wang, Feng Liu and M. Y. Chou, Nano Lett. **12**, 3833 (2012).

[132] Y. Hasegawa and M. Kohmoto Phys. Rev. B, **88**, 125426 (2013).

[133] M. V. Moskalets, *Scattering Matrix Approach to Non-Stationary Quantum Transport*. (National Technical University, Kharkiv Polytechnic Institute, Ukraine, 2011).

[134] U. Fano, Physical Review **72** (1): 26, (1947).

[135] J. Tworzydlo, B. Trauzettel, M. Titov, A. Rycerz and C. W. J. Beenakker, Phys. Rev. Lett. **96**, 246802, (2006).

[136] D. D. L. Chung, J. Mat. Sci. **37**, 1475 (2002).

[137] T. Kato, J. Phys. Soc. Jpn. **5**, 435 (1950).

[138] A. Messiah, Quantum Mechanics, North Holland, Amsterdam, **II** (1962).

[139] V. Fock, Z. Phys. **49**, 323 (1928).

[140] M. V. Berry, Proc. R. Soc. London, Ser. A **392**, 45 (1984).

[141] E. H. Hwang and S. Das Sarma, Phys. Rev. B **80**, 075417 (2009).

[142] M. Yankowitz, J. Xue and B. J. LeRoy, J. Phys.: Condens. Matter **26**, 303201 (2014).

[143] C-H. Park, L. Yang, Y.-W. Son, M. L. Cohen and S. G. Louie, Nature Phys. **4**, 213 (2008).

[144] M. Barbier, F. Peeters, P. Vasilopoulos and J. Pereira. Phys. Rev. B **77**, 115446 (2008).

[145] T. G. Pedersen, C. Flindt, J. Pedersen, N. A. Mortensen, A.-P. Jauho and K. Pedersen, Phys Rev. Lett. **100**, 136804 (2008).

[146] C.-H. Park, Y.-W. Son, L. Yang, M. L. Cohen and S. G. Louie, Nano Lett. **8**, 2920 (2008).

[147] C. H. Park, L. Yang, Y. W. Son, M. L. Cohen and S. G. Louie, Phys. Rev. Lett. **101**, 126804 (2008).

[148] N. Abedpour, A. Esmailpour, R. Asgari and M. R. R. Tabar, Phys. Rev. B **79**, 165412 (2009).

[149] R. P. Tiwari and D. Stroud, Phys. Rev. B **79**, 205435 (2009).

[150] C.-H. Park, Y.-W. Son, L. Yang, M. L. Cohen and S. G. Louie, Phys. Rev. Lett. **103**, 046808 (2009).

[151] L. Brey and H. A. Fertig, Phys. Rev. Lett. **103**, 046809 (2009).

[152] I. Snyman, Phys. Rev. B **80**, 054303 (2009).

[153] M. Barbier, P. Vasilopoulos and F. M. Peeters, Phys. Rev. B **80**, 205415, (2009).

[154] M. Barbier, P. Vasilopoulos and F. M. Peeters, Phys. Rev. B **81**, 075438 (2010).

[155] L.-G. Wang and S.-Y. Zhu, Phys. Rev. B **81**, 205444 (2010).

[156] J. Sun, H. A. Fertig and L. Brey, Phys. Rev. Lett. **105** 156801, (2010).

[157] S. Gattenlohner, W. Belzig and M. Titov, Phys. Rev. B **82**, 155417 (2010).

[158] F. Guinea and T. Low, Phil. Trans. R. Soc. A **368**, 5391 (2010).

[159] D. P. Arovas, L. Brey, H. A. Fertig, E-A. Kim and K. Ziegler, New J. Phys. **12**, 123020 (2010).

[160] P. Burset, A. Yeyati, L. Brey and H. Fertig. Phys. Rev. B **83** 195434 (2011).

[161] Y. Y. Kiselev and L. E. Golub, Phys. Rev. B **84** 235440 (2011).

[162] S. Wu, M. Killi and A. Paramekanti, Phys. Rev. B **85**, 195404 (2012).

[163] F. M. D. Pellegrino, G. G. N. Angilella and R. Pucci, Phys. Rev. B **85**, 195409 (2012).

[164] A. Esmailpour, H. Meshkin and M. Saadat, Physica E **50**, 57 (2013).

[165] Q. Wang, R. Shen, L. Sheng, B. G. Wang and D. Y. Xing, Phys. Rev. A **89**, 022121 (2014).

[166] S. Dubey, V. Singh, A. K. Bhat, P. Parikh, S. Grover, R. Sensarma, V. Tripathi, K. Sengupta and M. M.Deshmukh, Nano Lett. **13**, 3990 (2013).

[167] M. Drienovsky, F-X. Schrettenbrunner, A. Sandner, D. Weiss, J. Eroms, M-H. Liu, F. Tkatschenko and K. Richter, Phys. Rev. B **89**, 115421 (2014).

[168] L. Dell'Anna and A. De Martino, Phys. Rev. B **79**, 045420 (2009).

[169] F. Guinea, M. I. Katsnelson and A. K. Geim, Nature Phys. **6** 30 (2010).

[170] M. Taillefumier, V. K. Dugaev, B. Canals, C. Lacroix and P. Bruno, Phys. Rev. B **84**, 085427 (2011).

[171] M. Neek-Amal and F. M. Peeters, Appl. Phys. Lett. **104**, 173106 (2014).

[172] H. Tomori, A. Kanda, H. Goto, Y. Ootuka, K. Tsukagoshi, S. Moriyama, E. Watanabe and D. Tsuya, Applied Physics Express **4**, 075102 (2011).

[173] A. Reserbat-Plantey, D. Kalita, Z. Han, L. Ferlazzo, S. Autier-Laurent, K. Komatsu, C. Li, R. Weil, A. Ralko, L. Marty, S. Guéron, N. Bendiab, H. Bouchiat and V. Bouchiat, Nano Lett. **14** 5044 (2014).

[174] M. Mucha-Kruczyński, J. R. Wallbank and V. I. Fal'ko, Phys. Rev. B **88**, 205418 (2013).

[175] P. Moon and M. Koshino Phys. Rev. B **90**, 155406 (2014).

[176] J. M. B. Lopes dos Santos, N. M. R. Peres and A. H. Castro Neto, Phys. Rev. Lett. **99**, 256802 (2007).

[177] R. Bistritzer and A. H. MacDonald, Phys. Rev. B **81** 245412 (2010).

[178] R. Bistritzer and A. H. MacDonald, Proc. Natl Acad. Sci. **108**, 12233 (2011).

[179] J. M. B. Lopes dos Santos, N. M. R. Peres and A. H. Castro Neto, Phys. Rev. B **86**, 155449 (2012).

[180] P. Moon and M. Koshino, Phys. Rev. B **87**, 205404 (2013).

[181] P. Moon and M. Koshino, Phys. Rev. B **85**, 195458 (2012).

[182] G. Giovannetti, P. A. Khomyakov, G. Brocks, P. J. Kelly and J. van den Brink, Phys. Rev. B **76**, 073103 (2007).

[183] M. Kindermann and P. N. First, Phys. Rev. B **83**, 045425 (2011).

[184] S. Das Sarma, S. Adam, E. H. Hwang and E. Rossi, Rev. Mod. Phys. **83**, 407 (2011).

[185] I. Pletikosić, M. Kralj, P. Pervan, R. Brako, J. Coraux, A. T. N'Diaye, C. Busse and T. Michely, Phys. Rev. Lett. **102**, 056808 (2009).

[186] J. R. Wallbank, M. Mucha-Kruczyński and V. I. Fal'ko, Phys. Rev. B **88**, 155415 (2013).

[187] J. N. Fuchs, F. Piéchon, M. O. Goerbig and G. Montambaux, Euro. Phys. J B, **77**, 351 (2010).

[188] Y. Zhang, Z. Jiang, J. P. Small, M. S. Purewal, Y.-W. Tan, M. Fazlollahi, J. D. Chudow, J. A. Jaszczak, H. L. Stormer, and P. Kim, Phys. Rev. Lett. **96**, 136806, (2006).

[189] P. San-Jose, A. Gutiérrez, M. Sturla, and F. Guinea, Phys. Rev. B **90**, 075428 (2014).

[190] P. San-Jose, A. Gutiérrez, M. Sturla, and F. Guinea, Phys. Rev. B **90**, 115152 (2014).

[191] J. Jung, A. Raoux, Z. Qiao, and A. H. MacDonald, Phys. Rev. B **89**, 205414 (2014).

[192] G. Giovannetti, P. A. Khomyakov, G. Brocks, P. J. Kelly, and J. van den Brink, Phys. Rev. B **76**, 073103 (2007).

[193] F. A. Butler and E. Brown, Phys. Rev. **166**, 630, (1968).

[194] W. .G. Chambers, Phys. Rev. **140**, A135, (1965).

[195] J. R. Wallbank, M. Mucha-Kruczynski, X. Chen, V. I. Fal'ko, Ann. Phys. (Berlin), 1 (2015).

[196] A. Jeffrey, D. Zwillinger, Academic Press, "Table of Integrals, Series, and Products" sixth Edition.

[197] J. M. Luttinger, Phys. Rev. **84**, 814 (1951).

[198] W. Kohn, Phys. Rev. **115**, 1460 (1959).

[199] G. H. Wannier, Rev. Mod. Phys. **34**, 645 (1962).

[200] E. I. Blount, Phys. Rev. **126**, 1636 (1962).

[201] https://en.wikipedia.org/wiki/Fractal.

[202] https://en.wikipedia.org/wiki/Covariance_and_contravariance_of_vectors.